GOETHE UNIVERSITÄT FRANKFURT AM MAIN

MAX-PLANCK-GESELLSCHAFT

Understanding cellular and molecular mechanisms of zebrafish cardiomyocyte integrity and valve interstitial cell differentiation

Dissertation
zur Erlangung des Doktorgrades
der Naturwissenschaften

vorgelegt beim Fachbereich 15
der Johann Wolfgang Goethe-Universität
in Frankfurt am Main

von
Alessandra Gentile
aus Napoli, Italien

Frankfurt 2022
(D30)

vom Fachbereich Biowissenschaften (FB15) der Johann Wolfgang Goethe-Universität als Dissertation angenommen.

Dekan: Prof. Dr. Sven Klimpel

Gutachter: Prof. Dr. Didier Y. R. Stainier

Prof. Dr. Amparo Acker-Palmer

Datum der Disputation:

Reviewers

Prof. Dr. Didier Y. R. Stainier
Department of Developmental Genetics
Max Planck Institute for Heart and Lung Research
Bad Nauheim, Germany

and

Prof. Dr. Amparo Acker-Palmer
Department of Molecular and Cellular Neurobiology
Institute for Cell Biology and Neuroscience
Johann Wolfgang Goethe University
Frankfurt am Main, Germany

ERKLÄRUNG

Ich erkläre hiermit, dass ich mich bisher keiner Doktorprüfung im Mathematisch-Naturwissenschaftlichen Bereich unterzogen habe.

Frankfurt am Main, den .....

(Unterschrift)

VERSICHERUNG

Ich erkläre hiermit, dass ich die vorgelegte Dissertation über **„Understanding cellular and molecular mechanisms of cardiomyocyte integrity and valve interstitial cell differentiation“** selbständig angefertigt und mich anderer Hilfsmittel als der in ihr angegebenen nicht bedient habe, insbesondere, dass alle Entlehnungen aus anderen Schriften mit Angabe der betreffenden Schrift gekennzeichnet sind.

Ich versichere, die Grundsätze der guten wissenschaftlichen Praxis beachtet, und nicht die Hilfe einer kommerziellen Promotionsvermittlung in Anspruch genommen zu haben.

Einen Teil der vrliegende Ergebnisse der Arbeit sind in folgendem Publikationsorgan veröffentlicht:

Gentile A., Bensimon-Brito A., Priya R., Maischein HM., Piesker J., Günther S., Gunawan F., Stainier DYR.; The EMT transcription factor Snai1 maintains myocardial wall integrity by repressing intermediate filament gene expression. *eLife*, 2021; 10:e66143 doi:10.7554/eLife.66143

Gunawan F.*, **Gentile A.***, Gauvrit S., Stainier DYR., Bensimon-Brito A.*; Nfatc1 promotes interstitial cell formation during cardiac valve development in zebrafish. *Circulation Research*, 2020; 126:968–984, doi:10.1161/CIRCRESAHA.119.315992

Frankfurt am Main, den .....

(Unterschrift)

To all my mentors, in life and science

Table of contents

Abbreviations

List of the commonly used abbreviations

Abbreviation	Description
A	Atrium
AJ	Adherens junction
bp	Base pairs
BFP	Blue fluorescent protein
bHLH	Basic helix-loop-helix
BMP	Bone morphogenetic protein
CM	Cardiomyocyte
CRISPR	Clustered regularly interspaced short palindromic repeats
Cas9	Clustered regularly interspaced short palindromic repeat-associated 9
dpf	Days post-fertilization
desmb	*desmin b*
EC	Endothelial/endocardial cell
ECM	Extracellular matrix
EMT	Epithelial-to-mesenchymal transition
EndoMT	Endocardial-to-mesenchymal transition
EdU	5-ethynyl-2'-deoxyuridine
gRNA	Guide RNA
GFP	Green fluorescent protein
GO	Gene ontology
FACS	Fluorescence activated cell sorting
hpf	Hours post-fertilization
HRMA	High resolution melt analysis
MO	Morpholino
NFATc1	Nuclear factor of activated T-cell 1
nls	Nuclear localization signal

NCC	Neural crest cell
PCR	Polymerase chain reaction
PTC	Premature terminated codon
qPCR	Quantitative realtime polymerase chain reaction
RFP	Red fluorescent protein
Tg	Transgenic line
TUNEL	Terminal deoxynucleotidyl transferase dUTP nick end labeling
UAS	Upstream activating sequence
UTR	Untranslated region
V	Ventricle
VECs	Valve endocardial cells
VICs	Valve interstitial cells
ZO-1	Zona occludens 1

1. Introduction

The development of a complex organ including the heart requires precise spatial and temporal morphogenetic events, involving different cell types that interact with each other and respond to the surrounding extracellular matrix, as well as to intrinsic and extrinsic mechanical forces. This PhD thesis will focus specifically on: 1) the transcriptional regulation of the cardiac wall integrity; and 2) the cellular and molecular mechanisms behind the valve interstitial cells (VICs) establishment, using zebrafish as a model system.

1.1 Cardiac morphogenesis: an evolutionary prospective

In the animal kingdom, the emergence of the first heart-like structure has been dated back to 500 million years ago, when a simple tubular organ that lacks compartmentalization appeared in the ancestral bilaterian (Bishopric, 2005), functioning as a peristaltic pump resembling the vessel-like organ of tunicates and amphioxus (Olson, 2006). Later in the evolution, the insect "heart" is the first closed cardiac compartment with primitive valves (Bodmer, 1995). The evolution of the heart then required the addition of new structures and features due to a transition from an aquatic to a terrestrial environment. The amphibian heart differs from the simple two-chambered fish heart, with the amphibian heart possessing two separated atrium and one ventricle to allow for pulmonary circulation (Moorman and Christoffels, 2003; Simões-Costa et al., 2005). The need to better separate the oxygenated and deoxygenated blood in pulmonary and aortic circulation, respectively, is resolved with the development of the four-chambered hearts in terrestrial vertebrates (Simões-Costa et al., 2005; Olson, 2006; Grosskurth et al., 2008) (Figure 1.1). The vertebrate heart is a complex and powerful pump with a conduction system, valves, trabeculae, and coronary vasculature.

The vertebrate cardiac development starts at the end of gastrulation, when the three germ layers, ectoderm, mesoderm, and endoderm, gradually develop into the internal organ (Pérez-Pomares et al., 2009). Progenitor cells from the lateral plate mesoderm

start to migrate towards the midline to give rise to the heart, the first functional organ in the embryo (Harvey, 2002).

At this stage, the heart is a primitive structure, resembling the tubular heart of simple chordates. Several morphogenetic processes are then required to transform the primitive linear heart tube into a powerful pumping organ, with separate distinct chambers and valves (Harvey, 2002). All these processes are governed by a core set of evolutionarily conserved transcription factors that during evolution underwent gene duplication and epigenetic modification to allow the acquisition of specialized cardiac structures (Bruneau, 2002; Olson, 2006; Srivastava and Olson, 2000). Gene duplications and modifications in regulatory elements allow new gene expression patterns, leading to specialized structures and functions (Bruneau, 2002; Olson, 2006; Srivastava and Olson, 2000).

The common evolutionary origin of the different cardiac structures together with the conserved molecular pathway make possible to study cardiac development using a simple model organism, such as the two-chambered zebrafish heart.

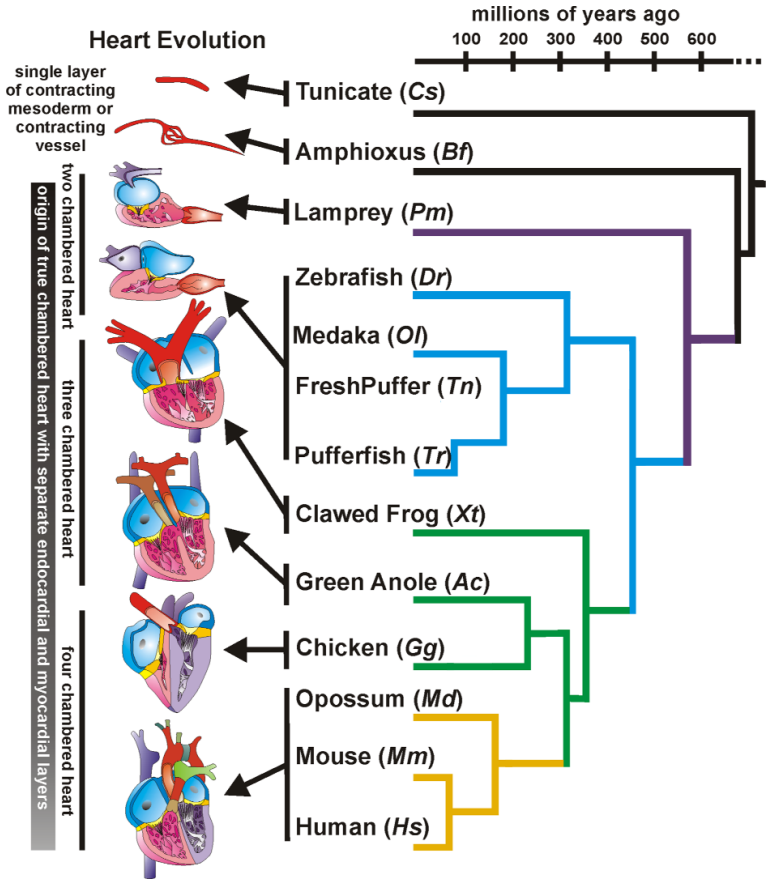

Figure 1.1: Phylogenetic tree of the evolution of the heart

Schematic illustrating the evolution of the heart structure from the Urochordata to Craniata. Image adapted from Plos One (Grosskurth et. al, 2008), Figure 8. License: CC BY 4.0.

1.2 Zebrafish heart: a simple structure to answer complex questions

The zebrafish heart is a two-chambered structure, with one ventricle and one atrium with an atrioventricular valve at the center, and composed of three cell layers: the outer myocardium and the inner endocardium separated by an extracellular matrix (cardiac jelly) (Figure 1.2), and later during development, the epicardium that covers the myocardium.

Although it has a simpler structure compared with the mammalian heart, the zebrafish heart is a powerful model system for cardiovascular research (Fishman and Stainier, 1994; Bakkers, 2011; Staudt and Stainier, 2012; Brown et al., 2016). The main advantages include the capability of zebrafish to survive without a functioning cardiovascular system for several days. Moreover, in the past decades, several new techniques have been developed to rapidly generate mutants and transgenic lines, allowing the study of cardiac morphology at the single-cell level under physiological conditions and of molecular mechanisms underlying heart development (Fishman and Stainier, 1994; Bakkers, 2011; Staudt and Stainier, 2012; Brown et al., 2016). In this work, I took advantage of all the features of the zebrafish as a model system to better understand heart morphogenesis, in the context of myocardial and valve development.

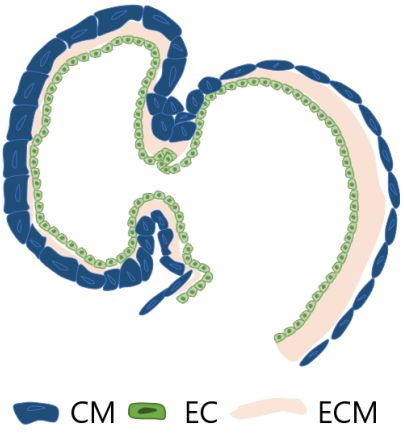

Figure 1.2: Zebrafish heart

Cartoon representing the zebrafish heart in the early stages of development. Cardiomyocytes (CMs), forming the outer layer of the heart, are represented in blue. Endocardial cells (ECs), forming the inner layer of the heart, are represented in green. Between CMs and ECs there is the extracellular matrix (ECM), here represented in light orange.

1.3 Zebrafish cardiac development: from cardiac progenitor specification and migration to two-chambered heart formation

The zebrafish cardiac development starts at around 5 hours post-fertilization (hpf) (Warga and Kimmel, 1990; Warga and Nüsslein-Volhard, 1999; Hallab et al., 2021). At the blastula stage, cardiac progenitors are located in the lateral fields on either side of the embryo, with endocardial progenitors placed anteriorly to the myocardial progenitors, remaining in these positions until the end of the gastrulation (Warga and Kimmel, 1990; Yelon et al., 1999). Concurrently, the dorsal forerunner cells (DFCs) that give rise to the Kupffer's vesicle are specified at the dorsal margin of the embryo (Oteíza et al., 2008). The Kupffer's vesicle controls cardiac left/right asymmetry (Essner et al., 2005). Indeed, the asymmetric distribution of the cilia in the dorsoanterior region of the Kupffer's contributes to establish the first cardiac asymmetry, by generating a directional fluid flow resulting in asymmetric gene expression (Wang et al., 2012). At the beginning of somitogenesis around (7 somite stage (ss)), cardiac precursors are found in the anterior lateral plate mesoderm (ALPM) (Warga and Kimmel, 1990; Yelon et al., 1999). Endocardial cells start to express endothelial-specific genes such as *fli1a* at 10 ss, whereas ventricular and atrial CMs start to differentiate at 12 ss and 15 ss respectively, expressing ventricular-specific (*nkx2.5*) and atrial-specific (*myh6*) factors (Glickman and Yelon, 2002; Staudt and Stainier, 2012). ECs then migrate towards the midline, where they fuse at 14 ss, followed by myocardial cells that will encapsulate the endocardium and give rise to the cardiac cone at 20 ss (Warga and Kimmel, 1990; Yelon et al., 1999). At 22 hpf, the atrium is positioned laterally and the ventricle is positioned medially (Yelon et al., 1999; Lombardo et al., 2019). The cardiac cone elongates to give rise to the heart tube by 24 hpf (Stainier, 2001). This structure is formed by atrial and ventricular CMs, and ECs, coming from the first heart field (FHF) (de Pater et al., 2009). From the beginning of development, an extracellular matrix (ECM), also known as cardiac jelly, forms between the two cell layers. At this stage, the contraction starts and propagates through the myocardium (Stainier, 2001). Although the valve is not formed yet, the contractile and compressive movements of the heart tube maximize the unidirectional blood flow from the atrium to the ventricle (Paul J. Scherz et al., 2008).

At 28 hpf, additional cells are recruited to the heart tube from the second heart field (SHF). At the same time, heart jogging occurs, in which the atrium moves to the left of the heart (Chen et al., 1997; Rohr et al., 2008). By 48 hpf, the heart undergoes looping and assumes an S-shape due to the growth of the chambers, proceeding until at least 54 hpf (Lombardo et al., 2019). During this process, the two-chambered heart starts to be separated by the constriction of the atrioventricular canal with changes in the shape of the myocardial wall (Beis, 2005). Concomitantly, the formation of a ventricular constriction gives rise to the outflow tract (OFT), including the *bulbus arteriosus* and aorta. The development of the OFT is completed by 96 hpf when it is covered by smooth muscle cells from the SHF (Hu et al., 2000). Starting around 56 and 60 hpf, two major morphogenetic processes start: valve formation and trabeculation (Beis, 2005; Paul J. Scherz et al., 2008; Peshkovsky et al., 2011; Staudt et al., 2014; Gunawan et al., 2019). Between 55 hpf and 72 hpf, epicardial cells attach to the myocardium to entirely cover it, to form the most outer mesothelial layer of the heart (Serluca, 2008; Peralta et al., 2013, 2014; Weinberger et al., 2020). Finally, the development of the conduction system is completed by 100 hpf (Chi et al., 2008). Once the chamber formation is complete, another cell type contributes to the heart morphogenesis, neural crest cells (NCCs) that derive from the ectoderm. These cells contribute to the maturation of the great vessels, to the OFT and the valve (Cavanaugh et al., 2015).

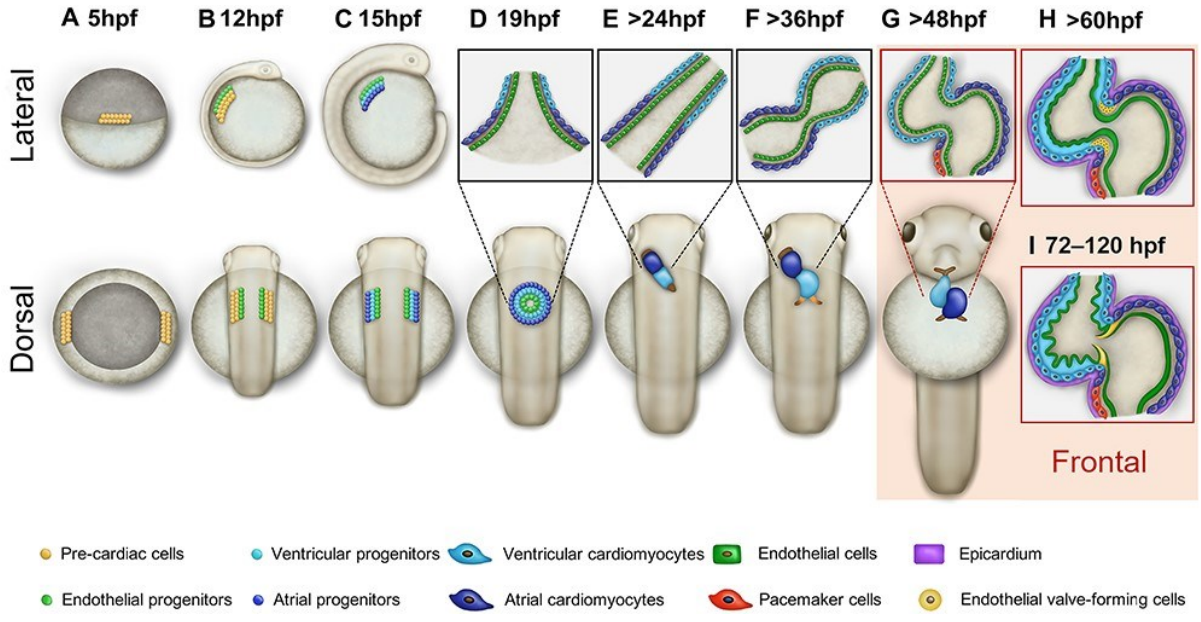

Figure 1.3: Zebrafish cardiac developmental from 5 hpf to 120 hpf

Cartoon representing zebrafish cardiac development. **A-H)** Lateral and dorsal representation of the zebrafish embryo. Cardiac progenitor cells (yellow) are already present at 5 hpf (A). By 12 hpf endothelial progenitors appear (green cells) (B). At 15 hpf, the cardiac progenitors are distinguished in ventricular (light blue) and atrial (dark blue) progenitors (C). At 19 hpf there is the formation of the cardiac cone (D). At around 24 hpf the heart tube is formed (E). Starting from 36 hpf until 54 hpf, the heart starts to loop and there is the formation of the two chambers (F). At 48 hpf, the cardiac conduction system starts to form and there is the appearance of the pacemaker cells (in red) (G). At 60 hpf, the epicardial cells (purple) start to attach to the ventricle and later on the atrium (H). I) Frontal view of the zebrafish heart. The later stages of heart development include trabeculation and valvulogenesis (yellow cells). Image reprinted from Briefings in Functional Genomics (Hallab et. al, 2021), Figure 1. License: CC BY 4.0.

1.4 Cardiac morphogenesis: shaping the heart

The formation of a complex organ such as the heart requires complex morphogenetic events that result in cell shape changes and growth, as well as folding and elongation of the tissue. Different mechanisms, such as actomyosin dynamics, collective cell migration, and epithelial-to-mesenchymal transition (EMT) regulate tissue morphogenesis as well as tissue integrity. In the following sections, I will review the current knowledge on these morphogenetic events in the heart, mostly focusing on the myocardial and endocardial layers.

1.4.1 Myocardium: structure and maturation

The myocardium is the muscular layer of the cardiac wall and is composed of individual cells called cardiomyocytes (CMs) (Sequeira et al., 2014; Gautel and Djinović-Carugo, 2016). The cardiac wall can be considered as an epithelial-like tissue: CMs are polarized with their basal domain in contact with the cardiac jelly, and the apical domain facing the outside of the heart (Jiménez-Amilburu et al., 2016). CMs are the contractile units of the heart with specialized cytoskeletal structures, the myofibrils that generate contractile forces (Sequeira et al., 2014; Gautel and Djinović-Carugo, 2016). The myofibrils are composed of repeated subunits known as sarcomeres that are connected

at Z-discs. The sarcomere is in turn composed of two main components: 1) contractile proteins, such as thin actin and thick myosin filaments; 2) cytoskeletal proteins, such as actin, microtubules, and intermediate filaments (IFs) (Sequeira et al., 2014; Grimes et al., 2019). Muscle contraction results from the ATP hydrolysis that shortens the distance between Z-discs, which is dependent on the actin-myosin interactions (McKillop and Geeves, 1993; Lehman et al., 2000).

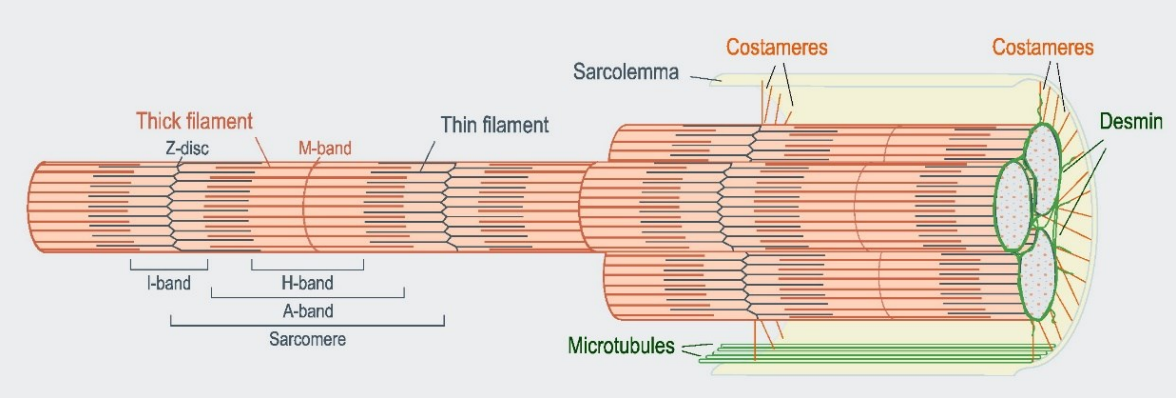

Figure 1.4.1: Cardiac muscle structure

Cartoon illustrating the anatomy of the cardiac muscle. The cardiac muscle is composed of the sarcomere, connected through the Z-disc. The repetition of the sarcomeres composes the myofibrils that are connected to the sarcolemma through the constameres. In direct contact with the myofibrils, there are cytoskeletal proteins as microtubules and intermediate filaments (Desmin). Figure adapted and reprinted from Biochimica et Biophysica Acta (BBA) – Biomembranes (Sequeira et al., 2013), Figure 1, with permission from Elsevier. License: 5253860022475.

1.4.2 Cardiomyocyte cytoskeleton

The cytoskeleton plays a key role during cell proliferation and migration, thus most of the studies were performed in proliferative cell types. For this reason, little is known about the non-contractile cytoskeletal proteins of CMs, such as microtubules, cytoplasmic actin, and IFs. Contrary to other cell types, CMs are in constant contractile stress, and they have low replicative capacity, suggesting that the regulation of the cytoskeletal proteins might be different (Grimes et al., 2019). In addition, it has been shown that the cytoskeletal proteins are in direct contact with sarcomeres at the

intercalated discs, mediating electrical and mechanical signaling events (Estigoy et al., 2009; Pruna and Ehler, 2020). In particular, the IF protein Desmin connects the sarcomere to the nucleus and the mitochondria (Capetanaki et al., 2015). Loss- or gain-of-function of Desmin have been associated with cardiomyopathies, known as desminopathies (Taylor Matthew R.G. et al., 2007; Capetanaki et al., 2015; Ramspacher et al., 2015; Chen et al., 2018). However, the mechanism by which Desmin maintains CM wall integrity remains poorly understood.

The intercalated discs connect adjacent CMs through adherens junctions (AJ or fascia adherens), gap junctions, and desmosomes, guaranteeing muscle integrity and contraction (Rampazzo et al., 2014) (Figure 1.4.2). One of the components of AJs that plays an essential role during heart development is N-cadherin. It has been shown that loss-of-function of N-cadherin in murine cardiac myocytes results in disruption of the intercalated discs assembly, leading to cardiomyopathy (Kostetskii et al., 2005). Similar to AJs, desmosomes are protein complexes that play an essential role in heart tissue integrity (Patel and Green, 2014). It has been shown that mutations in the desmosomal proteins are associated with heart diseases, such as arrhythmic cardiomyopathies (Saffitz, 2009; Wang et al., 2018).

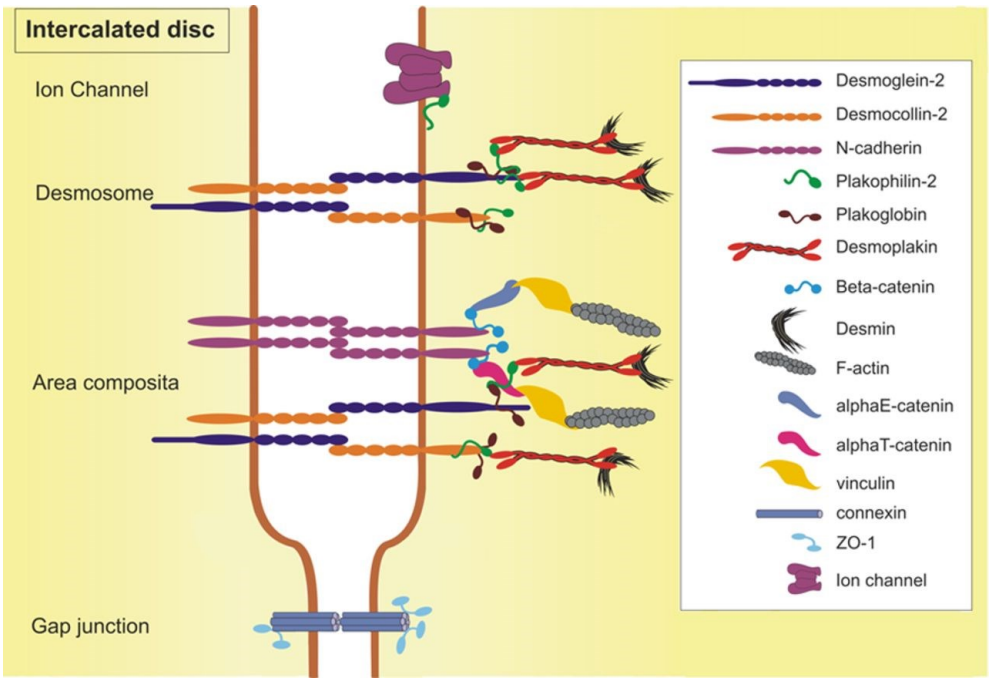

Figure 1.4.2: Intercalated disc structure

Schematic representing the junctions present at the intercalated disc. From the bottom, three types of junctions are found: gap junctions (connexin); area composita, heart-specific type of junctions, composed of adherns junctions (N-cadherin) and desmosome; classical desmosome (desmosomal cadherins); and ion channel. Image reprinted from Circulation: Cardiovascular Genetics, (Rampazzo et al., 2014), Figure 1, with permission from Wolters Kluwer Health, Inc. License: 5253860259067.

1.4.2 Cardiac trabeculation

The outer compact layer and the inner trabecular layer compose the cardiac wall (Han et al., 2016; del Monte-Nieto et al., 2018; Priya et al., 2020). The trabecular layer is composed of ridge-like structures the project into the ventricular lumen and increase contraction and blood pumping (Meyer and Birchmeier, 1995; Liu et al., 2010; Samsa et al., 2015). Trabeculation is a very tightly regulated process that involves multiple cellular and molecular processes. Although this process is highly conserved among vertebrates, differences were identified between zebrafish and mouse (Gunawan et al., 2021). At the cellular level, it has been shown that the onset of trabeculation in mice is driven by migration and oriented cell division (Li et al., 2016; Passer et al., 2016; Miao et al., 2019; Yue et al., 2020), whereas in zebrafish the major driver of trabecular CMs is cellular delamination (Liu et al., 2010; Gupta and Poss, 2012; Staudt et al., 2014; Jiménez-Amilburu et al., 2016; Priya et al., 2020). In particular, at 55 hpf a subset of CMs from the compact layer lose their apicobasal polarity and stochastically delaminate into the trabecular layer (Jiménez-Amilburu et al., 2016). Our group recently showed that this process of delamination is driven by actomyosin tension heterogeneity that is generated when the tissue starts to proliferate (Priya et al., 2020). Signaling pathways that have been involved in trabecular morphogenesis include Nrg/Erbb2 (Meyer and Birchmeier, 1995; Lee et al., 1995; Liu et al., 2010; Rasouli and Stainier, 2017) and Notch (Grego-Bessa et al., 2007; Samsa et al., 2015; Han et al., 2016; Salguero-Jiménez et al., 2018; Priya et al., 2020). Nrg is secreted from the endocardium and acts through the Erbb receptor in the myocardium, promoting proliferation (Liu et al., 2010; Wadugu and Kühn, 2012; Rasouli and Stainier, 2017; Uribe et al., 2018; Priya et al., 2020), delamination (Liu et al., 2010; Rasouli and Stainier, 2017; Priya et al., 2020) and ECM

deposition (del Monte-Nieto et al., 2018). While in mice, the inactivation of Notch in CMs does not impair cardiac development (Salguero-Jiménez et al., 2018), it has been shown that non-delaminating compact layer CMs in zebrafish activate Notch in a spatiotemporal manner and the patterning of myocardial wall occurs via lateral inhibition (Han et al., 2016; Priya et al., 2020). Moreover, increasing CM contractility is sufficient to induce delamination and trigger Notch activation even in the absence of Nrg/Erbb2 (Priya et al., 2020). Trabeculation and CM morphology are also influenced by unidirectional blood flow and contractility. It has been shown that when *cardiac troponin T type 2* (*tnnt2a*) or *atrial myosin heavy chain* (*myh6*) is lost and ventricular or atrial contractility is reduced, cardiac trabeculation is impaired (Staudt et al., 2014). Reduced blood flow and hemodynamic shear stress also lead to defective trabeculation, as shown in *gata1* morphants (Peshkovsky et al., 2011; Lee et al., 2016).

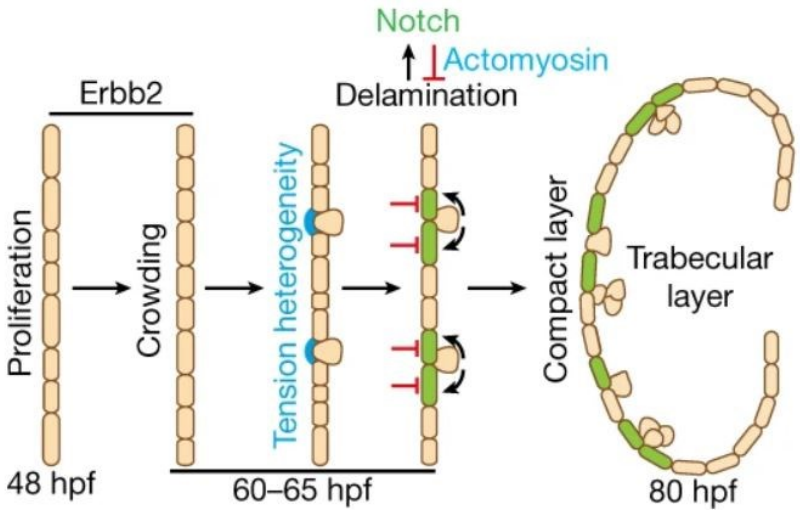

Figure 1.4.3: The process of trabeculation in zebrafish

During zebrafish cardiac development, the CMs proliferate and the tension heterogeneity that results from the crowding triggers the delamination of CMs. This process is mediated by Notch signaling in the compact layer CMs that blocks their delamination regulating their actomyosin cytoskeleton, and preserving myocardial wall architecture. Image reprinted from Nature, (Priya et al, 2020), Figure 4.

1.4.3 Cardiac wall integrity and homeostasis

The heart is constantly exposed to mechanical forces that arise from cardiac contraction and shear stress from blood flow. The cytoskeleton is very important in maintaining tissue integrity and in providing mechanical support (Sequeira et al., 2014; Gautel and Djinović-Carugo, 2016). Recently, it has been shown that contractility-induced mechanical forces play a role in cardiac wall integrity. Our group showed that loss of *vinculin* leads to disorganization of the myofilaments in the zebrafish heart (Fukuda et al., 2019). Moreover, increasing cardiac contractility in these mutants disrupts cardiac wall integrity and induces cell extrusion, suggesting that Vinculin plays an important role in myofilament maturation and cardiac wall integrity (Fukuda et al., 2019).

Cell extrusion is an important process in which cells are physically excluded from the tissue. Epithelial cells use cell extrusion not only to maintain tissue homeostasis but also for cell fate determination during development (Kocgozlu et al., 2016; Wee et al., 2020). Additionally, during morphogenesis cell extrusion can be used to generate new shapes and tissues (Priya et al., 2020; Zulueta-Coarasa and Rosenblatt, 2022). The process of extrusion is typically mediated by actomyosin contractility and cell-cell interactions. First, a contractile actomyosin ring is formed in the cortex of the extruding cell, leading to the formation of an actomyosin ring also in the neighboring cells, due to the tension generated. Then, by constricting the apical or basal domain, the ring pushes the cell out and the neighboring cells come closer (Zulueta-Coarasa and Rosenblatt, 2022). At the molecular level, the formation of the actomyosin ring is mediated by the Rho pathway (Wee et al., 2020; Duszyc et al., 2021). Interestingly, cell-cell and cell-matrix interactions need to be precisely regulated during extrusion (Le et al., 2021); however, the mechanisms behind this regulation remain poorly understood. Indeed, there is evidence that the downregulation of cell-cell adhesion around the extruding cell is needed to promote its elimination (Saitoh et al., 2017). On the other hand, it has also been shown that depletion of E-cadherin leads to impairment of the extruding process (Duszyc et al., 2021). More studies are needed to better elucidate the cellular processes of cell extrusion.

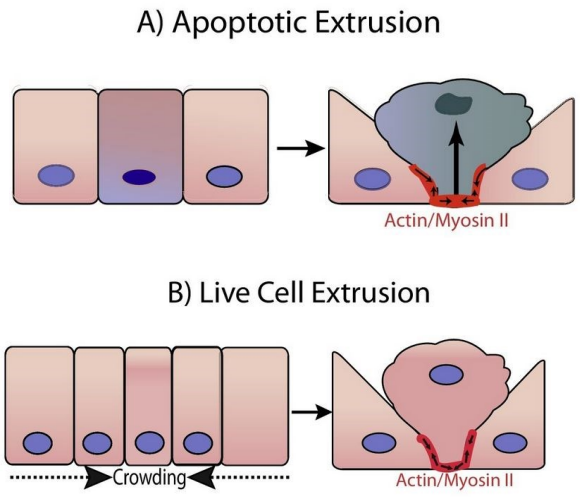

Figure 1.4.4: Epithelial cell extrusion

A-B) Epithelial cells can be eliminated from the layer through the process of apoptotic (A) or live cell (B) extrusion. This process takes place by a pulsatile contraction mediated by the actomyosin machinery. Image adapted and reprinted from Seminars in Cell & Developmental Biology, (Gudipaty and Rosenblatt, 2017), Figure 1, with permission from Elsevier. License: 5253860482172.

1.5 Development and function of the endocardium

The endocardium constitutes the inner cardiac layer and is important for the formation of the valve and trabeculae. As mentioned above, in zebrafish, the specification of the endocardial cells starts after gastrulation, when a cluster of cells express endothelial markers, such as Etv2 or Tie2 (Lee et al., 1994). Once specified and starting to migrate toward the midline to form the heart tube, endocardial cells express vascular markers or endocardial markers including Nfatc1 (Wong et al., 2012). As the heart continues to develop, the endocardial cells will contribute to the formation of the valve, as well as trabeculation and coronary formation. I will mostly focus on cardiac valve formation, and how the endocardium contributes to these critical structures.

1.5.1 Cardiac valve formation

The main function of the cardiac valves is to ensure unidirectional blood flow (O'Donnell and Yutzey, 2020). In the two-chambered zebrafish heart, cardiac valves

are located at the junction between the ventricle and the atrium, and between the ventricle and *bulbus arteriosus* (BA). They are composed of the valve endocardial cells (VECs), as well as the fibroblast-like valve interstitial cells (VICs) that secrete the surrounding ECM. The VICs are fundamental to maintain the cardiac valve structural integrity. The early steps of the atrioventricular (AV) and BA valve development involve the migration of VECs towards the cardiac jelly and fold into the valve leaflets (Gunawan et al., 2019). Similar to trabeculation, cardiac valve development is different between mammals and fish. It has been shown that in mouse, the first event of valvulogenesis is the expansion of the ECM followed by migration of the VECs into the ECM; these events form the cardiac cushion (O'Donnell and Yutzey, 2020). The VECs undergo endothelial-to-mesenchymal transition (EndoMT), losing their adhesion and eventually becoming VICs (Luna-Zurita et al., 2010). Our group has shown that in zebrafish, the formation of the AV valve does not require the expansion of the ECM, but instead, VECs collectively migrate into the ECM, maintain their adhesion, and form a folded structure at the end of their migration (Gunawan et al., 2019). Collective VEC collective migration is driven by focal adhesion (Gunawan et al., 2019). In the BA valve, it has been shown that VECs invaginate and form a folded tissue (Duchemin et al., 2019; Boezio et al., 2020; Sidhwani et al., 2020). Another important regulator of valvulogenesis is mechanical stress induced by blood flow. It has been shown that blood flow can activate mechanoresponsive ion channels, receptors, and transcription factors (Heckel et al., 2015; Steed et al., 2016a; Donat et al., 2018; Duchemin et al., 2019; Fontana et al., 2020; Sidhwani et al., 2020; Fukui et al., 2021; Paolini et al., 2021). For instance, KLF2 is expressed correspondingly to shear stress in both mouse and zebrafish (Chiplunkar et al., 2013; Steed et al., 2016a, p. 2; Goddard et al., 2017; Paolini et al., 2021). Mechanical forces are not only required for valve formation but also for its remodeling (Goddard et al., 2017; Qu et al., 2019). At the transcriptional level, one of the known regulators of valvulogenesis is the transcription factor Nfatc1. It has been shown that mouse *Nfatc1* loss of function mutants are embryonic lethal and display valve defects (Ranger et al., 1998; de la Pompa et al., 1998; Combs and Yutzey, 2009a; Wu et al., 2011). Although it has been described the presence of VICs in zebrafish adult and larval valves, the cellular and molecular mechanism by which they develop are

unknown. With this work, I describe the cellular processes behind VICs development and uncovered the molecular mechanisms of this morphogenetic process.

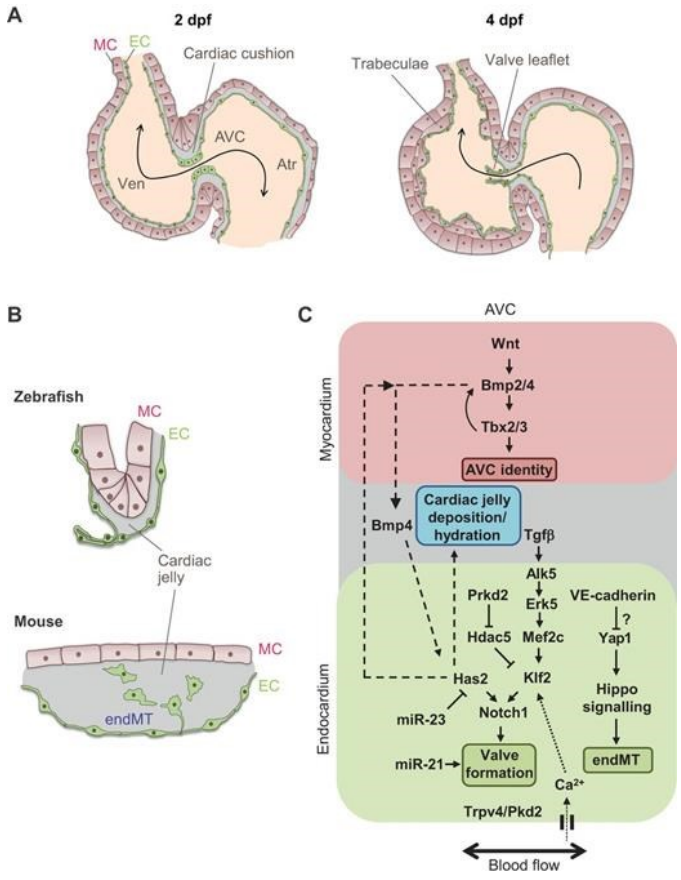

Figure 1.5.1: zebrafish cardiac valve formation

A) Cartoon representing zebrafish heart development, with a focus on valve formation. B) Cartoon comparing zebrafish and mouse development. In zebrafish the valve development starts with the collective migration of the valve endocardial cells, whereas in mouse endocardial cells undergo endothelial to mesenchymal transition (EndoMT), invading the extracellular matrix. C) Molecular factors involved in cardiac valve development. Image reprinted from Development (Haack et al., 2016), Figure 4, with permission from The Company of Biologists Limited.

1.6 Cardiac jelly: the extracellular matrix (ECM) of the heart

The cardiac jelly is the specialized ECM that separates the myocardium from the endocardium, providing chemical and mechanical signals to cardiac cells. The cardiac jelly composition can be divided into two types of ECM: the basement membrane, which

includes a network of core proteins, and the interstitial matrix, composed of elastic fibers, collagens, and proteoglycans (Frantz et al., 2010). ECM dynamics are fundamental during development, and not only the regulation of its production but also its degradation. Through synthesis and degradation, highly specialized ECM is generated to support organ morphogenesis.

The role of the ECM in cardiac development is important right from the early stages of development: the migration of the cardiac precursors is mediated by the deposition of the ECM component Fibronectin (George et al., 1997; Le A. Trinh and Stainier, 2004; Qiao et al., 2014). Indeed, zebrafish *fibronectin* mutants exhibit defects in cardiomyocyte migration, leading to cardia bifida (Le A. Trinh and Stainier, 2004). The same phenotype is observed when the matrix metalloproteases MMP2, which can degrade fibronectin, are inhibited (Linask et al., 2005), confirming that remodeling of the ECM is very important. Another important component of the cardiac jelly is Hyaluronic acid (HA), which is synthesized by the Hyaluronan synthases, including Has2. It has been shown that *has2* expression is asymmetric on the left side of the cardiac disc, opposite to the expression of BMP signaling on the right side. These data suggest that regionalization of the ECM is important for cardiac morphogenesis (Veerkamp et al., 2013). Moreover, the role of HA and its modulators is also observed during other stages of cardiac development. For example, loss-of-function of *cemip2* in zebrafish leads to impairment of looping morphogenesis (Smith et al., 2011; Totong et al., 2011; Hernandez et al., 2019).

Furthermore, ECM dynamics also drive endocardial morphogenesis. It has been shown that the ECM component encoding *fibrillin2* is important to maintain endocardial integrity (Mellman et al., 2012). During valve development, the ECM is fundamental for the formation of the VICs and it has been shown by zebrafish studies that Fibronectin is downstream of *klf2a*, suggesting that shear stress generated by the blood flow is involved in creating a regionalized ECM (Beis, 2005; Vermot et al., 2009a). Since the ECM is in between the myocardium and endocardium, its turnover facilitated the interaction between these tissues. Indeed, degradation of the ECM is observed before the onset of cardiac trabeculation (Cooley et al., 2012; del Monte-Nieto et al., 2018).

Although there is an increase in our understanding of ECM, little is known about the remodelers and the mechanisms behind the regionalized turnover. Further studies are needed to better understand the role of ECM dynamics during cardiac development.

1.7 Epicardial development

The epicardium is a population of mesothelial cells that cover the myocardial layer at later stages of embryonic (mammals)/larval (zebrafish) development. The epicardium first develops as a cluster of extracardiac cells, also called the proepicardial organ, situated dorsal to the developing heart (Simões and Riley, 2018; Quijada et al., 2020). From this structure, the preepicardial cells delaminate and attach to the myocardium, a process that is dependent on the presence of the pericardial fluid outside of the myocardium (Peralta et al., 2013). Once attached to the myocardium, the epicardial cells proliferate and cover the majority of the myocardial tissue. Once the attachment of the epicardium is complete, these cells undergo epithelial-to-mesenchymal transition to give rise to epicardial-derived cells (EPDC), which further contribute to the coronary vasculature and the fibroblasts in mature hearts (Simões and Riley, 2018; Quijada et al., 2020).

1.8 Epithelial-to-mesenchymal transition (EMT) during cardiac development

EMT is a key process during tissue and organ morphogenesis (Nieto et al., 2016). This process allows cells to be plastic and change from an epithelial/epithelial-like state to a mesenchymal state, and potentially migratory. During this process, two key events take place: 1) epithelial cells lose their polarity and intracellular adhesions, and 2) they activate EMT-promoting factors, which include a series of transcription factors (EMT-TFs) such as SNAIL1 and TWIST1.

During development, EMT is necessary since the beginning of embryogenesis. The first EMT occurs during implantation and formation of the placenta (Vićovac and Aplin, 1996). Later, during gastrulation, cells from the mesoendoderm undergo EMT giving rise to mesoderm and endoderm (Leptin and Grunewald, 1990; Baum et al., 2008; Lim

and Thiery, 2012). During embryonic development, EMT also occurs in the epithelial cells of the neuroectoderm, which leads to the formation of the neural crest cells (Christ et al., 1983; Dupin et al., 2007). During organogenesis, one of the organs that involves many EMT processes is the heart.

Several cycles of EMT occur in different cardiac cell populations during heart morphogenesis. First, cardiac progenitors undergo EMT to form the heart primordium during gastrulation. The transcription factor Snail1 is involved in the formation of these mesenchymal cardiac precursors cells. In particular, it has been shown in zebrafish that Snai1 is involved in the migration of the cardiac precursors (Qiao et al., 2014). Second, cardiac valves are formed as the endocardial cells in the atrioventricular and outflow canals undergo EMT (Luna-Zurita et al., 2010). The TGFβ pathway is involved in endocardial formation, and interestingly the transcription factor Twist1 is expressed in the early stages of endocardial development but downregulated during cardiac valve interstitial cell formation (Chakraborty et al., 2010). Lastly, epicardial cells undergo EMT to give rise to EPDCs (Simões and Riley, 2018; Quijada et al., 2020). In addition, EMT also drives the migration of NCCs that will contribute to the valve cell population (Phillips et al., 2013). It is important to note that most studies previously focused on endocardial and epicardial cells; however, little is known about myocardial EMT.

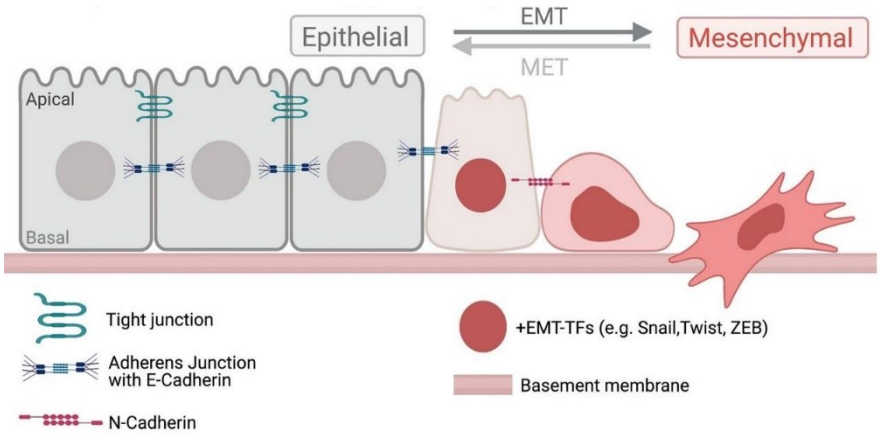

Figure 1.6: Epithelial-to-mesenchymal transition (EMT) process

Epithelial cells (in grey) can change from being polarized cells connected to each other through junctions to more migratory mesenchymal cells (in pink). This process is mediated by the

activation of transcription factors such as Snail and Twist. Image reprinted from Cell Communication and Signaling, (Amack et al., 2021), Figure 1, License: CC BY 4.0.

1.8.1 EMT-transcription factors (EMT-TFs)

Core canonical EMT-TF families belong to two main classes: zinc-finger (Snai1) and basic helix-loop-helix (bHLH) (Twist1) transcription factors (Stemmler et al., 2019).

1.8.2 The zinc finger transcription factor Snai1

The transcription factor Snai1 is a zinc-finger protein that is highly conserved from flies to mammals. It has an evolutionarily conserved SNAG domain at the N-terminal, important for binding of co-repressors, and a highly conserved zinc-finger domain at the C-terminus, by which it binds to core DNA sequences CANNTG, particularly E-box motifs, in its target gene regulatory regions. Other important domains in the Snai1 protein are a serine-rich domain and a nuclear export sequence, in the central region of the protein, which are important for the regulation of its stability and its subcellular mobility, respectively (Nieto et al., 1994; Nieto, 2002; Díaz et al., 2014; Baulida et al., 2019)(Figure 1.7).

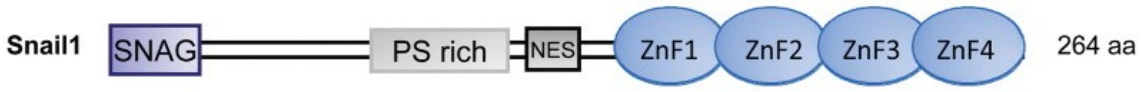

Figure 1.7: Snai1 protein structure

Cartoon of Snai1 protein structure. Image adapted and reprinted from Cell Adhesion and Migration, (Diaz et al., 2014), Figure 1, License: Copyright © Taylor & Francis Group, LLC

Snai1 was identified for the first time in Drosophila, where it acts as a repressor to inhibit the expression of neuroectodermal genes, playing a key role in the formation of the mesoderm and neural crest (Grau et al., 1984; Nüsslein-Volhard et al., 1984; Leptin, 1991). In particular, to regulate EMT, Snai1 binds to the E-box domain in the promoter region of *E-cadherin*, to inhibit its expression (Batlle et al., 2000; Cano et al., 2000). A similar role has been described also in mammalian cancer cells (Kaufhold and Bonavida, 2014). Moreover, it has been shown that Snai1 global knockout in mice is embryonic lethal due to impaired gastrulation (Carver et al., 2001). Snail1 is also

involved in the downregulation of other epithelial genes and associated with the upregulation of genes linked to mesenchymal markers (Cano et al., 2000). However, EMT-independent roles for Snai1 have been described as well, such as regulation of cellular contractility. During Drosophila gastrulation, Snai1 is implicated in the formation of the ventral furrow, where it induces the pulse contractions of medial-apical actomyosin networks that lead to apical constriction (Martin et al., 2010; Mason et al., 2013; Weng and Wieschaus, 2016)(Figure 1.8).

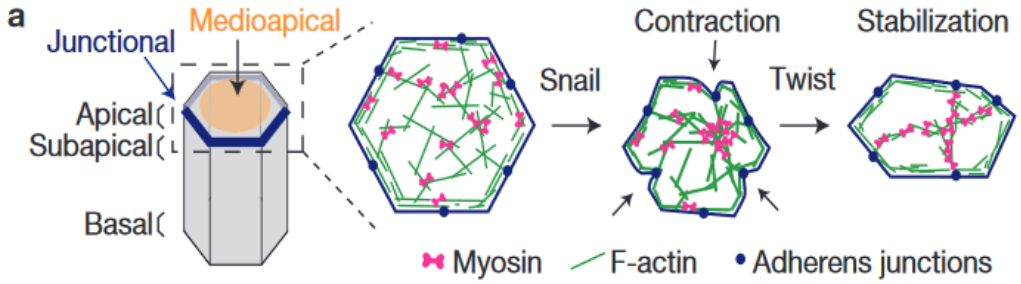

Figure 1.8: Schematic of epithelial cell apical constriction

During apical constriction, the initiation of the process is mediated by Snail and the stabilization of the cell shape by Twist1. Image adapted and reprinted from Nature Cell Biology, (Mason et al., 2013), Figure 1, License: 5241400239403.

During cardiac development, studies in mice have shown that endothelial conditional *Snai1* knockout leads to impairment of the endocardial cushion formation (Tao et al., 2011). In addition, Snai1 has been linked also to epicardial development in chicken (Tao et al., 2013). In zebrafish it has been shown that *snai1b*, one of the *snai1* paralogues, is implicated in myocardial precursor migration (Qiao et al., 2014). Defects caused by the loss of Snai1 function in all of these developmental events are linked to its activities in promoting EMT. However, a role for Snai1 in the later stages of cardiac development, in particular in the myocardial tissue, was largely unknown prior to my study. My PhD work (described in the Results section) uncovers a previously unsuspected role of Snai1b in maintaining cardiac wall integrity in zebrafish.

1.8.3 The helix-loop-helix (HLH) transcription factor Twist1

Twist1, a basic helix-loop-helix transcription factor, promotes EMT during different aspects of organogenesis. The basic domain binds to a consensus DNA sequence belonging to the E-box motif CANNG family, similar to Snai1. The helix-loop-helix domain is important for the homodimerization of the proteins and the interactions with different co-factors (Thisse et al., 1988; Díaz et al., 2014).

Figure 1.9: Twist1 protein structure

Cartoon of Snai1 protein structure. Image adapted and reprinted from Cell Adhesion and Migration, (Diaz et al., 2014), Figure 1, License: Copyright © Taylor & Francis Group, LLC

Similar to *snai1*, *twist1* was identified for the first time in Drosophila, where it was shown to control gastrulation and myogenesis (Leptin, 1991). It is conserved between flies and vertebrates. Its expression has been observed in mouse cranial mesoderm and neural crest-derived mesenchyme (Chen and Behringer, 1995). It has been shown that *Twist1* global knockout mice display craniosynostosis. Indeed, conditional knockout of Twist1 in the cranial mesoderm or the cranial neural crest leads to malformations of the cranium, facial skeleton, brain, and muscles (Bourgeois et al., 1998; Soo et al., 2002; Bialek et al., 2004). In humans, *TWIST1* loss-of-function mutations have been associated with Seathre-Chotzen syndrome (Reardon and Winter, 1994; Rose et al., 1997; el Ghouzzi et al., 1997; Howard et al., 1997; Gripp et al., 2000).

During cardiac development, Twist1 is expressed in the mesenchymal cells of the AVC and OFT endocardial cushion, where it promotes cell migration and cell proliferation, and then downregulated during cardiac valve remodeling (Shelton and Yutzey, 2008; Chakraborty et al., 2010). Interestingly, it has been shown that prolonged Twist1 expression in the mouse valve cells leads to aberrant valve morphogenesis, with increased cell proliferation and ectopic expression of endocardial cushion ECM proteins (Chakraborty et al., 2010). Similar to the defects observed in humans, loss of *twist1* in zebrafish has been linked to coronal suture formation defects (Teng et al., 2018). In this

thesis work, I describe how *twist1b* promotes endothelial-to-mesenchymal transition during the establishment of valve interstitial cells.

2. Aims of the study

During cardiac development, the heart undergoes several morphogenetic processes to become a functional organ. The different cell types – myocardium, endocardium, epicardium – in the heart assume different behaviors, interacting with each other and with the surrounding environment. During my PhD, I was interested in understanding the molecular regulation of cell behaviors behind two of the main cardiac morphogenetic events: cardiac wall maturation and cardiac valve formation. To better understand these processes, I took advantage of the zebrafish heart as a model system. The following characteristics of the zebrafish heart are fundamental for this study:

1) External and fast development of the embryos. The zebrafish embryos develop externally and rapidly. In addition, zebrafish can survive without a functional cardiovascular system up to 120 hpf, making it an ideal model to study cardiac defects that might cause embryonic lethality in other model systems.

2) Transparency and genetic manipulation of the embryos. To study the cellular behaviors of different cardiac cell types, it is important to look at them at the single-cell level and continuously over a long period of time. In addition, the heart is a beating organ, which not only undergoes several morphogenetic events but also has to withstand mechanical forces coming from the contraction of the organ itself and the shear stress of the blood flow.

The aims of my study are as follows:

Aim 1: Understanding the role of Snai1 in maintaining zebrafish cardiac wall integrity

As a beating organ, the heart has to withstand strong biomechanical forces and thus, the cardiac wall is constantly under pressure to maintain its integrity. I will examine how cardiac wall integrity is maintained at the cellular and molecular levels. In particular, my work will show an unsuspected role of the EMT transcription factor

Snai1 in maintaining the cardiac wall integrity, by regulating the expression of the intermediate filament gene, *desmb*.

Aim 2: Elucidating the establishment of zebrafish valve interstitial cells (VICs)

I will describe for the first time how VICs, which are critical components of the valve that secrete specialized ECM, are established during zebrafish valvulogenesis. My work will show how the process takes place at the cellular level. I will also uncover the molecular mechanism of VICs establishment and in particular the role of the transcription factor Nfatc1 and its downstream target *twist1b*.

3. Materials and methods

3.1 Materials

3.1.1 Antibiotics

Table 1: List of antibiotics used in the thesis with their respective working concentrations.

Antibiotic	Working concentration
Ampicillin	100 µg/ml
Penicillin	100 U/ml
Streptomycin	100 µg/ml

3.1.2 Antibodies

Table 2: List of antibodies used in the thesis with their respective dilution and supplier.

Antibody	Isotype	Dilution	Supplier	Catalog #
Anti-Alcama/Dm-Grasp	Mouse monoclonal	1:50	DSHB	ZN-8
Anti-Desmin	Rabbit monoclonal	1:100	Sigma	D8281
Anti-DIG-AP, Fab fragments		1:5,000	Roche	11 093 274 910
Anti-DIG-POD		1:500	Roche	11207733910
Anti-EGFP	Chicken polyclonal	1:800	Aves Lab	gfp-1020
Anti-Elastin1	Rabbit polyclonal	1:100	(Miao et al., 2007)	
Anti-Fibronectin	Rabbit polyclonal	1:100	Sigma	F3648
Anti-Fli1	Rabbit monoclonal	1:100	Abcam	Ab133485
Anti-mCherry	Mouse monoclonal	1:100	DSHB	GFP1020
Anti-mCherry	Mouse monoclonal	1:50	Takara Bio Clontech	632543
Anti-N-cadherin	Rabbit polyclonal	1:250	Abcam	Ab18203
Anti-p-myosin	Rabbit monoclonal	1:200	Abcam	Ab2480

Anti-tRFP	Rabbit polyclonal	1:200	Evrogen	AB233
Anti-Vimentin	Rabbit polyclonal	1:100	Genetex	GTX133061
Anti-ZO1	Mouse monoclonal	1:100	Thermo Fisher Scientific	33-9100
Anti-α-catenin epitope α-18	Rat monoclonal	1:300	Gift from Prof. Akira Nagafuchi	
Secondaries Alexa FluorTM 488-568-647 IgG (H+L)	Goat polyclonal	1:500	Thermo Fisher Scientific	

3.1.3 Bacterial strain

Table 3: List of bacterial strains used in the thesis with their purpose.

Bacterial strain	**Purpose**
DH5B	Competent cells

3.1.4 Buffers and solutions

Table 5: List of buffers and solutions along with their composition.

Buffer / Solution	**Composition**
0.1% PBST	0.1% Tween-20 1x PBS
10X PBS	5 PBS tablets (Sigma) 1 l distilled water
10x TBE	121 g Tris 62 g Boric Acid 7.4 g EDTA 1 liter of distilled water
1x MBS	dilute 5x MBS in distilled water and autoclave
1x PBDX	0.5% Triton X-100 1% DMSO 1% BSA 1x PBS
20x SSC	175.3 g NaCl 88.2 g Sodium citrate 800 ml of distilled water Adjusted to pH 7
5x MBS	88 mM NaCl 1 mM KCl

	2.4 mM $NaHCO_3$ 0.82 mM $MgSO_4 \cdot 7\ H_2O$ 0.33 mM $Ca(NO_3)_2 \cdot 4\ H_2O$ 0.41 mM $CaCl_2 \cdot 2\ H_2O$ 5 mM HEPES adjusted to pH 7.4
Alkaline Tris buffer	100 mM Tris-HCl pH 9.5 100 mM NaCl 0.1% Tween 20 Distilled water
Blocking buffer (immunostaining)	1x PBDX 1.5% goat serum
Blocking buffer (ISH)	2 mg/mL BSA 2% sheep serum 0.1% PBST
Egg water	3 g Instant Ocean 0.75 g Calcium sulfate dissolved 10 l of distilled water
Epon (50 g)	12.35 g 2-Dodecenylsuccinic acid anhydride (DDSA) 14.13 g Methylnadic anhydride (MNA) 23.52 g Glycid ether 100 0.65 g 2,4,6-Tris(dimethylaminomethyl)phenol (DMP)
FISH fix (100 mL)	100 ml Fish fix buffer – prewarmed at 60 °C 4 g PFA 1 ml 1M NaOH Adjusted pH to 7.35 with HCl
Fish fix buffer (1 l)	1x PBS 120 µl 1M $CaCl_2$ 40 g sucrose
HM (–) (ISH)	50% Formamide 5x SSC 0.1% Tween 20 adjusted to pH 6 with 1M Citric acid
HM (+) (ISH)	HM (–) Heparin 50 µg/mL tRNA 500 µg/mL
PBSTriton	0.1% Triton X-100 1x PBS
Richardson solution	Azure II Methylene blue di-Sodium tetraborate (Borax, water free) Distilled water

3.1.5 Centrifuges

Table 4: List of buffers and solutions along with their composition.

Centrifuge	Supplier
Centrifuge (1.5-2 ml tubes) 5424	Eppendorf
Centrifuge (1.5-2 ml tubes) 5424 R	Eppendorf
Centrifuge (15 ml, 50 ml tubes) 5810Rf	Eppendorf

3.1.6 Chemicals

Table 6: List of chemicals used in the thesis with their respective supplier.

Chemical	Supplier	Catalog #
10x NEBuffer 2.1	NEB	B7202S
10x NEBuffer 3.1	NEB	B7203S
1-Phenyl-2-thiourea (PTU)	Sigma	P7629
2,4,6-Tris(dimethylaminomethyl)phenol (DMP)	Serva	36975.01
2-Dodecenylsuccinic acid anhydride (DDSA)	Serva	20755.02
3-Isobutyl-1-methylxanthine (IBMX)	Sigma	I5879
5-ethynyl-2´-deoxyuridine (EdU)	Invitrogen	C10340
Acetone, anhydrous	VWR	83683.290
Agarose	Peqlab	35-1020
Agarose, low gelling temperature	Sigma	A9414
Alexa Fluor 568 Phalloidin	Thermo Scientific	A12380
Azure II	Carl Roth	7640.1
BM Purple AP substrate	Roche	11442074001
Bovine serum albumin (BSA)	Sigma	A2153
Cacodylic acid-Na-salt-3H_2O	Serva	15540.02
Calcium chloride ($CaCl_2$)	Merck	10035-04-8
Chloroform	Merck	102445
Citric acid	Sigma	27109
CutSmart buffer	NEB	B7204S
DAPI	Thermo Scientific	D1306
DIG RNA labeling mix (Sp6/T7)	Roche	11277073910
Dimethylsulfoxide (DMSO)	Sigma	D4540
di-Sodium tetraborate (Borax, water free)	Carl Roth	4403.1
DMEM high glucose, pyruvate	Thermo Scientific	D0819
DNA ladder (1 kb)	Thermo Scientific	SM0311

DNA ladder (100 bp)	Thermo Scientific	SM0241
Ethanol	Roth	K928.3
Fluorescence mounting media	Dako	S3023
Gel loading dye (6x)	Thermo Scientific	R0611
Glutaraldehyde	Carl Roth	4157.1
Glycid ether 100	Serva	21045.02
Goat serum	Sigma	G9023
Heparin	Sigma	136098-10-7
Hydrochloric acid (HCl)	Sigma	H1758
Hydrogen peroxide (H_2O_2)	Sigma	7722-84-1
Isopropanol	Roth	6752,4
Lipofectamine 3000 Transfection Reagent	Thermo Scientific	L3000015
Methanol	Roth	4627.5
Methylene blue	Sigma	M9140
Methylene blue	Carl Roth	A514.1
Methylnadic anhydride (MNA)	Serva	29452.03
Mineral oil	Sigma	M8410
Nuclease-free water	Ambion	AM9938
O-dianisidine	Sigma	119-90-4
Osmium tetroxide, 4% aqueous solution	Science Services	E19190
Paraformaldehyde (PFA)	Sigma	P6148
Penicillin-Streptomycin	Thermo Scientific	15140122
Phenol red	Sigma	P0290
Phosphate-buffered saline (PBS) tablets	Sigma	P4417
Pronase	Roche	10165921001
Proteinase K	Roche	1092766
Sheep serum	Sigma	ABIN925265
Sodium citrate	Sigma	18996-35-5
Sodium hydroxide (NaOH)	Sigma	221465
Sucrose	Sigma	S0389
SYBR safe	Invitrogen	S33102
T4 ligase buffer	Takara	SD0267
Tricaine (ethyl-m-aminobenzoate methanesulfonate)	Pharmaq	NA
Tris	Sigma	5429.2
Tris hydrochloride (Tris-HCl)	Sigma	RES3098T-B701X
Triton X-100	Sigma	RES3103T-A101X
Trizol	Ambion	15596018
tRNA	Sigma	9014-25-9
Tween-20	Sigma	P1379

Uranyl acetate·$2H_2O$	Serva	77870.01

3.1.7 Databases

Table 7: List of databases.

Database	**URL**
Ensembl	www.ensembl.org
PubMed	pubmed.ncbi.nih.gov
RefSeq	www.ncbi.nlm.nih.gov/refseq/
Uniprot	www.uniprot.org
Zfin	zfin.org

3.1.8 Enzymes

Table 8: List of enzymes used in the thesis with their respective supplier.

Enzyme	**Supplier**
BamHI-HF	NEB
DpnI	NEB
DNase I	Qiagen
DyNAmo ColorFlash SYBR Green PCR mix	Thermo Scientific
EcoRI-HF	NEB
HindIII	NEB
NheI	NEB
NotI	NEB
KAPA 2G fast DNA polymerase	Kapa Biosystem
PrimeSTAR max DANN polymerase	Takara
RNasin ribonuclease inhibitor	Promega
SalI	NEB
SmaI	NEB
T4 DNA ligase	Takara
T7 RNA polymerase	Promega
XbaI	NEB
XhoI	NEB

3.1.9 Growth media

Table 9: List of growth media used in the thesis along with their composition.

Growth medium	**Composition**
SOC medium	Tryptone 2% + Yeast extract 0.5% + NaCl 0.05% + KCl 0.0186%

	dissolve in distilled water and adjust pH 7, then add $MgCl_2$ 10mM + D-glucose 20 mM, then autoclave
LB agar	Roth
LB medium	Roth
HEK293T medium	DMEM + Glutamax + 10% FBS + 1% penicillin-streptomyocin

3.1.10 Kits

Table 10: List of kits used in the thesis with their respective supplier.

Kit	**Supplier**	**Catalog #**
Click-iT™ EdU Alexa Fluor™ 647 Imaging Kit	Invitrogen	C10340
Dual-Luciferase® Reporter Assay	Promega	E1910
GeneJET gel extraction kit	Thermo Scientific	K0691
GeneJET PCR purification kit	Thermo Scientific	K0701
GeneJET plasmid miniprep kit	Thermo Scientific	K0502
In situ cell death detection kit, fluorescein	Roche	11684795910
In-Fusion® HD Cloning Plus	Takara Bio	638910
Maxima First Strand cDNA kit	Thermo Scientific	K1641
MEGAshortscript T7 kit	Ambion	AM1354
miRNeasy micro kit	Qiagen	217084
mMESSAGE mMACHINE kit (T3)	Ambion	AM1348
mMESSAGE mMACHINE kit (T7)	Ambion	AM1344
pGEM-T-easy vector kit	Promega	A1360
RNA clean and concentrator	Zymo Research	R1016
SMART-seq v4 Ultra Low Input RNA kit	Takara Clontech	R400753

3.1.11 Laboratory supplies

Table 11: List of laboratory supplies used in the thesis with their respective supplier.

Laboratory supply	**Supplier**
Bacterial culture tube	Sarstedt
Beakers	VWR
CELLSTAR cell culture multi-well plates (96, 48, 24, 12, 6 well plates)	Greiner bio-one
Centrifuge tubes (1.5 ml, 2 ml)	Sarstedt
Conical flasks (100 ml, 500 ml)	VWR
Falcons (15 ml, 50 ml)	Greiner bio-one

Forceps	Dumont
Glass bottles (50 ml, 100 ml, 250 ml, 500 ml, 1000 ml)	Duran
Glass bottom dish	MatTek
Insulin syringes	Terumo
Laboratory film	Parafilm
Latex gloves	Roth
Microloader pipette tips	Eppendorf
Nitrile gloves	VWR
PCR tubes (200 µl)	Sarstedt
Petri dish (90 mm, 60 mm, 35 mm)	Grainer bio-one
Pipetboy	Integra
Pipette filter tips	Grainer bio-one
Pipette tips	Grainer bio-one
Pipettes (2 µl, 20 µl, 200 µl, 1000 µl)	Gilson
Scalpel	Braun

3.1.12 Microscopes

Table 12: List of microscopes used in the thesis with their respective supplier.

Microscope	**Supplier**
Stereomicroscope Stemi 2000	Zeiss
Stereomicroscope SMZ18	Nikon
Stereomicroscope SMZ25	Nikon
Confocal microscope LSM700	Zeiss
Confocal microscope LSM800 Observer	Zeiss
Confocal microscope LSM880	Zeiss
Spinning Disk microscope, cell observer SD	Zeiss

3.1.13 Miscellaneous laboratory equipment

Table 13: List of miscellaneous laboratory equipment used in the thesis with their respective supplier.

Equipment	**Supplier**
Bacterial incubator	Heraeus
Bacterial incubator shaker	Infors HAT
Cell culture CO_2 incubators	Thermo Scientific
Cell culture laminar flow hoods	Thermo Scientific
CFX connect real time PCR detection system	Bio Rad
Dark reader transilluminator	Clare chemical
Eco Real-Time PCR System	Illumina
Electrophoresis power supply	Bio Rad
G560E Vortex Genie 2	Scientific Industries

Gel Doc EZ system	Bio Rad
HB-10 UVP	Analytic Jena
Heating block	VWR
Injection micromanipulator	World precision instruments
LabChip Gx Touch 24	Perkin Elmer
Micropipette puller P-1000	Sutter instruments
Microscale	Novex
Microwave	Bosh
Nanodrop 2000c	Thermo Scientific
NextAdvance Bullet Blender® Homogenizer	Scientific instrument services
NextSeq500 instrument	Illumina
PCR mastercycler Pro	Eppendorf
Printer P95	Mitsubishi
Slot grid (Copper) 2x1mm	Plano
Ultracut E microtome	Reichert-Jung
Weighing balance	Sartorius
Zebrafish aqua culture system	Tecniplast
Zebrafish breeding tanks	Tecniplast
Zebrafish incubator	Binder

3.1.14 Oligonucleotides

Table 14: List of oligonucleotides used in the thesis with their sequence and purpose.

Description	**Gene**	**Sequence**	**Primer**
CRISPR	*snai1b*	GTAGTTTGGCTTCTTGT	Exon1
CRISPR	*snai1b*	GTCTATAAGTGGCGCAG	Promoter
CRISPR	*twist1b*	AAGGACGTTATTCCAGCATG	5'UTR
CRISPR	*twist1b*	TCGTCGTCATAAGACTCGCG	3'UTR
CRISPR	*nfatc1*	TACGGCCCTGAGCTCGA	Exon
PCR - ISH probe	*snai1b*	AAGATGCCACGCTCATTTCT	Forward
PCR - ISH probe	*snai1b*	AGAAAGGCACCTTGTGGTTG	Reverse
PCR - dominant negative plasmid	*twist1b*	GTGAGATGCAGACATGGACCAA	Forward
PCR - dominant negative plasmid	*twist1b*	ATGCCCGAAGAGCCCGCG	Reverse
PCR - ISH probe	*twist1b*	ACCCTCATGCTGGAATAACG	Forward
PCR - ISH probe	*twist1b*	GAGGCTTCAATTCCCATTTTC	Reverse
PCR - overexpression plasmid	*snai1b*	ATGCCACGCTCATTTCTTGT	Forward
PCR - overexpression plasmid	*snai1b*	GAGCGCCGGACAGCAGCC	Reverse

PCR - overexpression plasmid	*desmb*	ATGAGCCACTCTTATGCCAC	Forward
PCR - overexpression plasmid	*desmb*	CATGAGGTCCTGCTGGTG	Reverse
PCR - ISH probe	*desmb*	TCACGGGTGGAGGTAGAAAG	Forward
PCR - ISH probe	*desmb*	TAATACGACTCACTATAGGCATCAC GTGTCTCGATGGTC	Reverse
PCR - plasmid for the luciferase assay	800 bp *desmb* promoter	GAAAGCATAGTCTGCTTTCTCG	Forward
PCR - plasmid for the luciferase assay	800 bp *desmb* promoter	GAGCGCCGGACAGCAGCC	Reverse
HRM - genotyping	*snai1b ex1*	ATGCCACGCTCATTTCTTGTCAA	Forward
HRM - genotyping	*snai1b ex1*	AATTTCACTCTCACCAGTCTGA	Reverse
HRM - genotyping	*snai1b promoter*	ACCTTCTTGTTGTGAGGCGA	Forward
HRM - genotyping	*nfatc1*	GTAGTCCATCACTGCCTGCT	Forward
HRM - genotyping	*nfatc1*	TGAGACTTGGGTTGGACATCAA	Reverse
HRM - genotyping	*twist1b*	ACGCGTGGAATTGTATTTCAC	Forward
HRM - genotyping	*twist1b*	GAGGCTTCAATTCCCATTTTC	Reverse
qPCR	*snai1b*	CAGTGAACTGGAGAGTCAGACTG	Forward
qPCR	*snai1b*	CACTGCGGGACGACTGCATA	Reverse
qPCR	*snai1a*	CAACTTCAGAGTTCAGCATGC	Forward
qPCR	*snai1a*	CTGGTGAAGTGTCGTTCTGAC	Reverse
qPCR	*desmb*	GGACAACCTGGCAGATGACC	Forward
qPCR	*desmb*	GCCTGCAGCTCACGGATTTC	Reverse
qPCR	*rpl13a*	TCTGGAGGACTGTAAGAGGTATGC	Forward
qPCR	*rpl13a*	AGACGCACAATCTTGAGAGCAG	Reverse
qPCR	*nfatc1*	TGTGAAAGCACTAGCGGGAG	Forward
qPCR	*nfatc1*	TGGTAGAATGCGTGAGGTCG	Reverse
qPCR	*twist1b*	TTAAATGGTCAAACCGTGAG	Forward
qPCR	*twist1b*	GCACATATTTCCAACATTCG	Reverse
qPCR	*twist1a*	ATGTCAACATCTCACTAACG	Forward
qPCR	*twist1a*	AATCCTTATTTTCGCCCTTG	Reverse
qPCR	*myl7*	GGCTCTTCCAATGTCTTCTCC	Forward
qPCR	*myl7*	GGACTCCAGCTCTTCATCAC	Reverse
qPCR	*kdrl*	TCTTCACTCTTCACGTGCTTTTTAG	Forward
qPCR	*kdrl*	GAAGGTGTGTATCTCCATCAGGAA	Reverse
qPCR	*lo01*	CAGCATGTCCGTGTACGTCT	Forward
qPCR	*lo01*	CGTGTGGGTAAACTGCTCCT	Reverse

qPCR	*ggt7*	GTCATACGAGCTGCAGGACA	Forward
qPCR	*ggt7*	CACAATACCACTGCCAAACG	Reverse
Morpholino	*tnnt2a*	CATGTTTGCTCTGATCTGACACGCA	ATG-MO

3.1.15 Plasmids

Table 15: List of plasmids used in the thesis with their respective resistance and source.

Plasmid	**Resistance**	**Source**
pT3TS-nlsCas9nls vector	Ampicillin	Addgene
pT7-gRNA vector	Ampicillin	Addgene
pGEM-T	Ampicillin	Promega
pCDNA3.1	Ampicillin	Addgene
pCS2z vector	Ampicillin	Addgene
pCMV-Tol2	Ampicillin	Addgene
pGl4.14-luc; SV40:hRLuc	Ampicillin	(Bensimon-Brito et al., 2020)
UAS:twist1b^{DN}-GFP	Ampicillin	(Gunawan Felix et al., 2020)
UAS:snai1b-p2a-GFP	Ampicillin	(Gentile et al., 2021)
-0.2myl7:snai1b-p2a-GFP	Ampicillin	(Gentile et al., 2021)
-0.2myl7:desmb-p2a-GFP	Ampicillin	(Gentile et al., 2021)
pGl4.14-0.8desmb-luc	Ampicillin	(Gentile et al., 2021)
pCMV-snai1b-GFP	Ampicillin	(Gentile et al., 2021)

3.1.16 Software

Table 16: List of software used in the thesis with their respective purpose.

Software	**Purpose**
Adobe Illustrator	Image formatting
BLAST	Bioinformatics analysis
CRISPOR	gRNA design
Ensembl	Genomic Sequences
FastQC	Bioinformatics analysis
Gitools	Bioinformatics analysis
ImageJ, Imaris (Bitplane), ZEN (Zeiss)	Image processing
Microsoft Office	Writing, data analysis, image formatting
Primer 3	Primer design
Prism (GraphPad Software)	Data analysis
SnapGene (Insightful Science)	Sequence analysis, primer design

3.1.17 Zebrafish food

Table 17: List of zebrafish food used at different developmental stages.

Food	**Developmental stage**

Brine Shrimp	5 dpf – 12 dpf
SDS 100	> 12 dpf – 1 month
SDS 200	> 1 month – 2 months
SDS 300	> 2 months – 3 months
SDS 400	Adult fish

3.1.18 Zebrafish lines

Table 18: List of zebrafish lines used in the thesis along with the publications where they were first described.

Line	**Details**	**Publication**
AB	Wild type	
Tg(myl7:EGFP-Hsa.HRAS)s883Tg	CM membrane reporter	(D'Amico et al., 2007)
Tg(myl7:BFP- CAAX)^{bns193}	CM membrane reporter	(Guerra et al., 2018)
Tg(myl7:H2B-EGFP)^{zf521Tg}	Nuclear CM reporter	(Mickoleit et al., 2014)
Tg(myl7:mVenus-gmnn)^{ncv43Tg}	Proliferating CM reporter	(Jiménez-Amilburu et al., 2016)
Tg(-0.2myl7:snai1b-p2a-GFP) ^{bns555}	CM-specific *snai1b* overexpression	(Gentile et al., 2021)
Tg(-0.2myl7:EGFP-podocalyxin) ^{bns10}	CM polarity marker	(Jiménez-Amilburu et al., 2016)
Tg(fli1a:Gal4)^{ubs4}	EC driver	(Zygmunt et al., 2011)
Tg(UAS:snai1b-p2a-GFP) ^{bns442}	UAS driving *snai1b* overexpression	(Gentile et al., 2021)
snai1b^{bn351}	*snai1b* mutant	(Gentile et al., 2021)
Tg(nfatc1:Gal4)^{mu286}	Nfatc1 driver	(Pestel et al., 2016)
Tg(UAS:GFP)^{nkuasgfp1a}	UAS driving GFP expression	(Asakawa et al., 2008)
Tg(UAS:RFP)^{nkuasrfp1a}	UAS driving RFP expression	(Asakawa et al., 2008)
Tg(UAS:Kaede)^{rk8}	UAS driving Kaede expression	(Herwig et al., 2011)
Tg(kdrl:nls-mCherry)^{iS4}	EC reporter	(Fujita et al., 2011)
Tg(ve-cad:ve-cad^{ts}*)*^{uq11bh}	VE-cadherin tension reporter	(Lagendijk et al., 2017)
Tg(kdrl:Cre)^{s898}	Lineage tracing EC-derived cells	(Bertrand et al., 2010)
Tg(sox10:Cre^{ERT2}*, myl7:GFP)*^{t007}	Lineage tracing NCC-derived cells	(Mongera et al., 2013)
Tg(-3.5ubb:loxP-EGFP-loxP-mCherry)^{cz1701}	Switch line for lineage tracing	(Mosimann et al., 2011)

TgBAC(cryaa:GFP, tcf21:Cre^{ERT2})^{pd42}	Lineage tracing epicardial-derived cells	(Kikuchi et al., 2011)
Tg(myl7:Cre^{ER})^{pku328}	Lineage tracing CM-derived cells	(Xiao et al., 2016)
Tg(ubi:ssNcan-GFP)^{uq25bh}	Hyaluronic acid binding protein reporter	(Bertrand et al., 2010)Grassini et al, 2018
Tg(Hhex:GFP)^{bns321}	Hhex reporter	(Gunawan et al., 2020)
Tg(UAS:twist1b^{DN}-GFP)^{bns387}	UAS driving *twist1b* dominant negative form	(Gunawan et al., 2020)
nfatc1^{bns276}	*nfatc1* mutants	(Gunawan et al., 2020)
twist1b^{bns353}	*twist1b* mutants	(Gunawan et al., 2020)
TgBAC(vegfaa:EGFP)^{pd260}	VEGF reporter	(Karra et al., 2018)

3.2 Methods

3.2.1 Zebrafish maintenance and breeding

Zebrafish husbandry was performed under standard conditions (Westerfiels, 2000) and under institutional (MPG) and national (German) ethical and animal welfare regulations, and approved by the Animal Protection Committee (Tierschutzkommission) of the Regierungspräsidium Darmstadt. Tecniplast aquaculture system was used to keep zebrafish adult in 3.5 l tanks at a stock of 10 zebrafish/l, under the following conditions: water temperature of 27-27.5°C, pH around 7-7.5, and conductivity 750-800 µS/cm. The room temperature was kept at 29°C and a light-dark cycle of 14 hours of light and 10 hours of dark was maintained. Feeding was performed 3 to 5 times a day, according to age, with granular food and live food (*Artemia salina*).

Both female and male fish derived from the AB strain were used. Matings were performed in the afternoon using specific tanks provided with a net, to separate the fish from the bottom of the tank, and a divider, to separate the female from the male, preventing mating during the night. The next morning, dividers were removed and the eggs were collected in egg water in 9 cm Petri dishes. Zebrafish embryos were kept in a 28°C incubator and dead or unfertilized eggs were removed. Staged of the embryos

was performed at 75% epiboly for synchronization. To prevent pigmentation, the next day PTU (0.0045%) was added to the egg water, and if needed chorions were removed by pronase (10 mg/ml) treatment.

3.2.2 Microinjection

To genetically modify the embryos, microinjection at the one-cell stage was performed. To prepare microinjection plates, agarose (2%) was dissolved in egg water and poured into a 9 cm petri dish. The lanes were created with a special mold put on top of the solution until solidification. To prepare the needles for injection, borosilicate glass capillaries and a micropipette puller were used. A platinum heater filament was used to heat the center of the capillary, kept under tension to obtain two needles. To perform the injections, the needle was loaded using a micro loader pipette tip and fixed on a micromanipulator. Then, the needle was cut using forceps and the pressure conditions of the micromanipulator were calibrated to allow a small droplet to come out of the needle. Embryos were injected at the one-cell stage.

3.2.3 DNA and RNA isolation from zebrafish embryos

To extract DNA and RNA, first, the embryos were homogenized in TRIzol using a NextAdvance Bullet Blender® Homogenizer. Then, chloroform was added to the samples and the aqueous phase separated from the organic phase. The aqueous phase containing the RNA was then mixed with isopropanol and stored at -20°C. The organic phase containing the DNA was precipitated with 70% ethanol. To genotype the samples, proteinase K was added to the pellet, to allow protein degradation. After genotyping, RNA from 3 up to 5 embryos with the same genotype was pooled together and extracted by precipitation. The RNA was then quantified and or immediately used for cDNA synthesis or stored at 80°C.

3.2.4 Embryonic heart isolation and RNA extraction

Hearts were dissected from embryos/larvae between 48 to 96 hpf and with endocardial or myocardial markers, according to the experiment. Embryos or larvae were

anesthetized with tricaine and placed in a Petri dish containing DMEM/10% FBS. Hearts were manually dissected using insulin needles. When necessary, the body of the larva was used for genotyping. 12, 30, or >100 hearts were pooled together, according to the experiment, and kept on ice. The samples were then processed for digestion for FACS sorting or for total RNA extraction. For RNA extraction, the samples were spinned to remove the medium solution and TRIzol was added. The RNA was then extracted by precipitation or using miRNeasy micro kit combined with on-column DNase digestion, according to the experiment.

3.2.5 cDNA synthesis and real-time quantitative PCR (RT-qPCR)

At least 500 ng of total RNA was used for reverse transcription using Maxima First Strand cDNA synthesis kit, with the following conditions:

Step	**Temperature**	**Time**
1	25°C	10 minutes
2	50°C	15 minutes
3	85°C	5 minutes

The cDNA was then diluted 1:2 in nuclease-free water. For all the experiments, DyNAmo ColorFlash SYBR Green qPCR Mix was used on a CFX connect Real-time System with the following conditions:

Step	**Temperature**	**Time**
Pre-amplification	95°C	7 minutes
Amplification (x39 cycles)	95°C	10 seconds
	60°C	30 seconds
Melting curve	60°C to 92°C	1°C increment each 5 seconds

Each biological replicate was obtained from three technical replicates. Gene expression values were normalized using the housekeeping gene *rpl13a* and fold change was calculated using the $2^{-\Delta\Delta Ct}$ method.

3.2.6 RNA-sequencing

Total RNA and library integrity were verified with LabChip Gx Touch 24 (Perkin Elmer). Approximately 10 ng of total RNA was used as input for SMART-Seq® v4 Ultra® Low Input RNA Kit (Takara Clontech) for cDNA pre-amplification. Obtained full-length cDNA was checked on LabChip GX Touch 24 and fragmented by Ultrasonication by E220 machine (Covaris). Final Library Preparation was performed by Low Input Library Prep Kit v2 (Takara Clontech). Sequencing was performed on a NextSeq500 instrument (Illumina) using v2 chemistry, resulting in an average of 30M reads per library with 1x75bp single end setup. The resulting raw reads were assessed for quality, adapter content, and duplication rates with FastQC (available online at http://www.bioinformatics.babraham.ac.uk/projects/fastqc). Trimmomatic version 0.39 was used to trim reads with a quality drop below a mean of Q20 in a window of 10 nucleotides (Bolger et al., Trimmomatic: a flexible trimmer for Illumina sequence data). Only reads between 30 and 150 nucleotides were used in subsequent analyses. Trimmed and filtered reads were aligned versus the Ensembl Zebrafish genome version DanRer11 (GRCz11.92) using STAR 2.6.1d with the parameter "outFilterMismatchNoverLmax 0.1" to increase the maximum ratio of mismatches to mapped length to 10% (Dobin et al., 2013). The number of reads aligning to genes was counted with feature Counts 1.6.5 tool from the Subread package (Liao et al., 2014). Only reads mapping at least partially inside exons were admitted and aggregated per gene, while reads overlapping multiple genes or aligning to multiple regions were excluded from further analyses. Differentially expressed genes were identified using DESeq2 version 1.18.1 (Love et al., 2014). The Ensembl annotation was enriched with UniProt data (release 06.06.2014) based on Ensembl gene identifiers (Activities at the Universal Protein Resource (UniProt)).

For the gene ontology analysis, all genes with a p-value ≤ 0.05 were used as a query list. Genes with > 5 normalized reads in at least one sample were used as a background list. The analysis was performed with the Gitools 2.3.1 (http://www.gitools.org) software. Z-scores were calculated using the default settings and multiple test correction with Benjamini Hochberg FDR was performed.

This subsection has been quoted *verbatim* from Gentile et al., *eLife*, 2021; DOI:10.7554/eLife.66143.

3.2.7 Fluorescence-activated cell sorting (FACS)

Manually dissected hearts were dissociated into single-cell suspensions, washing them with 1 ml HBSS (Hanks' Balanced Salt Solution). Then they were incubated in 100 µl Enzyme 1 and 5 µl Enzyme 2 (Pierce Cardiomyocytes Dissociation Kit) for 20 minutes at 30°C on a shaker (300-350 rpm), mechanically dissociating them by pipetting every 5 minutes. Adding 1 ml DMEM/FBS, the reaction was stopped and centrifuged for 3 minutes. After discarding the supernatant, 400 µl DMEM/FBS was added to the solution and transferred into a 40 µl-filtered FACS tube. DAPI was added to the samples to distinguish between live/dead cells. Before the samples, negative controls of non-fluorescent hearts or single-color fluorescent hearts were sorted to adjust the gate. A gate to distinguish cells from debris on a scatter plot of forward scatter (FSC-A) amplitude vs side scatter amplitude (SSC-A) was selected. An additional gate to distinguish single cells from doublets and multimers was set. Cells were collected by FACS sorting on a BD FACSAria™ III machine. The cells were sorted directly in TRIzol RT-qPCR experiments and frozen at -80°C.

3.2.8 *E. coli* competent cell preparation

DH5α competent cells were inoculated in LB liquid medium at 37°C ON. The next morning, 1 ml of the overnight culture was added to 200 ml of LB liquid medium and left in the shaker for 4 hours at 37°C. Then, the culture was placed on ice for 20 minutes, cells were centrifuged at 4°C for 10 minutes at 4000 rpm. The supernatant medium was discarded and the pellet was left to dry. The pellet was resuspended in 5 ml cold 0.1M $CaCl_2$ and kept on ice for 5 min. Then the culture was centrifuged at 4°C for 5 minutes at 4000 rpm. LB medium was discarded again and the pellet was dried. The final pellet was resuspended in a cold solution made of 0.1M $CaCl_2$ + 15% glycerol. Last,

20 µl of suspension cells were aliquoted in 1.5 ml tubes and snap-frozen quickly. Competent cells were stored at -80 °C.

3.2.9 Cloning

Cloning of genes of interest was performed using primers specifically designed for In-Fusion Cloning. Each primer contains a 20 bp homology arm for the vector, a restriction enzyme site compatible with that used to linearize the vector, and a 20 bp homology arm for the gene of interest to amplify. When necessary, the plasmid was linearized by restriction digestion at 37°C for 2 hours, with the following conditions:

Component	**Concentration**
Plasmid DNA	2-5 µg
10x Buffer	1x
Restriction enzyme	5 units
Water	to 50 µl

The insert was amplified by PCR using PrimeStar Max DNA polymerase with the following conditions:

Step	**Temperature**	**Time**	
Initial denaturation	98° C	2 minutes	
Denaturation Annealing Extension	98° C 55-60° C 72° C	15 seconds 30 seconds 30 minute/kb	35 cycles
Final extension	72° C	5 minutes	
Hold	4° C	Indefinite time	

The correct digestion of the vector and the amplification of the insert were confirmed using gel electrophoresis on 1% gel agarose in 1x TBE/Sybr Safe (2.5 µl/100 ml TBE) for 40 minutes at 160 V. Then the DNA was isolated using a Gel Purification kit or PCR Purification kit and the concentration was measured using a NanoDrop. The insert and the vector were ligated using the In-Fusion enzyme, with a reaction with the following conditions:

Component	Concentration/Volume
Linear Vector	50-100 ng
Insert	Molar ratio vector:insert=1:3
In-fusion master mix	0.4 µl
Water	to 2.5 µl

The reaction was then incubated for 15 minutes at 55°C and then 10 minutes on ice. The 5 µl reaction was then used to transform E. coli competent cells. By colony PCR clones were selected for a successful integration using primer spanning vector-insert boundary. The conditions of the colony PCR are the following:

Step	Temperature	Time	
Initial denaturation	98° C	2 minutes	
Denaturation Annealing Extension	98° C 55° C 72° C	15 seconds 30 seconds 30 minute/kb	35 cycles
Final extension	72° C	5 minutes	
Hold	4° C	Indefinite time	

Positive clones were placed in a 5ml LB medium with ampicillin and kept in the bacterial shaker at 37°C overnight. The next morning, the culture was centrifuged at 14000 rpm for 2 minutes and the supernatant was discarded. The DNA contained in the pellet was isolated using GeneJET Plasmid Miniprep Kit following the manufacturer's instructions. The plasmid DNA was then eluted in 25 µl of water. The plasmid DNA was subsequently sent for sequencing to confirm the correct integration using the GATC Biotech (Constance).

3.2.10 *E. coli* competent cell transformation

E.Coli competent cells (25 µl) were thawed on ice for a few minutes. Plasmids or ligation mix to transform were added to the competent cells and placed on ice for 10 minutes. Then, heat shock was done at 42° C for 50 seconds followed by incubation on ice for 5.

Next, transformed bacteria were plated in 30 mm Petri dishes prepared with LB agar containing ampicillin and incubated at 37°C overnight.

3.2.11 TA cloning

TA cloning was performed using the pGEM-T-easy vector kit, for sequencing CRISPR/Cas9-induced mutations or for creating templates for *in vitro* RNA transcription. The reaction was assembled as follows:

Component	**Volume**
pGEM-T easy vector	1 µl
2x Buffer	5 µl
PCR product	2 µl
TA DNA ligase	1 µl
Water	to 10 µl

The mix was incubated at room temperature for 2 hours or overnight at 4°C. The mix was then transformed into competent cells. Competent cells were plated on agar plates covered with ampicillin and with β-galactosidase. Positive colonies were selected based on a blue-white screen.

3.2.12 Immunostaining

Embryos or larvae were collected, treated with PTU at 24 hpf to prevent pigmentation, and fixed in 4% PFA for 2 hours at room temperature, after stopping the heart with 0.4% Tricaine to prevent it from collapsing during fixation. After exchanging the fixative with PBS/0.1% Tween washes, yolks were removed using forceps, incubated in 0.1 M glycine for 10 minutes, and then washed with PBS/1% BSA/1%DMSO/0.5% Triton-X (PBDT), and blocked with PBDT/10% goat serum before incubating in the primary antibody at 4°C overnight. The embryos were washed in PBDT and incubated in secondary antibody for 2 hours at room temperature, then incubated with DAPI (2 µg/ml) for 10 minutes and washed with PBS/0.1% Tween.

Sections from 15 to 90 dpf animals and adult hearts were washed in 0.1 M glycine (Sigma) and permeabilized for 7 minutes at -20°C in acetone, then incubated in a

blocking solution of PBDX (1% (w/v) Bovine Serum Albumin, 1% (v/v) DMSO, 1% (v/v) Triton-X100 in PBS) with 15% (v/v) goat serum for >2 hours at room temperature before incubation with primary antibodies in blocking solution overnight at 4°C. Slides were washed several times with PBDX, incubated with Alexa Fluor conjugated secondary antibodies (1:500) overnight at 4°C and 0.0002% (w/v) DAPI, and mounted with DAKO Fluorescence mounting medium.

This subsection has been quoted *verbatim* from Gentile et al., *eLife*, 2021; DOI:10.7554/eLife.66143 and Gunawan*, Gentile* et al., *Circ Res* 2020; DOI: 10.1161/CIRCRESAHA.119.315992 for the scientific accuracy of the terms.

3.2.13 EdU incorporation assay

Zebrafish embryos, larvae, and juveniles (up to 20 dpf) were incubated in 0.5 mM EdU in egg water/0.5% DMSO for 24 hours. Animals up to 144 hpf were incubated in 24-well plates and from 10 to 20 dpf in 6-well plates. Adult fish were intraperitoneally injected with 20 μL of 10 mM EdU (diluted in PBS) 24 hours before organ harvesting. Whole animals up to 10 dpf or sectioned 20 and 30 dpf fish and adult hearts were fixed in 4% paraformaldehyde and incubated in a Click-iT EdU Alexa Fluor 647 Kit for 30 minutes.

This subsection has been quoted *verbatim* from Gunawan*, Gentile* et al., *Circ Res* 2020; DOI: 10.1161/CIRCRESAHA.119.315992 for the scientific accuracy of the terms.

3.2.14 Cryosections

All samples were fixed in 4% paraformaldehyde for 1 hour at room temperature. 20 and 30 dpf fish and dissected adult hearts were embedded for cryosections, as previously described (Mateus et al., 2015). 10 μm thick cryosections were cut using a Leica CM3050S cryostat and kept at -20˚C until further use. Before use, slides were thawed for 10 minutes at room temperature and the gelatin was removed in PBS at 37˚C.

This subsection has been quoted *verbatim* from Gunawan*, Gentile* et al., *Circ Res* 2020; DOI: 10.1161/CIRCRESAHA.119.315992 for the scientific accuracy of the terms.

3.2.15 TUNEL assay

Embryos at 50 hpf were fixed in 4% PFA for 2 hours at room temperature, washed in PBS/0.1% Tween, and manually deyolked with insulin needles. Samples were dehydrated and stored in 100% MeOH at -20°C overnight. After rehydration, embryos were processed for antibody staining as previously described. Subsequently, samples were permeabilized with 0.1% Sodium Citrate in PBS for 2 minutes on ice. After washing in PBS/0.3% Triton-X, embryos for the positive control were incubated for 15 minutes at 37°C with DNAaseI. All the embryos were incubated for 1 hour at 37°C in the TUNEL solution (In Situ Cell Death Detection Kit Fluorescein – Roche). After washes, embryos were mounted for imaging.

This subsection has been quoted *verbatim* from Gentile et al., *eLife*, 2021; DOI:10.7554/eLife.66143.

3.2.16 Whole mount *in situ* hybridization

To generate DNA templates for RNA probes wild-type cDNA was amplified using a reverse oligonucleotide containing the T7 promoter sequence. DIG-labeled probes were synthesized *in vitro* using a MegaScript T7 Transcription Kit. *in situ* hybridization was performed as previously described (Thisse and Thisse, 2008). Briefly, larvae were fixed in 4% paraformaldehyde overnight at 4°C and then washed with RNase-free PBS/0.1% Tween for 1 hour. They were permeabilized in serial methanol dilutions for 5 minutes each and then incubated overnight at −20°C. They were subsequently rehydrated in PBS/Tween for 1 hour, incubated in 1 μg/ml Proteinase K for 30 minutes, and fixed again in 4% paraformaldehyde for 20 minutes. After washing with PBS/Tween for 1 hour, the larvae were incubated in hybridization buffer (Hyb buffer; 50% formamide, 5× SSC, 0.1% Tween-20, 50 μg/ml heparin, and 500 μg/ml tRNA) at 65°C for ≥2 hours.

They were subsequently incubated in DIG-labeled RNA probe (1 µg/ml in Hyb buffer) at 65°C overnight. We performed serial dilutions with Hyb buffer/2× SSC at 65°C, then 0.2× SSC/PBS/Tween at room temperature. We subsequently incubated the embryos for 3–4 hours in blocking buffer (1× PBS/Tween, 2% sheep serum, and 2 mg/ml BSA), and anti-DIG antibody (1:5,000) at 4°C overnight. After washing in PBS/Tween for 1 hour, the embryos were incubated in alkaline Tris buffer (100 mM Tris-CL, pH 9.5, 100 mM NaCl, and 0.1% Tween-20) for 15 minutes, and BM Purple staining solution until the desired staining intensity.

This subsection has been quoted *verbatim* from Gunawan*, Gentile* et al., *Circ Res* 2020; DOI: 10.1161/CIRCRESAHA.119.315992 for the scientific accuracy of the terms.

3.2.17 CRISPR/Cas9-mediated mutagenesis

To generate mutant lines, guide RNAs (gRNAs) were designed using a CRISPOR program (https://crispor.tefor.net/).

To generate *snai1b* promoter-less allele, two gRNAs were designed: one targeting the proximal promoter (5'-GTCTATAAGTGGCGCAG-3') and another targeting exon 1, immediately after the sequence encoding the SNAG domain (5'- GTAGTTTGGCTTCTTGT -3'), resulting in a deletion of 1300 bp. For *nfatc1* mutants, the gRNA was designed to target exon 3, upstream of the DNA-binding domain-encoding sequence (5'-TACGGCCCTGAGCTCGA-3'). For *twist1b*, a full locus deletion (1120 base pair deletion) was generated by targeting the 5' and 3' UTRs of the *twist1b* gene (5'-AAGGACGTTATTCCAGCATG-3' and 5'-TCGTCGTCATAAGACTCGCG-3'). The gRNAs were transcribed using a MegaShortScript T7 Transcription Kit (Thermo Fisher Scientific). *cas9* mRNA was transcribed using an mMESSAGE mMACHINE ™ T3 Transcription Kit (Thermo Fisher Scientific) using pT3TS-nCas9n as a template. The RNAs were purified with an RNA Clean and Concentrator Kit (Zymo Research). gRNAs (~12.5 pg/embryo for each gRNA) and *cas9* mRNA (~300 pg/embryo) were co-injected at the one-cell stage.

This subsection has been quoted *verbatim* from Gentile et al., *eLife*, 2021; DOI:10.7554/eLife.66143 and Gunawan*, Gentile* et al., *Circ Res* 2020; DOI: 10.1161/CIRCRESAHA.119.315992 for the scientific accuracy of the terms.

3.2.18 Genomic DNA preparation for genotyping and high-resolution melt analysis (HRM)

To genotype embryos/larvae after each experiment or adult fish using fin clipping, genomic DNA was isolated. Embryos/larvae were placed individually in 0.2 µl tubes. 9 to 18 µl (embryos/larvae) or 450 µl (fin clip) of 10 mM NaOH were added and incubated at 95°C for 10 minutes followed by the addition of 1:10 1 mM Tris-HCl (pH 8) to stop the reaction. After genomic DNA isolation, the HRM reaction was performed, with the following mix:

Component	**Volume**
PCR Master Mix	5 µl
Forward primer	0.5 µl
Reverse primer	0.5 µl
Genomic DNA	2 µl
Water	to 10 µl

The HRM reaction condition was the following:

Step	**Temperature**	**Time**	
Polymerase activation	95° C	7 minutes	
PCR amplification	95° C 60° C	10 seconds 15 seconds	For 35 cycles
HRM analysis	95° C 60° C 95° C	15 seconds 10 seconds 15 seconds	

3.2.19 Transmission electron microscopy (TEM)

Larvae were collected at 60 hpf from wild-type or mutant incross. The embryos were immediately fixed in ice-cold 1% PFA, 2% glutaraldehyde in 0.1 M sodium cacodylate buffer (pH 7.4) for 30 minutes on ice, and then stored at 4°C overnight. Samples were washed in 0.1 M sodium cacodylate buffer and postfixed in 2% (w/v) OsO_4, followed by *en bloc* staining with 2% uranyl acetate. Samples were dehydrated with a graded series of washes in acetone, transferred to acetone/Epon solutions, and eventually embedded in Epon. Ultra-thin sections (approximately 70 nm thick) obtained with a Reichert-Jung Ultracut E microtome were collected on copper slot grids. Sections were post-stained with 2% uranyl acetate for 20 minutes and 1% lead citrate for 2 minutes. Sections were examined with a Jeol JEM-1400 Plus transmission electron microscope (Jeol, Japan), operated at an accelerating voltage of 120 kV. Digital images were recorded with an EM-14800 Ruby Digital CCD camera unit (3296px x 2472px).

This subsection has been quoted *verbatim* from Gentile et al., *eLife*, 2021; DOI:10.7554/eLife.66143.

3.2.20 Chemical treatment

To increase the heart contractility, embryos were treated with 100 µm IBMX dissolved in DMSO for 12 to 24 hours. Control embryos were treated for the same time at the same DMSO concentration. 15 PTU-treated embryos were incubated with IBMX in a 6-well plate in a final volume of 5 ml and placed at 28°C.

3.2.21 Blastomere transplantation and morpholino injection

Cells obtained from mid-blastula stage donor embryos were transplanted along the blastoderm margin of age-matched host embryos. A *tnnt2a* ATG-MO was injected into the yolk at the one-cell stage at 0.3 ng per embryo. The embryos were then imaged at 52 hpf for both experiments.

This subsection has been quoted *verbatim* from Gentile et al., *eLife*, 2021; DOI:10.7554/eLife.66143.

3.2.22 Photoconversion

Kaede-expressing animals were embedded in 1% low-melting agarose in 0.2% tricaine to stop the heart for the duration of the imaging. First, a region of interest was selected. Then samples were photoconverted with 3 scans of the 405 nm wavelength laser (30% power) using a Zeiss LSM880 confocal microscope. The embryos were recovered and kept until further imaging 24 and 48 hours after photoconversion.

This subsection has been quoted *verbatim* from Gunawan*, Gentile* et al., *Circ Res* 2020; DOI: 10.1161/CIRCRESAHA.119.315992 for the scientific accuracy of the terms.

3.2.23 Activation of inducible Cre

Cre^{ERT2}-based recombination was induced with 5 μM 4-hydroxytamoxifen (Sigma) diluted in egg water from a 25 mM stock solution in ethanol (Kikuchi et al., 2010). Before dilution, the stock solution was heated at 65°C for 5 minutes. All Cre lines were crossed with the *ubb:switch* line. *sox10:*Cre^{ERT2} embryos were dechorionated and treated from 16 to 24 hpf; *myl7:*Cre^{ERT2} *and tcf21:*Cre^{ERT2} lines were treated from 72 to 120 hpf with daily changes of tamoxifen.

This subsection has been quoted *verbatim* from Gunawan*, Gentile* et al., *Circ Res* 2020; DOI: 10.1161/CIRCRESAHA.119.315992 for the scientific accuracy of the terms.

3.2.24 Luciferase assay

To generate the plasmid with a zebrafish *desmb* promoter driving Firefly Luciferase expression (pGl4.14-luc; SV40:hRLuc) (Bensimon-Brito et al., 2020), we cloned 800 bp of the promoter region of *desmb* using the following primers: forward - 5'-GAAAGCATAGTCTGCTTTCTCG -3' and reverse - 5'- GAGCGCCGGACAGCAGCC -3'. The zebrafish *snai1b* coding sequence was inserted downstream of the CMV promoter in the

pCMV-Tol2 plasmid (Addgene). The full-length *snai1b* coding sequence was amplified using the following primers: forward - 5'- ATGCCACGCTCATTTCTTGT -3' and reverse - 5'- GAGCGCCGGACAGCAGCCGGAC-3'. Per well in a 24-well plate, HEK-293T (Embryonic Kidney cells, ATCC Cat#CRL-3216) cells were transfected with 200 ng of the luciferase plasmid and 200 ng of pCMV-*snai1b* or the empty plasmid as control, as well as 1.5 µl Lipofectamine 3000 Transfection Reagent (Thermo Fisher Scientific). The cells were incubated with the transfection mix for 5–6 hours in DMEM+Glutamax (Thermo Fisher Scientific)/10% FBS Superior (Biochrom) without antibiotics. The cells were then incubated in DMEM+Glutamax/10% FBS/1% penicillin-streptomycin (PenStrep, Sigma) overnight. After 24 hours, they were rinsed in PBS and lysed with PLB buffer for Luciferase Assay (Promega). The supernatants were used to perform the luciferase assay, using the Dual-Luciferase® Reporter Assay System (Promega), following the manufacturer's instructions. Each experiment was carried out in triplicates (three wells per condition) in four independent experiments.

This subsection has been quoted *verbatim* from Gentile et al., *eLife*, 2021; DOI:10.7554/eLife.66143.

3.2.25 Generation of transgenic lines

To generate the *snai1b* overexpression lines, the full coding sequence was amplified by PCR using the following primers: forward - 5'- ATGCCACGCTCATTTCTTGT-3' and reverse - 5'- GAGCGCCGGACAGCAGCC-3'. The 765 bp amplicon was cloned into pT2-UAS and an iSce-I plasmid downstream of a *-0.2myl7* promoter and upstream of a P2A linker and GFP. To generate *Hhex* reporter line, the first intron of mouse *Hhex*, which has known enhancer activity (Migueles et al., 2017), was amplified by PCR using purified genomic DNA. This 1.2 kb fragment was inserted into a Tol2-containing vector (Addgene) upstream of the minimal *E1B* promoter and the GFP coding sequence(Sacilotto et al., 2013). To generate *Tg(UAS:twist1b^{DN}-GFP)*, the dominant-negative Twist1b (Twist1b^{DN}) protein with one amino acid substitution (Glu84Lys)(Das and Crump, 2012) was amplified from a *pME-twist1b^{DN}* plasmid (kind gift from Gage Crump). The amplicon was cloned into a pTol2-UAS (Addgene) vector

upstream of a P2A linker and GFP. All cloning experiments were performed using InFusion Cloning (System Biosciences). The plasmids were then injected into AB embryos at the one-cell stage (25 pg/embryo) together with *Tol2* mRNA (25 pg/embryo).

This subsection has been quoted *verbatim* from Gentile et al., *eLife*, 2021; DOI:10.7554/eLife.66143 and Gunawan*, Gentile* et al., *Circ Res* 2020; DOI: 10.1161/CIRCRESAHA.119.315992 for the scientific accuracy of the terms.

3.2.26 Generation of overexpression constructs

A full-length *snai1b* and *nfatc1* cDNA were cloned from 48 hpf. For *nfatc1* overexpression, a splice overlap extension PCR was used to introduce substitutions of 23 codons in the regulatory region of Nfatc1 (23 Serine to Alanine). The amplicons were then cloned into a pCS2+ vector (Addgene). *In vitro* transcription was performed using a mMESSAGE mMACHINE ™ T7 Transcription Kit (Thermo Fisher Scientific). Wild-type embryos were injected at the one-cell stage with 25 pg of *snai1b*, and 50 pg of *nfatc1*^{CA} or *gfp* mRNA. RNA from 40 4.5 hpf or 9 hpf embryos was extracted using a standard phenol/chloroform protocol.

To generate the *desmb* overexpression plasmid, the full coding sequence was amplified by PCR using the following primers: forward - 5'-ATGAGCCACTCTTATGCCAC-3' and reverse - 5'-CATGAGGTCCTGCTGGTG-3'. The 1419 bp amplicon was cloned into a iSce-I plasmid downstream of a *-0.2myl7* promoter and upstream of a P2A linker and GFP. All cloning experiments were performed using InFusion Cloning (System Biosciences). The plasmid was then injected into *Tg(myl7:BFP-CAAX)* embryos at the one-cell stage (25 pg/embryo) together with *Tol2* mRNA (25 pg/embryo) to obtain mosaic expression.

This subsection has been quoted *verbatim* from Gentile et al., *eLife*, 2021; DOI:10.7554/eLife.66143 and Gunawan*, Gentile* et al., *Circ Res* 2020; DOI: 10.1161/CIRCRESAHA.119.315992 for the scientific accuracy of the terms.

3.2.27 Image analysis

All immunostainings were analyzed in the YZ orthogonal plane to better visualize CM extrusion. The line scan function of Fiji was used to quantify fluorescence intensity at the junctional and basal domains. To visualize the fluorescence profile of N-cadherin immunostaining, a line of uniform thickness was drawn from junction to junction in adjacent CMs. To analyze the localization of α-catenin epitope α-18, p-myosin, and Desmin, a line of uniform thickness was drawn from the basal to the apical domain of CMs. To assess fluorescence intensity, the mean grey values were used, drawing a line of uniform thickness at the junctional (N-cadherin) or basal (α-catenin epitope α-18, p-myosin, and Desmin) domain of CMs. Images were processed and analyzed with Fiji. Background subtraction of rolling ball radius 20 was applied, followed by a mean filter of radius 1. Brightness and contrast were adjusted to remove any background fluorescence. Apical cell surface and aspect ratio were quantified using the line function of ImageJ. The total number of CMs was counted using the Spots function, and 3D cardiac surface rendering and ventricular volume quantification were obtained with the Surfaces function of the Imaris Bitplane Software.

This subsection has been quoted *verbatim* from Gentile et al., *eLife*, 2021; DOI:10.7554/eLife.66143.

3.2.28 Ventricular ejection fraction, ventricular fractional shortening, and heartbeat quantification

Embryos and larvae were mounted in 2% low-melting agarose without tricaine. 20-30 seconds movies were recorded with 5 ms exposure. Light intensity was kept to a minimum to avoid light-induced twitching.

For ejection fraction and fractional shortening measurements, the area of four consecutive diastoles and systoles was calculated using ImageJ software, following the calculation of the average diastole and systole area per embryo. The ejection fraction was calculated as a percentage using the formula below:

$$\%\ Ejection\ fraction = \frac{diastole - systole}{diastole} * 100$$

$$\%\ Fractional\ shortening = \frac{width\ at\ diastole - width\ at\ systole}{width\ at\ diastole} * 100$$

For the heartbeat, kymographs were generated using ImageJ software. Heartbeat was calculated as beats per minute (bpm) using the following formula:

$$bpm = \frac{\#\ heart\ contraction}{time\ (s)} * 60\ (s)$$

3.2.29 Imaging

Confocal microscopes were used to image stopped hearts. Embryos up to 10 dpf were mounted in 1% low-melting agarose with 0.2% tricaine, and the stopped hearts were imaged using a Zeiss LSM700, LSM800 observer, or LSM880 confocal microscope with a 20x or 40x dipping lens. Fixed embryos were mounted in 1% low-melting agarose and were imaged using a Zeiss LSM700 or LSM880 confocal microscope with a 20x or 40x dipping lens, and genotyped afterward. Sections from juvenile and adult hearts from 20 dpf onward were imaged using a LSM800 Observer 40X oil immersion lens. For whole-mount *in situ* hybridization, embryos were mounted on 1% agar and imaged using a Nikon SMZ25 microscope with a 40X objective.

For imaging beating hearts, a spinning disk microscope was used to acquire videos at 100 frames per second with the 40X water immersion lens (Zeiss Cell Observer spinning disk microscope). For heart measurement analysis, samples were mounted with 2% low-melting agarose without tricaine and 20-30 seconds movies were recorded with 5 ms exposure. The live zebrafish embryos from 52 to 70 hpf were mounted in 0.8% low-melting agarose containing 0.02% tricaine. The embryos were kept in PTU water containing 0.01% tricaine in a 28°C chamber throughout the live-imaging session. Time-lapse images of beating hearts were acquired with a 40X water

immersion objective at 100 frames per second. Developmental time points were collected every hour for 18 h with 25 z-stacks 1 µm apart.

Certain lines in this subsection have been quoted *verbatim* from Gentile et al., *eLife*, 2021; DOI:10.7554/eLife.66143 and Gunawan*, Gentile* et al., *Circ Res* 2020; DOI: 10.1161/CIRCRESAHA.119.315992 for the scientific accuracy of the terms.

3.2.30 Statistical analysis

All statistical analyses were performed in GraphPad Prism (Version 6.07). A Gaussian distribution was tested for every sample group using the D'Agostino-Pearson omnibus normality test. For the experiments that passed the normality test, all samples were further analyzed using the following parametric tests: the Student's t-test for comparison of 2 samples, or the one-way ANOVA test followed by correction for multiple comparisons with Dunn's Test for 3 or more samples. For all the experiments that did not pass the normality test, all samples were further analyzed using non-parametric tests: p-values were determined using the Mann-Whitney test for comparison of 2 samples, or the Kruskal-Wallis test followed by correction for multiple comparisons with Dunn's Test for 3 or more samples.

This subsection has been quoted *verbatim* from Gentile et al., *eLife*, 2021; DOI:10.7554/eLife.66143 and Gunawan*, Gentile* et al., *Circ Res* 2020; DOI: 10.1161/CIRCRESAHA.119.315992 for the scientific accuracy of the terms.

4. Results

4.1 The EMT transcription factor Snai1 maintains the zebrafish cardiac wall integrity by regulating intermediate filament genes

Part of this chapter has been published as an article in *eLife* (Gentile et al., *eLife* 2021; DOI:10.7554/eLife.66143). My contribution to the article is described as follows: conceptualization, formal analysis, validation, investigation, visualization, methodology, and writing (original draft, reviewing, and editing).

4.1.1 Snai1b is expressed in cardiomyocytes in the later stages of zebrafish cardiac development

In order to understand how cardiac wall integrity is maintained in the zebrafish heart, I searched for candidate transcription factors that regulate CM cytoskeletal and tissue integrity. Amongst the transcription factors involved in cardiac development, I focused on Snai1 (Nieto, 2002; Nieto et al., 2016), whose orthologues regulate cytoskeletal remodeling and epithelial tissue integrity in *Drosophila* (Martin et al., 2010; Weng and Wieschaus, 2016) and mammalian cell culture (Wee et al., 2020). It has been shown that *snai1b* is implicated in the migration of myocardial precursors towards the midline (Qiao et al., 2014), but a role in the later stages of myocardial wall development has not been reported yet. To visualize the expression pattern of *snai1b*, I performed a whole-mount *in situ* hybridization (WISH) at 50 hours post-fertilization (hpf) (Figure 4.1.1). At this stage, I detected the expression of *snai1b* in the head, gut, and somites (Figure 4.1.1). By combining WISH of *snai1b* with immunostaining using an MF20 antibody, that recognizes sarcomeres in muscle cells, I detected *snai1b* expression in the cardiac ventricle, as well as in the atrioventricular canal (AVC) region (Figure 4.1.1).

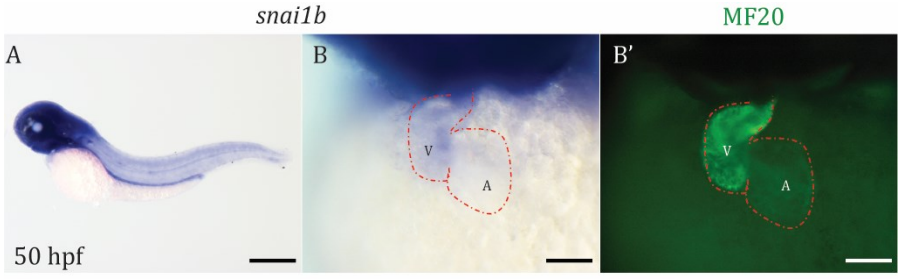

Figure 4.1.1: *snai1b* is expressed in the heart at 48 hpf

A) Whole-mount ISH of *snai1b* at 50 hpf, showing mRNA expression in the head, the gut, the trunk, and in the heart. **B-B')** *snai1b* expression in the heart, showing its expression in the ventricle and enrichment in the atrioventricular canal. **B')** MF20 staining. Scale bars: 50 μm. V, ventricle; A, atrium.

To have a better resolution of the heart, I embedded the embryos in gelatin to cryo-section them, to discriminate between myocardium and endocardium. Surprisingly, I detected *snai1b* expression in both endothelial cells (ECs) and cardiomyocytes (CMs) (Figure 4.1.2). This result suggests that *snai1b* is expressed in the CMs as early as 50 hpf.

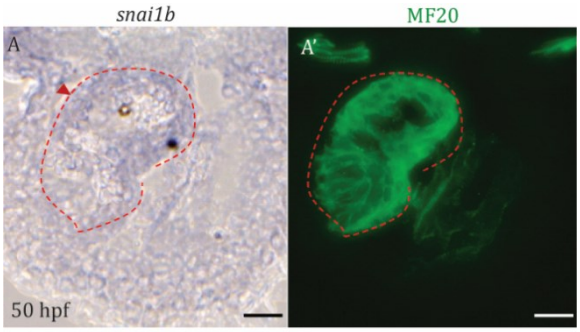

Figure 4.1.2: *snai1b* is expressed in the CMs at 48 hpf

A-A') Sections of the whole-mount ISH at 50 hpf. *snai1b* is expressed in the CMs (arrowhead). **A')** MF20 staining. Scale bars: 20 μm. V, ventricle; A, atrium

To analyze the expression levels of *snai1b* at the cellular level, I sorted ECs and CMs. Through fluorescence-activated cell sorting (FACS), I sorted ECs and CMs (using two different transgenic fluorescence lines (*Tg(myl7:GFP)* for CMs and *Tg(kdrl:nls-mCherry)* for ECs) from dissected zebrafish hearts at time points, 48 and 96 hpf. I then extracted RNA from sorted ECs and CMs, and performed qPCR analysis to detect the mRNA levels of *snai1b* (Figure 4.1.3). *snai1b* is strongly expressed in ECs at 48 hpf, as observed with WISH. However, I observed that the mRNA levels of *snai1b* become enriched in CMs at 96 hpf. Altogether, these data suggest that *snai1b* is expressed in CMs and has a potential function in CMs during the later stages of cardiac development.

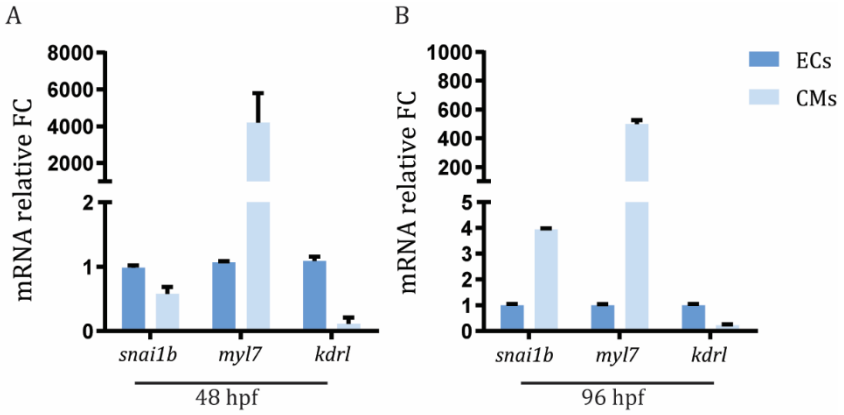

Figure 4.1.3: The expression of *snai1b* is enriched in CMs at 96 hpf

A-B) Relative mRNA levels of *snai1b*, *myl7,* and *kdrl* of sorted CMs and ECs at 48 (A) and 96 (B) hpf. **A)** *snai1b* is enriched in sorted ECs at 48 hpf. **B)** *snai1b* mRNA levels are increased in sorted CMs compared with sorted ECs at 96 hpf. n=3 biological replicates. Plot values represent means ± S.D. FC, fold change.

4.1.2 *snai1b* premature terminated codon (PTC) mutant allele does not phenocopy *snai1b* morphants

To functionally analyze *snai1b*, I generated loss-of-function mutant alleles of *snai1b.* To induce genomic lesion, I used the CRISPR/Cas9 technique and in particular, I used a gRNA targeting the first exon of *snai1b*, where the coding sequence for the SNAG domain is located (Figure 4.1.4). To verify the efficiency of my gRNA, I used high-resolution melt (HRM) analysis, amplifying 109 base pairs (bp) region around the sequence targeted by the gRNA and comparing the melting curve profile of injected embryos with uninjected ones (Figure 4.1.4).

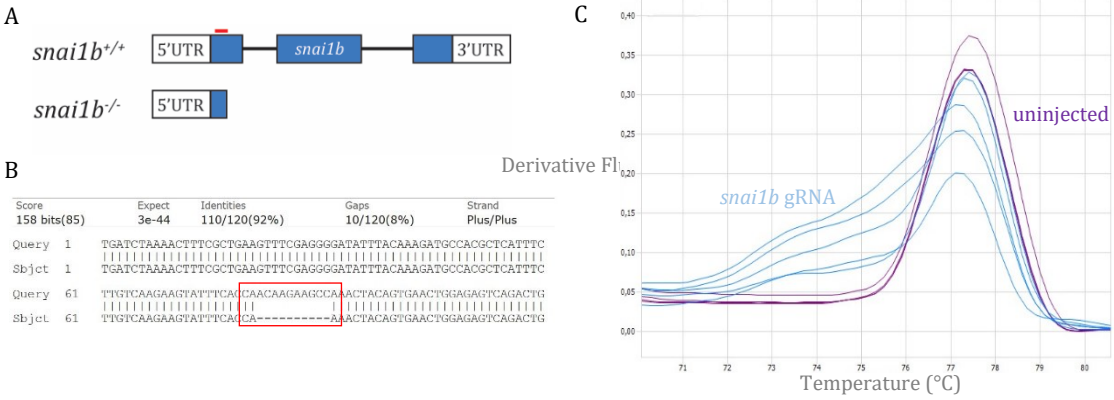

Figure 4.1.4: Generation of *snai1b* Δ10 allele

A) Schematic of *snai1b* Δ10 allele. The gRNA (red line) was used to generate a *snai1b* mutant allele with a premature stop codon in the first exon. **B)** Alignment of the wild-type sequence with the mutated sequence. The red box indicates the 10 bp deletion. **C)** Derivative melting curve of embryos injected with *snai1b* gRNA (blue lines) and uninjected embryos (purple lines).

After isolating the mutant alleles, I sequenced the F1 carrier fish and identified a 10 bp deletion in the first exon of *snai1b* (*snai1b*^{bns352}, Δ10). This mutation leads to a frameshift in the coding sequence and a premature terminated codon (PTC), with the formation of a truncated protein lacking the zinc finger DNA-binding domains of Snai1b (Figure 4.1.4).

Morphologically, the homozygous mutants were indistinguishable from wild types and able to reach adulthood (Figure 4.1.5). I did not observe the cardiac morphological defects reported in the morphant embryos (Qiao et al., 2014), including looping defects. To better understand the lack of phenotype in the mutant allele, I examined the expression levels of its paralogue *snai1a*, to examine whether the phenomenon of transcriptional adaptation can mask the mutant phenotype. qPCR analyses at 52 hpf showed a reduction of the mRNA of the *snai1b* mutant allele by 50%, suggesting a nonsense-mediated decay (NMD) response in *snai1b*^{bns352} mutants (Figure 4.1.5). As shown by our group, the mutant mRNA fragments can lead to the upregulation of the paralogous (El-Brolosy et al., 2019) which I observed here as the expression level of *snai1a* was upregulated by 1.5 fold (Figure 4.1.5).

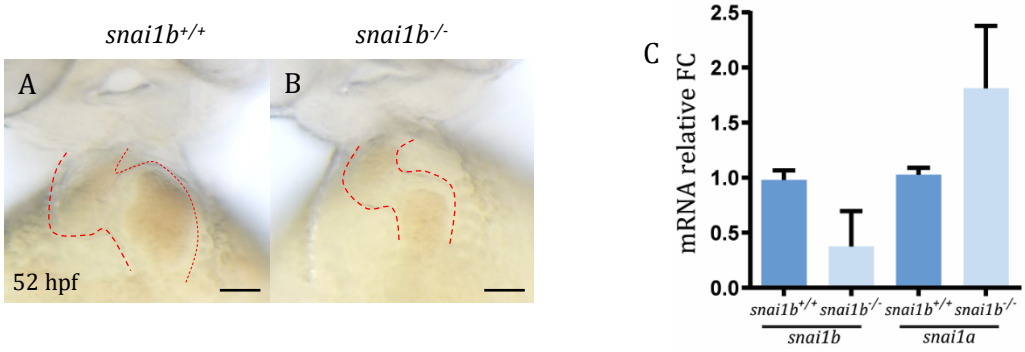

Figure 4.1.5: *snai1b* Δ10 mutant allele exhibit normal cardiac morphology and upregulation of *snai1a*

A-B') Brightfield images of 52 hpf *snai1b*$^{+/+}$ (A) and *snai1b*$^{-/-}$ (B) hearts. No morphology defects are observed in the mutant hearts. **C)** Relative mRNA levels of *snai1b* are significantly reduced in *snai1b*$^{-/-}$ hearts at 52 hpf, whereas *snai1a* expression levels appear upregulated, indicating transcriptional adaptation by the paralogue; n=4 biological replicates, 30 embryos each. Plot values represent means ± S.D. FC, fold change.

These data suggest that *snai1b* delta10 mutant allele leads to transcriptional adaptation, with the upregulation of the paralogue *snai1a* gene leading to a lack of phenotype.

4.1.3 *snai1b* promoter-less mutant allele exhibits cardiac morphology defects

To prevent transcriptional adaptation from *snai1a*, I decide to generate a promoter-less allele. In order to delete the proximal promoter of *snai1b*, I first performed an *in silico* analysis, to identify the putative promoter elements of the *snai1b* gene. I then used a combination of two gRNAs: one upstream to the predicted TATA box, and another in the first exon. To verify the efficiency of the gRNAs, I used the HRM analysis, amplifying 1500 bp region. In contrast to the previous analyses, to identify the F0 embryos, I analyzed the amplification level instead of the melting curve: amplification is detected only in the deletion, but not in the wild-type allele. Using this approach, I identified a 1206 bp deletion in the promoter region of *snai1b* (*snai1b*^{bns351}, promoter-less) (Figure 4.1.6).

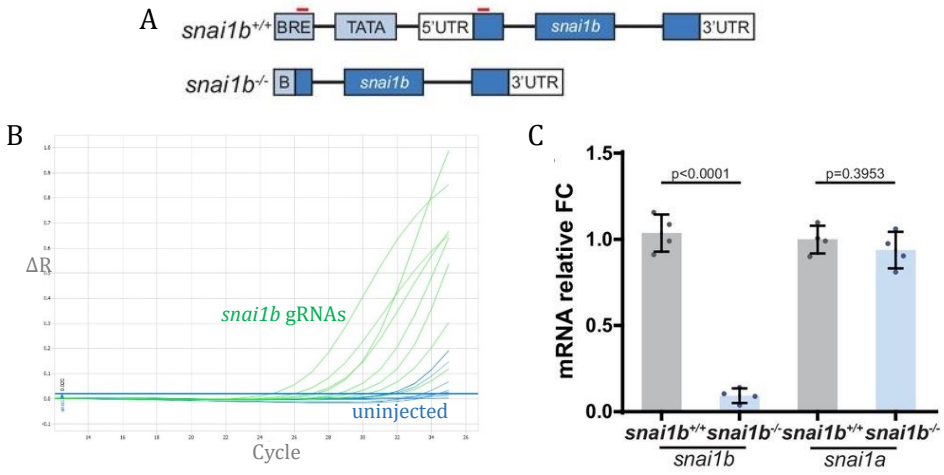

Figure 4.1.6: *snai1b* promoter-less allele does not upregulate *snai1a*

A) Cartoon representing *snai1b* promoter-less allele. Two gRNAs (red lines) were used to generate a *snai1b* mutant allele lacking 1300 bp upstream of the start codon. **B)** Expression profile of embryos injected with two gRNAs (green lines) and uninjected embryos (blue lines). In case of deletion, there is amplification. **C)** *snai1b* expression levels are significantly reduced in the mutant hearts at 48 hpf, whereas *snai1a* expression levels appear unchanged, indicating a lack of transcriptional adaptation by the paralogue; n=4 biological replicates, 30 embryos each. Plot values represent means ± S.D.; p-values determined by Student's t-test. BRE, transcription factor IIB response element; FC, fold change. Figure adapted and reprinted with permission from Gentile et al., 2021. License: CC BY 4.0.

By qPCR, I verified that in the mutants the mRNA levels of *snai1b* were almost undetectable at 52 hpf (Figure 4.1.6). I observed no transcriptional upregulation of the *snai1a* paralogue gene at 52 hpf (Figure 4.1.6). Since over 1000 bp were deleted, I also checked by qPCR that the expression levels of the neighboring gene were not affected (Figure 4.1.7), confirming that the big deletion of genomic DNA is not affecting the expression of other genes.

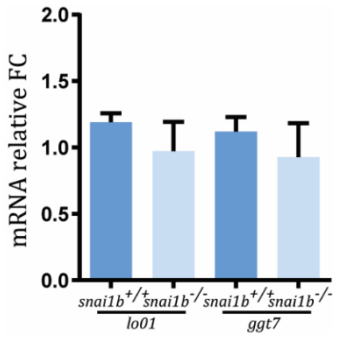

Figure 4.1.7: The deletion of the promoter of *snai1b* does not affect the neighboring genes

Relative mRNA levels of *snai1b* are significantly reduced in *snai1b*$^{-/-}$ hearts at 48 hpf, whereas *lo01* and *ggt7* expression levels appear unchanged, indicating that the neighbor genes are not affected; n=4 biological replicates, 30 embryos each. Plot values represent means ± S.D.; p-values determined by Student's t-test. FC, fold change.

Although the embryos do not display any gross morphology defects and about 70% of them reach adulthood, I observed that 50% of the mutant exhibit cardiac looping defects at 50 hpf (Figure 4.1.8). These data show that the *snai1b* promoter-less allele exhibit the early cardiac morphology defects observed in *snai1b* morphants.

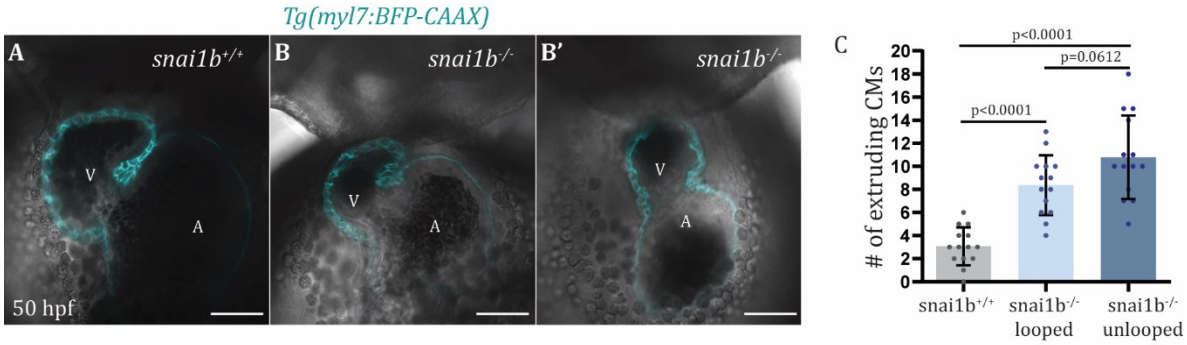

Figure 4.1.8: *snai1b* promote-less mutants display cardiac looping defects at 50 hpf
A-B') Confocal images of 50 hpf wild-type (A) and mutant (B-B') hearts, with 50% of mutant hearts exhibiting cardiac looping defects (B'). **C)** A similar number of extruding CMs is observed in unlooped mutant hearts compared with mutant looped hearts (*snai1b*$^{+/+}$, n =14; looped *snai1b*$^{-/-}$, n =14; unlooped *snai1b*$^{-/-}$, n=14). Plot values represent means ± S.D.; p-values determined by one-way ANOVA followed by multiple comparisons with Dunn test. Scale bars: 20 µm. V, ventricle; A, atrium; n number of embryos. Figure adapted and reprinted with permission from Gentile et al., 2021. License: CC BY 4.0.

4.1.4 *snai1b* promoter-less mutant allele exhibits extruding CMs

While examining the *snai1b* promoter-less heart, I noticed a surprising phenotype leading to an impairment of the cardiac wall integrity: extrusion of CMs away from the cardiac lumen. A low rate of extruding CMs is also observed in the wild-types embryos, but in heterozygous and homozygous *snai1b* mutants, including the one with looping defects, the number of extruding CMs was significantly increased compared with the wild-type siblings (Figure 4.1.9).

To better understand if the localization of extrusion of CMs was correlated with high mechanical stress in the heart, I analyzed the regional distribution of the CM extrusion (Figure 4.1.10). The frequency of extrusion was higher at the AVC, where CMs have to withstand stronger mechanical forces due to the shear stress of the blood flow and due to looping morphogenesis (Auman et al., 2007; Bornhorst et al., 2019; Dietrich et al.,

2014). To avoid potential secondary effects, I decided to focus my attention on the mutants that display unaffected cardiac looping.

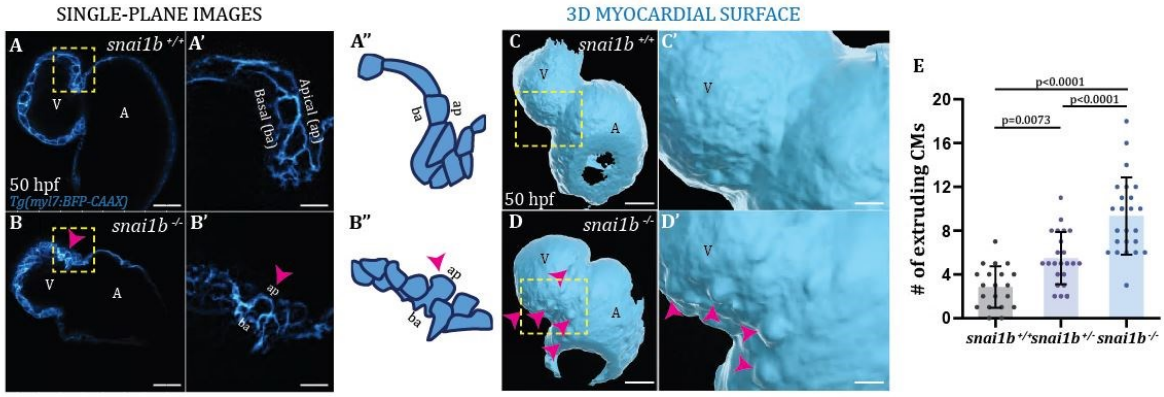

Figure 4.1.9: Snai1b maintains the cardiac wall integrity

A-B") Confocal images of *Tg(myl7:BFP-CAAX)* wild-type (A) and mutant (B) hearts at 50 hpf. Close-up of boxed areas (A', B'), and cartoon (A", B"). **C-D')** 3D surface rendering of the myocardium of *Tg(myl7:BFP-CAAX)* wild-type (C, C') and mutant (D, D') embryos at 50 hpf. Magenta arrowheads in B, B', B", D, D' point to CM extrusions. **E)** Extruding CMs are more in *Tg(myl7:BFP-CAAX)* mutant embryos compared with wild-type and heterozygous siblings at 50 hpf (*snai1b*$^{+/+}$, n =20; *snai1b*$^{+/-}$, n =23; *snai1b*$^{-/-}$, n=24). Plot values represent means ± S.D.; p-values determined by one-way ANOVA followed by multiple comparisons with Dunn test. Scale bars: 20 µm. V, ventricle; A, atrium; ap, apical; ba, basal; n, number of embryos. Figure adapted and reprinted with permission from Gentile et al., 2021. License: CC BY 4.0.

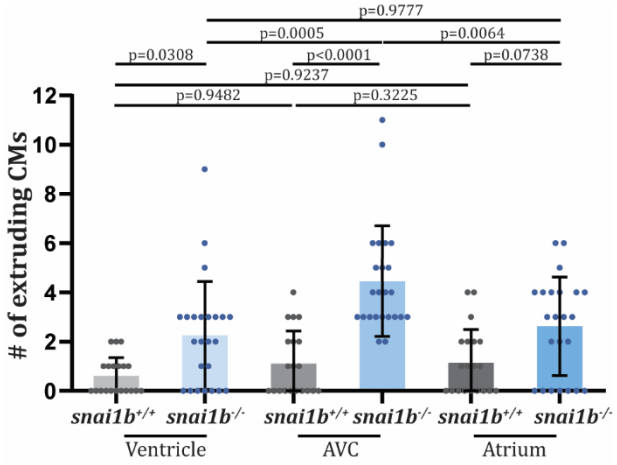

Figure 4.1.10: The majority of extruding CMs are localized at the atrioventricular canal region

The majority of extruding CMs in mutant hearts are localized in the AVC compared with the ventricle and atrium (*snai1b*$^{+/+}$, n =20; *snai1b*$^{-/-}$, n=24). Plot values represent means ± S.D.; p-values determined by one-way ANOVA followed by multiple comparisons with Dunn test. Figure adapted and reprinted with permission from Gentile et al., 2021. License: CC BY 4.0.

Extrusion of CMs can be observed as early as 48 hpf, but also later during larval stages as 78 and 100 hpf (Figure 4.1.11), suggesting that Snai1b is maintaining the myocardial wall integrity throughout the cardiac development.

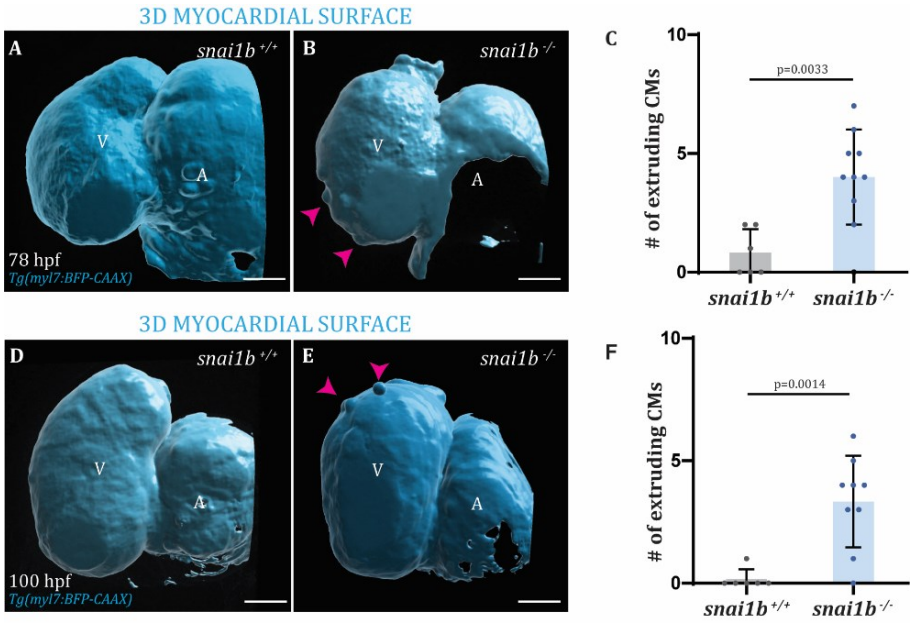

Figure 4.1.11: Increased CM extrusion in *snai1b* mutant larvae

A-F) 3D surface rendering of the heart at 78 and 100 hpf. Mutant larvae (B, E) display more extrusion of CMs (arrowheads) compared with wild-type larvae (A, D); quantification (C, F) (C, *snai1b*$^{+/+}$, n=6; *snai1b*$^{-/-}$, n=10; F, *snai1b*$^{+/+}$, n=12; *snai1b*$^{-/-}$, n=10). Plot values represent means ± S.D.; p-values determined by Student's t-test. Scale bars: 20 µm. V, ventricle; A, atrium; n, number of embryos. Figure adapted and reprinted with permission from Gentile et al., 2021. License: CC BY 4.0.

To better characterize the dynamics of the extruding CMs, I performed a time-lapse experiment on beating hearts over a period of 18 hours (Figure 4.1.12). Starting at 52 hpf, I observed that in the *snai1b* mutants a few extruding CMs completely detach from

the cardiac wall and remain in the pericardial cavity for several hours. I did not observe the same CM behavior in the beating heart of wild-type embryos. Altogether, these data suggest that Snai1b has a role in maintaining the cardiac wall integrity and preventing unnecessary extrusion of CMs.

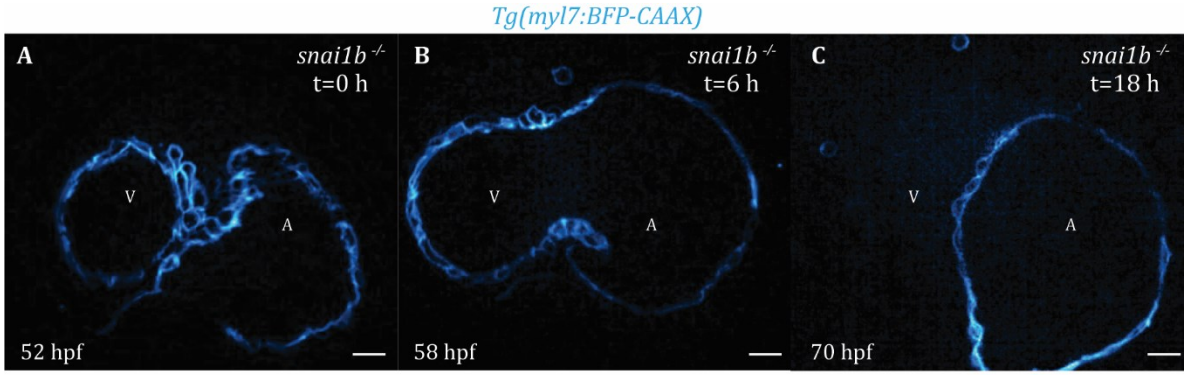

Figure 4.1.12: CMs in *snai1b*$^{-/-}$ hearts extrude from the cardiac wall and are visible in the pericardial cavity

A-C) Frames from time-lapse imaging of the beating heart of a mutant embryo to visualize extrusion of CMs at 52 (A), 58 (B), and 70 (C) hpf; extruded CMs are found in the pericardial cavity (arrowheads in B and C). Scale bars: 20 μm. V, ventricle; A, atrium. Figure adapted and reprinted with permission from Gentile et al., 2021. License: CC BY 4.0.

4.1.5 CM extrusion is not caused by cell death and affects heart morphology and function

Since epithelial cells remove dying cells by extrusion (Rosenblatt et al., 2001), I explored the possibility that extruding CMs were apoptotic cells. To test this hypothesis, I performed a deoxynucleotidyl transferase dUTP nick end labeling (TUNEL) comparing mutant embryos with wild-type siblings (Figure 4.1.13). Surprisingly, there was no difference in the rate of dying cells in the two groups. These data suggest that CM extrusion is not due to an increase in the rate of cell death.

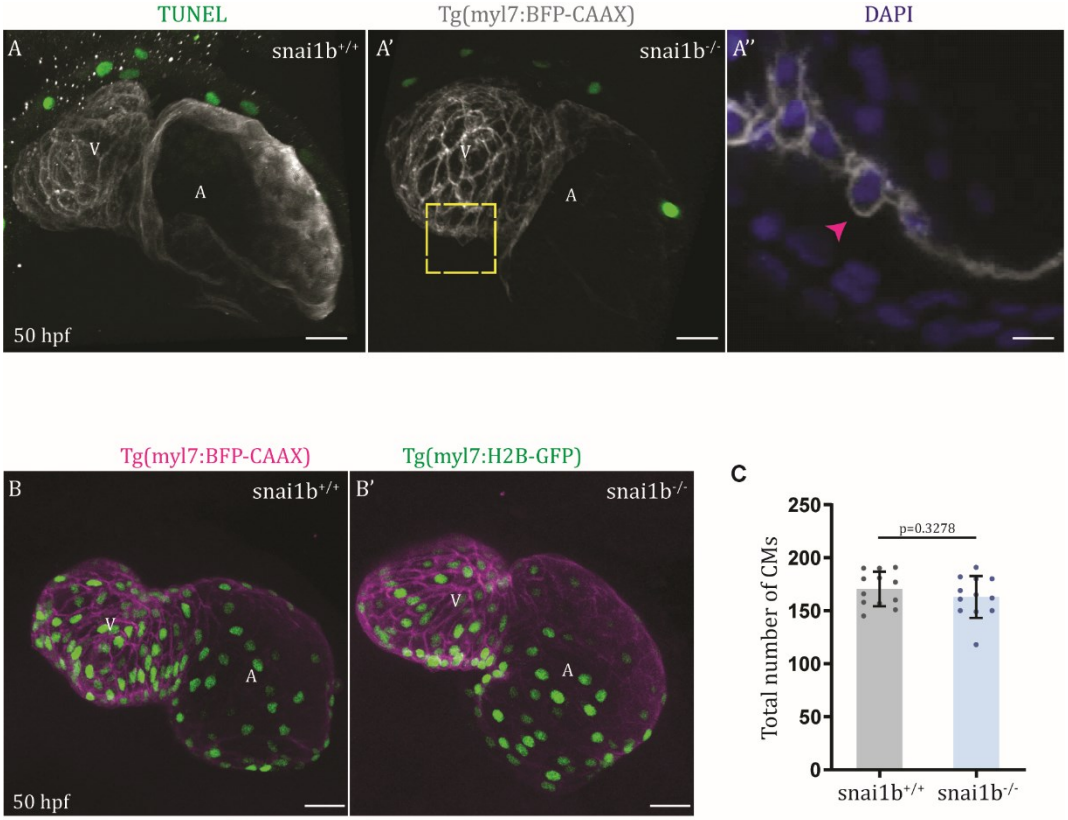

Figure 4.1.13: Extruding CMs are not dying cells

A-A") TUNEL assay analysis indicates that extruding CMs in *snai1b*$^{-/-}$ embryos are not apoptotic. Confocal images of *Tg(myl7:BFP-CAAX)* wild-type (A) and mutant (A'-A") hearts at 50 hpf. Close-up of extruding CM (arrowhead) labeled with DAPI, but not with TUNEL (A"). **B-B')** Confocal images of *Tg(myl7:H2B-GFP)* wild-type (B) and mutant (B') hearts at 52 hpf. **C)** The total number of CMs does not change significantly in mutant hearts (n=12) compared with wild-type hearts (n=12). Plot values represent means ± S.D.; p-value determined by Student's t-test. Scale bars: 20 µm (A-A', B-B'); 10 µm (A''). V, ventricle; A, atrium; n, number of embryos. Figure adapted and reprinted with permission from Gentile et al., 2021. License: CC BY 4.0.

Although I did not observe a significant reduction of CM number at 50 hpf but only 5 fewer cells on average (Figure 4.1.13), I observed a significant reduction in the number of CM that delaminated in the mutant larvae compared with wild-type larvae at 78 hpf (Figure 4.1.14). This reduction in the delaminating CMs results in fewer trabecular CMs at 100 hpf (Figure 4.1.14). These data suggest that the extrusion of CM leads to

impairment of CM maturation, particularly in the process of trabeculation, in the later stages of cardiac development.

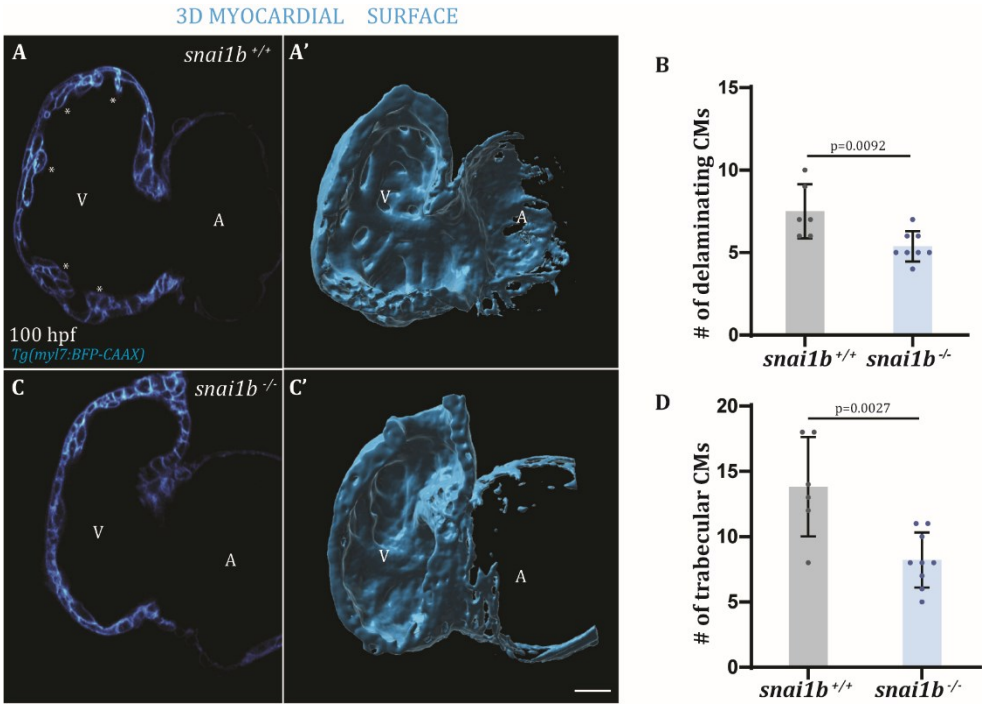

Figure 4.1.14: *snai1b* mutants display a reduced number of trabecular cardiomyocytes A-C') Confocal images and inner 3D surface rendering of trabecular CMs (asterisks in A) in 100 hpf mutant (C-C') and wild-type (A-A') larvae. **B-D)** Reduced number of delaminating (B) and trabecular (D) CMs are observed in mutant larvae compared with wild-type larvae at 78 (*snai1b*$^{+/+}$, n=6; *snai1b*$^{-/-}$, n=8) and 100 (*snai1b*$^{+/+}$, n=6; *snai1b*$^{-/-}$, n=9) hpf. Plot values represent means ± S.D.; p-values determined by Student's t-test. Scale bars: 20 µm. V, ventricle; A, atrium; n, number of embryos. Figure adapted and reprinted with permission from Gentile et al., 2021. License: CC BY 4.0.

To have a better understanding of the impact of CM extrusion at the cellular level, I analyzed the aspect ratio and the apical cell surface of the CMs at 52 and 74 hpf (Figure). I observed that at both time points the aspect ratio and apical cell surface of CMs were significantly reduced in the *snai1b* mutants compared with the wild types. At the tissue level, I also observed a reduction of the ventricular volume of *snai1b* mutants compared with the wild type at both 52 and 74 hpf (Figure 4.1.15). Altogether, these data suggest that Snai1b is required to maintain the cardiac wall integrity at the cellular and tissue levels.

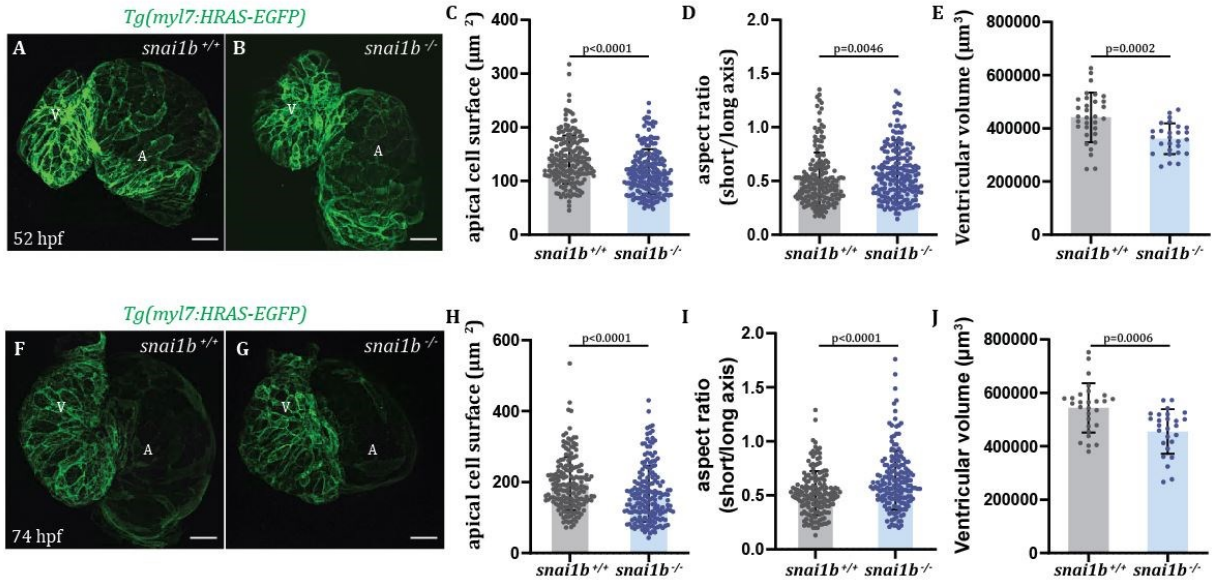

Figure 4.1.15: *snai1b* mutants exhibit altered CM morphology

A-B, F-G) Confocal images of *Tg(myl7:HRAS-EGFP)* wild-type (A, F) and mutant (B, G) hearts at 52 (A-B) and 74 (F-G) hpf. Mutant embryos display reduced CM apical cell surface (C, H), increased CM aspect ratio (D, I), and reduced ventricular volume (E, J) compared with wild-type embryos at 52 and 74 hpf. **C, H)** *snai1b*$^{+/+}$, N=190 at 52 hpf, N=173 at 74 hpf; *snai1b*$^{-/-}$, N=195 at 52 hpf, N=178 at 74 hpf. **D, I)** *snai1b*$^{+/+}$, N=183 at 52 hpf, N=162 at 74 hpf; *snai1b*$^{-/-}$, N=188, N=170 at 74 hpf. **E, J)** *snai1b*$^{+/+}$, n=32 at 52 hpf, n=28 at 74 hpf; *snai1b*$^{-/-}$, n=27 at 52 hpf, n=26 at 74 hpf. Plot values represent means ± S.D.; p-values determined by Mann-Whitney *U* test. Scale bars: 20 µm. V, ventricle; A, atrium; n, number of embryos; N, number of CMs. Figure adapted and reprinted with permission from Gentile et al., 2021. License: CC BY 4.0.

To confirm that impairment of the cardiac wall integrity due to the extrusion of the CMs has an impact on heart physiology, I measured heart rates, ejection fraction, and fractional shortening of *snai1b* mutants at 52 and 74 hpf (Figure 4.1.16). Although those parameters were not affected at the earlier time point, I observed a significant reduction of all three parameters in *snai1b* mutants compared with wild types at 74 hpf. These data suggest that disruption of the cardiac wall integrity subsequently impairs cardiac function.

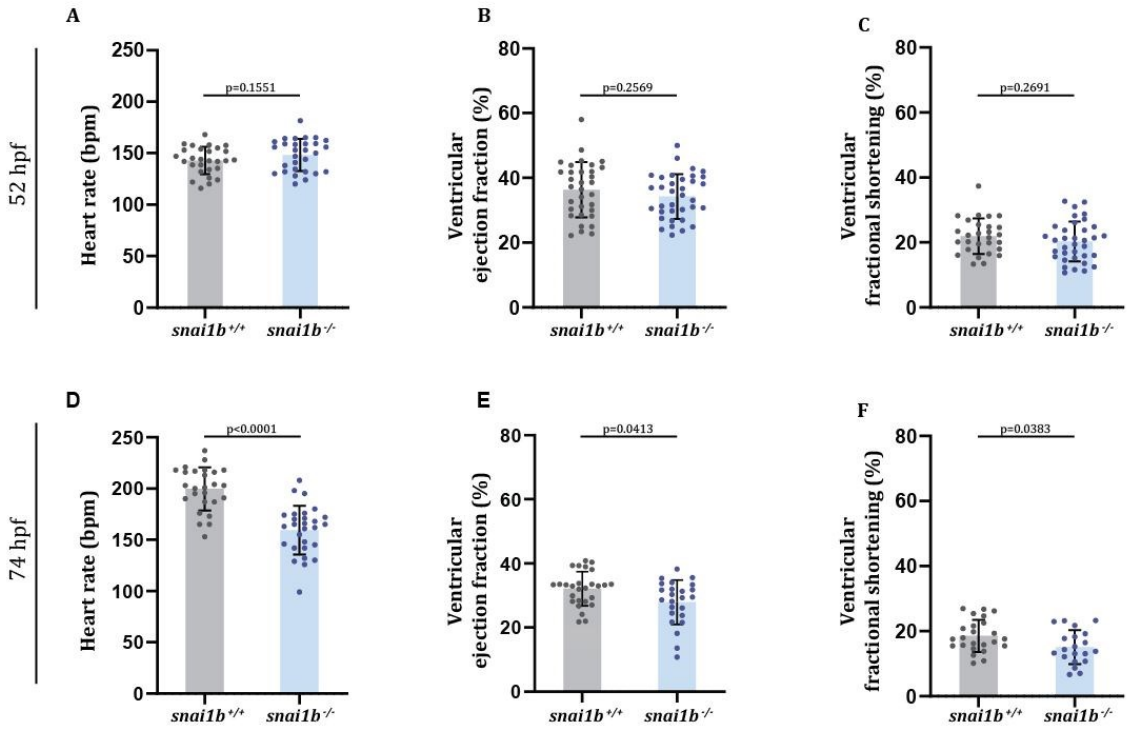

Figure 4.1.16: *snai1b* mutants display altered cardiac function at 74 hpf

A-F) Mutant embryos display no differences in heart rate (A), ventricular ejection fraction (B), or ventricular fractional shortening (C) compared with wild type embryos at 52 hpf (K, *snai1b*$^{+/+}$, n=28; *snai1b*$^{-/-}$, n=29; L, *snai1b*$^{+/+}$, n=33; *snai1b*$^{-/-}$, n=35; M, *snai1b*$^{+/+}$, n=28; *snai1b*$^{-/-}$, n=35), but display reduced heart rate (D), ventricular ejection fraction (E), and ventricular fractional shortening (F) compared with wild-type larvae at 74 hpf (N, *snai1b*$^{+/+}$, n=26; *snai1b*$^{-/-}$, n=28; P, *snai1b*$^{+/+}$, n=27; *snai1b*$^{-/-}$, n=24; O, *snai1b*$^{+/+}$, n=24; *snai1b*$^{-/-}$, n=20). Plot values represent means ± S.D.; p-values determined by Mann-Whitney *U* test. n, number of embryos. Figure adapted and reprinted with permission from Gentile et al., 2021. License: CC BY 4.0.

4.1.6 CM extrusion is influenced by heart contraction

As previously shown by our group, the mechanical forces induced by heart contractility influence the myocardial wall integrity (Fukuda et al., 2019, 2017; Rasouli et al., 2018). I hypothesize that reducing or abolishing the cardiac contractility could reduce CM extrusion, and conversely, increasing cardiac contractility could increase the number of CM extrusions. To test the first hypothesis, I injected the *tnnt2a* morpholino (Sehnert

et al., 2002) to prevent cardiac contraction in *snai1b* mutants and compared them with uninjected wild types at 50 hpf (Figure 4.1.17). Indeed, I observed that by stopping the heart contraction, the number of CM extrusions was significantly reduced and became comparable with the number of CM extrusions observed in the uninjected wild types.

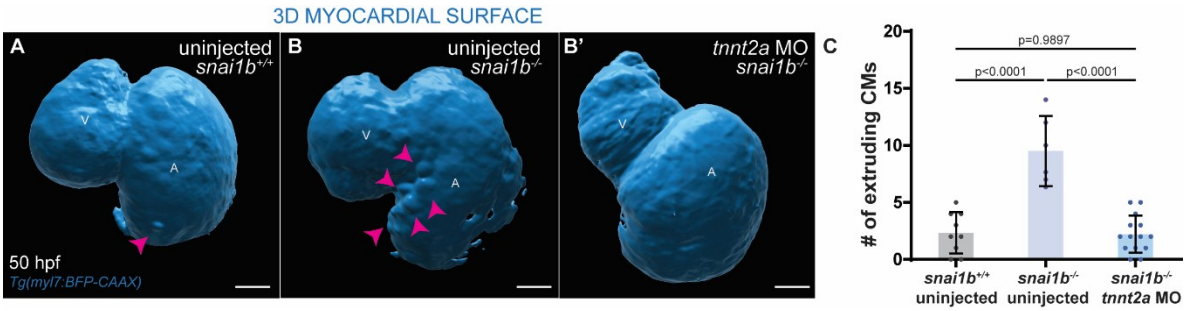

Figure 4.1.17: Extruding CMs are influenced by heart contraction

A-C) Reduced number of extruding CMs in mutants embryos are observed when heart contraction is blocked with *tnnt2a* MO. **A-B')** 3D surface rendering of the myocardium of wild-type (A) and mutant (B) uninjected embryos and mutant embryos injected with *tnnt2a* MO (B'). **C)** Magenta arrowheads in B point to extruding CMs in mutant embryos injected with *tnnt2a* MO (n=14) compared with uninjected mutant (n=6) and wild-type (n=9) embryos at 50 hpf. Plot values represent means ± S.D.; p-values determined by one-way ANOVA followed by multiple comparisons with Dunn test. Scale bars: 20 µm. V, ventricle; A, atrium; n, number of embryos. Figure adapted and reprinted with permission from Gentile et al., 2021. License: CC BY 4.0.

To test the second hypothesis, I treated the wild-types and mutant embryos starting from 24 hpf until 50 hpf with IBMX, a drug that is able to increase heart contraction. I observed a significant increase in the number of extruding CMs in the wild types treated with IBMX compared with the control embryos treated with DMSO, similar to the *snai1b* mutants (Figure 4.1.18). In the *snai1b* mutant embryos treated with IBMX, the number of CM extrusions was comparable with the embryos treated with DMSO, suggesting that there might be other mechanisms preventing the complete loss of CMs. Altogether, these data suggest that the number of CM extrusions is dependent on heart contraction.

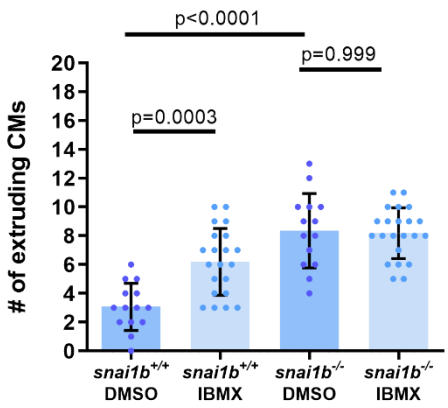

Figure 4.1.18: Increase cardiac contractility leads to an increased number of extruding CMs in wild-types embryos

The number of extruding CMs increases in wild-type embryos when treated with IBMX compared with DMSO at 52 hpf. whereas the number of extruding CMs does not change in mutant embryos treated with IBMX compared with DMSO (*snai1b*$^{+/+}$ DMSO, n=14; *snai1b*$^{+/+}$ IBMX, n=21; *snai1b*$^{-/-}$ DMSO, n=14; *snai1b*$^{-/-}$ IBMX, n=22). Plot values represent means ± S.D.; p-values determined by Mann-Whitney *U* test. n, number of embryos.

4.1.7 *snai1b* acts cell autonomously to maintain cardiac wall integrity

To test the cell-autonomously role of Snai1b in promoting myocardial wall integrity, I generated mosaic hearts by cell transplantation. I transplanted donor mutant CMs in host wild-types heart or vice versa. Interestingly, I observed that donor-derived *snai1b* wild-type CMs remained integrated into the *snai1b* mutant myocardial wall, whereas donor-derived *snai1b* mutant CMs in a *snai1b* wild-type heart were significantly more prone to extrude than their wild-type neighbors. These results suggest that *snai1b* is required in a CM-autonomous manner to maintain myocardial wall integrity.

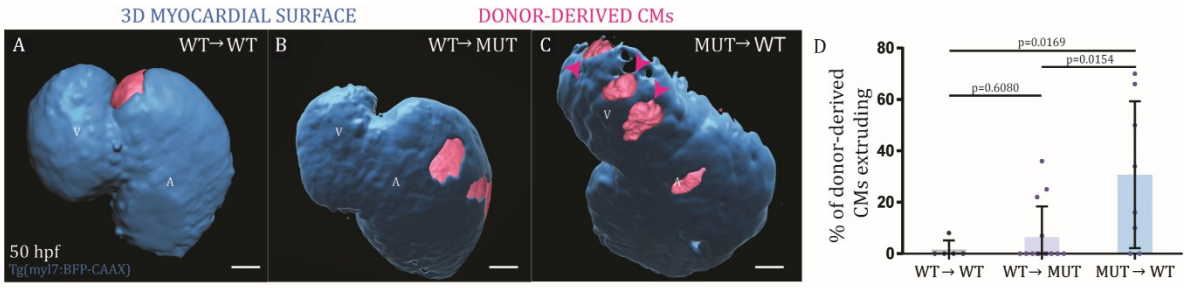

Figure 4.1.19: Snai1b acts in a cell-autonomous manner to maintain cardiac wall integrity

A-C) 3D surface rendering of the myocardium showing wild-type donor-derived CMs in wild-type (A) or mutant (B) heart, and mutant donor-derived CMs in a wild-type heart (C). **D)** The percentage of donor-derived CMs that extrude is higher when mutant donor-derived CMs are transplanted into wild-type hearts (n=8) than when wild-type donor-derived CMs are transplanted into wild-type (n=5) or mutant (n=14) hearts. Plot values represent means ± S.D.;

p-values determined by one-way ANOVA followed by multiple comparisons with Dunn test. Scale bars: 20 μm. V, ventricle; A, atrium; n, number of embryos. Figure adapted and reprinted with permission from Gentile et al., 2021. License: CC BY 4.0.

To further confirm the cell-specific role of Snai1b in maintaining cardiac wall integrity, I designed a construct to overexpress *snai1b* cDNA in a tissue-specific manner. First, I cloned the *snai1b* cDNA under the myocardial-specific promoter *myl7*. To visualize the *snai1b* construct in the cells, I tagged it with a GFP fluorophore, separated by a P2A sequence. I injected the construct in the one-cell stage mutant embryos and raised the fish to generate the established line (*Tg(myl7:snai1b-p2a-GFP)*) (Figure 4.1.20). After identifying a founder and raising the F1 generation, I observed them at 50 hpf (Figure 4.1.21). Notably, the number of CM extrusions in the *snai1b* CM-specific overexpressing mutant embryos was decreased when compared to the negative mutant siblings, and comparable to the number of extruding CMs observed in the wild-type embryos.

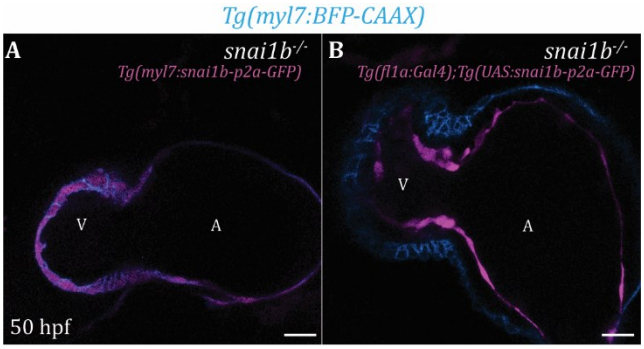

Figure 4.1.20: *snai1b* overexpression in CMs and ECs

A-B) Confocal images of 50 hpf mutant hearts overexpressing *snai1b* under a *myl7* (A) or *fli1a* (B) promoter. Scale bars: 20 μm. V, ventricle; A, atrium. Figure adapted and reprinted with permission from Gentile et al., 2021. License: CC BY 4.0.

To test if the rescue of the *snai1b* mutant phenotype was possible by overexpressing *snai1b* in ECs, I used the GAL4-UAS system, particularly an EC-specific Gal4 driver under the promoter *fli1a*. First, I cloned *snai1b* cDNA under the UAS promoter and tagged it with the GFP fluorophore separated by the P2A sequence. Then, I injected the construct into one-cell stage mutant embryos in *Tg(fli1a:GAL4)* background. I established a stable line (*Tg(UAS:snai1b-p2a-GFP)*) (Figure 4.1.20) and observed the effects of endothelial-specific overexpression of *snai1b* at 50 hpf (Figure 4.1.21); in the mutant embryos overexpressing snai1b specifically in the ECs the number of extruding CMs were

comparable with the negative mutant siblings. These data suggest that CM-specific, but not endothelial-specific, *snai1b* overexpression rescued the *snai1b* mutant CM extrusion phenotype, further indicating that Snai1b is required in CMs to suppress their extrusion away from the lumen.

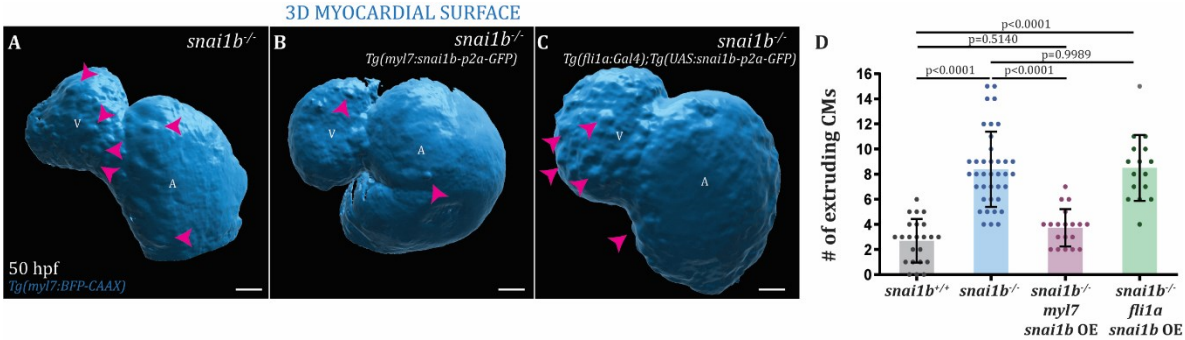

Figure 4.1.21: CM-specific *snai1b* rescue the extrusion phenotype

A-D) 3D surface rendering of the myocardium of a mutant embryo (A), and mutant embryo overexpressing *snai1b* under a *myl7* (B) or a *fli1a* (C) promoter. D) Magenta arrowheads point to extruding CMs in *snai1b*$^{-/-}$ embryos (n=19) overexpressing *snai1b* in CMs (N, P) compared with mutant embryos (M, P, n=38), comparable with wild-type embryos (n=24). No changes are observed in the number of extruding CMs in mutant embryos (n=16) when *snai1b* is overexpressed in endothelial cells (*fli1a*) (C-D). Plot values represent means ± S.D.; p-values determined by one-way ANOVA followed by multiple comparisons with Dunn test. Scale bars: 20 µm. V, ventricle; A, atrium; n, number of embryos. Figure adapted and reprinted with permission from Gentile et al., 2021. License: CC BY 4.0.

(Certain lines in this subsection have been quoted *verbatim* from Gentile et al., *eLife*, 2021; DOI:10.7554/eLife.66143 for the scientific accuracy of the terms).

4.1.8 Snai1b limits CM extrusion by regulating the actomyosin machinery

CMs lose their apicobasal polarity to delaminate into the cardiac lumen to form the trabecular networks (Jiménez-Amilburu et al., 2016; Staudt et al., 2014). To test wether extruding CMs undergo an EMT-like process and lose their apicobasal polarity, similar to delaminating CMs, I examined the polarity marker Podocalyxin using the transgenic

line *Tg(-0.2myl7:EGFP-Podxl)* at 50 hpf (Figure 4.1.22). Surprisingly, I could not observe any changes in the localization of Podocalyxin, as it remained on the apical side of the extruding CMs in mutant embryos, suggesting that the extruding CMs do not lose their apicobasal polarity.

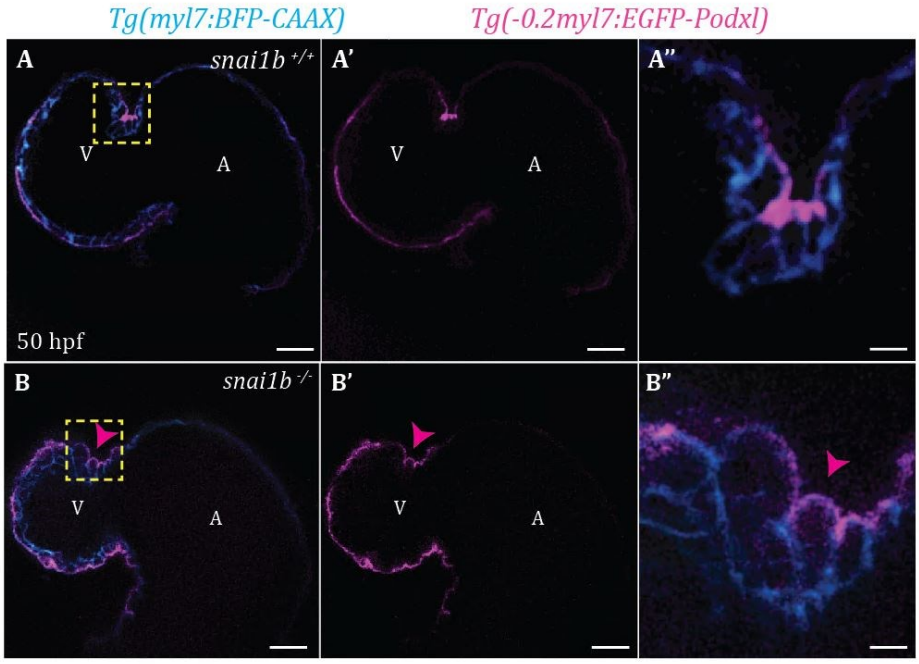

Figure 4.1.22: Extruding CMs in *snai1b* mutants exhibit apicobasal polarity

A-B") Confocal images of *Tg(myl7:BFP-CAAX); Tg(-0.2myl7:EGFP-podocalyxin)* wild-type (A-A') and mutant (B-B') hearts at 50 hpf. Close-up of boxed areas (A'', B''). The localization of the apical marker Podocalyxin does not change in the extruding CMs (arrowheads in B-B''). Scale bars: 20 µm (A-A', B-B'), 2 µm (A'', B''). V, ventricle; A, atrium. Figure adapted and reprinted with permission from Gentile et al., 2021. License: CC BY 4.0.

In epithelial cells, it has been shown that cell extrusion is important to limit tissue overcrowding, eliminate apoptotic cells to maintain tissue homeostasis, and/or determine cell fate (Kocgozlu et al., 2016; Wee et al., 2020). During the process of extrusion, the actomyosin machinery plays an important role. A contractile actomyosin ring is formed around the cell cortex to facilitate extrusion (Rosenblatt et al., 2001; Eisenhoffer et al., 2012; Kocgozlu et al., 2016). To test if the extrusion of CMs in *snai1b* mutants was facilitated by intracellular mechanical forces generated by the actomyosin machinery, I performed immunostaining for different tension markers. First, I

examined the localization of the α-catenin epitope α-18 (Yonemura et al., 2010), which recognized the open conformation of α-catenin. I observed that α-catenin epitope α-18 was localized mostly at the basal domain of the extruding CMs in mutant and wild-type siblings at 50 hpf (Figure 4.1.23), suggesting that the extruding CMs have increased cellular contractility. This result was confirmed with immunostaining for the activated, phosphorylated Myosin (Figure 4.1.24). p-myosin is normally enriched in the apical domain of CMs, which will give raise to trabecular CMs; however, I observed enrichment of p-myosin at the basal domain of the extruding CMs, in both mutant and wild-type extruding CMs, suggesting an increased cellular tension in the basal domains of extruding CMs. When a cell extrudes, cellular adhesion is also rearranged (Grieve and Rabouille, 2014; Lubkov and Bar-Sagi, 2014; Teng et al., 2017). To verify that this occurs in the extruding CMs, I performed immunostaining for N-cadherin, the most abundant adhesion molecule in the heart (Bagatto et al., 2006; Cherian et al., 2016), at 50 hpf (Figure 4.1.23). As expected, I observed an overall reduction of N-cadherin levels in the junctions of the extruding CMs in mutant hearts compared with those in wild-type siblings.

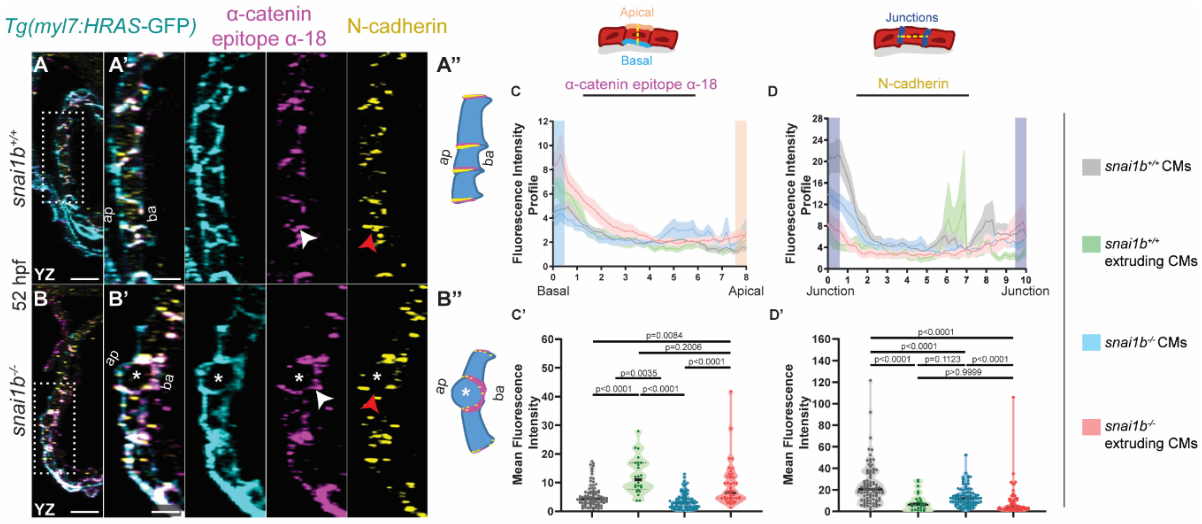

Figure 4.1.23: Extruding cardiomyocytes exhibit basal contractility and reduced adhesion

A-B″) Orthogonal projections in the YZ plane of a 52 hpf wild-type heart (A) immunostained for α-catenin epitope α-18, N-cadherin, and GFP compared with a mutant sibling heart (B). Close-

up of boxed areas of wild-type (A') and mutant (B') CMs. Cartoons represent the localization of activated α-catenin (magenta) in the basal domain of extruding CMs in mutant embryos and defects in N-cadherin (yellow) localization in the junctional domain of mutant CMs (A"-B"). **C-D') Fluorescence Intensity Profile (FIP) (C-D) and mean Fluorescence Intensity (mFI) (C'-D') of α-catenin epitope α-18 and N-cadherin immunostaining in 52 hpf wild-type and mutant CMs, and in wild-type and mutant extruding CMs. The α-catenin epitope α-18 is observed in the basal domain (white arrowhead in B') of extruding CMs (white asterisks in B') in mutant embryos, and a reduction in junctional N-cadherin (red arrowhead in B') is observed in mutant CMs. (FIP α-catenin epitope α-18: *snai1b*$^{+/+}$ CMs, N=179; *snai1b*$^{+/+}$ extruding CMs, N=60; *snai1b*$^{-/-}$ CMs, N=140; *snai1b*$^{-/-}$ extruding CMs, N=54; mFI α-catenin epitope α-18: *snai1b*$^{+/+}$ CMs, N=90; *snai1b*$^{+/+}$ extruding CMs, N=24; *snai1b*$^{-/-}$ CMs, N=88; *snai1b*$^{-/-}$ extruding CMs, N=44. FIP N-cadherin: *snai1b*$^{+/+}$ CMs, N=90; *snai1b*$^{+/+}$ extruding CMs, N=12; *snai1b*$^{-/-}$ CMs, N=98; *snai1b*$^{-/-}$ extruding CMs, N=49; mFI N-cadherin: *snai1b*$^{+/+}$ CMs, N=90; *snai1b*$^{+/+}$ extruding CMs, N=25; *snai1b*$^{-/-}$ CMs, N=92; *snai1b*$^{-/-}$ extruding CMs, N=70). Plot values represent means ± S.E.M.. In the violin plots, solid black lines indicate the median. p-values determined by Kruskal-Wallis test. Scale bars: 20 μm (A, B, E, F); 2 μm (A', B', E', F'). ap, apical; ba, basal; N, number of CMs. Figure adapted and reprinted with permission from Gentile et al., 2021. License: CC BY 4.0. Legend quoted *verbatim* from Gentile et al., *eLife*, 2021; DOI:10.7554/eLife.66143 for the scientific accuracy of the terms.

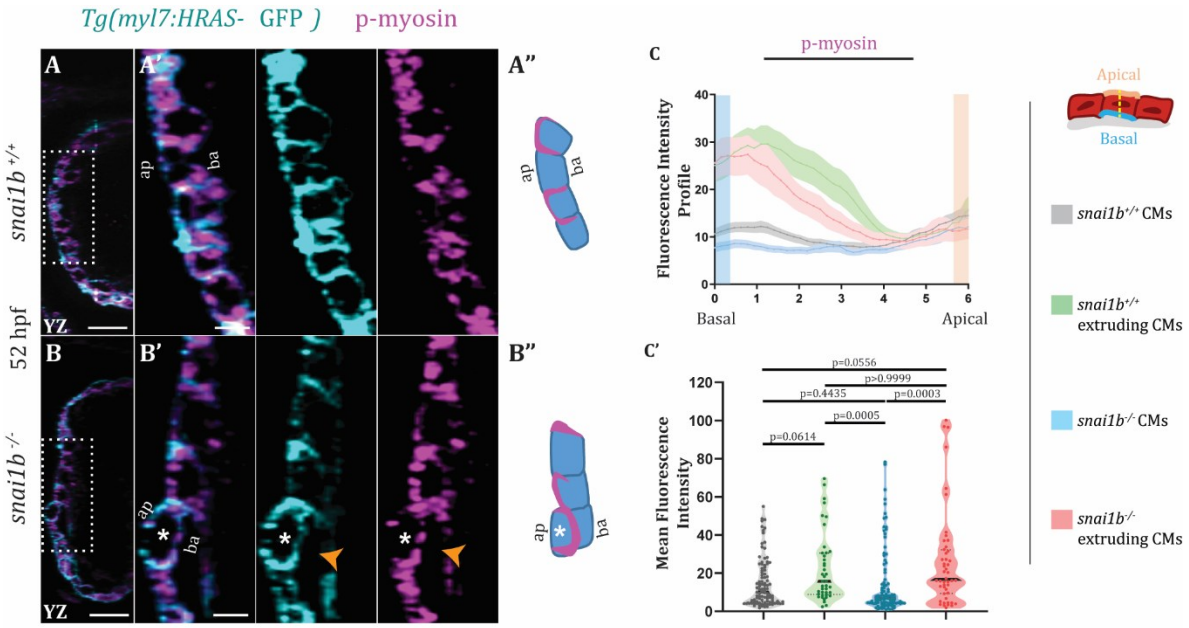

Figure 4.1.24: Extruding CMs exhibit enrichment of p-myosin in their basal domain A-B″) Orthogonal projections in the YZ plane of a 52 hpf mutant heart (B) immunostained for p-myosin and GFP compared with a wild-type sibling heart (A). Cartoons represent the basal enrichment of p-myosin (magenta) in extruding CMs in mutant embryos (A"-B"). **C-C')** FIP (C) and mFI (C') of p-myosin immunostaining in wild-type and mutant CMs, and in wild-type and mutant extruding CMs. p-myosin is enriched basally (orange arrowheads in B') in mutant extruding CMs in (white asterisks in B'). (FIP p-myosin: *snai1b*$^{+/+}$ CMs, N=204; *snai1b*$^{+/+}$ extruding CMs, N=60; *snai1b*$^{-/-}$ CMs, N=140; *snai1b*$^{-/-}$ extruding CMs, N=49; mFI p-myosin: *snai1b*$^{+/+}$ CMs, N=100; *snai1b*$^{+/+}$ extruding CMs, N=29; *snai1b*$^{-/-}$ CMs, N=153; *snai1b*$^{-/-}$ extruding CMs, N=48). Plot values represent means ± S.E.M.. In the violin plots, solid black lines indicate the median. p-values determined by Kruskal-Wallis test. Scale bars: 20 μm (A, B); 2 μm (A', B'). ap, apical; ba, basal; N, number of CMs. Figure adapted and reprinted with permission from Gentile et al., 2021. License: CC BY 4.0. Legend quoted *verbatim* from Gentile et al., *eLife*, 2021; DOI:10.7554/eLife.66143 for the scientific accuracy of the terms.

Altogether, these data suggest that the extruding CMs have increased cellular contractility and that Snai1 is required to regulate the localization of the adhesion molecule N-cadherin and to stabilize the actomyosin tension at the junctions, sustaining the tissue integrity.

(Certain lines in this subsection have been quoted *verbatim* from Gentile et al., *eLife*, 2021; DOI:10.7554/eLife.66143 for the scientific accuracy of the terms).

4.1.9 Snai1b regulates the expression level of the intermediate filament gene desmin *b*

To gain more insight into the molecular mechanisms behind the regulation of the cardiac wall integrity by the transcription factor Snai1b, I analyzed the heart transcriptome of the mutant embryos compared with the wild-type siblings. Since the earliest time point of the CM extrusions that was observed was 48 hpf, I performed the transcriptomic analysis at this time point. I manually dissected the hearts of the mutant and wild-type embryos, then extracted the RNA and performed RNA-sequencing in

collaboration with the Core Facility at MPI-HLR (Figure 4.1.25). In total, I found about 500 deregulated genes.

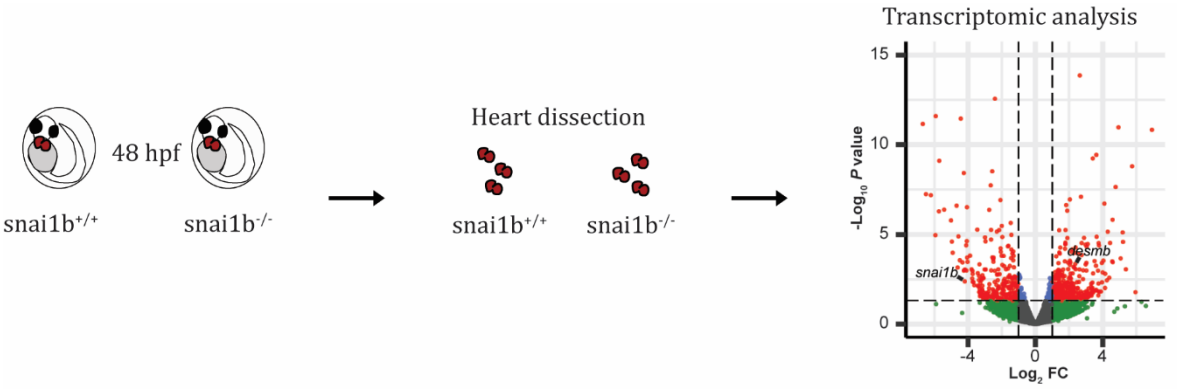

Figure 4.1.25: Schematic of the cardiac transcriptomic experiment

Cartoon represents the cardiac transcriptomic experiment. The RNA was extracted from 48 hpf dissected hearts and used for transcriptomic analysis. Figure adapted and reprinted with permission from Gentile et al., 2021. License: CC BY 4.0.

As Snai1 is known to be a repressor (Baulida et al., 2019), I mainly focused on upregulated genes in mutant hearts compared with wild-type hearts. In the 339 upregulated genes, I could find an enrichment of genes related to the cytoskeleton (gene ontology (GO) analysis) (Figure 4.1.26), and in particular upregulation of the intermediate filament (IF) genes (Figure 4.1.26). IFs are cytoskeletal networks that are important to maintain the mechanical properties of the cell (van Bodegraven and Etienne-Manneville, 2020). It is known that mutations in IF-associated proteins are associated with cardiomyopathies, however little is known about how they are regulated at the transcriptional level (Rainer et al., 2018). Among the several IFs been upregulated in the mutant heart transcriptome, the muscle-specific gene *desmin b* (*desmb*) was upregulated.

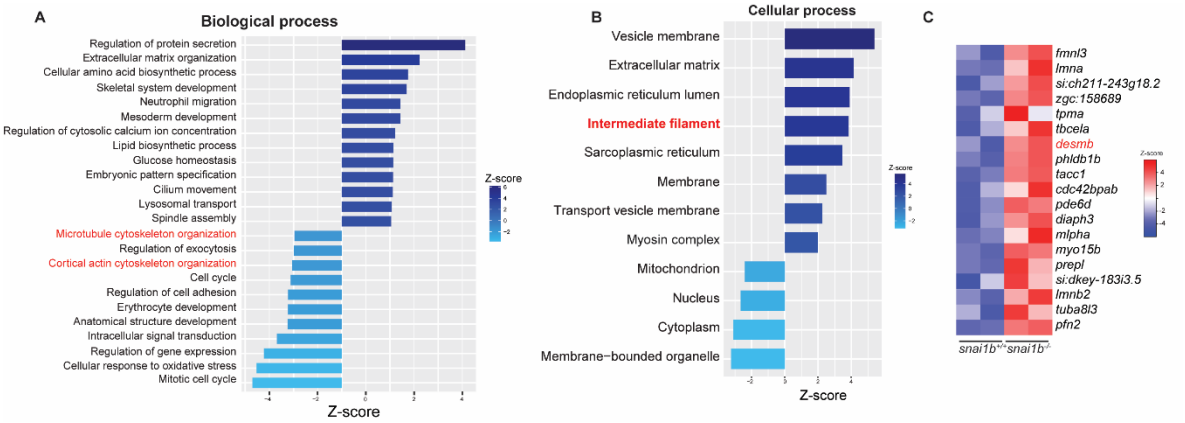

Figure 4.1.26: Intermediate filament genes are upregulated in *snai1b*$^{-/-}$ hearts

A) GO analysis of biological processes shows enrichment of cytoskeletal related genes (in red) in mutant hearts compared with wild-type hearts. **B)** GO analysis of cellular processes shows enrichment of intermediate filament components in mutant hearts. **C)** Heatmap of a list of upregulated cytoskeletal genes, including *desmb*. Figure adapted and reprinted with permission from Gentile et al., 2021. License: CC BY 4.0.

First, I looked at the expression pattern of *desmb* in wild-type embryos by WISH at 48 hpf (Figure 4.1.27); *desmb* is expressed in the trunk muscles and heart. Then, I performed the WISH in *snai1b* mutant embryos (Figure 4.1.27), observing a strong signal in the heart region. I also performed a qPCR analysis to quantitatively assess the expression level of *desmb* in dissected hearts and I observed an upregulation of *desmb* in *snai1b* mutant hearts compared with wild-type hearts at 48 hpf (Figure 4.1.27).

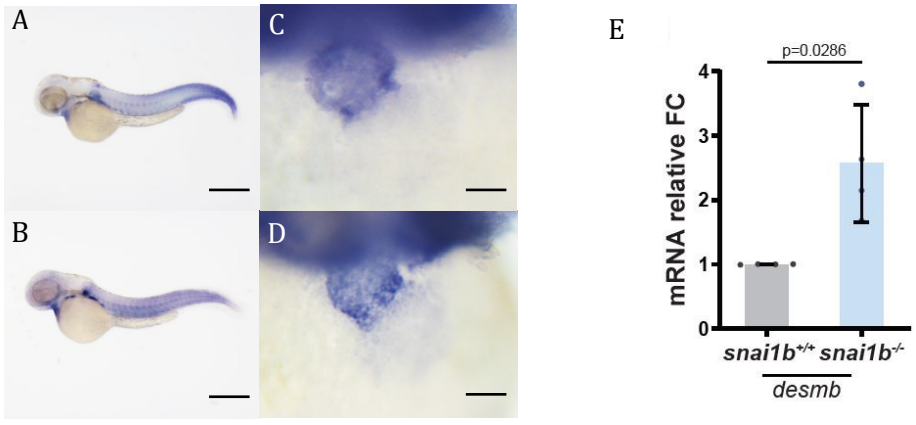

Figure 4.1.27: *desmb* mRNA levels are upregulated in *snai1b* mutants

A-B) Whole-mount ISH of *desmb* at 50 hpf, showing mRNA expression in the trunk, in the fin bud, and the heart, in *snai1b* wild-type (A) and mutants (B) embryos. C-D) *desmb* expression in the heart of *snai1b* wild-type (C) and mutants (D) embryos. A stronger signal is observed in *snai1b* mutants. **E)** *desmb* expression levels are significantly increased in mutant hearts at 48 hpf; n=4 biological replicates, 30 hearts each. Plot values represent means ± S.D.; p-values determined by Student's t-test; Scale bars: 50 µm. FC, fold change. Figure adapted and reprinted with permission from Gentile et al., 2021. License: CC BY 4.0.

To assess whether upregulation at the gene level is seen at the protein level, I performed immunostaining for Desmin at 52 hpf (Figure 4.1.28). In wild-type CMs, Desmin is mostly localized at the junctions level (Figure 4.1.28), where the desmosomes are predicted to localize. Interestingly, Desmin was present not only at elevated levels but also in ectopic locations in *snai1b* CMs; in particular, Desmin was found at the basal domain, similar to the actomyosin tension markers, suggesting his involvement in the cellular contractility and basal extrusion.

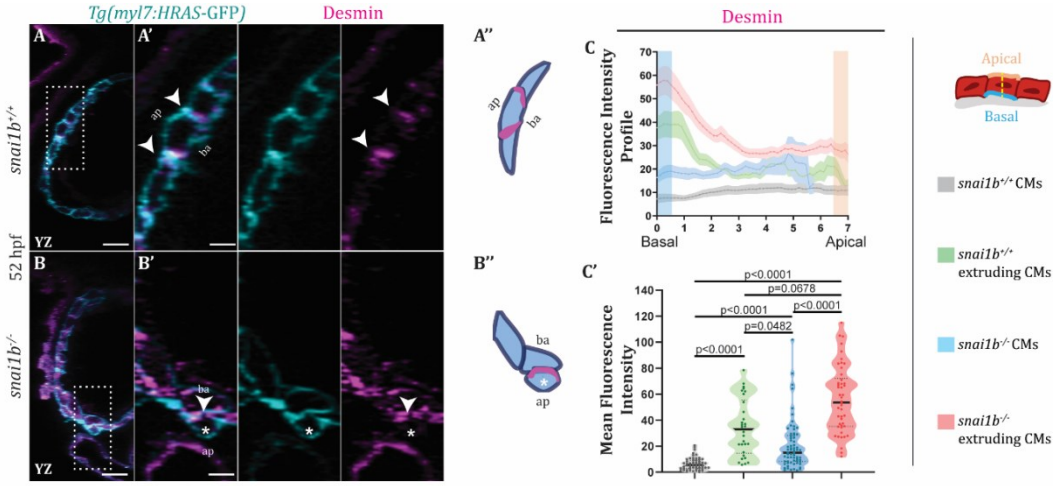

Figure 4.1.28: Desmin is enriched in the basal domain of the extruding CMs

A-B") Orthogonal projections in the YZ plane of a 52 hpf mutant heart (B) immunostained for Desmin and membrane GFP compared with a wild-type heart (A). Close-up of boxed areas of wild-type (A') and mutant (B') CMs. Schematics (Desmin in magenta) illustrate the basal enrichment of Desmin in extruding CMs in mutant embryos (A"-B"). **I-I')** FIP (I) and mFI (C') of Desmin in wild-type and mutant CMs, and in wild-type and mutant extruding CMs. Desmin immunostaining is observed throughout the mutant myocardium, with an enrichment in the basal domain (white arrowheads in A'-B') in extruding CMs (white asterisks in B'). (FIP:

snai1b$^{+/+}$ CMs, N=49; *snai1b*$^{+/+}$ extruding CMs, N=41; *snai1b*$^{-/-}$ CMs, N=45; *snai1b*$^{-/-}$ extruding CMs, N=41; mFI: *snai1b*$^{+/+}$ CMs, N=56; *snai1b*$^{+/+}$ extruding CMs, N=30; *snai1b*$^{-/-}$ CMs, N=65; *snai1b*$^{-/-}$ extruding CMs, N=46). Plot values represent means ± S.E.M. (C). In the violin plot (C'), solid black lines indicate the median. p-values determined by Kruskal-Wallis test (C'). Scale bars: 20 µm (A, B); 2 µm (A', B'). ap, apical; ba, basal; n, number of embryos; N, number of CMs. Figure adapted and reprinted with permission from Gentile et al., 2021. License: CC BY 4.0. Legend quoted *verbatim* from Gentile et al., *eLife*, 2021; DOI:10.7554/eLife.66143 for the scientific accuracy of the terms.

Altogether, these results suggest that Snai1 not only regulates *desmin* at the transcriptional level but is also involved in regulating the localization of the Desmin protein.

I further performed *snai1b* overexpression experiments to assess its effects on *desmb* expression. First, I injected the *snai1b* mRNA into one-cell stage wild-type embryos, with the *gfp* mRNA as a control. Analysis of *snai1b* and *desmb* transcript levels at 4.5 hpf (pre-gastrulation embryos) indicates that whereas *snai1b* expression is upregulated, *desmb* mRNA levels were reduced by >40% (Figure 4.1.29).

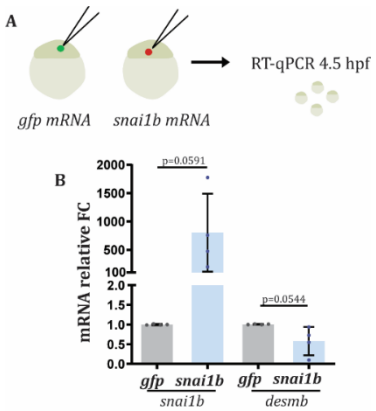

Figure 4.1.29: *snai1b* mRNA overexpression leads to downregulation of *desmb*

A-B) Cartoon of *gfp* and *snai1b* mRNA injections into one-cell stage embryos. *snai1b* and *desmb* mRNA levels were analyzed in injected embryos at 4.5 hpf. *snai1b* expression levels are significantly increased, whereas *desmb* expression levels are decreased at 4.5 hpf. n=4 biological replicates, 30 embryos each.

Plot values represent means ± S.D.; p-values determined by Student's t-test. FC, fold change. Figure adapted and reprinted with permission from Gentile et al., 2021. License: CC BY 4.0.

I then used the construct overexpressing *snai1b* in a myocardial-specific fashion and injected it into one-cell stage wild-type embryos to obtain a mosaic overexpression of *snai1b* in CMs, with *myl7:gfp* construct as the control. Once the embryos reached 48 hpf, I extracted RNA from dissected hearts to perform a qPCR analysis. Similar to the

previous result, *desmb* mRNA levels were significantly reduced when compared with the *myl7:gfp* controls, whereas *snai1b* mRNA was upregulated (Figure 4.1.30).

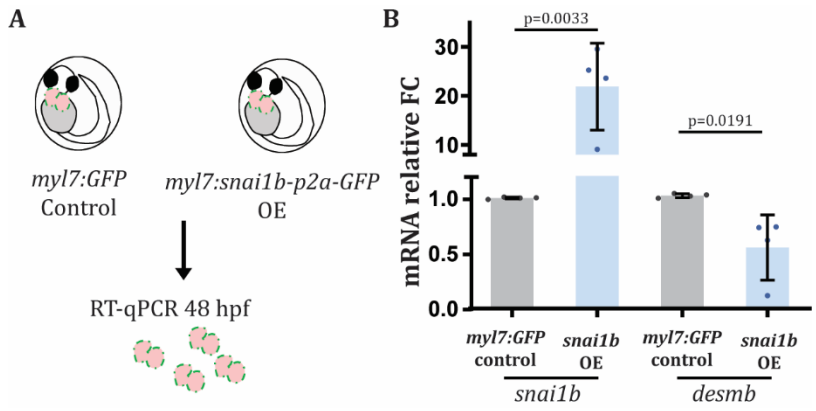

Figure 4.1.30: *snai1b* overexpression in CMs leads to downregulation of *desmb*
A) Cartoon of *snai1b* overexpression under a *myl7* promoter; *snai1b* and *desmb* mRNA levels analyzed at 48 hpf. **B)** *desmb* expression levels are significantly reduced in *snai1b* CM-specific overexpressing hearts at 48 hpf; n=4 biological replicates, 30 hearts each. Plot values represent means ± S.D. p-values determined by Student's t-test. FC, fold change. Figure adapted and reprinted with permission from Gentile et al., 2021. License: CC BY 4.0.

It has been shown that in mouse skeletal myoblasts Snai1 can bind to the proximal promoter of *Desmin* by ChIP-seq experiments (Soleimani et al., 2012). In addition, it has recently been shown that potential Snai1 binding sites are found in the promoter of *desmb* (Kayman Kürekçi et al., 2021). To test whether zebrafish Snai1b can repress the promoter activity of *desmb*, I performed a luciferase assay in HEK293T cells. I cloned 800 bp of the proximal promoter of *desmb* upstream of the Firefly *luciferase* gene, which contained putative Snai1 binding sites, as well as the open reading frame of *snai1b* under the constitutively active promoter CMV. The *luciferase* plasmid also contains *Renilla* luciferase which allows for normalization of the signal intensity. I then transfected the HEK293T cells for 6 hours with both plasmids together, and the two plasmids alone. 24 hours post-transfection, I lysed the cells and analyzed the luciferase signal intensity (Figure 4.1.31). Striking, the *desmb* promoter region alone was able to induce transcriptional activation of the Luciferase signal compared with the control. However, I observed that when Snai1b was co-expressed there was a significant

reduction of the Luciferase signal, suggesting that Snai1b can repress the promoter activity of *desmb*.

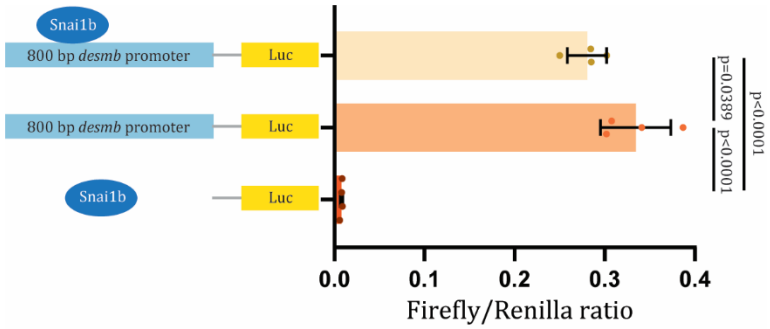

Figure 4.1.31: Snai1b binds to the proximal promoter of *desmb*

In vitro luciferase assay in HEK293T cells after co-transfection of pGL4.14-luciferase and pGL4.14-800 bp *desmb*-luciferase with pTol2-CMV-*snai1b* or alone. Reduced luciferase activity was detected when pTol2-CMW-*snai1b* was co-transfected with pGL4.14-800 bp *desmb*-luciferase. Plot values represent means ± S.D.; p-values determined by one-way ANOVA followed by multiple comparisons with Dunn test. Figure adapted and reprinted with permission from Gentile et al., 2021. License: CC BY 4.0. Legend quoted *verbatim* from Gentile et al., *eLife*, 2021; DOI:10.7554/eLife.66143 for the scientific accuracy of the terms.

Altogether, these data suggest that Snai1 regulates *desmb* transcription.

(Certain lines in this subsection have been quoted *verbatim* from Gentile et al., *eLife*, 2021; DOI:10.7554/eLife.66143 for the scientific accuracy of the terms).

4.1.10 Overexpression of *desmin b* promotes CM extrusion

It has been shown that both loss (Ramspacher et al., 2015; Taylor Matthew R.G. et al., 2007) and gain (Chen et al., 2018) of function of Desmin expression have been associated with cardiac defects. Thus, I hypothesized that the CM extrusions observed in *snai1b* mutants are due to the imbalance of the *desmb* expression. To test this hypothesis, I overexpressed *desmb* mosaically in CMs. First, I cloned the cDNA of *desmb* under a *myl7* promoter and upstream of the P2A sequence and the GFP. Then, I injected the construct in one-cell stage wild-type embryos using as control a *myl7:gfp* construct and observed them at 50 hpf (Figure 4.1.32). I observed that *desmb* overexpressing CMs were more prone to extrude compared with the *gfp* overexpressing CMs,

suggesting that IFs are needed at their endogenous levels to maintain the cardiac wall integrity.

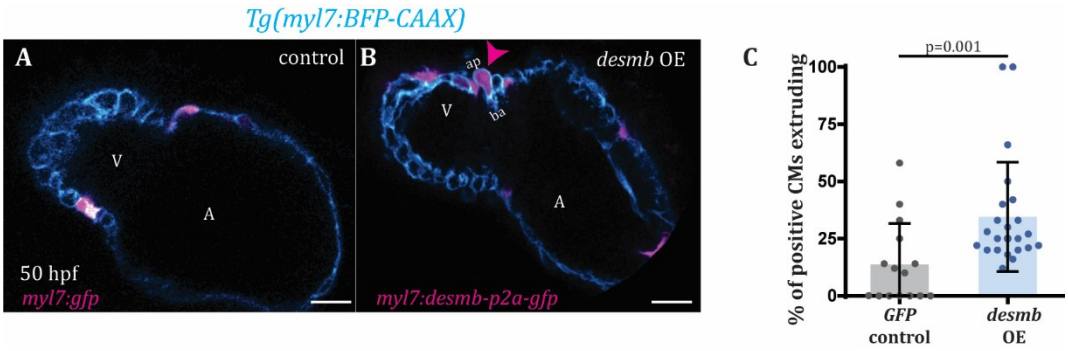

Figure 4.1.32: The overexpression of *desmb* in cardiomyocytes induces their extrusion
A-B) Confocal images of wild-type embryos injected with *myl7:GFP* (A) or with *myl7:desmb-p2a-GFP* (B) at 50 hpf. **C)** An increased number of CM extrusion is observed when *desmb* (n=23) is overexpressed compared with control (n=15) (magenta arrowheads in B, B'). Plot values represent means ± S.D.. p-values determined by Mann-Whitney *U* test. Scale bars: 20 µm. V, ventricle; A, atrium; ap, apical; ba, basal. Figure adapted and reprinted with permission from Gentile et al., 2021. License: CC BY 4.0.

I hypothesized that increased levels of Desmin induce CM extrusion by (1) disrupting desmosome organization leading to compromised cell-cell adhesion and/or (2) increasing cellular contractility at the basal domain. To test the first hypothesis, I examined the ultrastructure of CM desmosomes using transmission electron microscopy (TEM). In line with a previous study that shows that extruding epithelial cells exhibit intact desmosomes (Thomas et al., 2020), we did not observe any obvious defects in *snai1b* mutant CMs compared with wild-type CMs at 60 hpf (Figure 4.1.33). Moreover, the ultrastructure of the mutant fascia adherens compared with the wild-type fascia adherens was not different at the same time point (Figure 4.1.33).

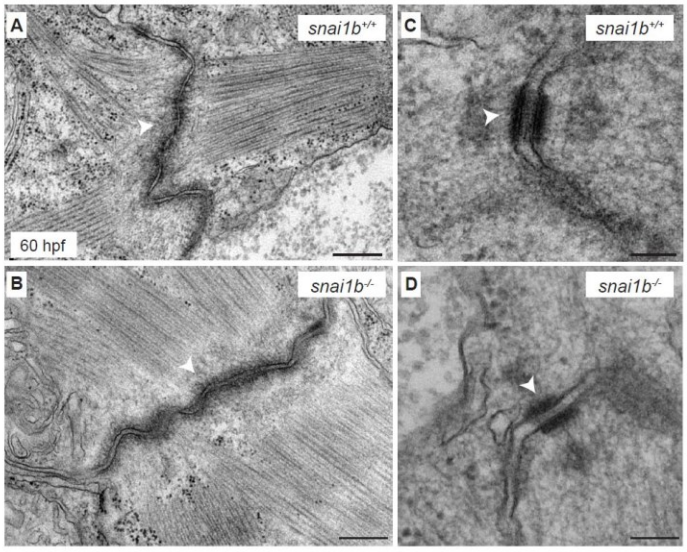

Figure 4.1.33: The organization of desmosome is maintained in *snai1b* mutants

A-D) Transmission electron microscopy (TEM) images showing the ultrastructure of fascia adherens (white arrowheads in A, B) and desmosomes (white arrowheads in C, D) in 60 hpf *snai1b*$^{+/+}$ and *snai1b*$^{-/-}$ CMs. Scale bars: 200 nm (A, B); 500 nm (C, D). Figure adapted and reprinted with permission from Gentile et al., 2021. License: CC BY 4.0.

To test whether overexpression of Desmin in CMs was associated with increased cell contractility, I performed immunostaining on *desmb* overexpressing hearts using the tension markers, the α-catenin epitope of α-18 and p-myosin, and Desmin antibodies. Similar to the experiment described above, using mosaic hearts allowed me to compare *desmb* non-overexpressing CMs with *demsb* overexpressing CMs. As expected, Desmin immunostaining exhibited a strong signal in the *desmb* overexpressing CMs, where Desmin was also localized at the basal domain of the overexpressing CMs (Figure 4.1.34). Interestingly, I observed that the tension markers, the α-catenin epitope of α-18 and p-myosin, were enriched in the basal domain of the *desmb* overexpressing CMs when compared with the neighbor CMs (Figure 4.1.35). Finally, I also checked if the overexpressing CMs lose their adhesion by using N-cadherin antibody. Indeed, *desmb* overexpressing CMs exhibit a reduction of N-cadherin in their junctions (Figure 4.1.36).

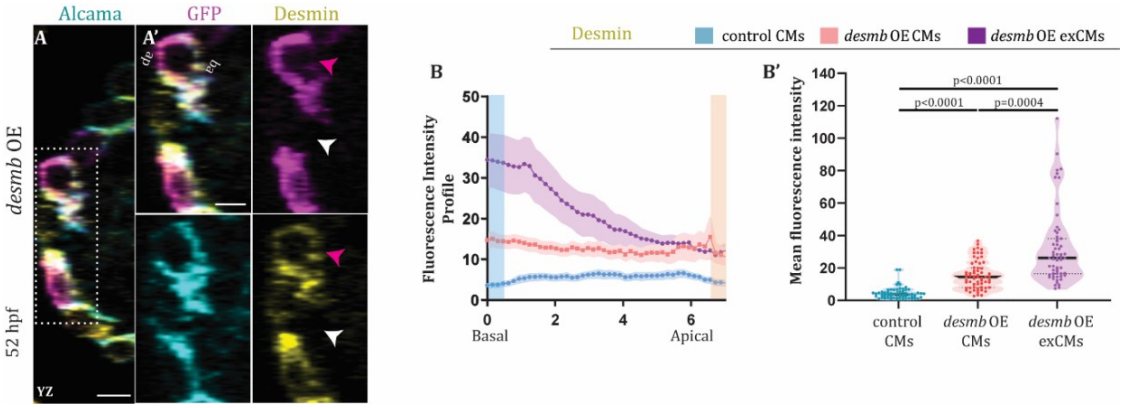

Figure 4.1.34: *desmb* overexpressing CMs display enrichment of Desmin basally

A-A') Orthogonal projections in the YZ plane of hearts from 52 hpf embryos injected with *myl7:desmb-p2a-GFP* and immunostained for Desmin, GFP, and Alcama (A-A'). Close-up of boxed areas of *desmb*-overexpressing and adjacent wild-type CMs (A'). **B-B')** FIP (B) and mFI (B') of Desmin in CMs that overexpress *desmb* (magenta arrowheads) and CMs that do not overexpress *desmb* (white arrowheads). Desmin immunostaining signals are enriched in the basal domain in *desmb* overexpressing CMs. FIP: *desmb* OE CMs, N=88; *desmb* OE extruding CMs, N=49; control CMs, N=86. mFI: *desmb* OE CMs, N=63; *desmb* OE extruding CMs, N=59; control CMs, N=64. Plot values represent means ± S.E.M.. In the violin plot, solid black lines indicate the median. p-values determined by Kruskal-Wallis test. Scale bars: 20 µm (A); 2 µm (A'). V, ventricle; A, atrium; ap, apical; ba, basal; n, number of embryos; N, number of CMs. Figure adapted and reprinted with permission from Gentile et al., 2021. License: CC BY 4.0. Legend quoted *verbatim* from Gentile et al., *eLife*, 2021; DOI:10.7554/eLife.66143 for the scientific accuracy of the terms.

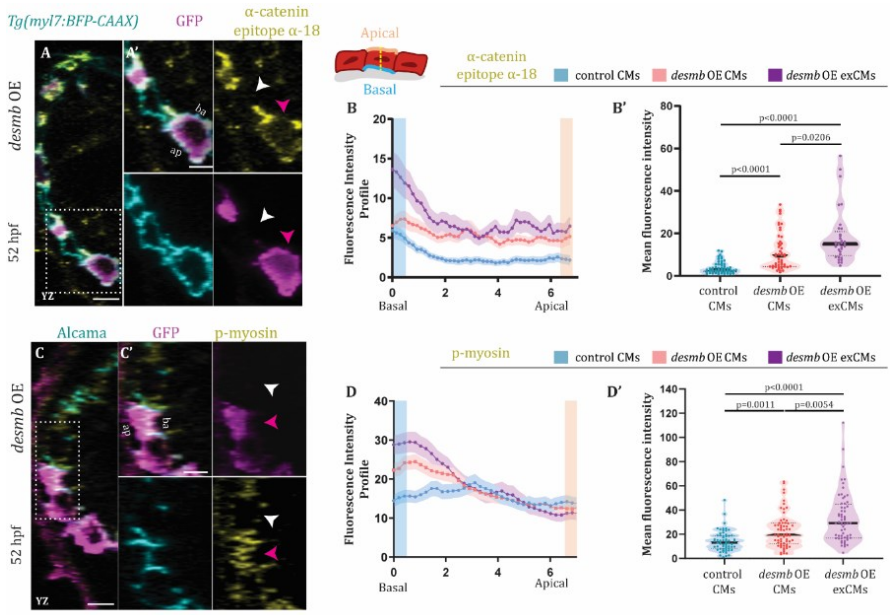

Figure 4.1.35: *desmb* overexpressing CMs display cellular contractility basally

A-A', C-C') Orthogonal projections in the YZ plane of hearts from 52 hpf embryos injected with *myl7:desmb-p2a-GFP* and immunostained for α-catenin epitope α-18, GFP, and BFP (A-A'), p-myosin, GFP, and Alcama (C-C'). Close-up of boxed areas of *desmb*-overexpressing and adjacent wild-type CMs (A', C'). **B-B', D-D')** FIP (B, D) and mFI (B', D') of α-catenin epitope α-18 (E-E'), p-myosin (G-G') in CMs that overexpress *desmb* (magenta arrowheads) and CMs that do not overexpress *desmb* (white arrowheads). α-catenin epitope α-18 and p-myosin immunostaining signals are enriched in the basal domain in *desmb* overexpressing CMs. FIP: *desmb* OE CMs, **B)** N=132, **D)** N=120; *desmb* OE extruding CMs, **B)** N=47, **D)** N=54; control CMs, **B)** N=153, **D)** N=133. mFI: *desmb* OE CMs, **B')** N=49, **D')** N=65; *desmb* OE extruding CMs, **B')** N=33, **D')** N=60; control CMs, **B')** N=55, **D')** N=62. Plot values represent means ± S.E.M. (B, D). In the violin plots (B', D'), solid black lines indicate the median. p-values determined by Kruskal-Wallis (B', D') test. Scale bars: 20 μm (A, C); 2 μm (A', C'). V, ventricle; A, atrium; ap, apical; ba, basal; n, number of embryos; N, number of CMs. Figure adapted and reprinted with permission from Gentile et al., 2021. License: CC BY 4.0. Legend quoted *verbatim* from Gentile et al., *eLife*, 2021; DOI:10.7554/eLife.66143 for the scientific accuracy of the terms.

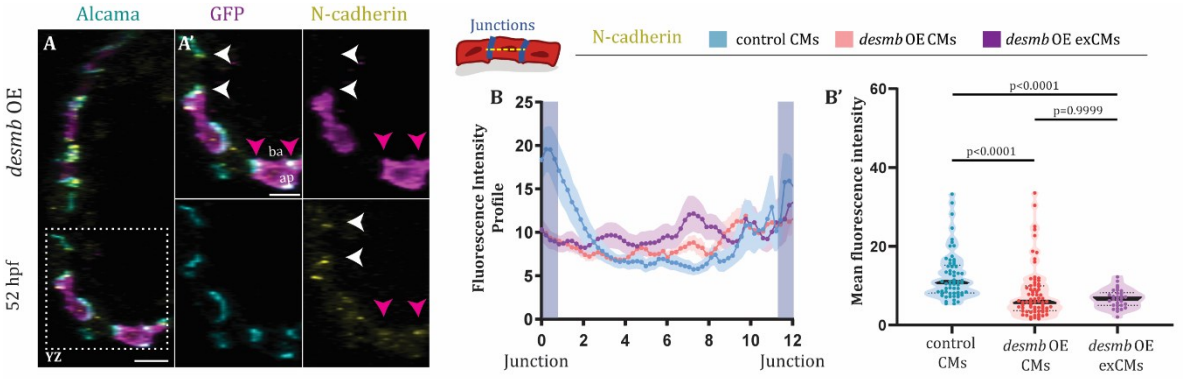

Figure 4.1.36: *desmb* overexpression in CMs leads to reduced N-cadherin at the junctions
A-A') Orthogonal projection in the YZ plane of the heart of an embryo injected with *myl7:desmb-p2a-GFP* and immunostained for N-cadherin, GFP, and Alcama at 52 hpf. Close-up of boxed area of *desmb*-overexpressing and adjacent control CMs (A'). **B-B')** FIP (B) and mFI (B') of N-cadherin in CMs that overexpress *desmb* (magenta arrowheads) and CMs that do not overexpress *desmb* (white arrowheads) CMs. N-cadherin immunostaining is reduced in the junctional domains in *desmb* overexpressing CMs. (FIP: *desmb* OE CMs, N=118; *desmb* OE extruding CMs, N=44; control CMs, N=95; mFI: *desmb* OE CMs, N=57; *desmb* OE extruding CMs, N=30; control CMs, N=61). Plot values represent means ± S.E.M.. In the violin plot, solid black lines indicate the median. p-values determined by Kruskal-Wallis test. Scale bars: 20 µm (A); 2 µm (A'). ap, apical; ba, basal; N, number of CMs. Figure adapted and reprinted with permission from Gentile et al., 2021. License: CC BY 4.0. Legend quoted *verbatim* from Gentile et al., *eLife*, 2021; DOI:10.7554/eLife.66143 for the scientific accuracy of the terms.

Altogether, these data suggest that increasing *desmb* expression in CMs compromises their adhesion and increases their basal actomyosin contractility, photocopying *snai1b* mutants.

4.1.11 Proposed model

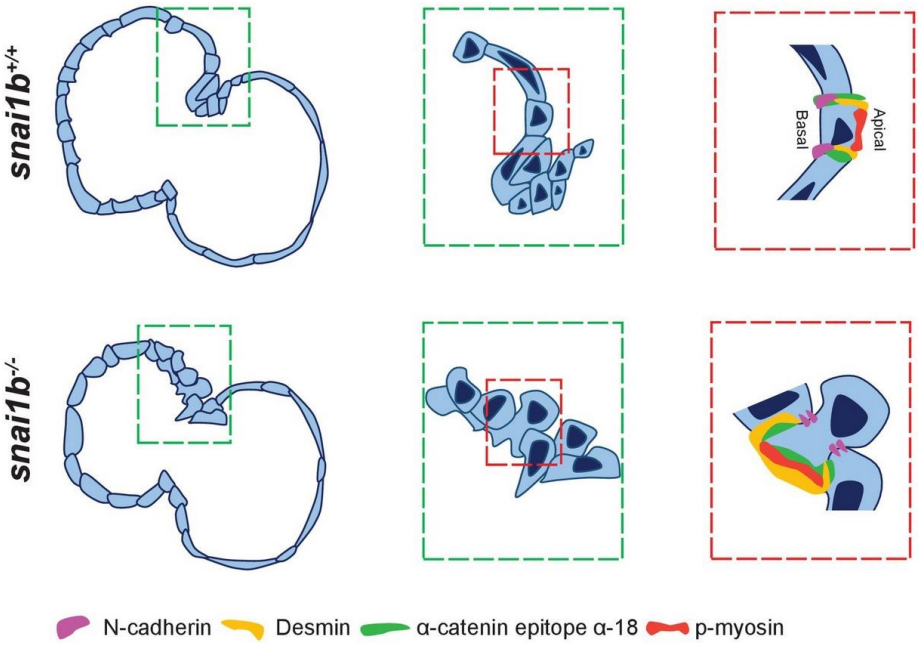

Figure 4.1.37: Proposed model (see text)

Figure adapted and reprinted with permission from Gentile et al., 2021. License: CC BY 4.0.

In this study, my data showed how the EMT transcription factor Snai1b maintains cardiac wall integrity (Figure 4.1.37).

In particular, I showed that when there is a loss-of-function of Snai1b, there is an impairment of cardiac wall integrity, as some of the CMs extrude away from the lumen. The extruding CMs show increased cellular contractility, as I observed enrichment of the actomyosin machinery in their basal domain and reduced adhesion molecules at the junctions. Transcriptomic analysis revealed that Snai1 is regulating the transcription levels of the intermediate filament gene *desmb*. In addition, CM-specific overexpression of *desmb* leads to increased cellular contractility and extrusion of the overexpressing CMs, phenocopying *snai1b* mutants. In conclusion, I proposed that Snai1b maintains the cardiac wall integrity, by regulating the expression of the intermediate filament gene, *desmb*.

4.2 The EMT transcription factor Twist1b is regulated by Nfatc1 during valve interstitial cells establishment

Part of this chapter has been published as an article in *Circulation Research* (Gunawan*, Gentile* et al., *Circ Res* 2020; DOI: 10.1161/CIRCRESAHA.119.315992). My contribution to the article is described as follows: conceptualization, formal analysis, validation, investigation, visualization, methodology, and writing (original draft, reviewing, and editing).

4.2.1 The establishment of the valve interstitial cell (VIC) population

The vertebrate cardiac valve is composed of valve endocardial cells (VECs) and valve interstitial cells (VICs) (Tao et al., 2012; Dutta and Lincoln, 2018). Although the zebrafish heart has been frequently used to study valve formation, no prior study has elucidated the mechanisms of VIC formation in this model system; addressing this missing information is important to ensure that zebrafish is an appropriate model to understand valve development in other vertebrates. To better understand how the single-layered endocardial tissue develops in a multi-layered valve structure, I performed high-resolution microscopy to visualize valvulogenesis at the single-cell level. Using the zebrafish transgenic lines *Tg(nfatc1:Gal4);(UAS:GFP)*, which labels VECs, and *Tg(kdrl:nls-mCherry)*, that labels all the endothelial cells.

As shown by our group, zebrafish valve development starts between 50 and 54 hpf in the superior leaflet and later on in the inferior leaflet, with collective VEC migration into the extracellular matrix (ECM) in the ventricle-to-atrium direction (Pestel et al., 2016; Steed et al., 2016a; Gunawan et al., 2019). The leading VEC extends protrusions into the ECM to form an S-shaped structure, in a process mediated by focal adhesions (Gunawan et al., 2019). To better understand how the VICs form in the valve, I focused my attention on the post-VEC migration stages. I observed that at around 72 hpf, the cells that had collectively migrated further invaded space between two endocardial cell layers at the AVC, which further formed the true valve leaflets. These cells display downregulation of endothelial markers, suggesting that they are losing their endothelial identity (Figure 4.2.1); I conclude that they form the first VICs. Following

this stage, the valve leaflets elongate into the lumen, and both the VECs and the VICs proliferate. The VICs exhibited more distinct extracellular gaps between each other, suggesting that they lost their intercellular adhesion and more ECM was deposited between them. I refer to this stage as the elongation stage, in which the valve is already functional and able to prevent retrograde blood flow.

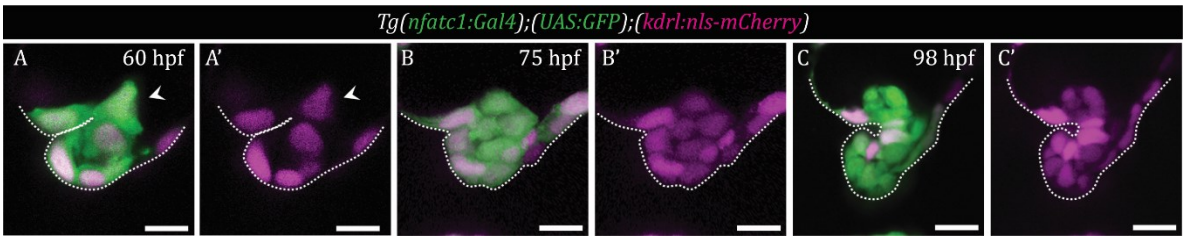

Figure 4.2.1: Early stages of valve development

A-C') Confocal images of the superior atrioventricular (AV) valve leaflet. Valve cells are marked by *Tg(nfatc1:Gal4); Tg(UAS:*GFP) expression and endocardial cells (ECs) marked by *Tg(kdrl:*nls-mCherry) expression. **A, A')** VECs collectively migrate from the ventricle towards the atrium at 60 hpf; arrowhead points to the leading cell. **B, B')** The collective EC migration is complete and VECs downregulate their endocardial identity at 75 hpf. **C, C')** Elongation of the valve leaflet is observed at 98 hpf. White dashed lines outline the valve leaflet. Scale bars: 10 μm. Figure adapted and reprinted with permission from Gunawan*, Gentile* et al., 2020. License: 5243661348761.

Interestingly, I observed that from 120 hpf to 20 days post fertilization (dpf), no major morphological changes appeared to occur. After 20 dpf, the number of VICs and the valve ECM significantly increased. At 30 dpf, I observed a valve structure resembling the adult valve, suggesting the mature valve is established within 30 days (Figure 4.2.2).

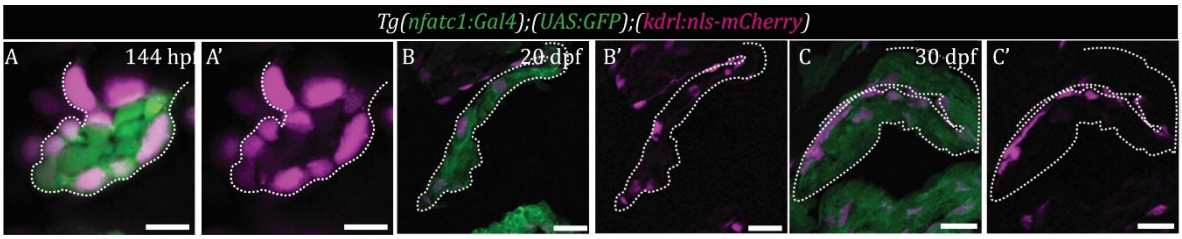

Figure 4.2.2: Later stages of valve development

A, A') VICs are established, they no longer express the EC transgenic marker, and they are surrounded by VECs at 144 hpf. **B, B')** Expansion of the VIC layer and further elongation of the valve leaflet is observed at 20 dpf. **C, C')** Establishment of the mature valve with a multilayered

VIC population and an expanded extracellular space is observed at 30 dpf. White dashed lines outline the valve leaflet. Scale bars: (A-A') 10 µm; (B-C') 20 µm. Figure adapted and reprinted with permission from Gunawan*, Gentile* et al., 2020. License: 5243661348761

In summary, the VICs establishment occurs in four main stages: 1) VEC collective migration, 2) VIC invasion, 3) valve leaflet elongation, and 4) maturation (Figure 4.2.3).

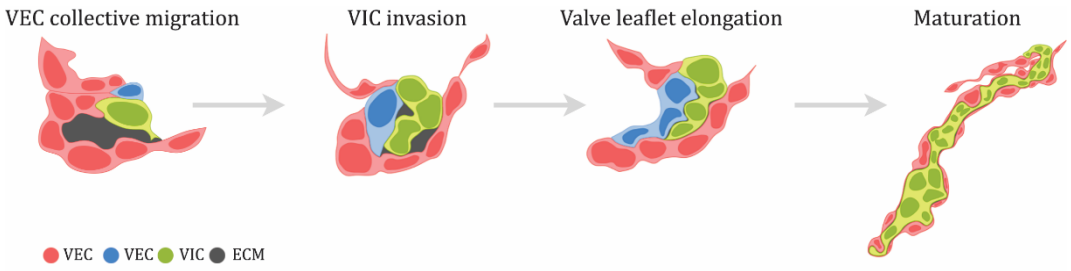

Figure 4.2.3: Schematic of zebrafish valve development

Figure adapted and reprinted with permission from Gunawan*, Gentile* et al., 2020. License: 5243661348761

To better characterize the VIC population and to determine when they become a distinct population, we searched for and successfully identified a new transgenic line that was driven by enhancer elements of the mouse *Hhex* gene, a known transcription factor in endothelial cells (Gauvrit et al., 2018). I examined the expression of *Tg(Hhex:GFP)* together with the endothelial transgenic line *Tg(fli1a:Gal4);(UAS:RFP)* (Figure 4.2.4). Although the GFP signal was expressed in the whole endocardium in the early stages, by the collective VEC migration stage, GFP appeared stronger in the leading VEC. The GFP signal then became more restricted to the VIC population, with lower expression in the ventricular VECs. By 20 dpf the GFP expression is no longer detectable in the valve, suggesting that *Tg(Hhex:GFP)* labels early developing VICs but not mature VICs. On the other hand, we were able to see the expression of the mesenchymal marker Vimentin, starting from 20 dpf (Figure 4.2.5), indicating that Vimentin is a good marker for mature VICs.

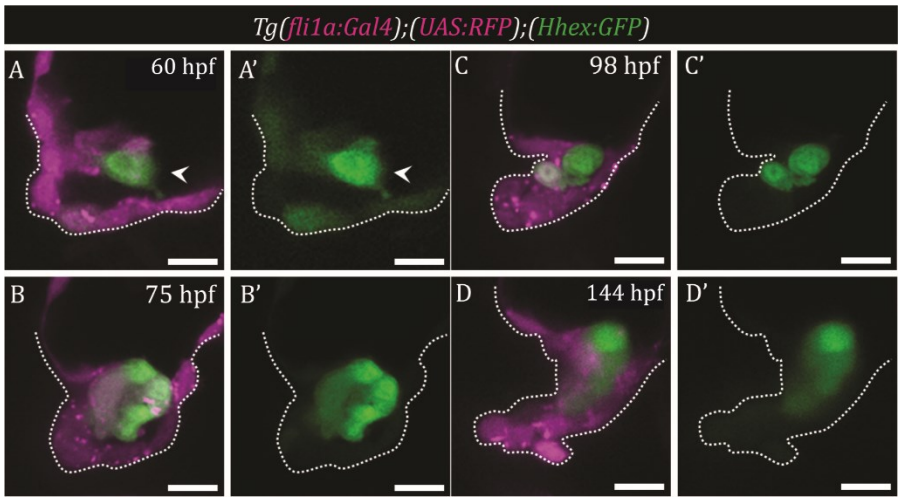

Figure 4.2.4: Establishment of VICs

A-D') VICs are marked by *Tg(Hhex:*GFP*)* expression and endocardial cells are marked by *Tg(fli1a:Gal4); Tg(UAS:*RFP) expression. Some ventricular VECs exhibit low *Tg(Hhex:*GFP*)* expression. **A, A')** *Tg(Hhex:*GFP*)* expression is highest in the leading EC (arrowhead) at the collective migration stage. **B-D')** VICs exhibit strong *Tg(Hhex:*GFP*)* expression at 75, 98, and 144 hpf. Scale bars: (A-D') 10 µm. Figure adapted and reprinted with permission from Gunawan*, Gentile* et al., 2020. License: 5243661348761**.**

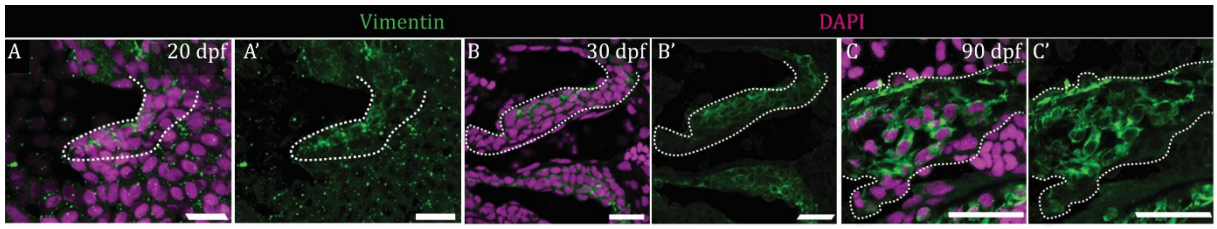

Figure 4.2.5: The mesenchymal marker Vimentin is expressed in the later stages of valve development

A-C') 20, 30, and 90 dpf, VICs marked by strong Vimentin expression. Scale bars: 20 µm. Figure adapted and reprinted with permission from Gunawan*, Gentile* et al., 2020. License: 5243661348761**.**

Taken together, these data suggest that the establishment of VICs starts as early as the migration stage and by 30 days there is a mature structure.

4.2.2 EndoMT occurs during zebrafish VIC formation

As I noticed a downregulation of the endothelial marker *kdrl* and the expression of the mesenchymal marker Vimentin, I asked whether the zebrafish VIC formation is driven by endothelial-to-mesenchymal transition (EndoMT). To determine if the VICs lose their adhesions, I examined the adhesion molecule VE-cadherin using the tension sensor line *Tg(ve-cad:ve-cad)* (Lagendijk et al., 2017) and the tight junction ZO-1 using an anti-ZO-1 antibody (Figure 4.2.6). During the early stages of valve formation, VE-cadherin was localized to intercellular junctions between migrating VECs. Strikingly, starting from 72 hpf VE-cadherin was still present in VECs but became downregulated in the VIC precursors. This loss of intercellular adhesion becomes more evident by 96 hpf.

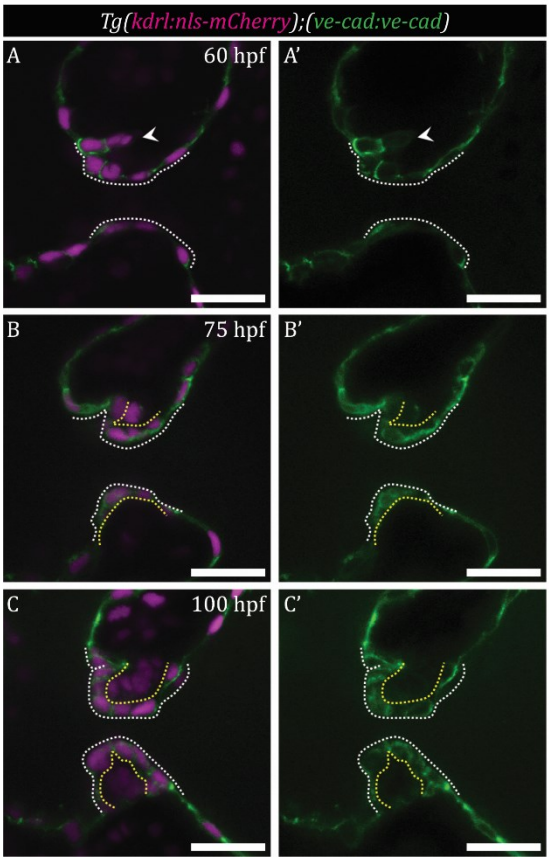

Figure 4.2.6: VICs lose their junctional VE-cadherin localization

A-C') Junctional VE-cadherin localization is assessed by *Tg(ve-cad:*VE-cad^{ts}*)* expression. Junctional VE-cadherin is observed between the migrating cells at 60 hpf (A) and becomes downregulated in the VIC precursors after the migration is complete at 75 (B, B') and 100 (C, C') hpf. White dashed lines outline the valve leaflet; yellow dashed lines outline the interstitial space. Arrowheads (A, A') point to the leading migrating cell. Scale bars, 20 µm. Figure adapted and reprinted with permission from Gunawan*, Gentile* et al., 2020. License: 5243661348761.

To examine the localization of ZO-1, I performed immunostaining in combination with *Tg(Hhex:GFP)* (Figure 4.2.7). Similar to VE-cadherin, ZO-1 was localized to intercellular junctions in the migrating VECs and become downregulated during the VIC invasion

stage. ZO-1 became completely absent in the VIC population during later stages of valve development (75 hpf onwards). These data suggest that VICs undergo EndoMT to become fully mesenchymal cells with no detectable intercellular adhesion.

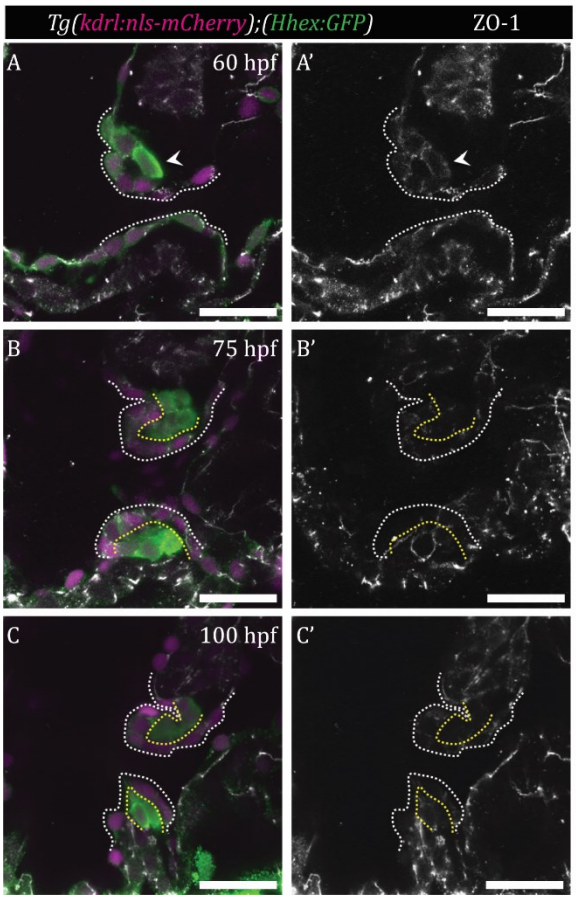

Figure 4.2.7: VICs lose their junctional ZO-1 localization

D-F') ZO-1 localization is assessed through I immunostaining, and VIC precursors are marked by *Tg(Hhex:*GFP) expression. Junctional ZO-1 is observed between the migrating cells at 60 hpf (A) and becomes downregulated in the VIC precursors after the migration is complete at 75 (B, B') and 100 (C, C') hpf. White dashed lines outline the valve leaflet; yellow dashed lines outline the interstitial space. Arrowheads (A, A') point to the leading migrating cell. Scale bars, 20 μm. Figure adapted and reprinted with permission from Gunawan*, Gentile* et al., 2020. License: 5243661348761.

4.2.3 VICs undergo two peaks of proliferation

To verify whether proliferation is involved in VIC establishment, I performed a cell proliferation assay using 5-Ethynyl-2'-deoxyuridine (EdU), a nucleotide analog incorporated in the DNA while cells are entering the S phase of the cell cycle. Starting from 48 hpf, I quantified the number of EdU-positive VECs and VICs, after 24-hour EdU incorporation periods (Figure 4.2.8). The first proliferation peak was between 72 and 96 hpf, during the VIC invasion stage, with around 30% of the VICs being EdU positive. Following this peak and until 15 dpf, the number of VICs EdU positive remained consistently around 10%. I observed a second peak of proliferation during the

maturation stage at 20 dpf when over 30% of VICs were EdU-positive. After this stage, the rate of proliferation progressively decreased until very few EdU-positive cells (almost 0%) were found in the adult stages. These data suggest that the VICs undergo two phases of proliferation: during 1) the invasion stage, and 2) the maturation stage.

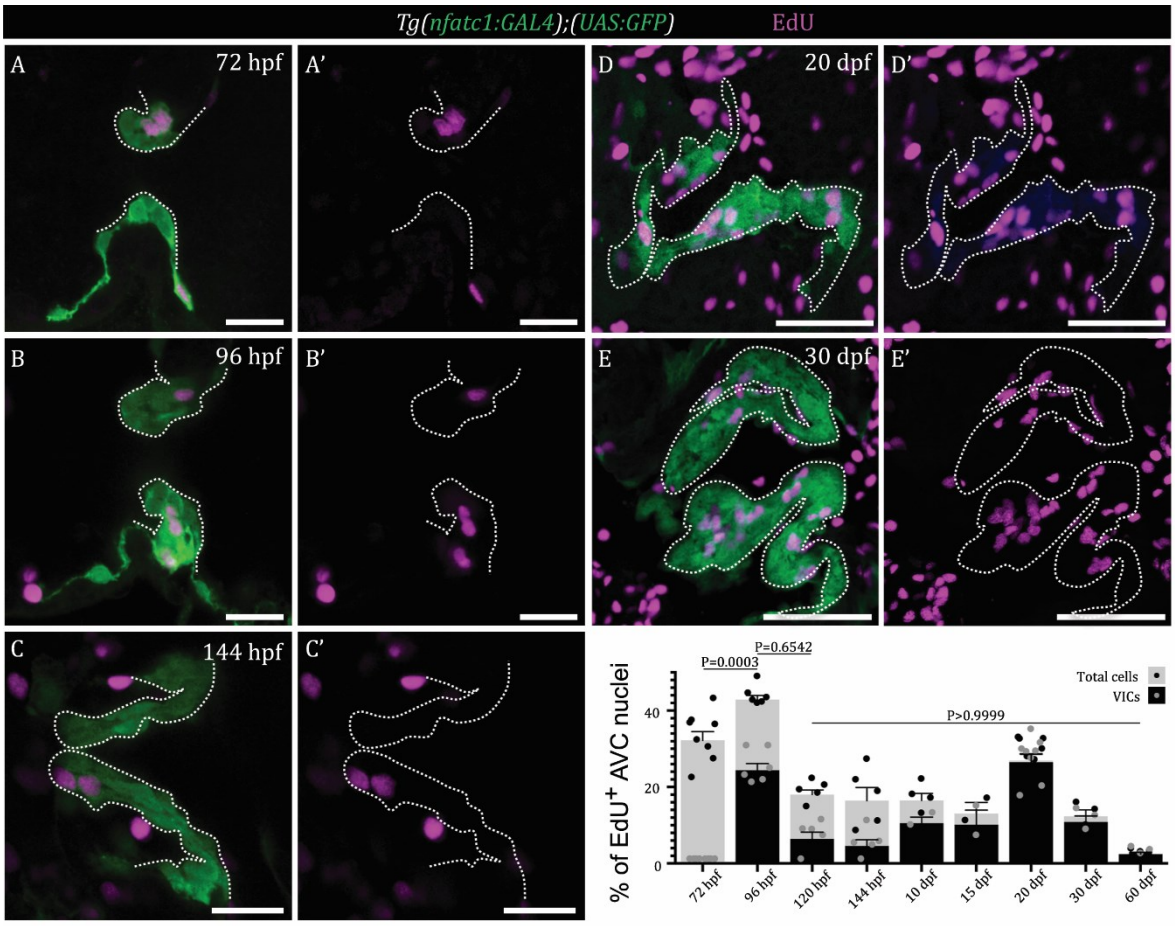

Figure 4.2.8: Proliferation profile of VICs shows two distinct peaks at the larval and juvenile stages. A-F) Proliferative activities are assessed through 24-hour EdU pulses at the indicated developmental stages. **A-E)** Representative images of EdU$^+$ cells, identified by *Tg(nfatc1:Gal4);Tg(UAS:*GFP) expression and low *Tg(kdrl:nls*-mCherry) expression. White dashed lines outline the valve leaflets. **F)** Overlay bar graph represents the ratio of EdU$^+$ to total AV cell number (grey bars, VECs; black bars, VICs), which reveals two peaks of proliferation, one at 96 hpf and the other at 20 dpf (72 hpf, n=8; 96 hpf, n=6; 120 and 144 hpf, n=5; 10 and 15 dpf, n=2; 20 dpf, n=8; and 30 and 60 dpf, n=3. Plot values represent means ± SEM; p-values were determined by the one-way ANOVA followed by multiple comparisons with Dunn's test. Figure S3E, E' is the same section as Figure 1F, F' and Online Figure I F, F'. Scale bars: (A-C) 10

μm, (D-E) 100 μm. Figure adapted and reprinted with permission from Gunawan*, Gentile* et al., 2020. License: 5243661348761.

4.2.3 The zebrafish valvular ECM is dynamic during development

The ECM has been implicated as a determining factor in cardiac valve function (Butcher and Markwald, 2007; Joziasse et al., 2008; Hinton and Yutzey, 2011; Tao et al., 2012; MacGrogan et al., 2014; Dutta and Lincoln, 2018). To better understand the dynamics of the ECM during zebrafish valve development, I assessed its composition by performing immunostaining for several ECM components. First, I examined the localization of Fibronectin, a known pro-migratory protein (Rozario and DeSimone, 2010). It has already been shown that Fibronectin is present during collective VEC migration. I confirmed the presence of Fibronectin in the early stages of valvulogenesis, throughout the elongation stage, but at 20 dpf, Fibronectin signals were undetectable, suggesting a change in the valve ECM composition.

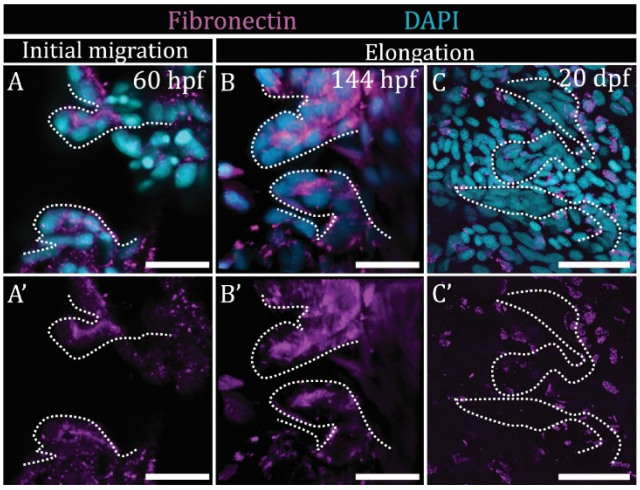

Figure 4.2.9: Expression pattern of Fibronectin

A-C') Fibronectin deposition is observed at the embryonic and larval stages (60 (A, A') and 144 (B, B') hpf), but not at the juvenile stage (20 dpf (C, C')). White dashed lines outline the valve leaflets. Scale bars: (A-B') 20 μm, (C, C'). Figure adapted and reprinted with permission from Gunawan*, Gentile* et al., 2020. License: 5243661348761.

Then, I examined another pro-migratory protein, Hyaluronic Acid (HA) (Rozario and DeSimone, 2010) (Figure 4.2.10). I used the transgenic line *Tg(ubi:HA-GFP)*, a reporter line that is reported to recapitulate HA localization. HA is also present in the early stages of valvulogenesis, but contrary to Fibronectin, it is possible to observe HA at all

stages up to the mature valve establishment, suggesting that HA is one of the main components of the valvular ECM.

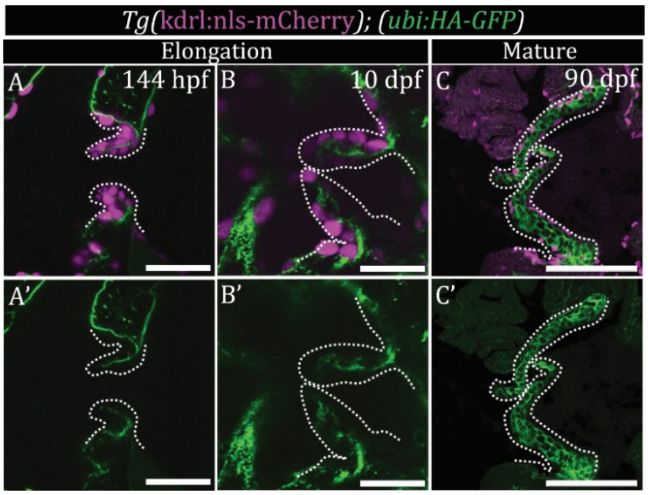

Figure 4.2.10: Expression pattern of HA

A-C') HA is observed at all stages of valvular development, including at the larval (A, A'), juvenile (B, B'), and mature valve (C, C') stages. White dashed lines outline the valve leaflets. Scale bars: (A-B') 20 μm, (C, C') 100 μm. Figure adapted and reprinted with permission from Gunawan*, Gentile* et al., 2020. License: 5243661348761**.**

As the valve functions to prevent retrograde blood flow and to withstand blood flow-induced mechanical stress (Butcher and Markwald, 2007; Joziasse et al., 2008; Hinton and Yutzey, 2011; MacGrogan et al., 2014), I examined Elastin1 (Figure 4.2.11), that confers flexibility to the structure (Rozario and DeSimone, 2010). Surprisingly during the early developmental stages, Elasin1 is undetectable; however, Elastin1 became detectable at 20 dpf, from which time Elastin1 signal became stronger in the mature valve.

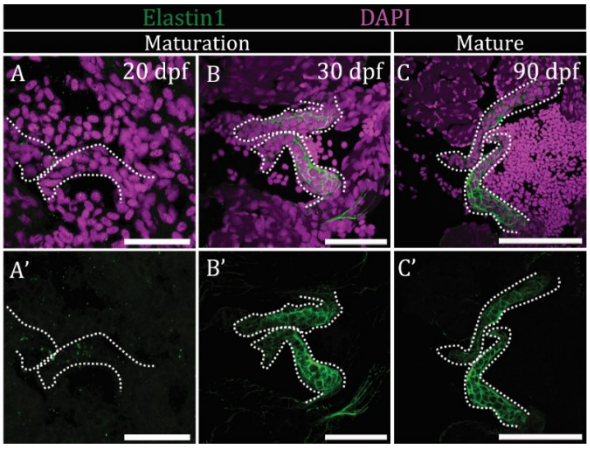

Figure 4.2.11: Expression pattern of Elastin1

A-C') Elastin1 immunostaining is very weak at the late larval stage (20 dpf; A, A'), but clearly present at the juvenile (30 dpf; B, B') and mature (90 dpf; C, C') stages. White dashed lines outline the valve leaflets. Scale bars: (A-B') 50 µm, (C, C') 100 µm. Figure adapted and reprinted with permission from Gunawan*, Gentile* et al., 2020. License: 5243661348761.

The mammalian adult valve presents a stratification of the ECM (Rutkovskiy et al., 2017). To test whether the zebrafish adult valve presents similar ECM stratification, I examined the expression pattern of *Tg(vegfaa:GFP)* (Figure 4.2.12), and I found a stronger signal in the VICs facing the atrium starting from 30 dpf, suggesting that the zebrafish adult valve is stratified.

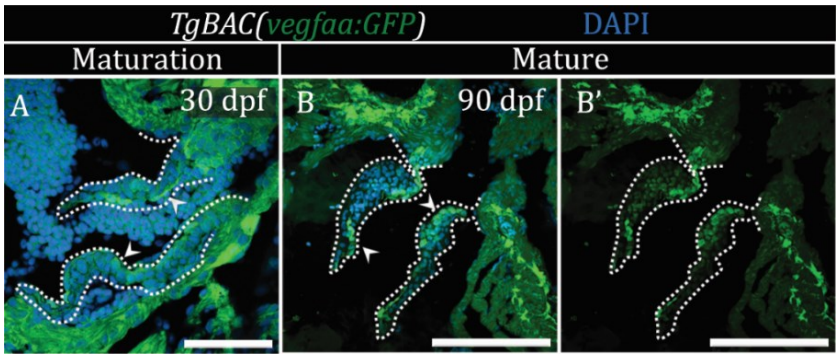

Figure 4.2.12: Expression pattern of *TgBAC(vegfaa:GFP)*

A-B') Stratification of *Tg(vegfaa:*GFP) expression is observed in the maturing (A) and mature (B, B') valve leaflets. White dashed lines outline the valve leaflets. Scale bars: (A) 50 µm, (B, B') 100 µm. Figure adapted and reprinted with permission from Gunawan*, Gentile* et al., 2020. License: 5243661348761.

Taken together, these data suggest that the valvular ECM is very dynamic, and progresses from a pro-migratory ECM in the early developmental stages to an elastic ECM in the mature valve.

4.2.4 Zebrafish VICs have different cellular origins

In the mammalian valve, the VIC population is composed of cells of different origins, such as endocardial cells (Liu et al., 2018), neural crest cells (NCCs) (Jain et al., 2011), and epicardial cells (Wessels et al., 2012). As mentioned, we showed that the first VICs

originate from migrating endocardial cells that gradually downregulate their endocardial identity. However, this result does not exclude the possibility that other cell types contribute to the VIC population later in development. To test this hypothesis, I performed a lineage tracing experiment using the Cre-LoxP recombination system. Using the floxed reporter line *Tg(ubb:loxP-GFP-loxP-mCherry)*, which recombined from GFP to mCherry in the presence of Cre, I analyzed endocardial cell contribution using *Tg(kdrl:Cre)* (Figure 4.2.13), NCC contribution using *Tg(sox10:CreERT2)* (Figure 4.2.14), epicardial contribution using *Tg(tcf21:CreERT2)* (Figure 4.2.15), and myocardial contribution using *Tg(myl7:CreERT2)* (Figure 4.2.15). The *Tg(kdrl:Cre)* line constitutively expresses CRE in endothelial cells. When I examined the valve at 120 hpf, I observed that the majority of VICs were recombined, suggesting that most VICs originate from endothelial cells. The same result was observed in the adult valve at 90 dpf.

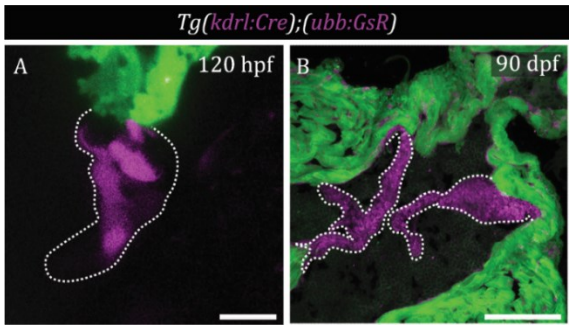

Figure 4.2.13: VICs derive from ECs

A-B) The majority of VICs derive from ECs, in early larval (A) and adult (B) AV leaflets. White dashed lines outline the valve leaflet. Scale bars: (A) 20 µm, (B) 100 µm. Figure adapted and reprinted with permission from Gunawan*, Gentile* et al., 2020. License: 524366134876.

The *Tg(sox10:CreERT2)* is a temporally inducible line upon treatment with tamoxifen. I induced the recombination at 10 hpf when NCCs start to delaminate from the neural tube and examined the contribution in the valve at 120 hpf. I observed that a few cells in the VIC population were recombined, suggesting that NCCs contribute to the VIC population. I also observed in the adult valve that a minor proportion of VICs was derived from NCCs.

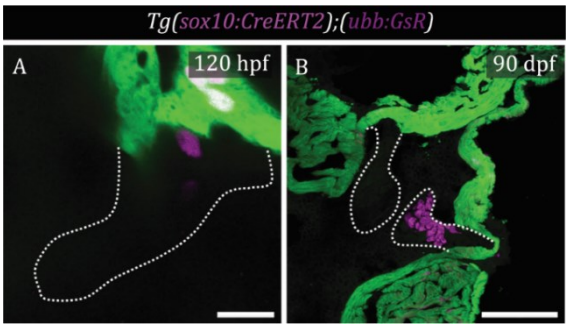

Figure 4.2.14: Few NCCs contribute to the VIC population

A-B) Few VICs derive from NCCs. White dashed lines outline the valve leaflet. Scale bars: (A) 20 µm, (B) 100 µm. Figure adapted and reprinted with permission from Gunawan*, Gentile* et al., 2020. License: 5243661348761**.**

On the other hand, when I examined the contribution from myocardial and epicardial cells, I did not observe any contribution to the valve.

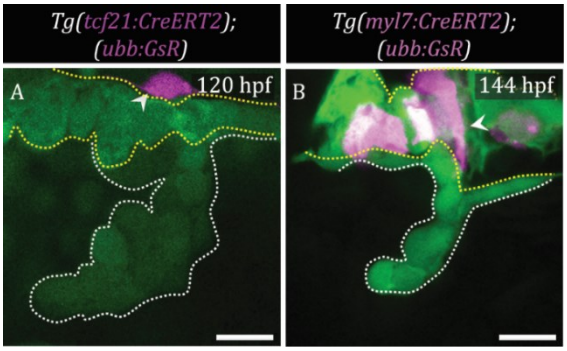

Figure 4.2.15: Myocardial and epicardial cells do not contribute to the VIC population

A-B) No epicardial- or myocardial contribution is observed in the valve at larval nor adult stages; arrowheads point to the epicardial (A) and myocardial (B) recombined cell. White dashed lines outline the valve leaflet; yellow dashed lines outline the myocardial layer. Figure adapted and reprinted with permission from Gunawan*, Gentile* et al., 2020. License: 5243661348761**.**

Taken together, these results suggest that the majority of the VICs are derived from the endocardium with a small contribution from NCCs.

4.2.5 The endocardial cells that express *nfatc1* at the earliest stage differentiate into the first VICs

To gain more insight into the EC contribution to the VIC population, I asked whether the first VECs migrating are the first to differentiate into VICs. I took advantage of the photoconvertible protein Kaede (Chow et al., 2018; Grassini et al., 2018), which switches from green to red when excited with 405 nm wavelength light. Driving the expression of Kaede in endothelial cells using *Tg(fli1a:Gal4)*, I specifically photoconverted the leading VEC at 56 hpf (Figure 4.2.16), and then imaged the same

fish after 48 hours and observed that the photoconverted cells were found exclusively in the VIC layer. Interestingly, these cells also extended protrusions towards the distal end of the leaflet, suggesting that they were invading the ECM. These data suggest that the first VECs that migrate into the ECM are the first cells that populate the VIC layer.

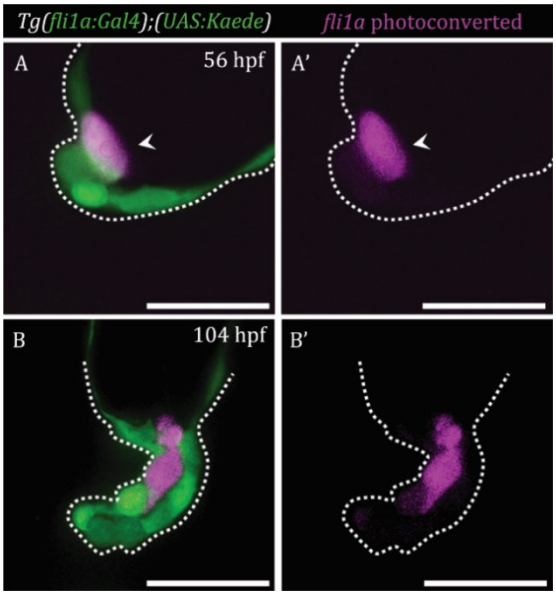

Figure 4.2.16: The first VECs that migrate into the ECM are the first VICs

A-B') Confocal images of Kaede photoconversion experiment (the same animal was imaged at 56 and 104 hpf). Photoconverted leading VEC at 56 hpf (A, A'; magenta cell, arrowhead) becomes the first VIC cells 48 hours later (B, B'). Scale bars: 20 μm. Figure adapted and reprinted with permission from Gunawan*, Gentile* et al., 2020. License: 5243661348761.

The reporter line *Tg(nfatc1:Gal4)* marks endocardial cells in the AVC as early stages as 38 hpf. To elucidate whether the *nfatc1* positive endocardial cells at 38 hpf are fated to become VICs, I drove the expression of Kaede in the *nfatc1* expressing cells and photoconverted them (Figure 4.2.17). I then examined the embryos, 24 and 48 hours later. Strikingly, I observed that all of the photoconverted cells were found in the migrating VECs at 62 hpf, and finally in the VIC layer 24 hours later. Taken together, these data suggest that the endocardium is patterned as early as the linear heart tube stage, and the cells that express *nfatc1* are fated to become VICs.

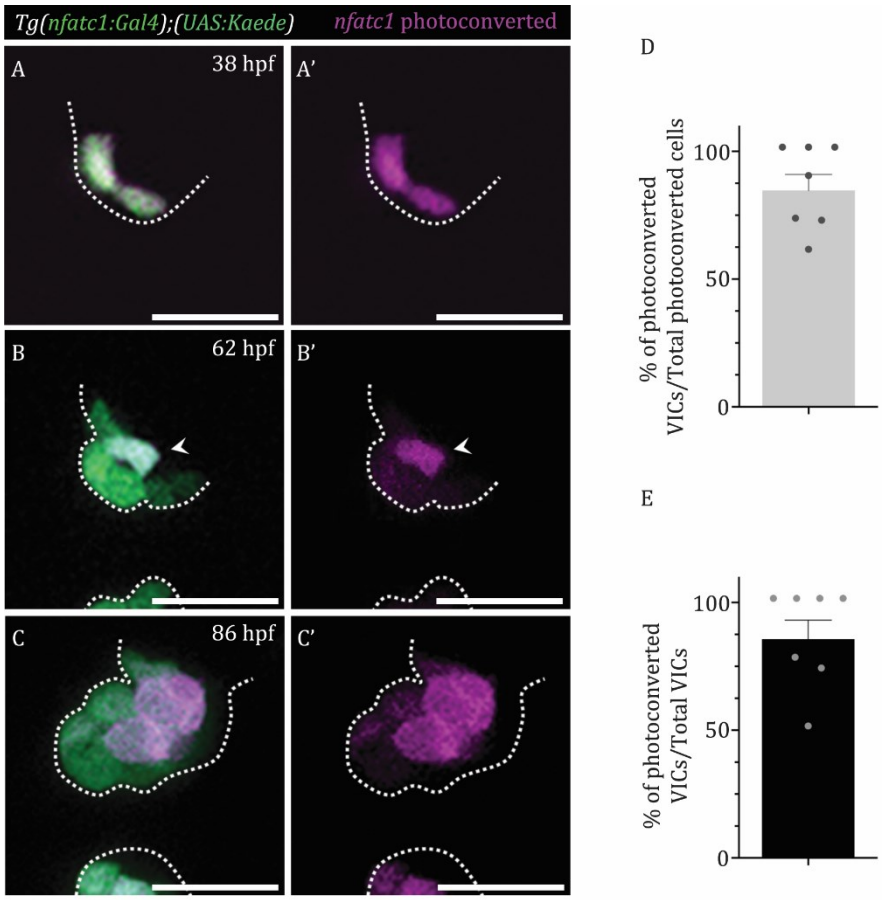

Figure 4.2.17: The ECs that express *nfatc1* at the earliest stage differentiate into the first VICs

A-C') *nfatc1*-expressing cells were photoconverted at 38 hpf (A, A') and imaged 24 (B, B') and 48 (C, C') hours later (the same animal was imaged at 38, 62, and 86 hpf). The cells that were photoconverted are found in the migrating cluster at 62 hpf (B, B'; arrowhead indicates leading cell) and become the VIC population at 86 hpf (C, C'). **D-E)** 80% of the photoconverted cells at 38 hpf became VICs at 86 hpf (D), and over 80% of the VICs corresponded to photoconverted cells at 38 hpf (E). Plot values represent means ± SEM. Scale bars: 20 μm. Figure adapted and reprinted with permission from Gunawan*, Gentile* et al., 2020. License: 5243661348761**.**

4.2.6 The transcription factor Nfatc1 is important for VIC establishment

Based on my observations that the *nfatc1* positive cells are fated to become VICs, I hypothesized that Nfatc1 regulates VIC formation. To test this hypothesis, the *nfatc1*

loss-of-function mutant allele with a 23 bp deletion (*nfatc1*^{bns276}) was generated, using the CRISPR/Cas9 technology, targeting the DNA binding domain. At the transcriptional level, *nfatc1* mutants exhibited around a 40% reduction in the mRNA levels when compared with *nfatc1* wild types, suggesting mutant mRNA degradation. Morphologically, the larvae do not exhibit any morphological defects until 72 hpf. Starting from 96 hpf, *nfatc1* mutants display pericardial edema, suggesting cardiac defects (Figure 4.2.18).

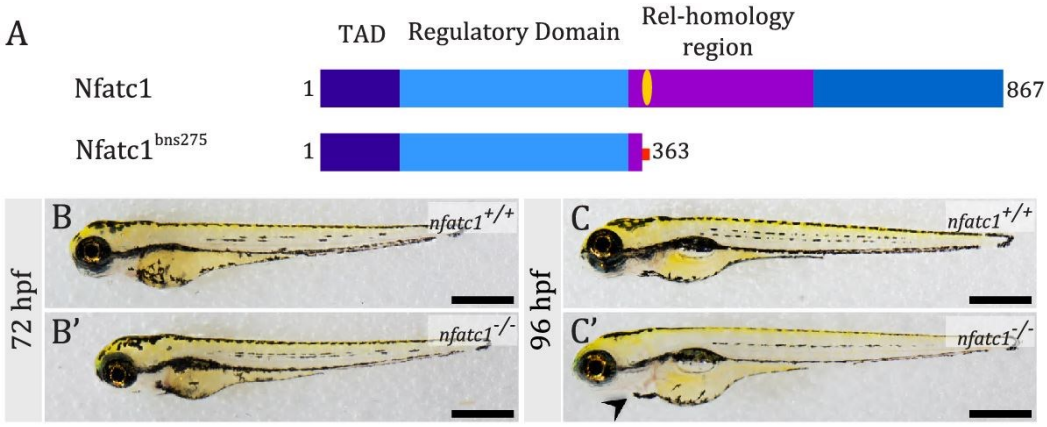

Figure 4.2.18: Generation of *nfatc1* mutants

A) The mutant protein is predicted to be truncated at the beginning of the DNA binding domain; red indicates new sequence downstream of the mutation. **B-C')** No gross morphology defects are observed in the mutant larvae compared with wild-type larvae at 72 hpf (B, B'), but pericardial edema (arrowhead) is observed in mutant larvae at 96 hpf (C, C'). Figure adapted and reprinted with permission from Gunawan*, Gentile* et al., 2020. License: 5243661348761**.**

To test the cellular basis of the cardiac phenotype, I analyzed *nfatc1* mutant hearts and their siblings. I did not observe any obvious defects in the morphology of the chambers (Figure 4.2.19). Quantification of the ventricular volume and the total number of endocardial cells did not reveal significant differences in the *nfatc1* mutants compared with their wild-type siblings until 120 hpf (Figure 4.2.19).

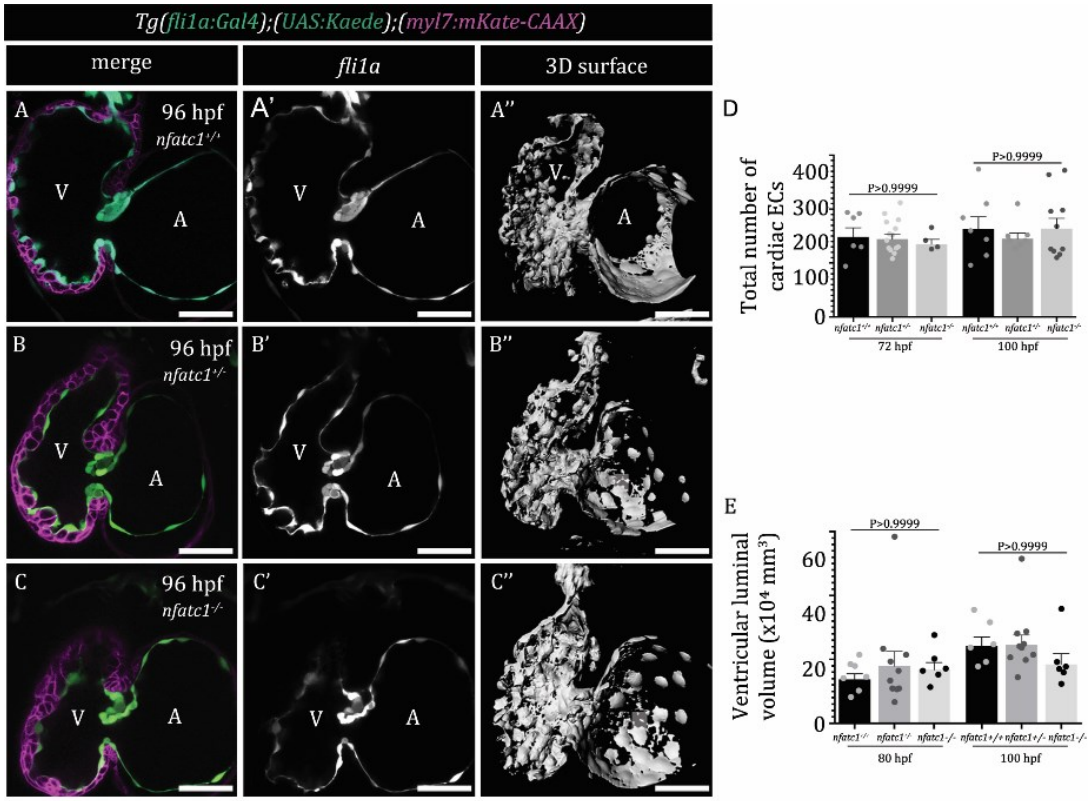

Figure 4.2.19: *nfatc1* mutants do not exhibit changes in the chamber volume or endocardial cell numbers

A-C'') Myocardial cells marked by *Tg(myl7:*mKate-CAAX) expression and ECs marked by *Tg(fli1a:Gal4); Tg(UAS:*Kaede) expression. **D-E)** No significant difference is observed in endocardial cell number (*nfatc1*$^{+/+}$, n=6, *nfatc1*$^{+/-}$, n=10, *nfatc1*$^{-/-}$, n=4 at 72 hpf; *nfatc1*$^{+/+}$, n=7, *nfatc1*$^{+/-}$, n=5, *nfatc1*$^{-/-}$, n=10 at 100 hpf) (D) or ventricular chamber volume (E) in *nfatc1*$^{-/-}$ (n=4 at 72 hpf; n=10 at 100 hpf) compared to *nfatc1*$^{+/+}$ (n=7 at 72 hpf; n=7 at 100 hpf) and *nfatc*$^{+/-}$ (n=13 at 72 hpf; n=7 at 100 hpf). A- atrium, V – ventricle. Plot values represent means ± SEM; p-values were determined by the one-way ANOVA test followed by multiple comparisons with Dunn's. Scale bars: 50 μm. Figure adapted and reprinted with permission from Gunawan*, Gentile* et al., 2020. License: 5243661348761.

Although the number of VECs was unchanged and the migration and elongation stages unaffected, we observed that by 96 hpf the number of VICs was reduced, with few larvae completely lacking the VIC layer.

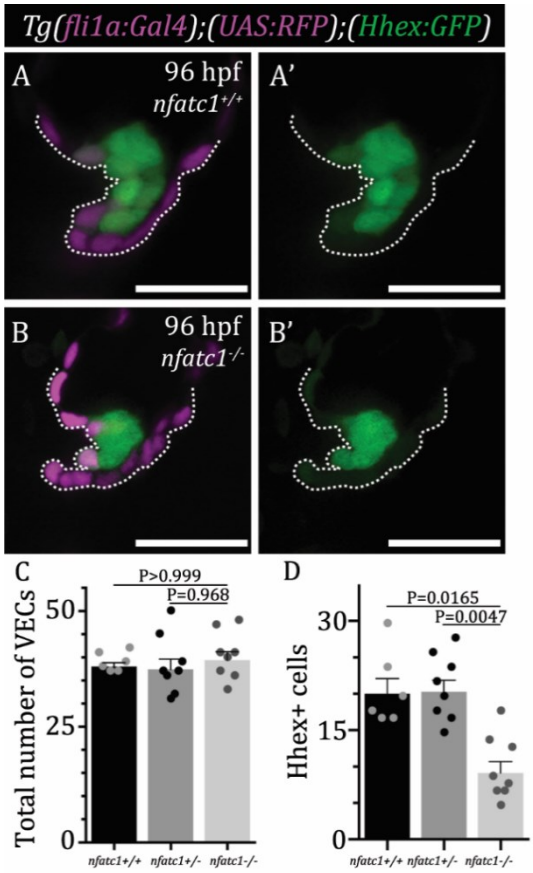

Figure 4.2.20: *nfatc1* mutants exhibit decreased VIC numbers

A-B') Fewer *Tg(Hhex:*GFP)-expressing cells are observed in mutant compared with wild-type valves. **C-D)** VICs (D), but not VECs (C), are significant reduced in mutant (n=8) compared with wild-type (n=6) and heterozygous (n=8) larvae. White dashed lines outline the valve leaflet. Plot values represent means ± SEM; p-values were determined by the one-way ANOVA followed by multiple comparisons with Dunn's test (F-J). Scale bars: 20 μm. Figure adapted and reprinted with permission from Gunawan*, Gentile* et al., 2020. License: 5243661348761**.**

ECM deposition was still present in *nfatc1* mutants compared with wild type; however, the layer appeared much thinner in the *nfatc1* mutants compared to their wild-type siblings, suggesting that reduction of VICs leads to reduced valve ECM, consistent with VIC function (Figure 4.2.21).

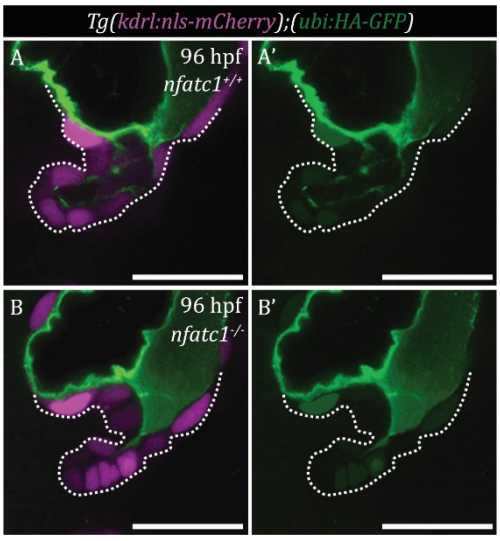

Figure 4.2.21: HA is deposited in *nfatc1* mutants

A-B') ECM is marked by *Tg(ubi:*HA) expression and VECs are marked by *Tg(kdrl:*nls-mCherry) expression. (A, A') In wild-type larvae, HA is detected around the VICs which are positioned between the two VEC monolayers. (B, B') In mutant larvae, no VICs are present and only a thin layer of HA is observed in the leaflet. White dashed lines outline the valve leaflets. Scale bars: 20 μm. Figure adapted and reprinted with permission from Gunawan*, Gentile* et al., 2020. License: 5243661348761.

These data suggest that loss of *nfatc1* leads to defects in VIC establishment. To better understand if the reduction in VICs was due to defects in proliferation, we used the EdU proliferation assay (Figure 4.2.22). I observed a reduction of EdU-positive cells at 72 and 96 hpf, suggesting that the loss of VICs is caused at least partially by a decreased proliferation of their precursors.

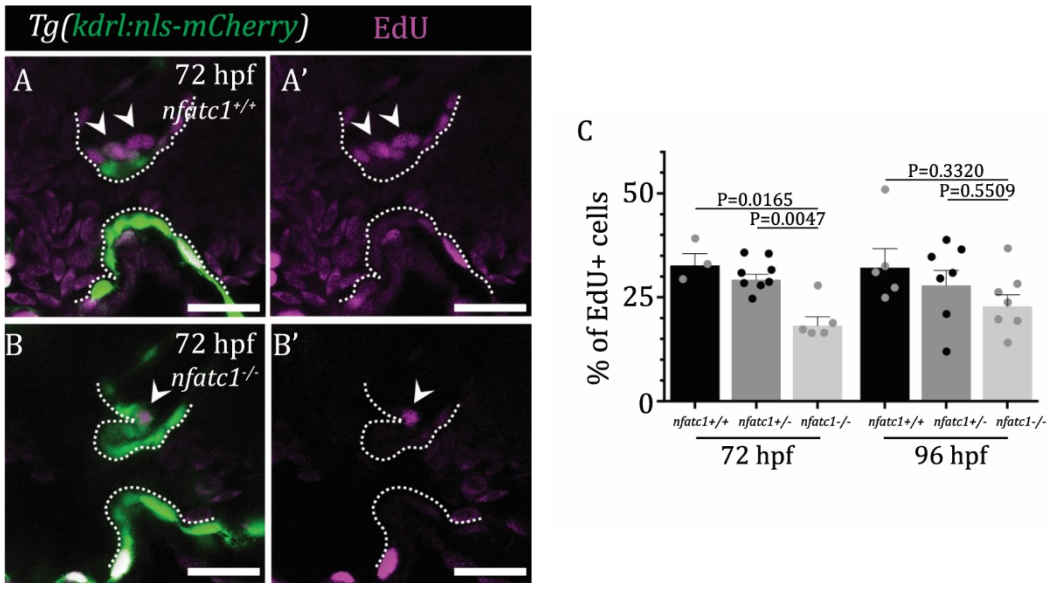

Figure 4.2.22: *nfatc1* mutants exhibit reduced proliferation in the valve

A-B') Fewer EdU+ (arrowheads) cells are observed in mutant (B-B') compared with wild-type (A, A') valves. **C)** Lower ratio of EdU+ VECs over total VECs is observed in 72 and 96 hpf mutant (n=5 at 72 hpf; n=7 at 96 hpf) compared with wild-type (n=3 at 72 hpf; n=5 at 96 hpf) and

heterozygous (n=8 at 72 hpf; n=7 at 96 hpf) larvae. White dashed lines outline the valve leaflet. Plot values represent means ± SEM; p-values were determined by the one-way ANOVA followed by multiple comparisons with Dunn's test. Scale bars: 20 µm. Figure adapted and reprinted with permission from Gunawan*, Gentile* et al., 2020. License: 5243661348761.

I also hypothesized that the reduction of VICs number was caused by reduced contribution from endocardial cells or NCCs. To test this hypothesis, using lineage-traced zebrafish, I quantified endocardial-derived VICs in *nfatc1* mutants at 120 hpf (Figure 4.2.23) and found a significantly lower number of these cells compared with the wild types. I then observed that NCC-derived VICs in *nfatc1* mutants at 10 dpf were absent, but present in the wild types (Figure 4.2.23). Taken together, these data suggest that Nfatc1 promotes the contribution of both endocardial- and neural crest-derived cells to the VIC population.

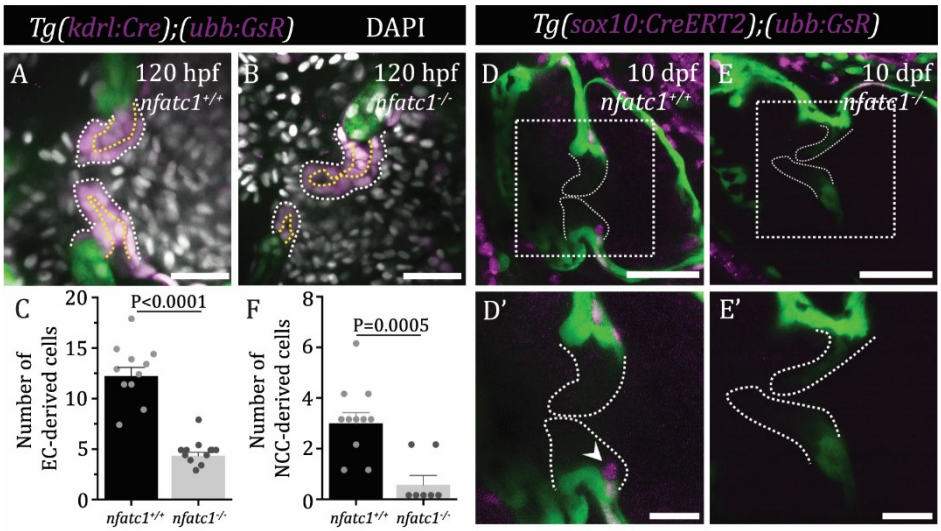

Figure 4.2.23: Fewer EC- and NCC-derived cells are observed in *nfatc1* mutants

A-B) Fewer EC-derived VICs are observed in mutant compared with wild-type larvae at 120 hpf. **C)** 60% of reduction in EC-derived VICs in mutant (average of 4.3 cells, n=12) compared with wild-type (average of 12.2 cells, n=11) larvae is observed. **D-E')** Fewer NCC-derived VICs are observed in mutant (E, E') compared with wild-type (D, D'; arrowhead) larvae at 10 dpf. **F)** 0.3 NCC-derived VIC on average are observed in mutant (n=7) compared with 3 in wild-type (n=11) larvae. Boxed area shown in D', E'. White dashed lines outline the valve leaflet; yellow dashed lines outline the VIC cells. Plot values represent means ± SEM; p-values were determined by the Mann-Whitney test. Scale bars: (B-C) 500 µm; (A-B, D'-E') 20 µm; (D, E) 50

μm. Figure adapted and reprinted with permission from Gunawan*, Gentile* et al., 2020. License: 5243661348761.

As mentioned above, the main function of the valve is to prevent retrograde blood flow (Butcher and Markwald, 2007; Joziasse et al., 2008; Hinton and Yutzey, 2011; MacGrogan et al., 2014); although VICs are known to be an important component of the valve, no study has assessed the effects of losing VICs on valve function. To test the hypothesis that the absence of VICs was correlated to dysfunctional cardiac valves, I used spinning disk microscopy to record videos of the beating heart. Strikingly, *nfatc1* mutants exhibit severe retrograde blood flow when compared with the wild-type siblings at 96 hpf (Figure 4.2.24). Quantitative correlative analysis indicates that this phenotype was not due to a shortening of the valve leaflet length, but instead to inefficient closure of the valve, with reduced contact between the superior and the inferior leaflets in the mutants.

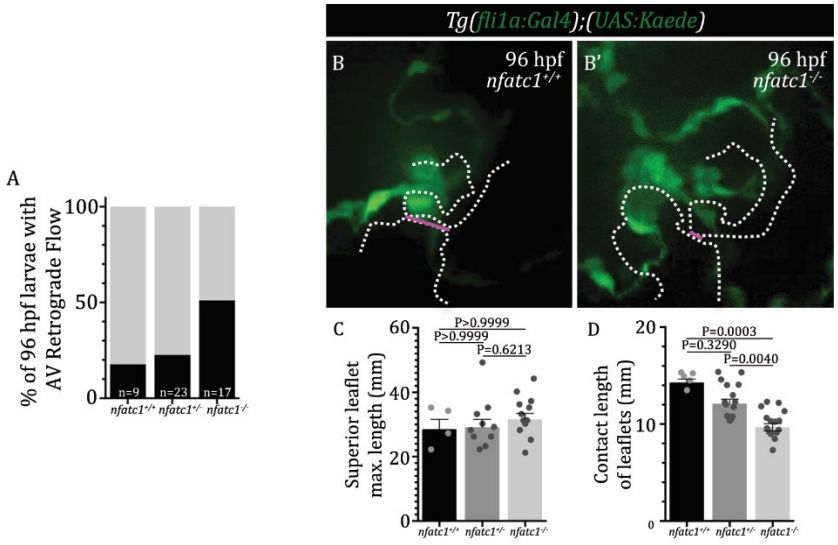

Figure 4.2.24: *nfatc1* mutants exhibit defective AV valve function

A) Mutant embryos exhibit significantly more frequent retrograde blood flow in the AV canal than wild-type or heterozygous siblings at 96 hpf. **B, B')** Wild-type valve leaflets close the cardiac lumen upon contraction, while (B') mutant valve leaflets fail to align and close the lumen. Pink line indicates the contact length between superior and inferior leaflets. **C)** Average maximum length of the superior leaflet is not significantly different between *nfatc1*$^{+/+}$ (n=4), *nfatc1*$^{+/-}$ (n=10) and *nfatc1*$^{-/-}$ (n=12). (D) Average length of contact between superior and

inferior leaflets is significantly lower in *nfatc1*$^{-/-}$ (n=14) compared to *nfatc1*$^{+/+}$ (n=5) and *nfatc1*$^{+/-}$ (n=14). White dashed lines outline the valve leaflets. (C, D) Plot values represent means ± SEM; p-values were determined by the one-way ANOVA test followed by multiple comparisons with Dunn's. Scale bars: 20 µm. Figure adapted and reprinted with permission from Gunawan*, Gentile* et al., 2020. License: 5243661348761.

Taken together, these data suggest that loss of Nfatc1 leads to a reduction of VIC precursor recruitment and proliferation, defects in VIC establishment, and ECM disorganization, which translates into cardiac valve dysfunction.

4.2.7 Nfatc1 regulates the transcription factor *twist1b* expression

To better understand how Nfatc1 regulates the VIC establishment, I searched for EndoMT-associated transcription factor candidate genes. Using cardiac transcriptomic datasets available in the lab (Gunawan et al., 2019), I focused on the transcription factors Snai1 and Twist1. As shown before, Snai1b is expressed in the heart and enriched in the AVC. While *twist1b* is expressed in the heart and enriched in the AVC region at 56 hpf, *twist1a* was not detectable in the heart (Figure 4.2.25).

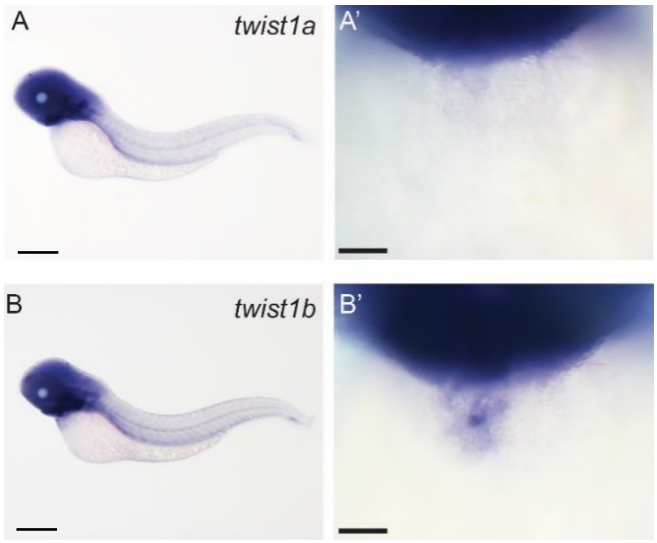

Figure 4.2.25: *twist1b* expression is enriched in the AVC

A-B) Whole-mount ISH of *twist1a* and *twist1b* at 56 hpf. **A'-B')** *twist1a* expression is very low in 56-hpf hearts (A-A'), while *twist1b* expression is detected at much higher levels, particularly in the AV canal (B-B'). Scale bar: 50 µm.

To further understand if Nfatc1 is a regulator of these transcription factors, I analyzed the promoter region of these genes to identify potential NFATC1 binding domains. Interestingly, I observed six NFAT binding domains in the *twist1b* promoter region, whereas in the *snai1b* promoter region I did not find any potential NFAT binding domains (Figure 4.2.26).

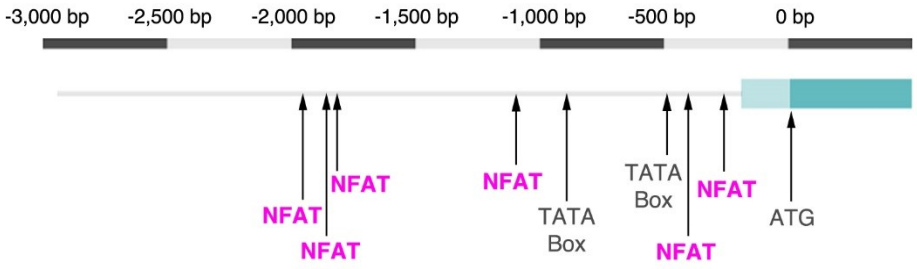

Figure 4.2.26: NFAT binding sites are found in the promoter region of *twist1b*

6 NFAT bindings sites are found within the 1.8 kb promoter region of *twist1b*.

Strikingly, *twist1b*, but not *snai1b*, was significantly downregulated in the *nfatc1* mutant hearts compared with the wild-type siblings at 72 hpf (Figure 4.2.27). To confirm these data, I performed WISH and observed that while *twist1b* expression in wild types is very strong in the AVC, its expression was undetectable in the *nfatc1* mutant hearts (Figure 4.2.27). These data suggest that Nfatc1 regulates the cardiac expression of *twist1b*.

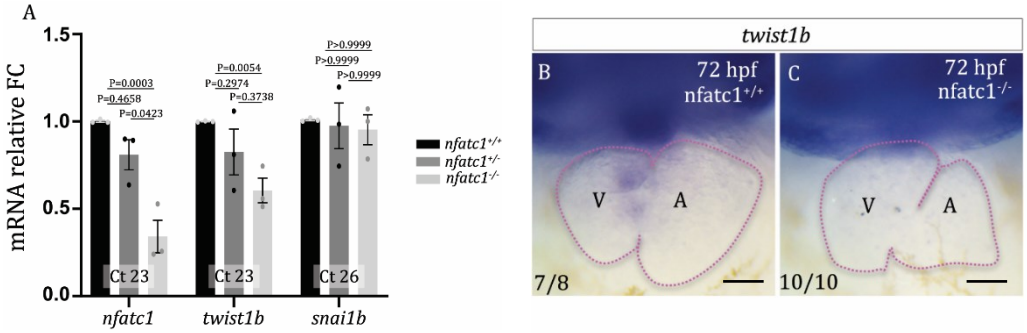

Figure 4.2.27: *twist1b* expression is downregulated in *nfatc1* mutants

A) *nfatc1* and *twist1b* expression levels are significantly reduced in mutants, whereas those of *snai1b* appear unchanged. n=3 biological replicates, 40 embryos each; Ct values are an average of the *nfatc1*$^{+/+}$ biological replicates; Ct value of *rpl13a* = 19. **B-C)** *in situ* hybridization for *twist1b* expression in 72 hpf hearts. Whereas *twist1b* expression appears enriched in the AV canal of wild-type hearts (B; 7/8 hearts), in mutant hearts (C; 10/10 hearts) is undetectable. Pink dashed lines outline the heart. A, atrium; V, ventricle. Plot values represent means ± SEM; p-values were determined by the one-way ANOVA followed by multiple comparisons with Dunn's test. Scale bars: 10 μm. Figure adapted and reprinted with permission from Gunawan*, Gentile* et al., 2020. License: 5243661348761.

To further test if Nfatc1 was sufficient to induce *twist1b* expression, I injected a constitutively active form of Nfatc1, a non-phosphorylatable form that is continuously localized to the nucleus (Saneyoshi et al., 2002), into the one-cell stage embryos. I observed an upregulation of mRNA levels of *twist1b* at the 80% epiboly, further confirming a role of Nfatc1 in regulating *twist1b* expression (Figure 4.2.28).

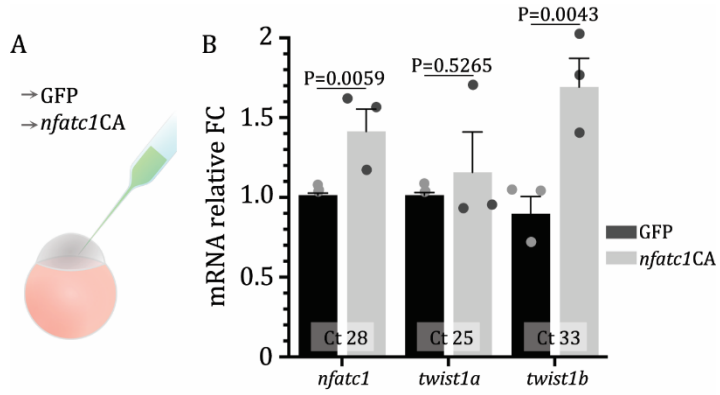

Figure 4.2.28: *twist1b* expression is regulated by Nfatc1

A) Cartoon of the injection experiment: GFP (control) or constitutively active Nfatc1 (*nfatc1*^{CA}) mRNA were injected in the one-cell stage. **B)** Relative *nfatc1* and *twist1b* expression levels are significantly upregulated in the *nfatc1*^{CA}-injected embryos, whereas those of *twist1a* are unchanged. n=3 biological replicates, 40 embryos each; Ct values are those in *gfp*-injected embryos; Ct value of *rpl13a* = 19. Plot values represent means ± SEM; p-values were determined by the Mann-Whitney test. Figure adapted and reprinted with permission from Gunawan*, Gentile* et al., 2020. License: 5243661348761.

To gain more insight into the role of the EMT transcription factor Twist1b, I first generated a tissue-specific overexpression of a dominant negative form of Twist1b. I drove the expression of Twist1b with a substitution, which prevents protein binding to DNA (Das and Crump, 2012), under the UAS promoter. To gain cellular resolution, I expressed this construct specifically in the valve cells using *Tg(nfatc1:Gal4)* (Figure 4.2.29). Strikingly, the larvae overexpressing the dominant negative form of Twist1b exhibited severe impairment of the valve formation, with 50% of them completely lacking valve leaflets. Interestingly, the analysis of the larvae that exhibited a normal-looking valve leaflet, revealed a complete lack of VICs (Figure 4.2.29). These data suggest the importance of the EndoMT-promoting factors in VIC formation.

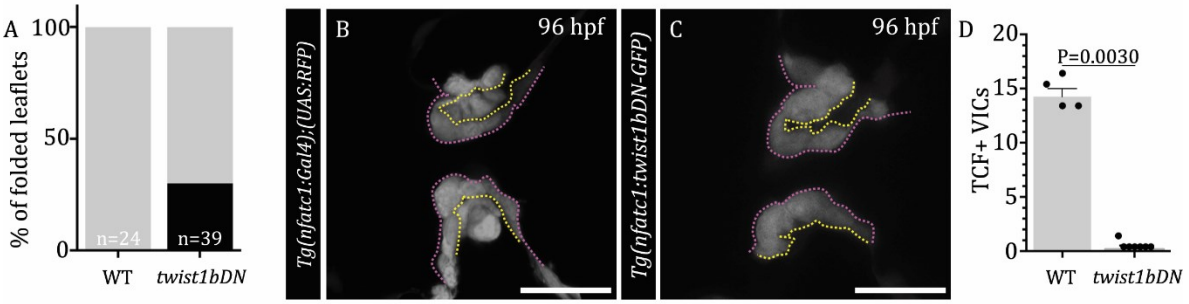

Figure 4.2.29: *twist1b* dominant negative expression in *nfatc1* positive cells causes malformed valves

A) The majority of *twist1b*^{DN}-expressing hearts do not fold the valve leaflets (control, n=15; *twist1bDN*, n=35). **B-C)** No VICs are found in *twist1b*^{DN}-expressing larvae (C) with folded valve leaflets in contrast to control (B). Pink dotted lines outline the valve leaflets; yellow dotted lines outline the VIC cells. **D)** The number of VICs is significantly lower in *twist1b*^{DN}-expressing larvae compared with control. Plot values represent means ± SEM; p-values were determined by the Mann-Whitney test. Scale bars: 20 μm. Figure adapted and reprinted with permission from Gunawan*, Gentile* et al., 2020. License: 5243661348761**.**

I then generated a *twist1b* loss-function allele. To prevent transcriptional adaption from its paralogue, I used two gRNAs targeting the 5' UTR and 3'UTR of *twist1b* to generate a full locus deletion (Figure 4.2.30). Although *twist1b* mutants do not show transcriptional adaptation from its paralogue, I did not observe any severe phenotype in the heart or increased retrograde blood flow of the mutant larvae, suggesting that other EndoMT-promoting factor genes might compensate for the loss of *twist1b*.

However, when the loss-of-function of *twist1b* occurs in the *nfatc1* heterozygous animals, I observed an increased percentage of animals exhibiting retrograde blood flow when compared with double heterozygous or *twist1b* mutants (Figure 4.2.30).

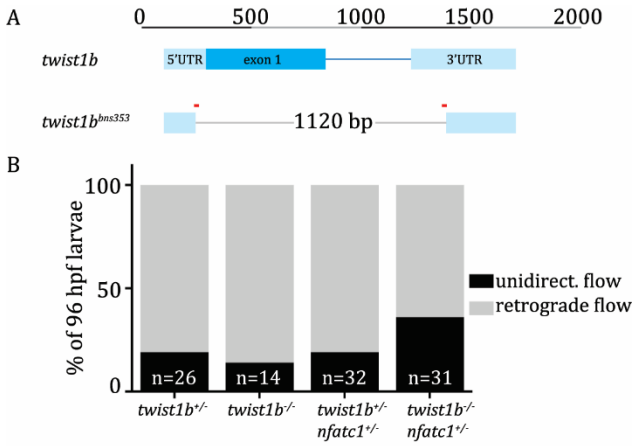

Figure 4.2.30: *twist1b* mutants do not exhibit any valve defects

A) Cartoon of *twist1b* full-locus allele with a 1120 base pair deletion. **B)** Loss of *twist1b* increases the frequency of retrograde blood flow in *nfatc1* heterozygous background (35% of *nfatc1*$^{+/-}$; *twist1b*$^{-/-}$ vs. 19% of *twist1b*$^{+/-}$, 14% of *twist1b*$^{-/-}$, and 18% of *nfatc1*$^{+/-}$; *twist1b*$^{+/-}$). Figure adapted and reprinted with permission from Gunawan*, Gentile* et al., 2020. License: 5243661348761.

Altogether, these results suggest that the function of Twist1b downstream of Nfact1 is critical for valve formation and function.

(Certain lines in this subsection have been quoted *verbatim* from Gunawan*, Gentile* et al., *Circ Res* 2020; DOI: 10.1161/CIRCRESAHA.119.315992 for the scientific accuracy of the terms).

4.2.8 Proposed model

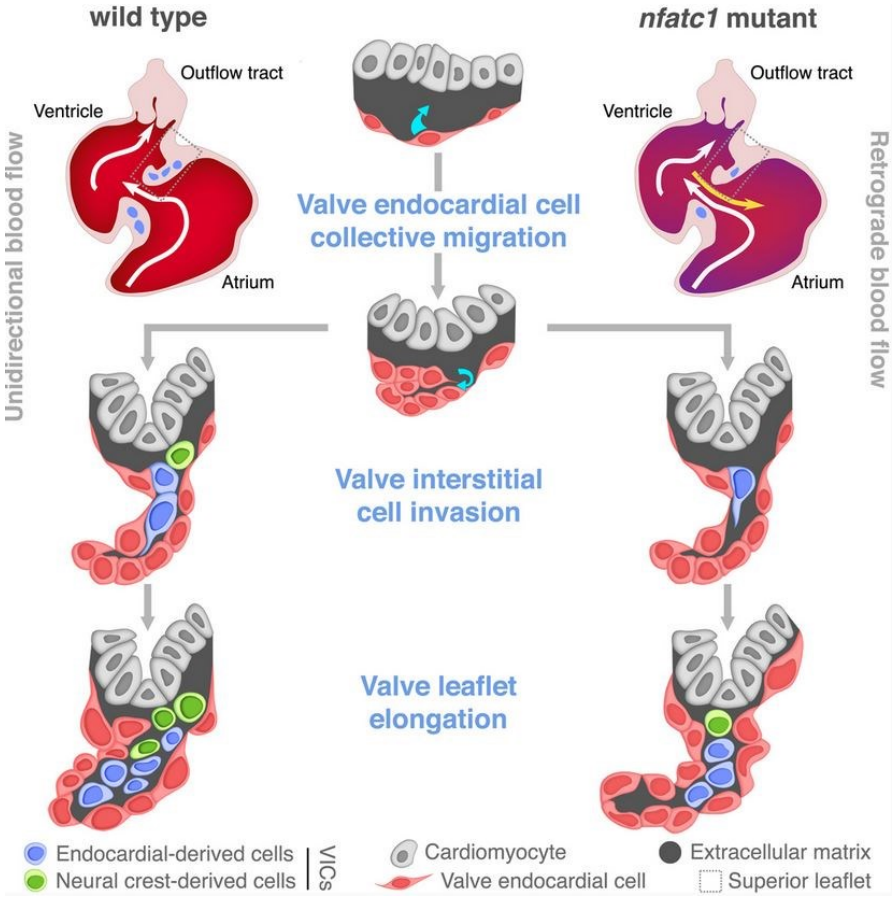

Figure 4.1.31: Proposed model (see text)

Figure adapted and reprinted with permission from Gunawan*, Gentile* et al., 2020. License: 5243661348761.

In this study, my data showed the establishment of VICs during zebrafish cardiac development, and the role of Nfatc1 in regulating VIC formation through its downstream target and EndoMT promoting gene *twist1b* (Figure 4.2.31). In particular, I showed that following collective migration, VECs invade the ECM between the two endocardial layers of the valve leaflet, undergoing EndoMT, losing their adhesion, and becoming VICs. My data then showed the there is an expansion of the VIC population and a change in the valvular ECM, from a pro-migratory environment to an elastic ECM. Most of the VICs are derived from endocardial cells, with a small contribution from the NCCs. Interestingly, my data showed that the first VECs that express *nfatc1* are the first to become VIC. In line with this result, the loss-of-function of *nfatc1* larvae exhibited

fewer VICs due to reduced proliferation and impaired recruitment of endocardial and NCCs during the early stages of VIC development. Finally, with the molecular analysis, I showed that *twist1b* acts downstream of Nfatc1, promoting EndoMT. Altogether, this study characterizes for the first time the cellular and molecular processes of zebrafish VIC formation and maturation and confirms that the zebrafish is a suitable model for vertebrate valve formation.

5. Discussion

5.1 The EMT transcription factor Snai1 maintains cardiac wall integrity

The beating organ heart has to withstand strong mechanical forces brought on by various morphogenetic processes during development (Auman et al., 2007; Dietrich et al., 2014; Bornhorst et al., 2019). For these reasons, it is important to have a strong cardiac wall that preserves heart function (Sequeira et al., 2014; Gautel and Djinović-Carugo, 2016). The advantage of using the zebrafish heart is the possibility to look at the morphogenetic processes without impairing its functionality using non-invasive live-imaging approaches. With this PhD work, I showed how the cardiac wall is maintained at the cellular and molecular level, uncovering a different function for the very well-known transcription factor Snai1.

5.1.1 *snai1b* is expressed in CMs during later stages of cardiac development

The transcription factor Snai1 is a known promoter of EMT (Nieto, 2002; Nieto et al., 2016). The EMT process allows the epithelial cells to be more plastic and become mesenchymal cells (Nieto et al., 2016). Several studies in the context of development and cancer, have shown that in epithelial cells Snai1 represses epithelial genes such as E-cadherin, and promotes the expression of mesenchymal genes such as Vimentin (Nieto, 2002). Its function is very well studied during gastrulation from flies (Martin et al., 2010; Weng and Wieschaus, 2016) to vertebrates (Wee et al., 2020). Although it is known that Snai1 is also involved in some aspects of cardiac development, such as left-right patterning (Murray and Gridley, 2006) and valve development (Tao et al., 2011), its role in later stages of CM development has not been uncovered. Our group has shown that CMs are polarized cells with an epithelial apico-basal polarity, as shown by the localization of the apical marker Podocalyxin and the basal marker Marck3a (Jiménez-Amilburu et al., 2016). In addition, our group showed that delaminating CMs lose their polarity to become trabecular CMs, suggesting that the myocardial wall can

be seen as an epithelial-like tissue (Jiménez-Amilburu et al., 2016). Given these data, I hypothesized that EMT-TFs are repressed in the CMs, which is needed to ensure that only delaminating CMs are losing their polarity during trabeculation. However, I observed that the EMT-TF Snai1b is needed to maintain CMs cytoskeletal architecture. Interestingly, through WISH, I found that among the EMT-TF factors expressed in the heart, Snai1 is expressed in CMs during their maturation, which opened interesting avenues. However, combining it with transcriptomic profiling of sorted cardiac cells, I showed that *snai1b* is enriched in CMs compared with ECs at 96 hpf, strengthening my hypothesis that it potentially has a role in the maturation of the myocardial layer. Contrary to my expectations, the phenotype that I observed in the loss-of-function of *snai1b* led to the extrusion of CMs away from the cardiac wall.

5.1.2 Snai1 regulates the actomyosin machinery

Elimination of an aberrant or dying cell and cell competition in a crowded tissue are two of the common causes of cell extrusion (Rosenblatt et al., 2001; Eisenhoffer et al., 2012; Kocgozlu et al., 2016) to preserve homeostasis. During cardiac development, compact layer CMs delaminate into the lumen to become trabecular CMs (Staudt et al., 2014; Cherian et al., 2016; Jiménez-Amilburu et al., 2016; del Monte-Nieto et al., 2018). Recently, our group showed that this process is driven by tension heterogeneity by crowding and resulting in cell delamination. In particular, this process leads to the activation of Notch signaling in CMs that will not delaminate. Notch activation represses the delamination of these CMs by perturbing their actomyosin cytoskeleton, thus preserving the cardiac wall integrity (Priya et al., 2020). A role for Snai1 in cell extrusion has been reported in *Drosophila* embryos (Martin et al., 2009) as well as in mammalian cell culture (Wee et al., 2020). As mentioned above, Snai1 function has also been linked to EMT-independent processes. Indeed, during gastrulation in *Drosophila*, medio-apical pulsations of contractile Myo-II are promoted by Snai1, and the contractile pulse drives apical constrictions (Martin et al., 2009, 2010; Mitrossilis et al., 2017). However, the transcriptional targets of Snai1, which promote cellular contractility in this system remain to be uncovered. Recent *in vitro* studies have reported that Snai1 expression induces a transcriptional network, leading to increased

cellular contractility through RhoA activation (Wee et al., 2020). Here, in my PhD thesis, I uncover a previously unsuspected role for the EMT-inducing factor Snai1 in limiting CM extrusions by regulating IF gene expression. Since I did not observed any obvious changes in the localization of the apical marker Podocalyxin, this function appears to be partly independent of Snai1's role in EMT. My work clearly shows the Snai1 is required for maintaining epithelial tissue integrity in a vertebrate organ, and add to the growing evidence that Snai1 has EMT-independent roles in epithelial tissues. I showed that the CM extrusions in *snai1b* mutants are associated with increased accumulation of actomyosin basally, providing more evidence for a role of Snai1 in regulating cell contractility through actin networks.

(Certain lines in this subsection have been quoted *verbatim* from Gentile et al., *eLife*, 2021; DOI:10.7554/eLife.66143 for the scientific accuracy of the terms).

5.1.3 Snai1 as a regulator of intermediate filament genes

To maintain tissue integrity, the cytoskeleton is fundamental to ensure that the cells adapt their morphology and their cell behavior to the surrounding environment (Gautel and Djinović-Carugo, 2016; Sequeira et al., 2014). Indeed, the main function of the cytoskeleton is to mechanically support the cells, through its components, such as actin, microtubules, and IFs (Sequeira et al., 2014). While actin and microtubules are extensively studied in different model systems, less attention has been given to the IFs until recently. Mutations in the IF genes are associated with several diseases, often characterized by the loss of tissue integrity. Contrary to the other cytoskeletal components that are ubiquitously expressed, IFs are expressed in a cell- and tissue-specific manner. For example, the IF network in glia is formed by GFAP, vimentin, and nestin, in muscle cells by desmin, in skin cells by keratins, and in mesenchymal cells by vimentin (van Bodegraven and Etienne-Manneville, 2020). Here, I show that Snai1b regulates *desmin b* in CMs and that Desmin is required for the maintenance of cardiac wall integrity. Although Vimentin (Kajita et al., 2014) and Keratin (Kadeer et al., 2017; Thomas et al., 2020) are known to accumulate at the interface between extruding cells and their neighbors, my work provides evidence that increased Desmin levels in CMs

are correlated with cell extrusion and mislocalization of the actomyosin machinery in the basal domain. These findings are consistent with previous studies that IFs can regulate the localization and activation of the actomyosin network, with factors such as Vimentin directly binding to actin and modulating RhoA activity (Jiu et al., 2017), and Keratin directly binding to Myosin (Kwan et al., 2015). Previously, it has been shown that Desmin has a role in maintaining nuclear membrane architecture in CMs (Heffler Julie et al., 2020), my results shed light on the function of Desmin in preventing CM extrusion and maintaining cardiac wall integrity. Furthermore, I report a previously uncharacterized function of Snai1 in regulating *desmin* expression. A recent study in zebrafish reported that Snai1b can potentially bind to the promoter of *desmin b* (Kayman Kürekçi et al., 2021). These results are supported by the luciferase assays that I performed in this study, as Snai1b appears to directly upregulate the expression of *desmin b in vitro*. As mentioned above, the transcriptional targets of Snai1 regulating cellular contractility are still unknown. Drosophila, which is devoid of IFs, is the primary model system in which Snai1 has been shown to regulate contractility, which precludes the possibility of identifying IFs being one of the downstream targets of Snai1. My study proposes one potential mechanism of Snai1 regulating cellular contractility through IFs, opening interesting new scenarios on how this transcription factor is involved in epithelial tissue homeostasis and integrity.

(Certain lines in this subsection have been quoted *verbatim* from Gentile et al., *eLife*, 2021; DOI:10.7554/eLife.66143 for the scientific accuracy of the terms).

5.1.4 Mechanical forces and heart morphogenesis

Cardiac contraction is essential in patterning the cardiac tissue. For example, it has been shown that blocking ventricular or atrial contraction leads to defects in intracardiac flow forces, CM morphology, and trabeculation networks (Auman et al., 2007; Chi et al., 2008; Peshkovsky et al., 2011; Staudt et al., 2014; Samsa et al., 2015; Rasouli et al., 2018). Similarly, heart contraction is important for valve formation (Bartman et al., 2004; Kalogirou et al., 2014). In order to promote heartbeat rhythmicity and

synchronicity, intercellular integrity is critical and is maintained by a cohesive cytoskeletal network (Sequeira et al., 2014). Here, I showed that Snai1 regulates the integrity of the zebrafish heart, suggesting that correct levels of Desmin are needed for maintaining cardiac wall integrity under contraction-induced mechanical pressure. Importantly, my results indicate that without Snai1 regulating the intracellular cytoskeletal network, heartbeat-induced mechanical forces can lead to an increase in cell extrusion. While it has been shown that an increase in cell contractility due to changes in morphology, adhesion, or cell density drives cell extrusion (Eisenhoffer et al., 2012; Levayer et al., 2016; Kocgozlu et al., 2016; Saw et al., 2017; Miroshnikova et al., 2018; Campinho et al., 2020; Priya et al., 2020), in my study I showed that external mechanical forces contribute to non-apoptotic CM extrusion during cardiac development and that actomyosin and IF cytoskeletal regulation is critical to prevent excessive CM extrusion. Although with lower frequency, the process of CM extrusion is observed also in the wild types, suggesting that a little number of extrusions are necessary for the turnover and homeostasis of the tissue. These data open new questions about how the cytoskeletal genes are regulated not only during development but also in pathological conditions.

In conclusion, my work uncovers molecular mechanisms that suppress cell extrusion in the tissue under constant mechanical pressure, and shows a context-dependent role for Snai1 in promoting EMT (Nieto et al., 2016), and also in maintaining tissue integrity during vertebrate organ development.

5.2 Nfatc1 regulates the establishment of valve interstitial cells

Cardiac valve function is fundamental for the well-being of the organism (Butcher and Markwald, 2007; Joziasse et al., 2008; Hinton and Yutzey, 2011; MacGrogan et al., 2014). A better understanding of the morphogenetic processes shaping the cardiac valves will help to determine the origins of heart valve disease. Although valve development has been extensively studied in chicks and mammals, these studies often rely on cell explants or fixed tissues, limiting studies of cell dynamics with single-cell resolution.

To circumvent these limitations, I used the zebrafish AV valve as a model system to uncover cellular and molecular mechanisms of valve development. Although several studies have focused on zebrafish valve development (Paul J. Scherz et al., 2008; Martin and Bartman, 2009; Steed et al., 2016b; Gunawan et al., 2019), none of them have shown how the formation and differentiation of VICs, the mesenchymal cells responsible for valve ECM secretion. Previous reports showed that VICs are generally the result of an EndoMT process where VECs undergo transcriptional changes to become mesenchymal (Shelton and Yutzey, 2008; Chakraborty et al., 2010; Luna-Zurita et al., 2010; Tao et al., 2011). Here, I showed for the first time that the establishment of zebrafish VICs occurs via Twist1b-mediated EndoMT that is regulated by the transcription factor Nfatc1.

5.2.1 VICs undergo EndoMT during zebrafish valvulogenesis

The vertebrate cardiac valves are composed of an outer layer of endocardial cells and an inner layer of fibroblast-like VICs (Kodigepalli et al., 2020). The formation of the mammalian and chick valves starts with an expansion of cardiac ECM that gives rise to cardiac cushions (O'Donnell and Yutzey, 2020), followed by EndoMT prior to the formation of the leaflets (Luna-Zurita et al., 2010). The expansion of the ECM in mammals and chick is responsible for the constriction of the AVC, potentially helping to reduce retrograde blood flow during embryonic developmental stages (Butcher and Markwald, 2007; Joziasse et al., 2008; Hinton and Yutzey, 2011; Tao et al., 2012; MacGrogan et al., 2014). In contrast, I found that zebrafish valve development starts with the collective migration of AV endocardial cells that form the valve leaflets. As shown by our group, this process is mediated by focal adhesions, implicating cell-ECM interactions in this collective migration (Gunawan et al., 2019). Here, I then observed that valve endocardial cells undergo complete EndoMT after invading the ECM between the valve leaflets, as evidenced by their loss of intercellular adhesion. Interestingly, the pre-valvular structure observed in zebrafish seems to be functional in reducing the retrograde blood flow in the early stages of valvulogenesis, resembling the mammalian ECM expansion. Moreover, it has also been shown that intracellular adhesion and communications are important for mammalian VIC formation (Bowen et al., 2015), similar to the collective behavior of zebrafish VICs. Altogether, these data suggest that

the cellular processes are similar between zebrafish and mammal valves, confirming zebrafish an excellent model to study valve formation.

5.2.2 Endocardial and NC cells contribute to zebrafish VIC population

In mouse, AV valve VICs mostly originate from ECs with a minor contribution from the epicardial cell, and OFT valve VICs originate from NCCs and ECs (Liu et al., 2018). Using lineage tracing experiments, I showed that the zebrafish AV valve has similar cellular origins. As expected, the majority of VICs appear to originate from endocardial cells. However, I observed that also NCCs contribute to this population. Although there is evidence that epicardial cells contribute to mammalian VICs (Wessels et al., 2012), I did not detect an obvious contribution to VICs from epicardial or myocardial cells. This could be a consequence of my experimental setup, as I performed the lineage tracing using tamoxifen induction in a narrow time window (from 72 and 120 hpf); thus I cannot exclude that these cell types contribute to the valve later in the development. Interestingly, it is known the VIC population is highly heterogeneous (Hinton et al., 2006; Horne et al., 2015), with different potential to undergo fibroblastic differentiation or respond to inflammatory conditions, both of which lead to pathological VIC conditions (Liu et al., 2007; Rutkovskiy et al., 2017). However, with the tools available it will be difficult to discriminate between the different functions of these different populations, without affecting the overall cardiac development. This opens interesting questions on the molecular mechanisms behind the non-endocardial cell contribution to VICs, which may be addressed better using zebrafish valve-specific tools.

5.2.3 ECM composition changes during zebrafish valvulogenesis

The ECM has a pivotal structural and signaling role during valve development (Rodgers et al., 2006; Steed et al., 2016b; Gunawan et al., 2019; Kodigepalli et al., 2020). One of the main components of the AV endocardial cushion is the glycosaminoglycan HA, which is present in both embryonic as well as adult zebrafish valves (Camenisch et al., 2000; Beis, 2005; Inai et al., 2013; Lagendijk et al., 2017; Bensimon-Brito et al., 2020). HA plays a crucial role, as it has been shown that both its loss and overproduction lead

to impairment of valve morphogenesis (Baldwin et al., 1994; Camenisch et al., 2000; Petz et al., 2019). Interestingly, I observed that the valve ECM composition changes according to the developmental stage. Indeed, I observed a pro-migratory ECM in the early stages during AV endocardial cell migration, as shown by the deposition of Fibronectin, and a more elastic ECM in the maturation stage with the presence of Elastin1, to give support and strength to the adult valve. However, in contrast to the mammalian valve (Rutkovskiy et al., 2017), no clear stratification was observed for the ECM components in the zebrafish valve (Schulz et al., 2019), which could be due to a lack of available tools for examining the right ECM molecules. On the other hand, I observed heterogeneity in the mature zebrafish VICs at the molecular level, as atrial-facing VICs express *Tg(vegfaa:*GFP) at higher levels compared to ventricular-facing VICs.

Many studies are now focusing on uncovering the exact composition of the endocardial cushion ECM (Silva et al., 2021), and this will help not only in having a better understanding of its structural role but also its signaling function. Indeed, the ECM acts as a reservoir of growth factors, cytokines, chemokines, proteases, and protease inhibitors. It will be interesting to identify the remodeler of the ECM and how they are regulated to shape the valve during development.

As mentioned, the VIC population, including the ECM that they secrete is very heterogeneous (Horne et al., 2015; Rutkovskiy et al., 2017). However, the cellular and molecular mechanisms leading to this heterogeneity are unknown, and it will be interesting to investigate whether these differences are due to the distinct origins of VICs or the molecular landscape within the cardiac valve leaflet.

5.2.4 Nfatc1 is regulating VIC establishment through the EMT transcription factor Twist1b

Valve development is regulated by different pathways, including Notch (Timmerman et al., 2004), TGFβ (Bensimon-Brito et al., 2019; Liebner et al., 2004; Paul J Scherz et al., 2008; Xiong et al., 2018), Klf2 (Goddard et al., 2017; Steed et al., 2016a; Vermot et al., 2009b) and Wnt (Goddard et al., 2017; Hurlstone et al., 2003). In particular, Notch

activation in the AV endocardium and BMP in the AV myocardium play an important role in restricting EndoMT of valve endocardial cells (Luna-Zurita et al., 2010; Papoutsi et al., 2018a). It has been shown that increased activation of Notch and BMP leads to an increased number of cells going to EndoMT, and impairment of valve leaflet morphology (Papoutsi et al., 2018a). In the mammalian valve, the expression of EMT transcription factors, such as Twist (Shelton and Yutzey, 2008; Chakraborty et al., 2010), Snai1 (Tao et al., 2011; Wu et al., 2011), and Yap (Zhang et al., 2014; Duchemin et al., 2019), increases during development. In line with these studies, I showed that the expression of the EndoMT transcription factor Twist1b is enriched in the AVC, and regulated by Nfatc1. Interestingly, I observed that *nfatc1* expression in the AV canal marks the VIC precursors in the linear zebrafish heart tube (34 hpf), an earlier time point than previously shown by other studies (Beis, 2005; Donat et al., 2018; Gunawan et al., 2019; Pestel et al., 2016; Paul J Scherz et al., 2008; Steed et al., 2016a). Little is known about the spatial patterning of the endocardium, with only one study showing that activation of Bmp2 and Notch can specify ventricular ECs into mesenchymal AV ECs (Papoutsi et al., 2018b). Valve morphogenesis is promoted by fluid flow-induced mechanical stress (Paolini and Abdelilah-Seyfried, 2018; Duchemin et al., 2019). More studies need to be conducted to understand if the specification of the AV endocardial cells is dependent on mechanosensitive pathways. Additionally, I showed that in a zebrafish loss-of-function model of *nfatc1* the recruitment of VICs precursors is reduced, VIC formation and valve elongation is defective. It has been proposed that murine NFATc1 becomes downregulated in cushion mesenchymal cells and inhibits EndoMT (Wu et al., 2011), but it is required to promote the proliferation of these mesenchymal cells (Combs and Yutzey, 2009a; Wu et al., 2011) as shown for the zebrafish Nfatc1. It remains unclear how these misregulated cellular events lead to defective valves. In addition, it remains to be determined whether NFATc1 is completely dispensable in the mouse VIC precursors and whether NFATc1 regulates the same target genes, including *twist1*, in different organisms. The fine-tuning of EndoMT is very important because, even when the valves seem morphologically normal, they may have functional defects, which will have a great impact on cardiac function. Importantly, I provide clear evidence that loss of VICs correlates to cardiac

valve dysfunction and retrograde blood flow as I observed in *nfatc1* loss-of-function. This reduction of VICs is associated with reduced contact length between the superior and the inferior leaflets, suggesting that VICs provide the necessary structural support to the cardiac valve leaflets. Thus, this study provides a framework to use zebrafish as a model for VIC development and function at the cellular and molecular levels.

(Certain lines in this subsection have been quoted *verbatim* from Gunawan*, Gentile* et al., *Circ Res* 2020; DOI: 10.1161/CIRCRESAHA.119.315992 for the scientific accuracy of the terms).

6. Conclusions

With this PhD work, I uncovered cellular and molecular mechanisms of two of the main morphogenetic events during the zebrafish cardiac development. In particular, I focused on how the tissue integrity of a beating organ as the heart is maintained (aim 1) and how a simple structure as the embryonic valve develops into a multilayered and functional mature valve (aim 2).

The conclusions for each aim are the following:

Aim 1: Role of Snai1 in maintaining zebrafish cardiac wall integrity

Using genetic, transcriptomic, and chimeric analyses, I identified that the transcription factor Snai1b is required in CMs for myocardial wall integrity. First, I showed that *snai1b* is expressed in CMs during the later stages of cardiac development. Then, I generated a loss-of-function of *snai1b* and observed that it leads to CM extrusion away from the cardiac lumen, remaining in the pericardial cavity for several hours. Additionally, I found that extruding CMs exhibit increased actomyosin contractility at their basal domain, as I observed the enrichment of canonical actomyosin markers, such as phosphorylated myosin and a-catenin. At the molecular level, I identified the dysregulation of cytoskeletal genes in the mutant heart transcriptome compared with the wild-type heart transcriptome. Interestingly, the muscle cell-specific IF gene *desmin b* was upregulated. To understand if the upregulation of *desmin b* was causing the CM extrusions, I confirmed my hypothesis by performing cardiomyocyte-specific *desmin b* overexpression. I observed that *desmin b* extruding CMs exhibited increased cellular contractility, recapitulating the *snai1b* mutant phenotype. Taken together, my data suggest that Snai1 maintains cardiac wall integrity by regulating the expression levels of the IF gene *desmin b*.

Aim 2: The establishment of zebrafish valve interstitial cells (VICs)
Using high-resolution imaging and genetic analyses, I uncovered cellular and molecular mechanisms of VICs establishment.

I observed that valve endocardial cells (VECs) collectively migrate into the cardiac jelly and form a two-layer structure. Then, VECs invade the extracellular matrix (ECM) between these two layers, undergoing endothelial-to-mesenchymal transition and becoming VICs. During this morphogenetic process, I observed that the cells lose their adhesions, and the ECM surrounding VICs changes from a pro-migratory to an elastic environment. In addition, I found that two peaks of proliferation drive the expansion of the VIC population. Interestingly, I observed that these cells are mostly derived from endocardial cells, with a small contribution from neural crest cells. Taking advantage of the photoconvertible protein Kaede, I showed that the first cells that express *nfatc1* are the first to become VICs, hypothesizing that it has an important role during VIC development. Indeed, loss-of-function of *nfatc1* exhibited significantly fewer VICs. I observed a reduction in VIC proliferation and impairment of recruitment of endocardial and neural crest cells in the *nfatc1* mutants compared with wild types. Importantly, I identified the downregulation of expression of the EMT-regulator *twist1b*. Altogether, these data suggest that Nfatc1 regulates VIC establishment through *twist1b*.

In conclusion, my work: 1) identified an unsuspected role of Snai1 in maintaining the integrity of the myocardial epithelium, opening new avenues for the study of its role in regulating cell contractility; 2) uncovered the function of Nfatc1 through Twist1b in the establishment of the VIC population, establishing a new model to study valve development and function.

7. Summaries

7.1 Zusammenfassung

Einblick in die zellulären und molekularen Mechanismen der Integrität der Kardiomyozyten des Zebrabärblings und der Differenzierung der interstitiellen Klappenzellen

Das Herz ist das erste funktionsfähige Organ, das sich im Embryo entwickelt (Harvey, 2002; Keegan et al., 2004; Ivanovitch et al., 2021). Es durchläuft mehrere morphogenetische Prozesse, bei denen verschiedene Zelltypen untereinander und mit der sie umgebenden extrazellulären Matrix interagieren. Dabei reagieren sie auf intrinsische und extrinsische mechanische Kräfte und nehmen dadurch unterschiedliche Verhaltensweisen an (Moorman und Christoffels, 2003; Simões-Costa et al., 2005; Olson, 2006; Grosskurth et al., 2008). Darüber hinaus steuern konservierte Transkriptionsfaktorkaskaden die Entwicklung des Herzens (Srivastava und Olson, 2000; Bruneau, 2002; Olson, 2006).

Im Wirbeltier beginnt die Entwicklung dieses Organs am Ende der Gastrulation, wenn die Vorläuferzellen vom Seitenplattenmesoderm in Richtung Mittellinie wandern (Harvey, 2002; Pérez-Pomares et al., 2009). In diesem Stadium ist das Herz eine primitive Struktur, ähnlich wie das schlauchförmige Herz der einfachen Chordaten (Harvey, 2002; Bishopric, 2005). Die wichtigsten Zelltypen, aus denen sich der Herzschlauch zusammensetzt, sind die Kardiomyozyten (CM), die kontraktilen Einheiten und Bestandteile der Herzwand, und die Endokardzellen (EC), die in der inneren Schicht des Herzens organisiert sind (Schleich et al., 2013; Brown et al., 2016). Mehrere morphogenetische Prozesse sind dann erforderlich, um den Herzschlauch in ein leistungsfähiges Pumporgan mit Kammern und Klappen zu verwandeln. Verschiedene zelluläre Mechanismen wie Aktomyosin-Dynamik, kollektive Zellmigration, epitheliale-mesenchymale Transition (EMT) und Proliferation regulieren die Integrität und Morphogenese des Gewebes.

Um einen besseren Einblick in das Zellverhalten während der Herzentwicklung zu bekommen, bedarf es eines Modellsystems, das die Untersuchung *in vivo* und mit Einzelzellauflösung ermöglicht. Das Zweikammerherz des Zebrabärblings bietet dank

des gemeinsamen evolutionären Ursprungs der vertebraten Herzstrukturen und der konservierten molekularen Regulatoren viele Vorteile für die Untersuchung des Zellverhaltens während der kardialen Morphogenese. Erstens entwickelt sich das Herz des Zebrabärblings relativ schnell und ist sehr gut für genetische Manipulationen geeignet, was die Untersuchung früher Entwicklungsstadien ermöglicht. Zweitens ist er transparent, sodass die Herzmorphogenese auf der Ebene einzelner Zellen und unter physiologischen Bedingungen untersucht werden kann Fishman und Stainier, 1994; Bakkers, 2011; Staudt und Stainier, 2012; Brown et al., 2016). Anhand des Zebrabärblingherzens als Modellsystem habe ich das Zellverhalten hinter zwei der wichtigsten morphogenetischen Ereignisse der Herzenentwicklung aufgedeckt: die Reifung der Herzwände und die Bildung der Herzklappen.

Der EMT-Transkriptionsfaktor Snai1 erhält die Integrität der Zebrabärbling-Herzwand durch die Regulierung von Genen für Intermediärfilamente aufrecht

Im ersten Teil dieser Studie habe ich untersucht, wie die Herzwand auf molekularer Ebene aufrechterhalten wird. Der Transkriptionsfaktor Snai1 ist ein bekannter Regulator der EMT (Nieto, 2002; Nieto et al., 2016) und wurde mit der Regulierung des Zytoskelettumbaus und der epithelialen Integrität in Verbindung gebracht (Martin et al., 2010; Mason et al., 2013; Weng und Wieschaus, 2016). Während der Herzentwicklung hat sich gezeigt, dass *snai1* an der Migration der Herzvorläufer und der Herzklappenentwicklung in einer EMT-abhängigen Weise beteiligt ist (Tao et al., 2011; Qiao et al., 2014). Einer der beiden Zebrabärbling-Paraloge, s*nai1b,* wird in den frühen Entwicklungsstadien exprimiert, und es wurde gezeigt, dass die Ausschaltung von s*nai1b* zu Defekten bei der Herzklappenbildung führt (Qiao et al., 2014). Über die Rolle von s*nai1b* in späteren Entwicklungsstadien ist jedoch wenig bekannt.

Um die mögliche Rolle von s*nai1b* während der späten kardialen Morphogenese zu untersuchen, habe ich sein Expressionsmuster beobachtet und festgestellt, dass seine Expression im Herzen bis 96 Stunden nach der Befruchtung (hpf) anhält. Darüber hinaus habe ich eine Mutation erzeugt, bei der 1206 bp in der Promotorregion deletiert wurden, um eine potenzielle Transkriptionsanpassung durch seinen Paralog *snai1a* zu umgehen. Interessanterweise rekapitulieren die *snai1b*-Mutanten die kardialen

Morphologiedefekte, die zuvor bei den *snai1b*-Morphanten berichtet wurden. Entgegen den Erwartungen habe ich einen Phänotyp identifiziert, der zu einer Beeinträchtigung der Integrität der Herzwand führt: Kardiomyozyten in *snai1b*-Mutanten extrudieren aus dem Herzlumen. Der Extrusionsphänotyp tritt bei den Mutanten im Vergleich zu den Wildtyp-Embryonen bereits ab 48 hpf häufiger auf und bleibt während der gesamten Entwicklung bestehen. Interessanterweise wurden der Extrusionsphänotyp vorallem am Atrioventrikularkanal (AVC) beobachtet, der Region mit dem stärksten Grad an mechanischen Kräften durch den Blutfluss. Mit Hilfe von Zeitrafferexperimenten über einen Zeitraum von mehr als 18 Stunden konnte ich beobachten, dass sich die mutierten Kardiomyozyten vollständig von der Herzwand lösen und mehrere Stunden lang in der Perikardhöhle verbleiben.

Die Extrusion der Kardiomyozyten führt zu Defekten sowohl auf zellulärer Ebene, mit defekter Kardiomyozyt-Morphologie, als auch auf Gewebeebene, mit reduziertem Ventrikelvolumen und reduziertem trabekulärem Netzwerk. Bei 48 hpf konnte ich keine physiologischen Defekte beobachten, aber ab 72 hpf zeigten die mutierten Herzen eine reduzierte Kontraktionsrate, ventrikuläre Auswurffraktion und fraktionelle Verkürzung.

Da die durch die Herzkontraktilität induzierten mechanischen Kräfte die Integrität der Herzmuskelwand beeinflussen (Fukuda et al., 2017; Rasouli et al., 2018; Fukuda et al., 2019), stellte ich die Hypothese auf, dass die Aufhebung der Herzkontraktilität die extrudierenden Kardiomyozyten reduzieren könnte. Um diese Hypothese zu verifizieren, habe ich das Morpholino *tnnt2a* (Sehnert et al., 2002) in die mutierten Embryonen injiziert und sie mit Wildtyp-Herzen verglichen. Wie vermutet, verringerte sich die Anzahl der Kardiomyozyten durch die Reduktion des mechanischen Stresses, der durch die Herzkontraktilität verursacht wird. Um zu überprüfen, ob die Kardiomyozyten-Extrusion von einer zellautonomen Funktion von *snai1b* abhängt, habe ich Transplantationsexperimente durchgeführt und beobachtet, dass die in Wildtyp-Herzen transplantierten mutierten Kardiomyozyten im Vergleich zu den in Mutantenherzen transplantierten wildtypische Kardiomyozyten eher zur Extrusion neigen. Diese Ergebnisse deuten darauf hin, dass *snai1b* auf zellautonome Weise für die Aufrechterhaltung der Integrität der Herzwand verantwortlich ist.

Der Extrusionsprozess kann ein aktiver Prozess sein, der von der Aktomyosin-Maschinerie angetrieben wird, oder ein passiver Prozess, der hauptsächlich auf die Beseitigung einer toten Zelle zurückzuführen ist (Rosenblatt et al., 2001, 2001; Eisenhoffer et al., 2012; Kocgozlu et al., 2016; Wee et al., 2020). Meine Daten zeigen, dass mutierte extrudierende Kardiomyozyten keine apoptotischen Zellen sind, sondern stattdessen eine erhöhte zelluläre Kontraktilität aufzuweisen scheinen. Um die zelluläre Kontraktilität zu untersuchen, habe ich Immunfärbungen für kanonische Marker der Aktomyosinspannung durchgeführt, darunter phosphoryliertes Myosin und das α-Catenin-Epitop α-18 (Yonemura et al., 2010), und ihre Anreicherung in den basalen Domänen der extrudierenden Kardiomyozyten beobachtet. Darüber hinaus zeigen extrudierende Kardiomyozyten gestörte intrazelluläre Verbindungen, wie die N-Cadherin-Färbung zeigt, was auf eine Schwächung der Zell-Zell-Adhäsion hindeutet.
Um die molekularen Mechanismen hinter der Snai1b-vermittelten Regulierung der Integrität der Herzwand besser zu verstehen, habe ich eine Transkriptomanalyse durchgeführt, um mutierte und wildtypische Herzen zu vergleichen. Ich beobachtete die Dysregulation von Zytoskelett-Genen, einschließlich der Hochregulierung eines Gens der Intermediärfilamente, *desmin b*. Wie die Immunfärbung zeigte, ist die Lokalisierung von Desmin in den mutierten extrudierenden Kardiomyozyten in der basalen Domäne angereichert, ähnlich wie bei Markern der Aktomyosin-Kontraktilität. Um zu testen, ob die erhöhte Konzentration von Desmin zur Extrusion der Kardiomyozyten führen könnte, habe ich eine Kardiomyozyt-spezifische Überexpression von *desmin b* durchgeführt und eine erhöhte Anzahl von extrudierenden Kardiomyozyten beobachtet, die den Phänotyp der *snai1b*-Mutante rekapitulieren. Ähnlich wie bei den *snai1b*-Mutanten zeigen Kardiomyozyten, die *desmin b* überexprimieren, eine Anreicherung des α-Catenin-Epitops α-1 und p-Myosin an der basalen Domäne. Insgesamt deuten diese Daten darauf hin, dass Snai1 die Integrität der Herzwand zum Teil dadurch aufrechterhält, dass es die Expression des Intermediärfilament-Gens *desmin b* unterdrückt.

Nfatc1 reguliert den EMT-Transkriptionsfaktor Twist1b während der Entwicklung der Herzklappen

Im zweiten Teil dieser Studie habe ich mich auf das Verhalten von Klappenzellen während der Herzklappenentwicklung konzentriert. Interstitielle Klappenzellen (VICs) sind wichtig für die Struktur und Funktion der Klappen, da sie spezielle ECM absondern, die den Klappen biomechanische Festigkeit verleiht Hinton et al., 2006; Butcher und Markwald, 2007; Joziasse et al., 2008; MacGrogan et al., 2014; O'Donnell und Yutzey, 2020). Obwohl die Herzklappenentwicklung im Huhn und im Säugetier ausgiebig untersucht wurde, beruhen diese Studien oft auf Zellexplantaten oder fixiertem Gewebe, was eine Auflösung der Zelldynamik erschwert. Darüber hinaus hat sich noch keine Studie mit den Folgen des Verlusts interstitieller Klappenzellen für die Herzklappenfunktion befasst. Um diese Einschränkungen zu umgehen, habe ich den Zebrabärbling als Modellsystem verwendet, um die zellulären und molekularen Mechanismen der Herzklappenentwicklung aufzudecken.

Vor meiner Studie war nur wenig über die Ansiedlung der interstitiellen Klappenzellen, die während der späteren Herzentwicklung stattfindet, und die Bildung einer komplexen Klappe im erwachsenen Organismus bekannt. Um mehr Einblicke in diesen Prozess zu gewinnen, habe ich transgene Linien verwendet, die Klappenendokardzellen (VECs) markieren. Nach der kollektiven Migration der Klappenendokardzellen habe ich beobachtet, dass die Zellen, die die Migration anführen, in die ECM zwischen der endokardialen Schicht eindringen und sich zu interstitiellen Klappenzellen entwickeln, eine Phase, das ich als Invasionsphase der interstitiellen Klappenzellen bezeichne. Sobald die ersten interstitiellen Klappenzellen im interstitiellen Raum eindringen, erscheinen die Klappen voll funktionsfähig, verschließen das Lumen und verhindern somit den retrograden Blutfluss. Ich habe beobachtet, dass die interstitiellen Klappenzellen nach der kollektiven Zellmigration ihre endothelialen Marker herunterregulieren, ihre Zellverbindungen verlieren und schließlich den mesenchymalen Marker Vimentin exprimieren, was darauf hindeutet, dass die interstitiellen Klappenzellen eine vollständige endokardiale-mesenchymale Transition (EndoMT) durchlaufen.

Die Herzklappenentwicklung setzt sich mit der Verlängerung des Klappenflügels und der Proliferation und Expansion von Klappenendokardzellen und interstitiellen Klappenzellen fort (Elongationsphase). Das Wachstum der interstitiellen

Klappenzellen wird durch zwei große Proliferationsschübe bestimmt. Im Laufe der Entwicklung der Herzklappe habe ich gezeigt, dass die ECM die interstitiellen Klappenzellen eindeutig umgibt und dass die ECM im Laufe der Entwicklung ihre Zusammensetzung von pro-migratorischen Proteinen (z.B. Fibronectin) zu matrisomischen Proteinen mit elastischen Eigenschaften (z.B. Elastin) ändert.

In der Säugetierklappe stellen die interstitiellen Klappenzellen eine heterogene Zellpopulation dar, die sich aus Zellen unterschiedlicher Herkunft zusammensetzt (Hinton et al., 2006; Horne et al., 2015). Wie erwartet, tragen die endokardialen Zellen am meisten zu den interstitiellen Klappenzellen des Zebrabärblings bei, aber es wurde auch beobachtet, dass die Zellen der Neuralleiste einen kleinen Beitrag leisten. Durch Zellverfolgung per Photokonversion des fluoreszierenden Kaede-Proteins in atrioventrikulären Endothelzellen vor der Migrationsphase konnte ich zeigen, dass die ersten Klappenendokardzellen, die *nfatc1* exprimieren, dazu bestimmt sind, interstitielle Klappenzellen zu werden, was auf eine frühzeitige Musterbildung und Spezifikation des Endokards hindeutet. Da bekannt ist, dass die Bildung von Klappen bei Säugetieren den Transkriptionsfaktor NFATC1 erfordert (Combs und Yutzey, 2009b; Wu et al., 2011), stelle ich die Hypothese auf, dass Nfatc1 die Bildung von interstitiellen Klappenzellen bei Zebrabärblingen reguliert. Um diese Hypothese zu verifizieren, habe ich eine Funktionsverlustmutation von *nfatc1* generiert, der die DNA-Bindungsdomäne anvisiert. Diese Mutanten wiesen nach 72 hpf ein Perikardödem und eine gestörte Durchblutung auf, was auf eine Beeinträchtigung der Klappenstruktur und einen ineffizienten Verschluss der Klappen zurückzuführen war. Obwohl die Anzahl der Klappenendokardzellen unverändert blieb und die Migrations- und Elongationsstadien nicht beeinflusst wurden, waren die interstitiellen Klappenzellen in den *nfatc1*-Mutanten reduziert oder fehlten ganz. Die Verringerung der interstitiellen Klappenzellen wurde durch eine geringere Proliferation und einen geringeren Beitrag der frühen Klappenendokardzellen und der Zellen der Neuralleiste zu dieser Zellpopulation verursacht. Meine Ergebnisse zeigen also, dass die interstitiellen Klappenzellen eine grundlegende Rolle bei der Förderung der Herzklappenfunktion spielen, um den retrograden Blutfluss zu verhindern. Insgesamt deuten diese Daten darauf hin, dass der Verlust von Nfatc1 zu einer Verringerung der Rekrutierung und

Proliferation von Vorläuferzellen von interstitiellen Klappenzellen, zu Defekten bei der Ansiedlung derselben und zu einer Desorganisation der ECM und damit zu einer Fehlfunktion der Herzklappe führt.

Meine Ergebnisse zeigen, dass die Entwicklung der interstitiellen Klappenzellen im Zebrabärbling ein EMT-gesteuerter Prozess ist. Aus diesem Grund, habe ich die genetischen und funktionellen Interaktionen zwischen Nfact1 und EMT-Transkriptionsfaktoren, die in der AVC angereichert sind, analysiert. Durch In-silico-Analyse konnte ich mehrere NFAT-Bindungsstellen in der Promotorregion des EMT-fördernden Gens *twist1b* identifizieren. Durch In-situ-Hybridisierung und qPCR-Analyse konnte ich feststellen, dass *twist1b* in den Herzen der *nfatc1*-Mutanten im Vergleich zu den Wildtypen herunterreguliert ist, was darauf hindeutet, dass Nfatc1 die Expression von *twist1b* reguliert. Um einen besseren Einblick in die Rolle von Twist1b während der Herzklappenentwicklung zu bekommen, habe ich eine dominant negative Form von *twist1b* speziell in Herzklappenzellen überexprimiert und eine Funktionsverlustallel von *twist1b* erzeugt. Bemerkenswerterweise wurden in den Klappenflügel, die dominant-negativen Twist1b überexprimierende Zellen enthielten, keine interstitiellen Klappenzellen mehr beobachtet. Obwohl der Funktionsverlust von *twist1b* keine schwerwiegenden Phänotypen in der Klappe aufwies, was möglicherweise auf eine funktionelle Kompensation durch andere EMT-fördernde Faktoren zurückzuführen ist. Ich konnte einen erhöhten Anteil von Tieren mit retrogradem Blutfluss in Kombination mit heterozygoten nfatc1-Allelen beobachten. Diese Daten deuten darauf hin, dass Twist1b stromabwärts von Nfatc1 wirkt, um die Klappenbildung und -funktion zu fördern.

Schlussfolgerungen

Zusammenfassend lässt sich sagen, dass meine Arbeit (1) eine unerwartete Rolle von Snai1 bei der Aufrechterhaltung der Integrität des Herzmuskelepithels aufgedeckt und damit neue Perspektiven für eine Rolle dieses Transkriptionsfaktors bei der Regulierung der zellulären Kontraktilität und der Aufrechterhaltung der Integrität des Epithelgewebes eröffnet hat, sowie (2) zum ersten Mal die Beteiligung von Nfatc1 an der Bildung interstitieller Klappenzellen durch Regulierung des EMT-fördernden Faktors Twist1b bei Zebrabärblingen beschreibt.

7.2 English summary

Understanding cellular and molecular mechanisms of zebrafish cardiomyocytes integrity and valve interstitial cells differentiation

The heart is the first functional organ that develops in the embryo (Harvey, 2002; Keegan et al., 2004; Ivanovitch et al., 2021). To become a functional organ, it undergoes several morphogenetic processes that involve different cell types interacting with each other and responding to the surrounding extracellular matrix, as well as intrinsic and extrinsic mechanical forces, assuming different behaviors (Moorman and Christoffels, 2003; Simões-Costa et al., 2005; Olson, 2006; Grosskurth et al., 2008). Additionally, transcription factor networks, some of which are conserved among vertebrates, control the development (Srivastava and Olson, 2000; Bruneau, 2002; Olson, 2006).

Vertebrate cardiac development starts at the end of gastrulation when the progenitor cells migrate from the lateral plate mesoderm towards the midline (Harvey, 2002; Pérez-Pomares et al., 2009). At this stage, the heart is a primitive structure, similar to the tubular heart of the simple chordates (Harvey, 2002; Bishopric, 2005). The main cell types that composed the heart tube are cardiomyocytes (CMs), the contractile units and constituents of the cardiac wall, and endocardial cells (ECs), organized in the inner layer of the heart (Schleich et al., 2013; Brown et al., 2016). Several morphogenetic processes are then required to transform the heart tube into a powerful pumping organ, with chambers and valves. Different cellular mechanisms, such as actomyosin dynamics, collective cell migration, epithelial-to-mesenchymal transition (EMT), and proliferation regulate tissue integrity and morphogenesis.

In order to have a better understanding of cell behavior during cardiac development, it is necessary to find a model system that allows the investigation in vivo and at single-cell resolution. Thanks to the common evolutionary origin of the different cardiac structures, together with conserved molecular regulators, the two-chambered zebrafish heart offers many advantages to study cell behavior during cardiac morphogenesis. First, zebrafish develops externally at a relatively fast rate and is highly amenable to genetic manipulations, which make studying early developmental stages possible. Second, it is transparent, which allows us to study heart morphogenesis at a single-cell level and under physiological conditions (Fishman and Stainier, 1994;

Bakkers, 2011; Staudt and Stainier, 2012; Brown et al., 2016). Here, using the zebrafish heart as a model system, I uncovered the cell behavior behind two of the main cardiac morphogenetic events: cardiac wall maturation and cardiac valve formation.

The EMT transcription factor Snai1 maintains the zebrafish cardiac wall integrity by regulating intermediate filament genes

In the first part of this study, I investigated how the cardiac wall is maintained at the molecular level. The transcription factor Snai1 is a well-known regulator of the EMT (Nieto, 2002; Nieto et al., 2016), and has been implicated in the regulation of cytoskeletal remodeling and epithelial integrity (Martin et al., 2010; Mason et al., 2013; Weng and Wieschaus, 2016). During cardiac development, it has been shown that Snai1 is involved in myocardial precursors migration and valve development in an EMT-dependent manner (Tao et al., 2011; Qiao et al., 2014). Snai1b, one of the two zebrafish paralogues, is expressed at the early stages of development, and it has been shown that *snai1b* knockdown leads to cardiac looping defects (Qiao et al., 2014). However, little is known about the role of Snai1b during later stages of development.

To investigate the potential role of Snai1b during late cardiac morphogenesis, I observed its expression pattern and noted that its expression persists in the heart until 96 hours post fertilization (hpf). I further generated a mutational allele, deleting 1206 bp in the promoter region that circumvents potential transcriptional adaptation by its paralogue *snai1a*, and the *snai1b* mutants interestingly recapitulate the cardiac morphology defects previously reported in the *snai1b* morphants. Contrary to expectations, I identified a phenotype that leads to impairment of the cardiac wall integrity: CMs in *snai1b* mutants extrude away from the cardiac lumen. The extrusion phenotype is observed in high frequency in the mutants when compared with the wild-type embryos as early as 48 hpf and persists throughout the development. Interestingly, they were observed with higher frequency at the atrioventricular canal (AVC), the region with the strongest degree of mechanical forces from blood flow and AVC constriction. Using a time-lapse experiment for a period of over 18 hours, I observed that mutant CMs completely detach from the cardiac wall and remain in the pericardial cavity for several hours.

The extrusion of CMs leads to defects at both cellular level, with defective CM morphology, and tissue level, with reduced ventricular volume and reduced trabecular network. I did not observe any physiological defects at 48 hpf but starting from 72 hpf mutant hearts exhibited reduced contraction rate, ventricular ejection fraction, and fractional shorting.

Since the mechanical forces induced by heart contractility influence the myocardial wall integrity (Fukuda et al., 2017; Rasouli et al., 2018; Fukuda et al., 2019), I hypothesize that abolishing cardiac contractility may affect the extruding CMs. To test this hypothesis, I injected the *tnnt2a* morpholino (Sehnert et al., 2002) into the mutant embryos and compared them with wild-type hearts. As hypothesized, reducing the mechanical stress brought on by cardiac contractility decreased the number of CM extrusions. In order to verify if the CM extrusion was depending on a cell-autonomous function of Snai1b, I performed transplant experiments and I observed that the mutant CMs transplanted into wild-type hearts are more prone to extrude compared with wild-type CMs transplanted into mutant hearts. These results suggest that Snai1b is acting in a cell-autonomous manner to maintain cardiac wall integrity.

The extrusion process can be an active process, driven by the actomyosin machinery, or a passive process, mainly due to the elimination of a dead cell (Rosenblatt et al., 2001, 2001; Eisenhoffer et al., 2012; Kocgozlu et al., 2016; Wee et al., 2020). My data show that mutant extruding CMs are not apoptotic cells, but instead, appear to exhibit increased cellular contractility. To examine cellular contractility, I performed immunostaining for canonical markers of actomyosin tension, including phosphorylated myosin and the α-catenin epitope α-18 (Yonemura et al., 2010), and observed their enrichment at the basal domains of extruding CMs. Moreover, extruding CMs display disrupted intracellular junctions, as revealed by N-cadherin staining, suggesting weakening cell-cell adhesion.

To better understand the molecular mechanisms behind Snai1b-mediated regulation of cardiac wall integrity, I performed transcriptomic analysis to compare mutant and wild-type hearts. I observed the dysregulation of cytoskeletal genes, including the upregulation of an intermediate filament (IF) gene *desmin b*. As revealed by immunostaining, the localization of Desmin in the mutant extruding CMs is enriched in

the basal domain, similar to markers of actomyosin contractility. To test if the increased level of Desmin could lead to extrusion of the CMs, I performed CM-specific overexpression of *desmin b* and observed an increased number of extruding CMs, recapitulating *snai1b* mutant phenotype. Similar to *snai1b* mutants, *desmin b* overexpressing CMs exhibit enrichment at the basal domain of α-catenin epitope α-1 and p-myosin. Altogether, these data suggest that Snai1 maintains the cardiac wall integrity partly by repressing the expression of the IF gene *desmin b*.

The EMT transcription factor Twist1b is regulated by Nfatc1 during valve interstitial cells establishment

In the second part of this study, I focused on the behavior of valve cells during cardiac development. Valve interstitial cells (VICs) are important for the structure and function of the valves, as they secrete specialized ECM that confers biomechanical strength to the valves (Hinton et al., 2006; Butcher and Markwald, 2007; Joziasse et al., 2008; MacGrogan et al., 2014; O'Donnell and Yutzey, 2020). Although valve development has been extensively studied in chicks and mammals, these studies often rely on cell explants or fixed tissues, making it difficult to have the resolution of the cell dynamics. In addition, no study has addressed the consequence of loss of VICs for cardiac valve function. To circumvent these limitations, I used the zebrafish as a model system to uncover cellular and molecular mechanisms of valve development.

Prior to my study, little is known about the establishment of the VICs, which occurred during later cardiac development, and the formation of a complex valve in adult organisms. To gain more insights into this process, I used transgenic lines that label valve endocardial cells (VECs). After collective VECs migration, I observed that the cells leading the migration invade the ECM between the endocardial layer to become VICs, a stage I refer to as the VIC invasion stage. As soon as the first VICs appear in the interstitial space, the valves appear fully functional, closing the lumen and preventing retrograde blood flow. I observed that post collective cell migration, VICs downregulate their endothelial markers, lose their adhesions, and eventually express the mesenchymal marker Vimentin, indicating that VICs undergo a complete endocardial-to-mesenchymal transition (EndoMT).

The development of the valve continues with the elongation of the valve leaflet and the proliferation and expansion of VECs and VICs (elongation stage). Two major peaks of proliferation contribute to VIC population growth. As the development of the valve proceeds, I showed that the ECM clearly surrounds the VICs, and the ECM changes its composition from pro-migratory proteins (e.g. Fibronectin) to matrisome proteins with elastic properties (e.g. Elastin) throughout development.

In the mammalian valve, VICs constitute a heterogeneous cell population, composed of cells with different origins (Hinton et al., 2006; Horne et al., 2015). As expected, the endocardial cells are the major contributors to the zebrafish VIC population, but also observed a minor contribution from neural crest cells. Kaede photoconversion tracing of AV ECs prior to the migration phase reveals that the first valve endocardial cells that express *nfatc1* are the ones fated to become VICs, suggesting an early patterning and specification of the endocardium. As it is known that mammalian valve formation requires the transcription factor NFATC1 (Combs and Yutzey, 2009b; Wu et al., 2011), I hypothesize that Nfatc1 regulates zebrafish VICs formation. To test this hypothesis, I generated a loss-of-function of *nfatc1*, targeting the DNA binding domain. These mutants exhibited pericardial edema and impaired circulation at 72 hpf, which were caused by impairment of the valve structure as well as inefficient closure of the valves. Although the number of VECs was unchanged and the migration and elongation stages were unaffected, VICs were reduced or absent in *nfatc1* mutants. The reduction of VICs was caused by a reduced proliferation of and contribution from early VECs and neural crest cells to the VIC population. Thus, my results show that VICs have a fundamental role in promoting cardiac valve function to prevent retrograde blood flow. Altogether, these data suggest that loss of Nfatc1 exhibits a reduction of VIC precursor recruitment and proliferation, defects in VIC establishment, and ECM disorganization, leading to dysfunctional cardiac valve.

Furthermore, as my results show an EMT-driven process during VIC establishment in the zebrafish valve, I analyzed genetic and functional interactions between Nfact1 and EMT transcription factors enriched in the AVC. Through *in silico* analysis, I identified several NFAT binding sites in the promoter region of the EMT-promoting gene *twist1b*. By *in situ* hybridization and qPCR analysis, I observed that *twist1b* was downregulated

in the *nfatc1* mutant hearts compared with wild types, suggesting that Nfatc1 upregulates *twist1b* expression. To better understand the role of Twist1b during valve development, I overexpressed a dominant negative form of Twist1b specifically in valve cells and generated a loss-of-function mutational allele of *twist1b*. Strikingly, no VICs were ever observed in the valve leaflets with dominant-negative Twist1b overexpressing cells. Although *twist1b* loss-of-function did not exhibit severe phenotypes in the valve, potentially due to functional compensation by other EMT-promoting factors. I observed an increased proportion of animals with retrograde blood flow in combination with heterozygous *nfatc1* alleles. These data suggest the Twist1b functions downstream of Nfatc1 to promote valve formation and function.

Conclusions

In conclusion, my work: 1) identified an unsuspected role of Snai1 in maintaining the integrity of the myocardial epithelium, opening new avenues in its role in regulating cellular contractility and maintaining epithelial tissue integrity; 2) uncovered for the first time that Nfatc1 is involved in zebrafish VIC establishment, by regulating the EMT-promoting factor *twist1b*.

8. Bibliography

Asakawa K, Suster ML, Mizusawa K, Nagayoshi S, Kotani T, Urasaki A, Kishimoto Y, Hibi M, Kawakami K. 2008. Genetic dissection of neural circuits by Tol2 transposon-mediated Gal4 gene and enhancer trapping in zebrafish. *Proceedings of the National Academy of Sciences*. doi:10.1073/pnas.0704963105

Auman HJ, Coleman H, Riley HE, Olale F, Tsai H-J, Yelon D. 2007. Functional Modulation of Cardiac Form through Regionally Confined Cell Shape Changes. *PLOS Biology* **5**:e53. doi:10.1371/journal.pbio.0050053

Bagatto B, Francl J, Liu B, Liu Q. 2006. Cadherin2 (N-cadherin) plays an essential role in zebrafish cardiovascular development. *BMC Developmental Biology* **6**:23. doi:10.1186/1471-213X-6-23

Bakkers J. 2011. Zebrafish as a model to study cardiac development and human cardiac disease. *Cardiovasc Res* **91**:279–288. doi:10.1093/cvr/cvr098

Baldwin HS, Lloyd TR, Solursh M. 1994. Hyaluronate degradation affects ventricular function of the early postlooped embryonic rat heart in situ. *Circulation Research* **74**:244–252. doi:10.1161/01.RES.74.2.244

Bartman T, Walsh EC, Wen K-K, McKane M, Ren J, Alexander J, Rubenstein PA, Stainier DYR. 2004. Early Myocardial Function Affects Endocardial Cushion Development in Zebrafish. *PLOS Biology* **2**:e129. doi:10.1371/journal.pbio.0020129

Batlle E, Sancho E, Francí C, Domínguez D, Monfar M, Baulida J, García De Herreros A. 2000. The transcription factor snail is a repressor of E-cadherin gene expression in epithelial tumour cells. *Nat Cell Biol* **2**:84–89. doi:10.1038/35000034

Baulida J, Díaz VM, García de Herreros A. 2019. Snail1: A Transcriptional Factor Controlled at Multiple Levels. *J Clin Med* **8**. doi:10.3390/jcm8060757

Baum B, Settleman J, Quinlan MP. 2008. Transitions between epithelial and mesenchymal states in development and disease. *Seminars in Cell & Developmental Biology*, Cell Shape and Tissue Morphogenesis **19**:294–308. doi:10.1016/j.semcdb.2008.02.001

Beis D. 2005. Genetic and cellular analyses of zebrafish atrioventricular cushion and valve development. *Development*. doi:10.1242/dev.01970

Bensimon-Brito A, Ramkumar S, Boezio GLM, Guenther S, Kuenne C, Helker CSM, Sánchez-Iranzo H, Iloska D, Piesker J, Pullamsetti S, Mercader N, Beis D, Stainier DYR. 2020. TGF-β Signaling Promotes Tissue Formation during Cardiac Valve Regeneration in Adult Zebrafish. *Developmental Cell* **52**:9-20.e7. doi:10.1016/j.devcel.2019.10.027

Bensimon-Brito A, Ramkumar S, Boezio GLM, Guenther S, Kuenne C, Helker CSM, Sánchez-Iranzo H, Iloska D, Piesker J, Pullamsetti S, Mercader N, Beis D, Stainier DYR. 2019. TGF-β Signaling Promotes Tissue Formation during Cardiac Valve

Regeneration in Adult Zebrafish. *Developmental Cell*. doi:10.1016/j.devcel.2019.10.027

Bertrand JY, Chi NC, Santoso B, Teng S, Stainier DYR, Traver D. 2010. Hematopoietic stem cells derive directly from aortic endothelium during development. *Nature* **464**:108–111. doi:10.1038/nature08738

Bialek P, Kern B, Yang X, Schrock M, Sosic D, Hong N, Wu H, Yu K, Ornitz DM, Olson EN, Justice MJ, Karsenty G. 2004. A twist code determines the onset of osteoblast differentiation. *Dev Cell* **6**:423–435. doi:10.1016/s1534-5807(04)00058-9

Bishopric NH. 2005. Evolution of the Heart from Bacteria to Man. *Annals of the New York Academy of Sciences* **1047**:13–29. doi:10.1196/annals.1341.002

Bodmer R. 1995. Heart development in Drosophila and its relationship to vertebrates. *Trends in Cardiovascular Medicine*, Migration of Leukocytes Across the Vascular Intima **5**:21–28. doi:10.1016/1050-1738(94)00032-Q

Boezio GL, Bensimon-Brito A, Piesker J, Guenther S, Helker CS, Stainier DY. 2020. Endothelial TGF-β signaling instructs smooth muscle cell development in the cardiac outflow tract. *eLife* **9**:e57603. doi:10.7554/eLife.57603

Bornhorst D, Xia P, Nakajima H, Dingare C, Herzog W, Lecaudey V, Mochizuki N, Heisenberg C-P, Yelon D, Abdelilah-Seyfried S. 2019. Biomechanical signaling within the developing zebrafish heart attunes endocardial growth to myocardial chamber dimensions. *Nature Communications* **10**:4113. doi:10.1038/s41467-019-12068-x

Bourgeois P, Bolcato-Bellemin AL, Danse JM, Bloch-Zupan A, Yoshiba K, Stoetzel C, Perrin-Schmitt F. 1998. The variable expressivity and incomplete penetrance of the twist-null heterozygous mouse phenotype resemble those of human Saethre-Chotzen syndrome. *Hum Mol Genet* **7**:945–957. doi:10.1093/hmg/7.6.945

Bowen CJ, Zhou J, Sung DC, Butcher JT. 2015. Cadherin-11 coordinates cellular migration and extracellular matrix remodeling during aortic valve maturation. *Developmental Biology* **407**:145–157. doi:10.1016/j.ydbio.2015.07.012

Brown DR, Samsa LA, Qian L, Liu J. 2016. Advances in the Study of Heart Development and Disease Using Zebrafish. *J Cardiovasc Dev Dis* **3**:13. doi:10.3390/jcdd3020013

Bruneau BG. 2002. Transcriptional regulation of vertebrate cardiac morphogenesis. *Circ Res* **90**:509–519. doi:10.1161/01.res.0000013072.51957.b7

Butcher JT, Markwald RR. 2007. Valvulogenesis: the moving target. *Philosophical Transactions of the Royal Society B: Biological Sciences* **362**:1489–1503. doi:10.1098/rstb.2007.2130

Camenisch TD, Spicer AP, Brehm-Gibson T, Biesterfeldt J, Augustine ML, Calabro A, Kubalak S, Klewer SE, McDonald JA. 2000. Disruption of hyaluronan synthase-2 abrogates normal cardiac morphogenesis and hyaluronan-mediated

transformation of epithelium to mesenchyme. *J Clin Invest* **106**:349–360. doi:10.1172/JCI10272

Campinho P, Lamperti P, Boselli F, Vilfan A, Vermot J. 2020. Blood Flow Limits Endothelial Cell Extrusion in the Zebrafish Dorsal Aorta. *Cell Reports* **31**:107505. doi:10.1016/j.celrep.2020.03.069

Cano A, Pérez-Moreno MA, Rodrigo I, Locascio A, Blanco MJ, del Barrio MG, Portillo F, Nieto MA. 2000. The transcription factor Snail controls epithelial–mesenchymal transitions by repressing E-cadherin expression. *Nature Cell Biology* **2**:76–83. doi:10.1038/35000025

Capetanaki Y, Papathanasiou S, Diokmetzidou A, Vatsellas G, Tsikitis M. 2015. Desmin related disease: a matter of cell survival failure. *Current Opinion in Cell Biology*, Cell architecture **32**:113–120. doi:10.1016/j.ceb.2015.01.004

Carver EA, Jiang R, Lan Y, Oram KF, Gridley T. 2001. The mouse snail gene encodes a key regulator of the epithelial-mesenchymal transition. *Mol Cell Biol* **21**:8184–8188. doi:10.1128/MCB.21.23.8184-8188.2001

Cavanaugh AM, Huang J, Chen J-N. 2015. Two developmentally distinct populations of neural crest cells contribute to the zebrafish heart. *Developmental Biology* **404**:103–112. doi:10.1016/j.ydbio.2015.06.002

Chakraborty S, Wirrig EE, Hinton RB, Merrill WH, Spicer DB, Yutzey KE. 2010. Twist1 promotes heart valve cell proliferation and extracellular matrix gene expression during development in vivo and is expressed in human diseased aortic valves. *Dev Biol* **347**:167–179. doi:10.1016/j.ydbio.2010.08.021

Chen CY, Caporizzo MA, Bedi K, Vite A, Bogush AI, Robison P, Heffler JG, Salomon AK, Kelly NA, Babu A, Morley MP, Margulies KB, Prosser BL. 2018. Suppression of detyrosinated microtubules improves cardiomyocyte function in human heart failure. *Nature Medicine* **24**:1225–1233. doi:10.1038/s41591-018-0046-2

Chen JN, van Eeden FJ, Warren KS, Chin A, Nüsslein-Volhard C, Haffter P, Fishman MC. 1997. Left-right pattern of cardiac BMP4 may drive asymmetry of the heart in zebrafish. *Development* **124**:4373–4382.

Chen ZF, Behringer RR. 1995. twist is required in head mesenchyme for cranial neural tube morphogenesis. *Genes Dev* **9**:686–699. doi:10.1101/gad.9.6.686

Cherian AV, Fukuda R, Augustine SM, Maischein H-M, Stainier DYR. 2016. N-cadherin relocalization during cardiac trabeculation. *Proc Natl Acad Sci U S A* **113**:7569–7574. doi:10.1073/pnas.1606385113

Chi NC, Shaw RM, Jungblut B, Huisken J, Ferrer T, Arnaout R, Scott I, Beis D, Xiao T, Baier H, Jan LY, Tristani-Firouzi M, Stainier DYR. 2008. Genetic and Physiologic Dissection of the Vertebrate Cardiac Conduction System. *PLOS Biology* **6**:e109. doi:10.1371/journal.pbio.0060109

Chiplunkar AR, Lung TK, Alhashem Y, Koppenhaver BA, Salloum FN, Kukreja RC, Haar JL, Lloyd JA. 2013. Krüppel-Like Factor 2 Is Required for Normal Mouse Cardiac Development. *PLoS One* **8**:e54891. doi:10.1371/journal.pone.0054891

Chow RW-Y, Lamperti P, Steed E, Boselli F, Vermot J. 2018. Following Endocardial Tissue Movements via Cell Photoconversion in the Zebrafish Embryo. *JoVE (Journal of Visualized Experiments)* e57290. doi:10.3791/57290

Christ B, Jacob M, Jacob HJ. 1983. On the origin and development of the ventrolateral abdominal muscles in the avian embryo. An experimental and ultrastructural study. *Anat Embryol (Berl)* **166**:87–101. doi:10.1007/BF00317946

Combs MD, Yutzey KE. 2009a. VEGF and RANKL regulation of NFATc1 in heart valve development. *Circulation Research*. doi:10.1161/CIRCRESAHA.109.196469

Combs MD, Yutzey KE. 2009b. VEGF and RANKL Regulation of NFATc1 in Heart Valve Development. *Circulation Research* **105**:565–574. doi:10.1161/CIRCRESAHA.109.196469

Cooley MA, Fresco VM, Dorlon ME, Twal WO, Lee NV, Barth JL, Kern CB, Iruela-Arispe ML, Argraves WS. 2012. Fibulin-1 is required during cardiac ventricular morphogenesis for versican cleavage, suppression of ErbB2 and Erk1/2 activation, and to attenuate trabecular cardiomyocyte proliferation. *Developmental Dynamics* **241**:303–314. doi:10.1002/dvdy.23716

D'Amico L, Scott IC, Jungblut B, Stainier DYR. 2007. A Mutation in Zebrafish hmgcr1b Reveals a Role for Isoprenoids in Vertebrate Heart-Tube Formation. *Current Biology* **17**:252–259. doi:10.1016/j.cub.2006.12.023

Das A, Crump JG. 2012. Bmps and Id2a act upstream of twist1 to restrict ectomesenchyme potential of the cranial neural crest. *PLoS Genetics*. doi:10.1371/journal.pgen.1002710

de la Pompa JL, Timmerman LA, Takimoto H, Yoshida H, Elia AJ, Samper E, Potter J, Wakeham A, Marengere L, Langille BL, Crabtree GR, Mak TW. 1998. Role of the NF-ATc transcription factor in morphogenesis of cardiac valves and septum. *Nature* **392**:182–186. doi:10.1038/32419

de Pater E, Clijsters L, Marques SR, Lin Y-F, Garavito-Aguilar ZV, Yelon D, Bakkers J. 2009. Distinct phases of cardiomyocyte differentiation regulate growth of the zebrafish heart. *Development* **136**:1633–1641. doi:10.1242/dev.030924

del Monte-Nieto G, Ramialison M, Adam AAS, Wu B, Aharonov A, D'Uva G, Bourke LM, Pitulescu ME, Chen H, de la Pompa JL, Shou W, Adams RH, Harten SK, Tzahor E, Zhou B, Harvey RP. 2018. Control of cardiac jelly dynamics by NOTCH1 and NRG1 defines the building plan for trabeculation. *Nature* **557**:439–445. doi:10.1038/s41586-018-0110-6

Díaz V, Viñas-Castells R, García de Herreros A. 2014. Regulation of the protein stability of EMT transcription factors. *Cell Adhesion & Migration* **8**:418–428. doi:10.4161/19336918.2014.969998

Dietrich A-C, Lombardo VA, Veerkamp J, Priller F, Abdelilah-Seyfried S. 2014. Blood Flow and Bmp Signaling Control Endocardial Chamber Morphogenesis. *Developmental Cell* **30**:367–377. doi:10.1016/j.devcel.2014.06.020

Dobin A, Davis CA, Schlesinger F, Drenkow J, Zaleski C, Jha S, Batut P, Chaisson M, Gingeras TR. 2013. STAR: ultrafast universal RNA-seq aligner. *Bioinformatics* **29**:15–21. doi:10.1093/bioinformatics/bts635

Donat S, Lourenço M, Paolini A, Otten C, Renz M, Abdelilah-Seyfried S. 2018. Heg1 and Ccm1/2 proteins control endocardial mechanosensitivity during zebrafish valvulogenesis. *eLife*. doi:10.7554/eLife.28939

Duchemin A-L, Vignes H, Vermot J. 2019. Mechanically activated piezo channels modulate outflow tract valve development through the Yap1 and Klf2-Notch signaling axis. *eLife* **8**:e44706. doi:10.7554/eLife.44706

Dupin E, Calloni G, Real C, Gonçalves-Trentin A, Le Douarin NM. 2007. Neural crest progenitors and stem cells. *Comptes Rendus Biologies*, Thérapie cellulaire régénérative / Regenerative cell therapy **330**:521–529. doi:10.1016/j.crvi.2007.04.004

Duszyc K, Gomez GA, Lagendijk AK, Yau M-K, Nanavati BN, Gliddon BL, Hall TE, Verma S, Hogan BM, Pitson SM, Fairlie DP, Parton RG, Yap AS. 2021. Mechanotransduction activates RhoA in the neighbors of apoptotic epithelial cells to engage apical extrusion. *Current Biology* **31**:1326-1336.e5. doi:10.1016/j.cub.2021.01.003

Dutta P, Lincoln J. 2018. Calcific Aortic Valve Disease: a Developmental Biology Perspective. *Curr Cardiol Rep* **20**:21. doi:10.1007/s11886-018-0968-9

Eisenhoffer GT, Loftus PD, Yoshigi M, Otsuna H, Chien C-B, Morcos PA, Rosenblatt J. 2012. Crowding induces live cell extrusion to maintain homeostatic cell numbers in epithelia. *Nature* **484**:546–549. doi:10.1038/nature10999

el Ghouzzi V, Le Merrer M, Perrin-Schmitt F, Lajeunie E, Benit P, Renier D, Bourgeois P, Bolcato-Bellemin AL, Munnich A, Bonaventure J. 1997. Mutations of the TWIST gene in the Saethre-Chotzen syndrome. *Nat Genet* **15**:42–46. doi:10.1038/ng0197-42

El-Brolosy MA, Kontarakis Z, Rossi A, Kuenne C, Günther S, Fukuda N, Kikhi K, Boezio GLM, Takacs CM, Lai S-L, Fukuda R, Gerri C, Giraldez AJ, Stainier DYR. 2019. Genetic compensation triggered by mutant mRNA degradation. *Nature* **568**:193–197. doi:10.1038/s41586-019-1064-z

Essner JJ, Amack JD, Nyholm MK, Harris EB, Yost HJ. 2005. Kupffer's vesicle is a ciliated organ of asymmetry in the zebrafish embryo that initiates left-right development of the brain, heart and gut. *Development* **132**:1247–1260. doi:10.1242/dev.01663

Estigoy CB, Pontén F, Odeberg J, Herbert B, Guilhaus M, Charleston M, Ho JWK, Cameron D, dos Remedios CG. 2009. Intercalated discs: multiple proteins perform

multiple functions in non-failing and failing human hearts. *Biophys Rev* **1**:43. doi:10.1007/s12551-008-0007-y

Fishman MC, Stainier DY. 1994. Cardiovascular development. Prospects for a genetic approach. *Circ Res* **74**:757–763. doi:10.1161/01.res.74.5.757

Fontana F, Haack T, Reichenbach M, Knaus P, Puceat M, Abdelilah-Seyfried S. 2020. Antagonistic Activities of Vegfr3/Flt4 and Notch1b Fine-tune Mechanosensitive Signaling during Zebrafish Cardiac Valvulogenesis. *Cell Reports* **32**:107883. doi:10.1016/j.celrep.2020.107883

Frantz C, Stewart KM, Weaver VM. 2010. The extracellular matrix at a glance. *Journal of Cell Science* **123**:4195–4200. doi:10.1242/jcs.023820

Fujita M, Cha YR, Pham VN, Sakurai A, Roman BL, Gutkind JS, Weinstein BM. 2011. Assembly and patterning of the vascular network of the vertebrate hindbrain. *Development* **138**:1705–1715. doi:10.1242/dev.058776

Fukuda R, Gunawan F, Beisaw A, Jimenez-Amilburu V, Maischein H-M, Kostin S, Kawakami K, Stainier DYR. 2017. Proteolysis regulates cardiomyocyte maturation and tissue integration. *Nature Communications* **8**:14495. doi:10.1038/ncomms14495

Fukuda R, Gunawan F, Ramadass R, Beisaw A, Konzer A, Mullapudi ST, Gentile A, Maischein H-M, Graumann J, Stainier DYR. 2019. Mechanical Forces Regulate Cardiomyocyte Myofilament Maturation via the VCL-SSH1-CFL Axis. *Developmental Cell* **51**:62-77.e5. doi:10.1016/j.devcel.2019.08.006

Fukui H, Chow RW-Y, Xie J, Foo YY, Yap CH, Minc N, Mochizuki N, Vermot J. 2021. Bioelectric signaling and the control of cardiac cell identity in response to mechanical forces. *Science* **374**:351–354. doi:10.1126/science.abc6229

Gautel M, Djinović-Carugo K. 2016. The sarcomeric cytoskeleton: from molecules to motion. *Journal of Experimental Biology* **219**:135–145. doi:10.1242/jeb.124941

Gauvrit S, Villasenor A, Strilic B, Kitchen P, Collins MM, Marín-Juez R, Guenther S, Maischein H-M, Fukuda N, Canham MA, Brickman JM, Bogue CW, Jayaraman P-S, Stainier DYR. 2018. HHEX is a transcriptional regulator of the VEGFC/FLT4/PROX1 signaling axis during vascular development. *Nat Commun* **9**:2704. doi:10.1038/s41467-018-05039-1

Gentile A, Bensimon-Brito A, Priya R, Maischein H-M, Piesker J, Guenther S, Gunawan F, Stainier DY. 2021. The EMT transcription factor Snai1 maintains myocardial wall integrity by repressing intermediate filament gene expression. *eLife* **10**:e66143. doi:10.7554/eLife.66143

George EL, Baldwin HS, Hynes RO. 1997. Fibronectins Are Essential for Heart and Blood Vessel Morphogenesis But Are Dispensable for Initial Specification of Precursor Cells. *Blood* **90**:3073–3081. doi:10.1182/blood.V90.8.3073

Glickman NS, Yelon D. 2002. Cardiac development in zebrafish: coordination of form and function. *Semin Cell Dev Biol* **13**:507–513. doi:10.1016/s1084952102001040

Goddard LM, Duchemin AL, Ramalingan H, Wu B, Chen M, Bamezai S, Yang J, Li L, Morley MP, Wang T, Scherrer-Crosbie M, Frank DB, Engleka KA, Jameson SC, Morrisey EE, Carroll TJ, Zhou B, Vermot J, Kahn ML. 2017. Hemodynamic Forces Sculpt Developing Heart Valves through a KLF2-WNT9B Paracrine Signaling Axis. *Developmental Cell*. doi:10.1016/j.devcel.2017.09.023

Grassini DR, Lagendijk AK, De Angelis JE, Da Silva J, Jeanes A, Zettler N, Bower NI, Hogan BM, Smith KA. 2018. Nppa and Nppb act redundantly during zebrafish cardiac development to confine AVC marker expression and reduce cardiac jelly volume. *Development* **145**:dev160739. doi:10.1242/dev.160739

Grau Y, Carteret C, Simpson P. 1984. MUTATIONS AND CHROMOSOMAL REARRANGEMENTS AFFECTING THE EXPRESSION OF SNAIL, A GENE INVOLVED IN EMBRYONIC PATTERNING IN DROSOPHILA MELANOGASTER. *Genetics* **108**:347–360. doi:10.1093/genetics/108.2.347

Grego-Bessa J, Luna-Zurita L, del Monte G, Bolós V, Melgar P, Arandilla A, Garratt AN, Zang H, Mukouyama Y-S, Chen H, Shou W, Ballestar E, Esteller M, Rojas A, Pérez-Pomares JM, de la Pompa JL. 2007. Notch signaling is essential for ventricular chamber development. *Dev Cell* **12**:415–429. doi:10.1016/j.devcel.2006.12.011

Grieve AG, Rabouille C. 2014. Extracellular cleavage of E-cadherin promotes epithelial cell extrusion. *J Cell Sci* **127**:3331–3346. doi:10.1242/jcs.147926

Grimes KM, Prasad V, McNamara JW. 2019. Supporting the heart: Functions of the cardiomyocyte's non-sarcomeric cytoskeleton. *J Mol Cell Cardiol* **131**:187–196. doi:10.1016/j.yjmcc.2019.04.002

Gripp KW, Zackai EH, Stolle CA. 2000. Mutations in the human TWIST gene. *Hum Mutat* **15**:150–155. doi:10.1002/(SICI)1098-1004(200002)15:2<150::AID-HUMU3>3.0.CO;2-D

Grosskurth SE, Bhattacharya D, Wang Q, Lin JJ-C. 2008. Emergence of Xin Demarcates a Key Innovation in Heart Evolution. *PLOS ONE* **3**:e2857. doi:10.1371/journal.pone.0002857

Guerra A, Germano RF, Stone O, Arnaout R, Guenther S, Ahuja S, Uribe V, Vanhollebeke B, Stainier DY, Reischauer S. 2018. Distinct myocardial lineages break atrial symmetry during cardiogenesis in zebrafish. *eLife* **7**:e32833. doi:10.7554/eLife.32833

Gunawan F, Gentile A, Fukuda R, Tsedeke AT, Jiménez-Amilburu V, Ramadass R, Iida A, Sehara-Fujisawa A, Stainier DYR. 2019. Focal adhesions are essential to drive zebrafish heart valve morphogenesis. *The Journal of cell biology*. doi:10.1083/jcb.201807175

Gunawan F, Priya R, Stainier DYR. 2021. Sculpting the heart: Cellular mechanisms shaping valves and trabeculae. *Curr Opin Cell Biol* **73**:26–34. doi:10.1016/j.ceb.2021.04.009

Gunawan Felix, Gentile Alessandra, Gauvrit Sébastien, Stainier Didier Y.R., Bensimon-Brito Anabela. 2020. Nfatc1 Promotes Interstitial Cell Formation During Cardiac Valve Development in Zebrafish. *Circulation Research* **126**:968–984. doi:10.1161/CIRCRESAHA.119.315992

Gupta V, Poss KD. 2012. Clonally dominant cardiomyocytes direct heart morphogenesis. *Nature* **484**:479–484. doi:10.1038/nature11045

Hallab JC, Nim HT, Stolper J, Chahal G, Waylen L, Bolk F, Elliott DA, Porrello E, Ramialison M. 2021. Towards spatio-temporally resolved developmental cardiac gene regulatory networks in zebrafish. *Briefings in Functional Genomics* **20**:427–433. doi:10.1093/bfgp/elab030

Han P, Bloomekatz J, Ren J, Zhang R, Grinstein JD, Zhao L, Burns CG, Burns CE, Anderson RM, Chi NC. 2016. Coordinating cardiomyocyte interactions to direct ventricular chamber morphogenesis. *Nature* **534**:700–704. doi:10.1038/nature18310

Harvey RP. 2002. Patterning the vertebrate heart. *Nat Rev Genet* **3**:544–556. doi:10.1038/nrg843

Heckel E, Boselli F, Roth S, Krudewig A, Belting H-G, Charvin G, Vermot J. 2015. Oscillatory Flow Modulates Mechanosensitive klf2a Expression through trpv4 and trpp2 during Heart Valve Development. *Curr Biol* **25**:1354–1361. doi:10.1016/j.cub.2015.03.038

Heffler Julie, Shah Parisha P., Robison Patrick, Phyo Sai, Veliz Kimberly, Uchida Keita, Bogush Alexey, Rhoades Joshua, Jain Rajan, Prosser Benjamin L. 2020. A Balance Between Intermediate Filaments and Microtubules Maintains Nuclear Architecture in the Cardiomyocyte. *Circulation Research* **126**:e10–e26. doi:10.1161/CIRCRESAHA.119.315582

Hernandez L, Ryckebüsch L, Wang C, Ling R, Yelon D. 2019. Tmem2 restricts atrioventricular canal differentiation by regulating degradation of hyaluronic acid. *Developmental Dynamics* **248**:1195–1210. doi:10.1002/dvdy.106

Herwig L, Blum Y, Krudewig A, Ellertsdottir E, Lenard A, Belting H-G, Affolter M. 2011. Distinct cellular mechanisms of blood vessel fusion in the zebrafish embryo. *Curr Biol* **21**:1942–1948. doi:10.1016/j.cub.2011.10.016

Hinton RB, Lincoln J, Deutsch GH, Osinska H, Manning PB, Benson DW, Yutzey KE. 2006. Extracellular Matrix Remodeling and Organization in Developing and Diseased Aortic Valves. *Circulation Research* **98**:1431–1438. doi:10.1161/01.RES.0000224114.65109.4e

Hinton RB, Yutzey KE. 2011. Heart Valve Structure and Function in Development and Disease. *Annual Review of Physiology* **73**:29–46. doi:10.1146/annurev-physiol-012110-142145

Horne TE, VandeKopple M, Sauls K, Koenig SN, Anstine LJ, Garg V, Norris RA, Lincoln J. 2015. Dynamic Heterogeneity of the Heart Valve Interstitial Cell Population in Mitral Valve Health and Disease. *Journal of Cardiovascular Development and Disease* **2**:214–232. doi:10.3390/jcdd2030214

Howard TD, Paznekas WA, Green ED, Chiang LC, Ma N, Ortiz de Luna RI, Garcia Delgado C, Gonzalez-Ramos M, Kline AD, Jabs EW. 1997. Mutations in TWIST, a basic helix-loop-helix transcription factor, in Saethre-Chotzen syndrome. *Nat Genet* **15**:36–41. doi:10.1038/ng0197-36

Hu N, Sedmera D, Yost HJ, Clark EB. 2000. Structure and function of the developing zebrafish heart. *Anat Rec* **260**:148–157. doi:10.1002/1097-0185(20001001)260:2<148::AID-AR50>3.0.CO;2-X

Hurlstone AFL, Haramis APG, Wienholds E, Begthel H, Korving J, Van Eeden F, Cuppen E, Zivkovic D, Plasterk RHA, Clevers H. 2003. The Wnt/β-catenin pathway regulates cardiac valve formation. *Nature* **425**:633–637. doi:10.1038/nature02030.Published

Inai K, Burnside JL, Hoffman S, Toole BP, Sugi Y. 2013. BMP-2 Induces Versican and Hyaluronan That Contribute to Post-EMT AV Cushion Cell Migration. *PLOS ONE* **8**:e77593. doi:10.1371/journal.pone.0077593

Ivanovitch K, Soro-Barrio P, Chakravarty P, Jones RA, Bell DM, Mousavy Gharavy SN, Stamataki D, Delile J, Smith JC, Briscoe J. 2021. Ventricular, atrial, and outflow tract heart progenitors arise from spatially and molecularly distinct regions of the primitive streak. *PLoS Biol* **19**:e3001200. doi:10.1371/journal.pbio.3001200

Jain R, Engleka KA, Rentschler SL, Manderfield LJ, Li L, Yuan L, Epstein JA. 2011. Cardiac neural crest orchestrates remodeling and functional maturation of mouse semilunar valves. *J Clin Invest* **121**:422–430. doi:10.1172/JCI44244

Jiménez-Amilburu V, Rasouli SJ, Staudt DW, Nakajima H, Chiba A, Mochizuki N, Stainier DYR. 2016. In Vivo Visualization of Cardiomyocyte Apicobasal Polarity Reveals Epithelial to Mesenchymal-like Transition during Cardiac Trabeculation. *Cell Reports* **17**:2687–2699. doi:10.1016/j.celrep.2016.11.023

Jiu Y, Peränen J, Schaible N, Cheng F, Eriksson JE, Krishnan R, Lappalainen P. 2017. Vimentin intermediate filaments control actin stress fiber assembly through GEF-H1 and RhoA. *J Cell Sci* **130**:892–902. doi:10.1242/jcs.196881

Joziasse IC, van de Smagt JJ, Smith K, Bakkers J, Sieswerda G-J, Mulder BJM, Doevendans PA. 2008. Genes in congenital heart disease: atrioventricular valve formation. *Basic Res Cardiol* **103**:216–227. doi:10.1007/s00395-008-0713-4

Kadeer A, Maruyama T, Kajita M, Morita T, Sasaki A, Ohoka A, Ishikawa S, Ikegawa M, Shimada T, Fujita Y. 2017. Plectin is a novel regulator for apical extrusion of RasV12-transformed cells. *Scientific Reports* **7**:44328. doi:10.1038/srep44328

Kajita M, Sugimura K, Ohoka A, Burden J, Suganuma H, Ikegawa M, Shimada T, Kitamura T, Shindoh M, Ishikawa S, Yamamoto S, Saitoh S, Yako Y, Takahashi R, Okajima T, Kikuta J, Maijima Y, Ishii M, Tada M, Fujita Y. 2014. Filamin acts as a key regulator in epithelial defence against transformed cells. *Nature Communications* **5**:4428. doi:10.1038/ncomms5428

Kalogirou S, Malissovas N, Moro E, Argenton F, Stainier DYR, Beis D. 2014. Intracardiac flow dynamics regulate atrioventricular valve morphogenesis. *Cardiovascular Research* **104**:49–60. doi:10.1093/cvr/cvu186

Karra R, Foglia MJ, Choi W-Y, Belliveau C, DeBenedittis P, Poss KD. 2018. Vegfaa instructs cardiac muscle hyperplasia in adult zebrafish. *PNAS* **115**:8805–8810. doi:10.1073/pnas.1722594115

Kaufhold S, Bonavida B. 2014. Central role of Snail1 in the regulation of EMT and resistance in cancer: a target for therapeutic intervention. *Journal of Experimental & Clinical Cancer Research* **33**:62. doi:10.1186/s13046-014-0062-0

Kayman Kürekçi G, Kural Mangit E, Koyunlar C, Unsal S, Saglam B, Ergin B, Gizer M, Uyanik I, Boustanabadimaralan Düz N, Korkusuz P, Talim B, Purali N, Hughes SM, Dincer PR. 2021. Knockout of zebrafish desmin genes does not cause skeletal muscle degeneration but alters calcium flux. *Scientific Reports* **11**:7505. doi:10.1038/s41598-021-86974-w

Keegan BR, Meyer D, Yelon D. 2004. Organization of cardiac chamber progenitors in the zebrafish blastula. *Development* **131**:3081–3091. doi:10.1242/dev.01185

Kikuchi K, Gupta V, Wang J, Holdway JE, Wills AA, Fang Y, Poss KD. 2011. tcf21+ epicardial cells adopt non-myocardial fates during zebrafish heart development and regeneration. *Development* **138**:2895–2902. doi:10.1242/dev.067041

Kikuchi K, Holdway JE, Werdich AA, Anderson RM, Fang Y, Egnaczyk GF, Evans T, MacRae CA, Stainier DYR, Poss KD. 2010. Primary contribution to zebrafish heart regeneration by gata4+ cardiomyocytes. *Nature*. doi:10.1038/nature08804

Kocgozlu L, Saw TB, Le AP, Yow I, Shagirov M, Wong E, Mège R-M, Lim CT, Toyama Y, Ladoux B. 2016. Epithelial Cell Packing Induces Distinct Modes of Cell Extrusions. *Current Biology* **26**:2942–2950. doi:10.1016/j.cub.2016.08.057

Kodigepalli KM, Thatcher K, West T, Howsmon DP, Schoen FJ, Sacks MS, Breuer CK, Lincoln J. 2020. Biology and Biomechanics of the Heart Valve Extracellular Matrix. *J Cardiovasc Dev Dis* **7**:E57. doi:10.3390/jcdd7040057

Kostetskii I, Li J, Xiong Y, Zhou R, Ferrari VA, Patel VV, Molkentin JD, Radice GL. 2005. Induced Deletion of the N-Cadherin Gene in the Heart Leads to Dissolution of the Intercalated Disc Structure. *Circulation Research* **96**:346–354. doi:10.1161/01.RES.0000156274.72390.2c

Kwan R, Chen L, Looi K, Tao G-Z, Weerasinghe SV, Snider NT, Conti MA, Adelstein RS, Xie Q, Omary MB. 2015. PKC412 normalizes mutation-related keratin filament

disruption and hepatic injury in mice by promoting keratin–myosin binding. *Hepatology* **62**:1858–1869. doi:https://doi.org/10.1002/hep.27965

Lagendijk AK, Gomez GA, Baek S, Hesselson D, Hughes WE, Paterson S, Conway DE, Belting H-G, Affolter M, Smith KA, Schwartz MA, Yap AS, Hogan BM. 2017. Live imaging molecular changes in junctional tension upon VE-cadherin in zebrafish. *Nat Commun* **8**:1402. doi:10.1038/s41467-017-01325-6

Le A. Trinh, Stainier DYR. 2004. Fibronectin Regulates Epithelial Organization during Myocardial Migration in Zebrafish. *Developmental Cell* **6**:371–382. doi:10.1016/S1534-5807(04)00063-2

Le AP, Rupprecht J-F, Mège R-M, Toyama Y, Lim CT, Ladoux B. 2021. Adhesion-mediated heterogeneous actin organization governs apoptotic cell extrusion. *Nat Commun* **12**:397. doi:10.1038/s41467-020-20563-9

Lee J, Fei P, Packard RRS, Kang H, Xu H, Baek KI, Jen N, Chen J, Yen H, Kuo C-CJ, Chi NC, Ho C-M, Li R, Hsiai TK. 2016. 4-Dimensional light-sheet microscopy to elucidate shear stress modulation of cardiac trabeculation. *J Clin Invest* **126**:1679–1690. doi:10.1172/JCI83496

Lee KF, Simon H, Chen H, Bates B, Hung MC, Hauser C. 1995. Requirement for neuregulin receptor erbB2 in neural and cardiac development. *Nature* **378**:394–398. doi:10.1038/378394a0

Lee RK, Stainier DY, Weinstein BM, Fishman MC. 1994. Cardiovascular development in the zebrafish. II. Endocardial progenitors are sequestered within the heart field. *Development* **120**:3361–3366. doi:10.1242/dev.120.12.3361

Lehman W, Hatch V, Korman V, Rosol M, Thomas L, Maytum R, Geeves MA, Van Eyk JE, Tobacman LS, Craig R. 2000. Tropomyosin and actin isoforms modulate the localization of tropomyosin strands on actin filaments11Edited by W. Baumeister. *Journal of Molecular Biology* **302**:593–606. doi:10.1006/jmbi.2000.4080

Leptin M. 1991. twist and snail as positive and negative regulators during Drosophila mesoderm development. *Genes Dev* **5**:1568–1576. doi:10.1101/gad.5.9.1568

Leptin M, Grunewald B. 1990. Cell shape changes during gastrulation in Drosophila. *Development* **110**:73–84. doi:10.1242/dev.110.1.73

Levayer R, Dupont C, Moreno E. 2016. Tissue Crowding Induces Caspase-Dependent Competition for Space. *Curr Biol* **26**:670–677. doi:10.1016/j.cub.2015.12.072

Li Jingjing, Miao L, Shieh D, Spiotto E, Li Jian, Zhou B, Paul A, Schwartz RJ, Firulli AB, Singer HA, Huang G, Wu M. 2016. Single-Cell Lineage Tracing Reveals that Oriented Cell Division Contributes to Trabecular Morphogenesis and Regional Specification. *Cell Rep* **15**:158–170. doi:10.1016/j.celrep.2016.03.012

Liao Y, Smyth GK, Shi W. 2014. featureCounts: an efficient general purpose program for assigning sequence reads to genomic features. *Bioinformatics* **30**:923–930. doi:10.1093/bioinformatics/btt656

Liebner S, Cattelino A, Gallini R, Rudini N, Iurlaro M, Piccolo S, Dejana E. 2004. β-catenin is required for endothelial-mesenchymal transformation during heart cushion development in the mouse. *Journal of Cell Biology*. doi:10.1083/jcb.200403050

Lim J, Thiery JP. 2012. Epithelial-mesenchymal transitions: insights from development. *Development* **139**:3471–3486. doi:10.1242/dev.071209

Linask KK, Han M, Cai DH, Brauer PR, Maisastry SM. 2005. Cardiac morphogenesis: Matrix metalloproteinase coordination of cellular mechanisms underlying heart tube formation and directionality of looping. *Developmental Dynamics* **233**:739–753. doi:10.1002/dvdy.20377

Liu AC, Joag VR, Gotlieb AI. 2007. The Emerging Role of Valve Interstitial Cell Phenotypes in Regulating Heart Valve Pathobiology. *The American Journal of Pathology* **171**:1407–1418. doi:10.2353/ajpath.2007.070251

Liu J, Bressan M, Hassel D, Huisken J, Staudt D, Kikuchi K, Poss KD, Mikawa T, Stainier DYR. 2010. A dual role for ErbB2 signaling in cardiac trabeculation. *Development* **137**:3867–3875. doi:10.1242/dev.053736

Liu K, Yu W, Tang M, Tang J, Liu X, Liu Q, Li Y, He L, Zhang L, Evans SM, Tian X, Lui KO, Zhou B. 2018. A dual genetic tracing system identifies diverse and dynamic origins of cardiac valve mesenchyme. *Development* **145**:dev167775. doi:10.1242/dev.167775

Lombardo VA, Heise M, Moghtadaei M, Bornhorst D, Männer J, Abdelilah-Seyfried S. 2019. Morphogenetic control of zebrafish cardiac looping by Bmp signaling. *Development* **146**. doi:10.1242/dev.180091

Love MI, Huber W, Anders S. 2014. Moderated estimation of fold change and dispersion for RNA-seq data with DESeq2. *Genome Biology* **15**:550. doi:10.1186/s13059-014-0550-8

Lubkov V, Bar-Sagi D. 2014. E-Cadherin-Mediated Cell Coupling Is Required for Apoptotic Cell Extrusion. *Current Biology* **24**:868–874. doi:10.1016/j.cub.2014.02.057

Luna-Zurita L, Prados B, Grego-Bessa J, Luxán G, del Monte G, Benguría A, Adams RH, Pérez-Pomares JM, de la Pompa JL. 2010. Integration of a Notch-dependent mesenchymal gene program and Bmp2-driven cell invasiveness regulates murine cardiac valve formation. *J Clin Invest* **120**:3493–3507. doi:10.1172/JCI42666

MacGrogan D, Luxán G, Driessen-Mol A, Bouten C, Baaijens F, Pompa JL de la. 2014. How to Make a Heart Valve: From Embryonic Development to Bioengineering of Living Valve Substitutes. *Cold Spring Harb Perspect Med* **4**:a013912. doi:10.1101/cshperspect.a013912

Martin AC, Gelbart M, Fernandez-Gonzalez R, Kaschube M, Wieschaus EF. 2010. Integration of contractile forces during tissue invagination. *J Cell Biol* **188**:735–749. doi:10.1083/jcb.200910099

Martin AC, Kaschube M, Wieschaus EF. 2009. Pulsed contractions of an actin–myosin network drive apical constriction. *Nature* **457**:495–499. doi:10.1038/nature07522

Martin RT, Bartman T. 2009. Analysis of heart valve development in larval zebrafish. *Dev Dyn* **238**:1796–1802. doi:10.1002/dvdy.21976

Mason FM, Tworoger M, Martin AC. 2013. Apical domain polarization localizes actin-myosin activity to drive ratchet-like apical constriction. *Nat Cell Biol* **15**:926–936. doi:10.1038/ncb2796

Mateus R, Lourenço R, Fang Y, Brito G, Farinho A, Valério F, Jacinto A. 2015. Control of tissue growth by Yap relies on cell density and F-actin in zebrafish fin regeneration. *Development* **142**:2752–2763. doi:10.1242/dev.119701

McKillop DF, Geeves MA. 1993. Regulation of the interaction between actin and myosin subfragment 1: evidence for three states of the thin filament. *Biophysical Journal* **65**:693–701. doi:10.1016/S0006-3495(93)81110-X

Mellman K, Huisken J, Dinsmore C, Hoppe C, Stainier DY. 2012. Fibrillin-2b regulates endocardial morphogenesis in zebrafish. *Developmental Biology* **372**:111–119. doi:10.1016/j.ydbio.2012.07.015

Meyer D, Birchmeier C. 1995. Multiple essential functions of neuregulin in development. *Nature* **378**:386–390. doi:10.1038/378386a0

Miao L, Li Jingjing, Li Jian, Lu Y, Shieh D, Mazurkiewicz JE, Barroso M, Schwarz JJ, Xin H-B, Singer HA, Vincent PA, Zhong W, Radice GL, Wan LQ, Fan Z-C, Huang G, Wu M. 2019. Cardiomyocyte orientation modulated by the Numb family proteins–N-cadherin axis is essential for ventricular wall morphogenesis. *PNAS* **116**:15560–15569. doi:10.1073/pnas.1904684116

Miao M, Bruce AEE, Bhanji T, Davis EC, Keeley FW. 2007. Differential expression of two tropoelastin genes in zebrafish. *Matrix Biology* **26**:115–124. doi:10.1016/j.matbio.2006.09.011

Mickoleit M, Schmid B, Weber M, Fahrbach FO, Hombach S, Reischauer S, Huisken J. 2014. High-resolution reconstruction of the beating zebrafish heart. *Nature Methods* **11**:919–922. doi:10.1038/nmeth.3037

Migueles RP, Shaw L, Rodrigues NP, May G, Henseleit K, Anderson KGV, Goker H, Jones CM, de Bruijn MFTR, Brickman JM, Enver T. 2017. Transcriptional regulation of Hhex in hematopoiesis and hematopoietic stem cell ontogeny. *Developmental Biology*. doi:10.1016/j.ydbio.2016.12.021

Miroshnikova YA, Le HQ, Schneider D, Thalheim T, Rübsam M, Bremicker N, Polleux J, Kamprad N, Tarantola M, Wang I, Balland M, Niessen CM, Galle J, Wickström SA. 2018. Adhesion forces and cortical tension couple cell proliferation and differentiation to drive epidermal stratification. *Nature Cell Biology* **20**:69–80. doi:10.1038/s41556-017-0005-z

Mitrossilis D, Röper J-C, Le Roy D, Driquez B, Michel A, Ménager C, Shaw G, Le Denmat S, Ranno L, Dumas-Bouchiat F, Dempsey NM, Farge E. 2017. Mechanotransductive cascade of Myo-II-dependent mesoderm and endoderm invaginations in embryo gastrulation. *Nature Communications* **8**:13883. doi:10.1038/ncomms13883

Mongera A, Singh AP, Levesque MP, Chen Y-Y, Konstantinidis P, Nüsslein-Volhard C. 2013. Genetic lineage labeling in zebrafish uncovers novel neural crest contributions to the head, including gill pillar cells. *Development* **140**:916–925. doi:10.1242/dev.091066

Moorman AFM, Christoffels VM. 2003. Cardiac Chamber Formation: Development, Genes, and Evolution. *Physiological Reviews* **83**:1223–1267. doi:10.1152/physrev.00006.2003

Mosimann C, Kaufman CK, Li P, Pugach EK, Tamplin OJ, Zon LI. 2011. Ubiquitous transgene expression and Cre-based recombination driven by the ubiquitin promoter in zebrafish. *Development* **138**:169–177. doi:10.1242/dev.059345

Murray SA, Gridley T. 2006. Snail family genes are required for left–right asymmetry determination, but not neural crest formation, in mice. *PNAS* **103**:10300–10304. doi:10.1073/pnas.0602234103

Nieto MA. 2002. The snail superfamily of zinc-finger transcription factors. *Nature Reviews Molecular Cell Biology* **3**:155–166. doi:10.1038/nrm757

Nieto MA, Huang RY-J, Jackson RA, Thiery JP. 2016. EMT: 2016. *Cell* **166**:21–45. doi:10.1016/j.cell.2016.06.028

Nieto MA, Sargent MG, Wilkinson DG, Cooke J. 1994. Control of cell behavior during vertebrate development by Slug, a zinc finger gene. *Science* **264**:835–839. doi:10.1126/science.7513443

Nüsslein-Volhard C, Wieschaus E, Kluding H. 1984. Mutations affecting the pattern of the larval cuticle inDrosophila melanogaster. *Wilhelm Roux' Archiv* **193**:267–282. doi:10.1007/BF00848156

O'Donnell A, Yutzey KE. 2020. Mechanisms of heart valve development and disease. *Development* **147**:dev183020. doi:10.1242/dev.183020

Olson EN. 2006. Gene Regulatory Networks in the Evolution and Development of the Heart. *Science*. doi:10.1126/science.1132292

Oteíza P, Köppen M, Concha ML, Heisenberg C-P. 2008. Origin and shaping of the laterality organ in zebrafish. *Development* **135**:2807–2813. doi:10.1242/dev.022228

Paolini A, Abdelilah-Seyfried S. 2018. The mechanobiology of zebrafish cardiac valve leaflet formation. *Curr Opin Cell Biol* **55**:52–58. doi:10.1016/j.ceb.2018.05.007

Paolini A, Fontana F, Pham V-C, Rödel CJ, Abdelilah-Seyfried S. 2021. Mechanosensitive Notch-Dll4 and Klf2-Wnt9 signaling pathways intersect in guiding

valvulogenesis in zebrafish. *Cell Rep* **37**:109782. doi:10.1016/j.celrep.2021.109782

Papoutsi T, Luna-Zurita L, Prados B, Zaffran S, de la Pompa JL. 2018a. Bmp2 and Notch cooperate to pattern the embryonic endocardium. *Development* **145**:dev163378. doi:10.1242/dev.163378

Papoutsi T, Luna-Zurita L, Prados B, Zaffran S, de la Pompa JL. 2018b. Bmp2 and Notch cooperate to pattern the embryonic endocardium. *Development (Cambridge)*. doi:10.1242/dev.163378

Passer D, van de Vrugt A, Atmanli A, Domian IJ. 2016. Atypical Protein Kinase C-Dependent Polarized Cell Division Is Required for Myocardial Trabeculation. *Cell Rep* **14**:1662–1672. doi:10.1016/j.celrep.2016.01.030

Patel DM, Green KJ. 2014. Desmosomes in the Heart: A Review of Clinical and Mechanistic Analyses. *Cell Communication & Adhesion* **21**:109–128. doi:10.3109/15419061.2014.906533

Peralta M, González-Rosa JM, Marques IJ, Mercader N. 2014. The Epicardium in the Embryonic and Adult Zebrafish. *J Dev Biol* **2**:101–116. doi:10.3390/jdb2020101

Peralta M, Steed E, Harlepp S, González-Rosa JM, Monduc F, Ariza-Cosano A, Cortés A, Rayón T, Gómez-Skarmeta J-L, Zapata A, Vermot J, Mercader N. 2013. Heartbeat-Driven Pericardiac Fluid Forces Contribute to Epicardium Morphogenesis. *Current Biology* **23**:1726–1735. doi:10.1016/j.cub.2013.07.005

Pérez-Pomares JM, González-Rosa JM, Muñoz-Chápuli R. 2009. Building the vertebrate heart - an evolutionary approach to cardiac development. *Int J Dev Biol* **53**:1427–1443. doi:10.1387/ijdb.072409jp

Peshkovsky C, Totong R, Yelon D. 2011. Dependence of cardiac trabeculation on neuregulin signaling and blood flow in zebrafish. *Dev Dyn* **240**:446–456. doi:10.1002/dvdy.22526

Pestel J, Ramadass R, Gauvrit S, Helker C, Herzog W, Stainier DYR. 2016. Real-time 3D visualization of cellular rearrangements during cardiac valve formation. *Development* **143**:2217–2227. doi:10.1242/dev.133272

Petz A, Grandoch M, Gorski DJ, Abrams M, Piroth M, Schneckmann R, Homann S, Müller J, Hartwig S, Lehr S, Yamaguchi Y, Wight TN, Gorressen S, Ding Z, Kötter S, Krüger M, Heinen A, Kelm M, Gödecke A, Flögel U, Fischer JW. 2019. Cardiac Hyaluronan Synthesis Is Critically Involved in the Cardiac Macrophage Response and Promotes Healing After Ischemia Reperfusion Injury. *Circ Res* **124**:1433–1447. doi:10.1161/CIRCRESAHA.118.313285

Phillips HM, Mahendran P, Singh E, Anderson RH, Chaudhry B, Henderson DJ. 2013. Neural crest cells are required for correct positioning of the developing outflow cushions and pattern the arterial valve leaflets. *Cardiovasc Res* **99**:452–460. doi:10.1093/cvr/cvt132

Priya R, Allanki S, Gentile A, Mansingh S, Uribe V, Maischein H-M, Stainier DYR. 2020. Tension heterogeneity directs form and fate to pattern the myocardial wall. *Nature* 1–5. doi:10.1038/s41586-020-2946-9

Pruna M, Ehler E. 2020. The intercalated disc: a mechanosensing signalling node in cardiomyopathy. *Biophys Rev* **12**:931–946. doi:10.1007/s12551-020-00737-x

Qiao L, Gao H, Zhang T, Jing L, Xiao C, Xiao Y, Luo N, Zhu H, Meng W, Xu H, Mo X. 2014. Snail modulates the assembly of fibronectin via α5 integrin for myocardial migration in zebrafish embryos. *Scientific Reports* **4**:4470. doi:10.1038/srep04470

Qu X, Violette K, Sewell-Loftin MK, Soslow J, Saint-Jean L, Hinton RB, Merryman WD, Baldwin HS. 2019. Loss of flow responsive Tie1 results in Impaired Aortic valve remodeling. *Dev Biol* **455**:73–84. doi:10.1016/j.ydbio.2019.07.011

Quijada P, Trembley MA, Small EM. 2020. The Role of the Epicardium During Heart Development and Repair. *Circ Res* **126**:377–394. doi:10.1161/CIRCRESAHA.119.315857

Rainer PP, Dong P, Sorge M, Fert-Bober J, Holewinski RJ, Wang Y, Foss CA, An SS, Baracca A, Solaini G, Glabe CG, Pomper MG, Van Eyk JE, Tomaselli GF, Paolocci N, Agnetti G. 2018. Desmin Phosphorylation Triggers Preamyloid Oligomers Formation and Myocyte Dysfunction in Acquired Heart Failure. *Circ Res* **122**:e75–e83. doi:10.1161/CIRCRESAHA.117.312082

Rampazzo A, Calore M, van Hengel J, van Roy F. 2014. Intercalated discs and arrhythmogenic cardiomyopathy. *Circ Cardiovasc Genet* **7**:930–940. doi:10.1161/CIRCGENETICS.114.000645

Ramspacher C, Steed E, Boselli F, Ferreira R, Faggianelli N, Roth S, Spiegelhalter C, Messaddeq N, Trinh L, Liebling M, Chacko N, Tessadori F, Bakkers J, Laporte J, Hnia K, Vermot J. 2015. Developmental Alterations in Heart Biomechanics and Skeletal Muscle Function in Desmin Mutants Suggest an Early Pathological Root for Desminopathies. *Cell Reports* **11**:1564–1576. doi:10.1016/j.celrep.2015.05.010

Ranger AM, Grusby MJ, Hodge MR, Gravallese EM, de la Brousse FC, Hoey T, Mickanin C, Baldwin HS, Glimcher LH. 1998. The transcription factor NF-ATc is essential for cardiac valve formation. *Nature* **392**:186–190. doi:10.1038/32426

Rasouli SJ, El-Brolosy M, Tsedeke AT, Bensimon-Brito A, Ghanbari P, Maischein H-M, Kuenne C, Stainier DY. 2018. The flow responsive transcription factor Klf2 is required for myocardial wall integrity by modulating Fgf signaling. *eLife* **7**:e38889. doi:10.7554/eLife.38889

Rasouli SJ, Stainier DYR. 2017. Regulation of cardiomyocyte behavior in zebrafish trabeculation by Neuregulin 2a signaling. *Nat Commun* **8**:15281. doi:10.1038/ncomms15281

Reardon W, Winter RM. 1994. Saethre-Chotzen syndrome. *J Med Genet* **31**:393–396. doi:10.1136/jmg.31.5.393

Rodgers LS, Lalani S, Hardy KM, Xiang X, Broka D, Antin PB, Camenisch TD. 2006. Depolymerized Hyaluronan Induces Vascular Endothelial Growth Factor, a Negative Regulator of Developmental Epithelial-to-Mesenchymal Transformation. *Circulation Research* **99**:583–589. doi:10.1161/01.RES.0000242561.95978.43

Rohr S, Otten C, Abdelilah-Seyfried S. 2008. Asymmetric involution of the myocardial field drives heart tube formation in zebrafish. *Circ Res* **102**:e12-19. doi:10.1161/CIRCRESAHA.107.165241

Rose CS, Patel P, Reardon W, Malcolm S, Winter RM. 1997. The TWIST gene, although not disrupted in Saethre-Chotzen patients with apparently balanced translocations of 7p21, is mutated in familial and sporadic cases. *Hum Mol Genet* **6**:1369–1373. doi:10.1093/hmg/6.8.1369

Rosenblatt J, Raff MC, Cramer LP. 2001. An epithelial cell destined for apoptosis signals its neighbors to extrude it by an actin- and myosin-dependent mechanism. *Current Biology* **11**:1847–1857. doi:10.1016/S0960-9822(01)00587-5

Rozario T, DeSimone DW. 2010. The extracellular matrix in development and morphogenesis: A dynamic view. *Developmental Biology*, Special Section: Morphogenesis **341**:126–140. doi:10.1016/j.ydbio.2009.10.026

Rutkovskiy A, Malashicheva A, Sullivan G, Bogdanova M, Kostareva A, Stensløkken K, Fiane A, Vaage J. n.d. Valve Interstitial Cells: The Key to Understanding the Pathophysiology of Heart Valve Calcification. *Journal of the American Heart Association* **6**:e006339. doi:10.1161/JAHA.117.006339

Sacilotto N, Monteiro R, Fritzsche M, Becker PW, Sanchez-del-Campo L, Liu K, Pinheiro P, Ratnayaka I, Davies B, Goding CR, Patient R, Bou-Gharios G, De Val S. 2013. Analysis of Dll4 regulation reveals a combinatorial role for Sox and Notch in arterial development. *Proceedings of the National Academy of Sciences*. doi:10.1073/pnas.1300805110

Saffitz JE. 2009. Desmosome Mutations in Arrhythmogenic Right Ventricular Cardiomyopathy. *Circulation: Cardiovascular Genetics* **2**:415–417. doi:10.1161/CIRCGENETICS.109.909366

Saitoh S, Maruyama T, Yako Y, Kajita M, Fujioka Y, Ohba Y, Kasai N, Sugama N, Kon S, Ishikawa S, Hayashi T, Yamazaki T, Tada M, Fujita Y. 2017. Rab5-regulated endocytosis plays a crucial role in apical extrusion of transformed cells. *PNAS* **114**:E2327–E2336. doi:10.1073/pnas.1602349114

Salguero-Jiménez A, Grego-Bessa J, D'Amato G, Jiménez-Borreguero LJ, de la Pompa JL. 2018. Myocardial Notch1-Rbpj deletion does not affect NOTCH signaling, heart development or function. *PLoS One* **13**:e0203100. doi:10.1371/journal.pone.0203100

Samsa LA, Givens C, Tzima E, Stainier DYR, Qian L, Liu J. 2015. Cardiac contraction activates endocardial Notch signaling to modulate chamber maturation in zebrafish. *Development* **142**:4080–4091. doi:10.1242/dev.125724

Saneyoshi T, Kume S, Amasaki Y, Mikoshiba K. 2002. The Wnt/calcium pathway activates NF-AT and promotes ventral cell fate in Xenopus embryos. *Nature* **417**:295–299. doi:10.1038/417295a

Saw TB, Doostmohammadi A, Nier V, Kocgozlu L, Thampi S, Toyama Y, Marcq P, Lim CT, Yeomans JM, Ladoux B. 2017. Topological defects in epithelia govern cell death and extrusion. *Nature* **544**:212–216. doi:10.1038/nature21718

Scherz Paul J., Huisken J, Sahai-Hernandez P, Stainier DYR. 2008. High-speed imaging of developing heart valves reveals interplay of morphogenesis and function. *Development* **135**:1179–1187. doi:10.1242/dev.010694

Scherz Paul J, Huisken J, Sahai-Hernandez P, Stainier DYR. 2008. High-speed imaging of developing heart valves reveals\ninterplay of morphogenesis and function. *Development*. doi:10.1242/dev.010694

Schleich J-M, Abdulla T, Summers R, Houyel L. 2013. An overview of cardiac morphogenesis. *Arch Cardiovasc Dis* **106**:612–623. doi:10.1016/j.acvd.2013.07.001

Schulz A, Brendler J, Blaschuk O, Landgraf K, Krueger M, Ricken AM. 2019. Non-pathological Chondrogenic Features of Valve Interstitial Cells in Normal Adult Zebrafish. *J Histochem Cytochem* **67**:361–373. doi:10.1369/0022155418824083

Sehnert AJ, Huq A, Weinstein BM, Walker C, Fishman M, Stainier DYR. 2002. Cardiac troponin T is essential in sarcomere assembly and cardiac contractility. *Nature Genetics* **31**:106–110. doi:10.1038/ng875

Sequeira V, Nijenkamp LLAM, Regan JA, van der Velden J. 2014. The physiological role of cardiac cytoskeleton and its alterations in heart failure. *Biochimica et Biophysica Acta (BBA) - Biomembranes*, Reciprocal influences between cell cytoskeleton and membrane channels, receptors and transporters **1838**:700–722. doi:10.1016/j.bbamem.2013.07.011

Serluca FC. 2008. Development of the proepicardial organ in the zebrafish. *Dev Biol* **315**:18–27. doi:10.1016/j.ydbio.2007.10.007

Shelton EL, Yutzey KE. 2008. Twist1 function in endocardial cushion cell proliferation, migration, and differentiation during heart valve development. *Dev Biol* **317**:282–295. doi:10.1016/j.ydbio.2008.02.037

Sidhwani P, Leerberg DM, Boezio GLM, Capasso TL, Yang H, Chi NC, Roman BL, Stainier DYR, Yelon D. 2020. Cardiac function modulates endocardial cell dynamics to shape the cardiac outflow tract. *Development* **147**:dev185900. doi:10.1242/dev.185900

Silva AC, Pereira C, Fonseca ACRG, Pinto-do-Ó P, Nascimento DS. 2021. Bearing My Heart: The Role of Extracellular Matrix on Cardiac Development, Homeostasis, and Injury Response. *Frontiers in Cell and Developmental Biology* **8**.

Simões FC, Riley PR. 2018. The ontogeny, activation and function of the epicardium during heart development and regeneration. *Development* **145**:dev155994. doi:10.1242/dev.155994

Simões-Costa MS, Vasconcelos M, Sampaio AC, Cravo RM, Linhares VL, Hochgreb T, Yan CYI, Davidson B, Xavier-Neto J. 2005. The evolutionary origin of cardiac chambers. *Developmental Biology* **277**:1–15. doi:10.1016/j.ydbio.2004.09.026

Smith KA, Lagendijk AK, Courtney AD, Chen H, Paterson S, Hogan BM, Wicking C, Bakkers J. 2011. Transmembrane protein 2 (Tmem2) is required to regionally restrict atrioventricular canal boundary and endocardial cushion development. *Development* **138**:4193–4198. doi:10.1242/dev.065375

Soleimani VD, Yin H, Jahani-Asl A, Ming H, Kockx CEM, van Ijcken WFJ, Grosveld F, Rudnicki MA. 2012. Snail Regulates MyoD Binding-Site Occupancy to Direct Enhancer Switching and Differentiation-Specific Transcription in Myogenesis. *Molecular Cell* **47**:457–468. doi:10.1016/j.molcel.2012.05.046

Soo K, O'Rourke MP, Khoo P-L, Steiner KA, Wong N, Behringer RR, Tam PPL. 2002. Twist function is required for the morphogenesis of the cephalic neural tube and the differentiation of the cranial neural crest cells in the mouse embryo. *Dev Biol* **247**:251–270. doi:10.1006/dbio.2002.0699

Srivastava D, Olson EN. 2000. A genetic blueprint for cardiac development. *Nature* **407**:221–226. doi:10.1038/35025190

Stainier DY. 2001. Zebrafish genetics and vertebrate heart formation. *Nat Rev Genet* **2**:39–48. doi:10.1038/35047564

Staudt D, Stainier D. 2012. Uncovering the molecular and cellular mechanisms of heart development using the zebrafish. *Annu Rev Genet* **46**:397–418. doi:10.1146/annurev-genet-110711-155646

Staudt DW, Liu J, Thorn KS, Stuurman N, Liebling M, Stainier DYR. 2014. High-resolution imaging of cardiomyocyte behavior reveals two distinct steps in ventricular trabeculation. *Development* **141**:585–593. doi:10.1242/dev.098632

Steed E, Faggianelli N, Roth S, Ramspacher C, Concordet JP, Vermot J. 2016a. Klf2a couples mechanotransduction and zebrafish valve morphogenesis through fibronectin synthesis. *Nature Communications* **7**. doi:10.1038/ncomms11646

Steed E, Faggianelli N, Roth S, Ramspacher C, Concordet J-P, Vermot J. 2016b. klf2a couples mechanotransduction and zebrafish valve morphogenesis through fibronectin synthesis. *Nat Commun* **7**:11646. doi:10.1038/ncomms11646

Stemmler MP, Eccles RL, Brabletz S, Brabletz T. 2019. Non-redundant functions of EMT transcription factors. *Nature Cell Biology* **21**:102–112. doi:10.1038/s41556-018-0196-y

Tao G, Kotick JD, Lincoln J. 2012. Chapter seven - Heart Valve Development, Maintenance, and Disease: The Role of Endothelial Cells In: Bruneau BG, editor. Current Topics in Developmental Biology, Heart Development. Academic Press. pp. 203–232. doi:10.1016/B978-0-12-387786-4.00006-3

Tao G, Levay AK, Gridley T, Lincoln J. 2011. Mmp15 is a direct target of Snai1 during endothelial to mesenchymal transformation and endocardial cushion development. *Developmental Biology* **359**:209–221. doi:10.1016/j.ydbio.2011.08.022

Tao G, Miller LJ, Lincoln J. 2013. Snai1 is important for avian epicardial cell transformation and motility. *Dev Dyn* **242**:699–708. doi:10.1002/dvdy.23967

Taylor Matthew R.G., Slavov Dobromir, Ku Lisa, Di Lenarda Andrea, Sinagra Gianfranco, Carniel Elisa, Haubold Kurt, Boucek Mark M., Ferguson Debra, Graw Sharon L., Zhu Xiao, Cavanaugh Jean, Sucharov Carmen C., Long Carlin S., Bristow Michael R., Lavori Philip, Mestroni Luisa. 2007. Prevalence of Desmin Mutations in Dilated Cardiomyopathy. *Circulation* **115**:1244–1251. doi:10.1161/CIRCULATIONAHA.106.646778

Teng CS, Ting M, Farmer DT, Brockop M, Maxson RE, Crump JG. 2018. Altered bone growth dynamics prefigure craniosynostosis in a zebrafish model of Saethre-Chotzen syndrome. *eLife* **7**:e37024. doi:10.7554/eLife.37024

Teng X, Qin L, Borgne RL, Toyama Y. 2017. Remodeling of adhesion and modulation of mechanical tensile forces during apoptosis in Drosophila epithelium. *Development* **144**:95–105. doi:10.1242/dev.139865

Thisse B, Stoetzel C, Gorostiza-Thisse C, Perrin-Schmitt F. 1988. Sequence of the twist gene and nuclear localization of its protein in endomesodermal cells of early Drosophila embryos. *EMBO J* **7**:2175–2183.

Thisse C, Thisse B. 2008. High-resolution in situ hybridization to whole-mount zebrafish embryos. *Nature Protocols*. doi:10.1038/nprot.2007.514

Thomas M, Ladoux B, Toyama Y. 2020. Desmosomal Junctions Govern Tissue Integrity and Actomyosin Contractility in Apoptotic Cell Extrusion. *Current Biology* **30**:682-690.e5. doi:10.1016/j.cub.2020.01.002

Timmerman LA, Grego-Bessa J, Raya A, Bertrán E, Pérez-Pomares JM, Díez J, Aranda S, Palomo S, McCormick F, Izpisúa-Belmonte JC, De La Pompa JL. 2004. Notch promotes epithelial-mesenchymal transition during cardiac development and oncogenic transformation. *Genes and Development*. doi:10.1101/gad.276304

Totong R, Schell T, Lescroart F, Ryckebüsch L, Lin Y-F, Zygmunt T, Herwig L, Krudewig A, Gershoony D, Belting H-G, Affolter M, Torres-Vázquez J, Yelon D. 2011. The novel transmembrane protein Tmem2 is essential for coordination of myocardial and endocardial morphogenesis. *Development* **138**:4199–4205. doi:10.1242/dev.064261

Uribe V, Ramadass R, Dogra D, Rasouli SJ, Gunawan F, Nakajima H, Chiba A, Reischauer S, Mochizuki N, Stainier DYR. 2018. In vivo analysis of cardiomyocyte proliferation during trabeculation. *Development* **145**:dev164194. doi:10.1242/dev.164194

van Bodegraven EJ, Etienne-Manneville S. 2020. Intermediate filaments against actomyosin: the david and goliath of cell migration. *Current Opinion in Cell Biology*, Cell Dynamics **66**:79–88. doi:10.1016/j.ceb.2020.05.006

Veerkamp J, Rudolph F, Cseresnyes Z, Priller F, Otten C, Renz M, Schaefer L, Abdelilah-Seyfried S. 2013. Unilateral Dampening of Bmp Activity by Nodal Generates Cardiac Left-Right Asymmetry. *Developmental Cell* **24**:660–667. doi:10.1016/j.devcel.2013.01.026

Vermot J, Forouhar AS, Liebling M, Wu D, Plummer D, Gharib M, Fraser SE. 2009a. Reversing blood flows act through klf2a to ensure normal valvulogenesis in the developing heart. *PLoS Biol* **7**:e1000246. doi:10.1371/journal.pbio.1000246

Vermot J, Forouhar AS, Liebling M, Wu D, Plummer D, Gharib M, Fraser SE. 2009b. Reversing blood flows act through klf2a to ensure normal valvulogenesis in the developing heart. *PLoS Biology*. doi:10.1371/journal.pbio.1000246

Vićovac L, Aplin JD. 1996. Epithelial-mesenchymal transition during trophoblast differentiation. *Acta Anat (Basel)* **156**:202–216. doi:10.1159/000147847

Wadugu B, Kühn B. 2012. The role of neuregulin/ErbB2/ErbB4 signaling in the heart with special focus on effects on cardiomyocyte proliferation. *Am J Physiol Heart Circ Physiol* **302**:H2139–H2147. doi:10.1152/ajpheart.00063.2012

Wang G, Manning ML, Amack JD. 2012. Regional cell shape changes control form and function of Kupffer's vesicle in the zebrafish embryo. *Developmental Biology* **370**:52–62. doi:10.1016/j.ydbio.2012.07.019

Wang L, Liu S, Zhang H, Hu S, Wei Y. 2018. Arrhythmogenic cardiomyopathy: Identification of desmosomal gene variations and desmosomal protein expression in variation carriers. *Exp Ther Med* **15**:2255–2262. doi:10.3892/etm.2018.5694

Warga RM, Kimmel CB. 1990. Cell movements during epiboly and gastrulation in zebrafish. *Development* **108**:569–580.

Warga RM, Nüsslein-Volhard C. 1999. Origin and development of the zebrafish endoderm. *Development* **126**:827–838.

Wee K, Hediyeh-zadeh S, Duszyc K, Verma S, Nanavati B, Khare S, Varma A, Daly RJ, Yap AS, Davis MJ, Budnar S. 2020. Snail induces epithelial cell extrusion by regulating RhoA contractile signaling and cell-matrix adhesion. *J Cell Sci*. doi:10.1242/jcs.235622

Weinberger M, Simões FC, Patient R, Sauka-Spengler T, Riley PR. 2020. Functional Heterogeneity within the Developing Zebrafish Epicardium. *Dev Cell* **52**:574-590.e6. doi:10.1016/j.devcel.2020.01.023

Weng M, Wieschaus E. 2016. Myosin-dependent remodeling of adherens junctions protects junctions from Snail-dependent disassembly. *J Cell Biol* **212**:219–229. doi:10.1083/jcb.201508056

Wessels A, van den Hoff MJB, Adamo RF, Phelps AL, Lockhart MM, Sauls K, Briggs LE, Norris RA, van Wijk B, Perez-Pomares JM, Dettman RW, Burch JBE. 2012. Epicardially derived fibroblasts preferentially contribute to the parietal leaflets of the atrioventricular valves in the murine heart. *Developmental Biology* **366**:111–124. doi:10.1016/j.ydbio.2012.04.020

WESTERFIELD M. 2000. The Zebrafish Book : A Guide for the Laboratory Use of Zebrafish. *http://zfin.org/zf_info/zfbook/zfbk.html*.

Wong KS, Rehn K, Palencia-Desai S, Kohli V, Hunter W, Uhl JD, Rost MS, Sumanas S. 2012. Hedgehog signaling is required for differentiation of endocardial progenitors in zebrafish. *Developmental Biology* **361**:377–391. doi:10.1016/j.ydbio.2011.11.004

Wu B, Wang Y, Lui W, Langworthy M, Tompkins KL, Hatzopoulos AK, Baldwin HS, Zhou B. 2011. Nfatc1 coordinates valve endocardial cell lineage development required for heart valve formation. *Circulation Research*. doi:10.1161/CIRCRESAHA.111.245035

Xiao C, Gao L, Hou Y, Xu C, Chang N, Wang F, Hu K, He A, Luo Y, Wang J, Peng J, Tang F, Zhu X, Xiong J-W. 2016. Chromatin-remodelling factor Brg1 regulates myocardial proliferation and regeneration in zebrafish. *Nat Commun* **7**:13787. doi:10.1038/ncomms13787

Xiong J, Kawagishi H, Yan Y, Liu J, Wells QS, Edmunds LR, Fergusson MM, Yu ZX, Rovira II, Brittain EL, Wolfgang MJ, Jurczak MJ, Fessel JP, Finkel T. 2018. A Metabolic Basis for Endothelial-to-Mesenchymal Transition. *Molecular Cell*. doi:10.1016/j.molcel.2018.01.010

Yelon D, Horne SA, Stainier DY. 1999. Restricted expression of cardiac myosin genes reveals regulated aspects of heart tube assembly in zebrafish. *Dev Biol* **214**:23–37. doi:10.1006/dbio.1999.9406

Yonemura S, Wada Y, Watanabe T, Nagafuchi A, Shibata M. 2010. α-Catenin as a tension transducer that induces adherens junction development. *Nature Cell Biology* **12**:533–542. doi:10.1038/ncb2055

Yue Y, Zong W, Li X, Li J, Zhang Youdong, Wu R, Liu Yazui, Cui J, Wang Q, Bian Y, Yu X, Liu Yao, Tan G, Zhang Yunfeng, Zhao G, Zhou B, Chen L, Xiao W, Cheng H, He A. 2020. Long-term, in toto live imaging of cardiomyocyte behaviour during mouse ventricle chamber formation at single-cell resolution. *Nat Cell Biol* **22**:332–340. doi:10.1038/s41556-020-0475-2

Zhang H, von Gise A, Liu Q, Hu T, Tian X, He Lingjuan, Pu W, Huang X, He Liang, Cai C-L, Camargo FD, Pu WT, Zhou B. 2014. Yap1 Is Required for Endothelial to

Mesenchymal Transition of the Atrioventricular Cushion. *J Biol Chem* **289**:18681–18692. doi:10.1074/jbc.M114.554584

Zulueta-Coarasa T, Rosenblatt J. 2022. The role of tissue maturity and mechanical state in controlling cell extrusion. *Current Opinion in Genetics & Development* **72**:1–7. doi:10.1016/j.gde.2021.09.003

Zygmunt T, Gay CM, Blondelle J, Singh MK, Flaherty KM, Means PC, Herwig L, Krudewig A, Belting H-G, Affolter M, Epstein JA, Torres-Vázquez J. 2011. Semaphorin-PlexinD1 Signaling Limits Angiogenic Potential via the VEGF Decoy Receptor sFlt1. *Developmental Cell* **21**:301–314. doi:10.1016/j.devcel.2011.06.033